People's Democratic Republic of Algeria
Ministry of Higher Education and Scientific Research

Ibn Khaldoun University -Tiaret-
Faculty of Material Sciences
Department of Physics

THESIS

Presented by
Mrs. GUETTAF Hadjer

In view of obtaining the degree of:
DOCTORATE IN SCIENCES

OPTION: Materials Physics

SPECIALTY: Physics

THEME

STUDY OF BINARY IONIC LIQUIDS BY DIELECTRIC SPECTROSCOPY AND DATA MINING.

Defended on: 28/01/2026

In front of the jury composed of:

Pr. BAGHDAD Rachid	**Univ. IBN KHALDOUN- Tiaret**	**President**
Pr. SASSI Mohamed	**Univ. AHMED BEN BELLA - Oran 1**	**Examiner**
Pr. BELHOCINE Mohamed	**Univ. AHMED BEN YAHIA ELWANCHARISSI - Tissemsilt**	**Examiner**
Pr. BADAOUI Mohamed	**Univ. IBN KHALDOUN -Tiaret**	**Examiner**
Pr. BELARBI El-habib	**Univ. IBN KHALDOUN -Tiaret**	**Supervisor**
Pr. BENKHETTOU Nour-Eddine	**Univ. Djillali Liabes - Sidi Belabbes**	**Co-Supervisor**
Pr. DEBDAB Mansour	**Univ. IBN KHALDOUN -Tiaret**	**Guest Examiner**

Academic Year: 2025/2026

Acknowledgements

*First and foremost, I would like to extend my deepest gratitude to Almighty **ALLAH** for granting me all that I possess and for always guiding my steps on the path of knowledge.*

*I want to express my sincere appreciation to my supervisor, **Professor El-Habib Belarbi**, who guided me with great patience throughout the preparation of this work. His invaluable assistance illuminated my path toward the successful completion of this research. I am sincerely thankful for his dedication, patience, and kindness.*

*I also express my sincere gratitude to **Professor Rachid BAGHDAD** of Ibn Khaldoun University, Tiaret, who did me the great honor of chairing the defense committee.*

*My warm thanks are extended to the examiners: **Professor Mohamed Sassi** of Ahmed Ben Bella University – Oran 1, **Professor Mohamed Belhocine** of Ahmed Ben Yahia Elwancharissi University – Tissemsilt, and **Professor Mohamed Badaoui** of the University of Tiaret. They deserve my utmost respect and heartfelt thanks for the interest they have shown in this work and for kindly agreeing to evaluate it.*

*I am equally grateful to **Professor Mansour DEBDAB** of the University of Tiaret, who did me the honor of serving as a guest examiner for this work.*

*My gratitude also extends to the entire team of the **Laboratory of Synthesis and Catalysis** at the University of Tiaret for their valuable support.*

*I would like to thank **all the professors at Ibn Khaldoun University** of Tiaret who contributed to my education, as well as the university staff for their valuable assistance.*

*Finally, I would like to express my heartfelt gratitude to **my parents**, **my husband SAFA Brahim**, **my kids**, **my entire family**, and all **my loved ones** for their unwavering encouragement and support, which have contributed significantly to the smooth progress of my studies.*

I dedicate this work

to

Husband

Brahim

My Angels

Anes

Sadja *Malak*

أَلَمۡ نَشۡرَحۡ لَكَ صَدۡرَكَ (1) وَوَضَعۡنَا عَنكَ وِزۡرَكَ (2) ٱلَّذِيٓ أَنقَضَ

ظَهۡرَكَ (3) وَرَفَعۡنَا لَكَ ذِكۡرَكَ (4) فَإِنَّ مَعَ ٱلۡعُسۡرِ يُسۡرًا (5) إِنَّ مَعَ

ٱلۡعُسۡرِ يُسۡرٗا (6) فَإِذَا فَرَغۡتَ فَٱنصَبۡ (7) وَإِلَىٰ رَبِّكَ فَٱرۡغَب (8)

CHAPTER III

DATAMINING AND EXPREMENTAL METHODS

CHAPITRE IV

RESULTS AND DISCUSSIONS

IV.1 Prediction and Classification of Binary Ionic Liquids.

IV.2. Studies of Thermal and Dielectric Properties of Binary Ionic Liquids

IV.3. High ionic conductivity for ionic and poly ionic liquids based on 1-(hydroxyethyl)-3-vinylimidazolium cation

List of Abbreviations

Chapter I:

- IL: Ionic Liquid
- RTIL: Room-Temperature Ionic Liquid
- $AlCl_3$: Aluminum Trichloride
- BF_4^-: Tetrafluoroborate
- PF_6^-: Hexafluorophosphate
- F^-: Fluoride
- Cl^-: Chloride
- Br^-: Bromide
- I^-: Iodide
- NO_3^-: Nitrate
- $CH_3SO_3^-$: Methanesulfonate
- $CF_3SO_3^-$: Trifluoromethanesulfonate
- $CH_3C_6H_4SO_3^-$ (OTs): Tosylate
- $CF_3CO_2^-$: Trifluoroacetate
- OTf: Triflate
- Acroc: Acronym of the Cation
- Acroa: Acronym of the Anion
- $N(CN)_2^-$ (DCA): Dicyanamide Anion
- T_f: Melting Point
- T_g: Glass Transition Temperature
- $C_6F_{18}P^-$ (FAP): Tris(pentafluoroethyl)trifluorophosphate
- $C_2F_6NO_4S_2^-$ (NTf_2 or TFSI): Bis(trifluoromethane)sulfonimide

Chapter II :

- **D**: Dielectric displacement
- $\vec{\mathbf{E}}$: Applied electric field
- $\vec{\mathbf{P}}$: Polarization
- ε_0: Permittivity of free space (vacuum permittivity)
- ε^*: Complex permittivity
- ε': Real permittivity or dielectric constant
- ε'': Imaginary permittivity or dielectric loss
- ε_s: Static permittivity or permittivity at very low frequencies ($f \approx 0$)
- ε_∞: Permittivity at infinite or very high frequencies
- $\Delta\varepsilon$: Relaxation strength
- χ^*: Complex electric susceptibility
- δ: Loss angle
- **f**: Frequency
- **t**: Time
- ω: Angular frequency
- **Ea**: Activation energy
- **k**: Boltzmann constant

Chapter III:

- X: Data matrix representing the normal operation of the system
- $\hat{X}$: Estimation of X by the PCA model
- E: Error term
- Σ : Covariance matrix of X
- N: Number of measured samples
- M: Number of variables (dimension of the measured data space)
- l: Number of retained components in the PCA model (dimension of the principal component subspace)
- k: Time index
- x_i: The ith component of the vector x
- $\bar{x}$: Mean vector of x
- x(i): Vector x without its ith component
- P: Matrix of eigenvectors of Σ
- $\hat{P}$: Matrix of the first l eigenvectors of Σ
- $\hat{t}$: Vector of the first l principal components
- λ : Superlattice modulation period
- λ_i : The ith eigenvalue of Σ
- P_i: The ith eigenvector of Σ corresponding to λ_i
- e_i: Estimation error on the ith variable
- e: Vector of estimation errors

- PCA: Principal Component Analysis
- PC1: First Principal Component
- PC2: Second Principal Component

Chapter IV:

- TGA: Thermogravimetric Analysis
- DTG: Derivative Thermogravimetry
- DSC: Differential Scanning Calorimetry
- $[BMIM]BF_4$: 1-Butyl-3-methylimidazolium tetrafluoroborate
- $[EtOHMIM^+]$ $[Cl^-]$: 1-(Hydroxyethyl)-3-methylimidazolium chloride

- [EtOHMIM^{+}] [$H_2PO_4^{-}$]: 1-(Hydroxyethyl)-3-methylimidazolium dihydrogen phosphate
- TXI: Triple-Resonance Probes
- D_2O: Deuterium Oxide
- DMSO: Dimethyl Sulfoxide
- OH: Hydroxyl
- CH_2OH: Hydroxymethyl
- CH_2: Methylene
- H_2O: Water
- CH_3: Methyl

List of Symbols

- **°C**: Degree Celsius (unit of temperature)
- **K**: Kelvin (unit of absolute temperature)
- **mPa·s**: Millipascal second (unit of viscosity)
- **$S \cdot m^{-1}$; $mS \cdot cm^{-1}$**: Siemens per meter; Millisiemens per centimeter (units of conductivity)
- **$g \cdot cm^{-3}$**: Gram per cubic centimeter (unit of density)
- **M; mM; µM**: Meter; Millimeter; Micrometer (units of detection limit)
- **min; s**: Minute; Second (units of response time)
- **$mg \cdot mL^{-1}$; $mol \cdot L^{-1}$**: Milligram per milliliter; Mole per liter (units of concentration)
- **J**: Joule (unit of energy)
- **C**: Coulomb (unit of electric charge)

GENERAL INTRODUCTION

GENERAL INTRODUCTION

In recent years, ionic liquids (ILs) have emerged as one of the most promising classes of advanced materials, drawing significant attention from researchers in the fields of chemistry, materials science, and electrochemistry. These compounds, composed entirely of organic cations and inorganic or organic anions, remain in a liquid state over a wide temperature range, often below 100°C. Their unique combination of properties—including negligible vapor pressure, high ionic conductivity, wide electrochemical stability window, and excellent thermal and chemical resistance—has positioned them as versatile materials for a variety of technological applications. Such applications span energy storage, catalysis, separation processes, green solvents, and electrochemical devices, including fuel cells and batteries.

Among the different families of ionic liquids, imidazolium-based systems are particularly notable due to their tunable physicochemical properties and structural flexibility. By varying the nature of the cation, the anion, or both, it is possible to finely adjust the viscosity, thermal stability, conductivity, and solvation behavior of the ionic liquid. This tunability opens the door to the rational design of ionic liquids with properties tailored to specific industrial and scientific applications. However, to achieve this level of control, it is essential to develop a deep understanding of the molecular interactions, polarization phenomena, and charge transport mechanisms that govern their macroscopic properties.

The present work aims to provide a comprehensive study of imidazolium-based ionic liquids, focusing on the interplay between their thermal, dielectric, and electrical properties. To achieve this, the research integrates experimental characterization with data-driven analytical approaches, combining thermal analysis, dielectric spectroscopy, and statistical modeling. The objective is to uncover the fundamental mechanisms underlying polarization and relaxation processes, while simultaneously employing data mining techniques to predict and correlate the observed behaviors with structural and compositional parameters.

The first chapter, entitled "Ionic Liquids for Tunable Properties," provides an overview of ionic liquids as functional materials, emphasizing their synthesis, classification, and physicochemical properties. It highlights the relationship between their chemical structure and macroscopic properties, as well as their potential

applications in various technological fields. This chapter establishes the scientific foundation for understanding why ionic liquids have become central to the development of modern electrochemical and energy-related systems.

The second chapter, Polarization and Dielectric Relaxation, explores the theoretical and experimental aspects of dielectric phenomena in materials. It discusses how the application of an external electric field induces different polarization mechanisms—electronic, ionic, dipolar, and interfacial—and how these processes are linked to dielectric relaxation behavior.

The third chapter, Data Mining and Experimental Methods, presents the methodological framework used in this study. It introduces data mining techniques such as Principal Component Analysis (PCA) and Partial Least Squares (PLS) regression, which are applied to identify patterns, correlations, and predictive models within complex experimental datasets. Furthermore, it details the experimental techniques employed—namely Differential Scanning Calorimetry (DSC), Thermogravimetric Analysis (TGA), and dielectric spectroscopy—used to characterize the thermal transitions, stability, and electrical properties of the studied materials. Special attention is given to Broadband Dielectric Spectroscopy (BDS) as a powerful technique for studying the frequency- and temperature-dependent response of ionic liquids. This chapter serves to connect microscopic molecular dynamics to the macroscopic dielectric response observed experimentally. The integration of data analysis with experimental measurements enables a more comprehensive and systematic interpretation of the results.

Finally, the fourth chapter, Results and Discussions, presents and analyzes the main findings of this work. It covers the experimental results obtained from dielectric and thermal measurements, as well as the outcomes of PCA and PLS data modeling. The chapter demonstrates how these complementary approaches contribute to understanding the relationship between molecular structure, charge dynamics, and macroscopic properties. In particular, it examines the dielectric relaxation processes, activation energies, and conductivity behaviors of both monomeric and polymeric imidazolium-based ionic liquids, highlighting their potential as solid-acid electrolytes or proton exchange membranes.

In conclusion, this thesis integrates theoretical analysis, experimental techniques, and data mining methods to achieve a comprehensive characterization of ionic liquids. By combining these perspectives, it seeks not only to elucidate the fundamental physicochemical mechanisms governing ionic liquid behavior but also to contribute to the design of new functional materials with optimized dielectric and thermal properties. The outcomes of this research have direct implications for energy storage technologies, electrochemical systems, and advanced materials engineering, representing an essential step toward the rational development of next-generation ionic liquid-based materials.

CHAPTER I

IONIC LIQUIDS FOR TUNABLE PROPERTIES

INTRODUCTION

Ionic liquids (ILs) are often described as liquid salts materials that, unlike common table salt, remain in liquid form at or near room temperature. What makes them especially interesting is how they are built: an organic cation paired with either an organic or inorganic anion. This flexible yet straightforward pairing gives rise to an enormous variety of structures and, in turn, a wide range of physical and chemical properties that researchers can "tune" to their needs [1, 2].

Because of this structural versatility, ionic liquids can be designed to have specific viscosities, melting points, polarities, and solubilities [3]. They also possess other remarkable properties, including high ionic conductivity [4], strong chemical and thermal stability [5], very low vapor pressure [6], low viscosity [7], and the ability to dissolve both organic and inorganic compounds [8]. These features collectively demonstrate why ionic liquids are often regarded as safer and more environmentally friendly alternatives to traditional volatile organic solvents. [9].

Ionic liquids (ILs) have a "designer" nature. By carefully choosing the proper cation–anion combination, it is possible to create a liquid with properties tailored for a particular task—whether that's in catalysis, organic synthesis, energy storage, medicine, or advanced materials. This unique tunability has placed ionic liquids at the center of a fast-growing field, with researchers worldwide exploring how to unlock their full potential.

In this chapter, we present a descriptive study of ionic liquids, binary ionic liquids, and poly(ionic liquids), focusing on their main characteristics and emphasizing the predominance of advantages over disadvantages in various aspects of their use.

I.1 Ionic Liquids

I.1.1 The evolution of Ionic Liquids

Ionic liquids (ILs), defined as ambient-temperature liquids composed primarily of ions, have been intermittently studied since the 19th century [10]. However, they started to appear regularly in the broader scientific literature only towards the close of the 20th century. Over the past few decades, the study of ILs has surged, leading to tens of thousands of scholarly

articles covering a wide array of potential applications and establishing them as a significant focus in contemporary chemistry. They have even been recognised, justifiably, as a unique area of study [11].

The recent investigations began with the electrochemical studies by Angell and colleagues, which provided practical methods for handling chloroaluminate species, rather than the alkali chloroaluminates that were common at the time [10, 12]. This group of air and moisture-sensitive materials has been considered as the first generation of ILs and includes dialkylimidazolium and alkylpyridinium chloroaluminates, as shown in Figure 1. However, due to challenges in handling these materials, the research focused primarily on battery applications, which are inherently hermetically sealed by default.

The situation changed when Wilkes and Zaworotko [13], and Cooper and O'Sullivan [14] simultaneously described the first room-temperature, air- and water-stable ionic liquids. These constitute the second generation ILs (Figure 1) and include cations such as alkylpyridinium and dialkylimidazolium with tetrafluoroborate ($[BF_4]^-$), hexafluorophosphate ($[PF_6]^-$), nitrate ($[NO_3]^-$), sulfate ($[SO_4]^-$), acetate ($[CH_3COO]^-$), methanesulfonate ($[CH_3SO_3]^-$), and trifluoromethanesulfonate ($[CF_3SO_3]^-$) anions [13]. ILs were soon recognised as more environmentally friendly alternatives to volatile organic compounds because they have little to no vapour pressure [15]. Because of this, early research focused heavily on investigating their use as electrolytes and solvents in chemical reactions. This was the start of the "ILs as green solvents" era [16]. Thinking then evolved further, recognising that ILs can be tuned to possess Lewis and Brønsted catalytic activity, allowing their simultaneous application as both catalysts and solvents [17].

Toward the end of the 20th century, ionic liquids came to be viewed as "designer solvents," with millions of possible combinations of cations and anions that can deliver a material to serve the target application in a task-specific way, paving the way for the third generation of ILs (Figure 1) [18].

Today, ILs can be found in almost every corner of science, including CO_2 capture, catalysis, electrolytes, separations, thermoelectric materials, pharmaceuticals, and biomaterials [19-22].

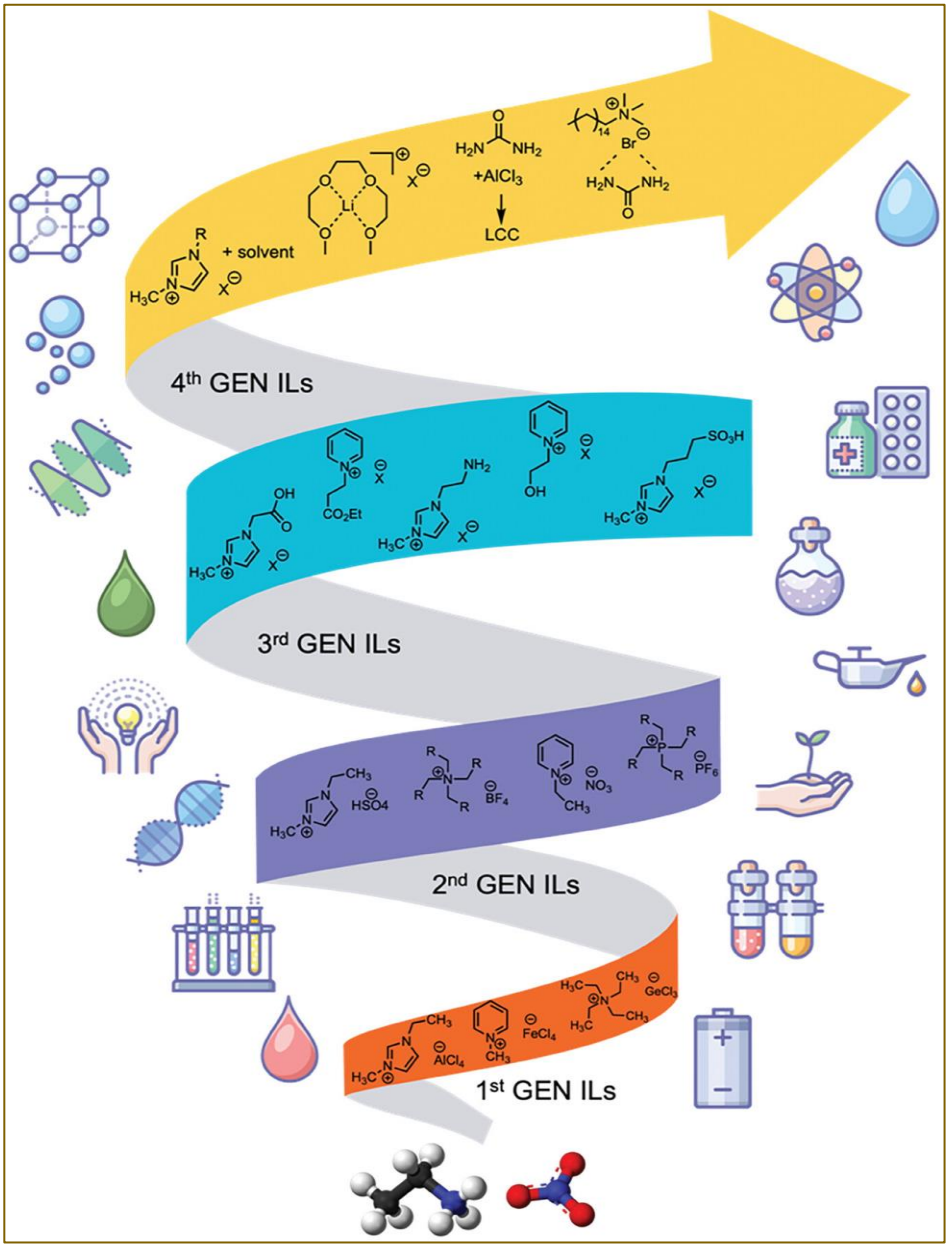

Figure.I.1 : *Ionic liquids went through conceptual development from the first to the fourth generations, with the latter introducing counterparts of ionic liquids. A generation is represented by each ribbon color, along with examples of the ILs which make up that generation. The icons on the sides represent the varied uses of ionic liquids (ILs) in different generations. Among these uses are as lubricants, solvents, catalysts, electrolytes in batteries and supercapacitors, and in space and medical applications. ILs are also used as azeotrope breakers, gas separations, phase change materials for thermal energy storage, polymer development, cellulose treatment, and gas absorption.*

I.1.2 Nomenclature of ionic liquids

As previously mentioned, ionic liquids are liquid salts that exhibit several distinctive features compared to traditional liquids. The features depend on the characteristics and dimensions of the cation and anion, as well as the equilibrium among Coulombic, van der Waals, hydrogen bonding, and π-π interactions. [23] Figure 2 illustrates the chemical structures of certain cations and anions. Ionic liquids (ILs) can be categorised as

monocationic, dicationic, or tricationic based on the quantity of charged atoms in the cation. Positive charges may reside on nitrogen, phosphorus, sulphur, or oxygen atoms, as well as on aromatic or non-aromatic heterocyclic structures. Anions, whether organic or inorganic, significantly influence the physical and chemical properties of the ionic liquid (IL) [24].

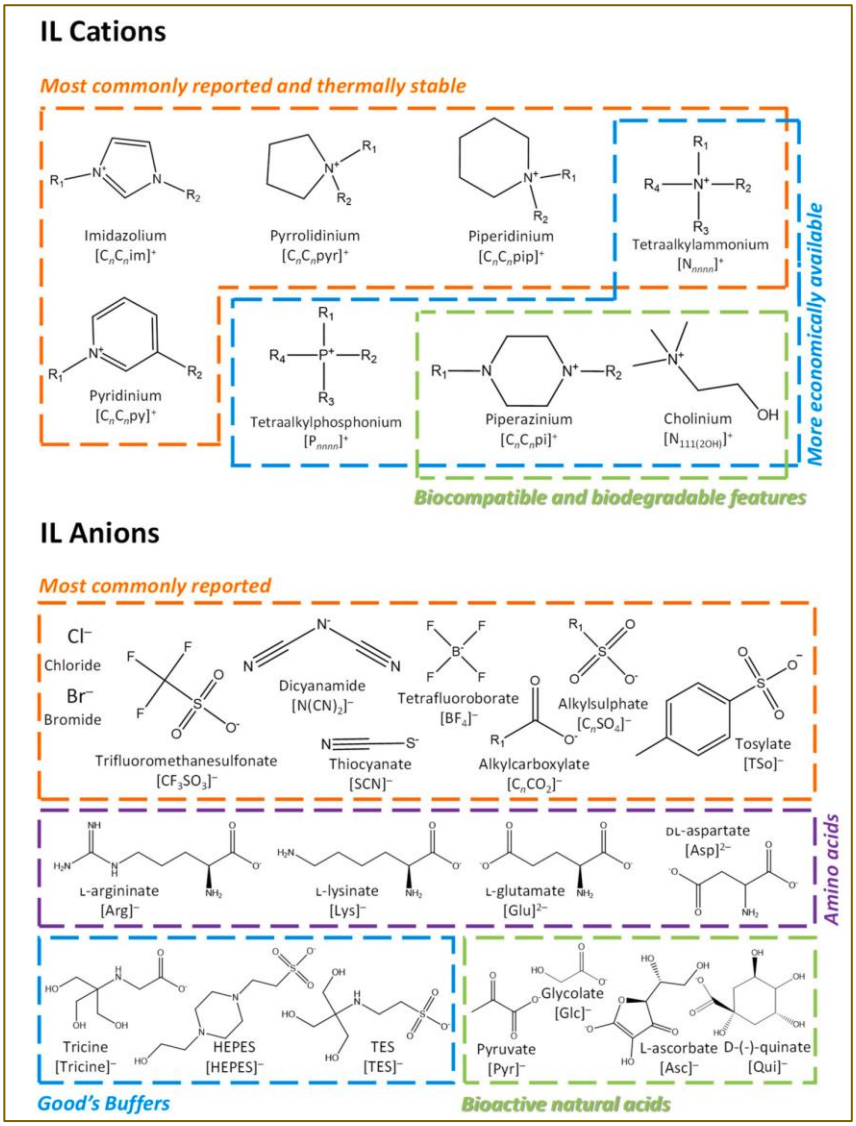

Figure.I.2: *Typical cationic and anionic structures employed in the construction of ionic liquids.*

I.2 Synthesis of imidazolium-based ionic liquids

Imidazolium-based ionic liquids are compounds rich in nitrogen heteroatoms, characterized by low melting points, high chemical stability, and superior ionization performance [25]. The use of imidazolium as a cation structure presents an interesting molecular strategy, owing to the stable positive charge on the aromatic ring, which functions as a versatile cation framework for ionic liquids.

The imidazolium cation ring typically contains two nitrogen atoms linked by a methylene group, as illustrated in Fig. 3. Thus, the nitrogen atoms in the imidazole ring are classified as N1 (amino nitrogen) donor and N3 (imino nitrogen) acceptor [26]. The preparation of imidazolium-based ionic liquids involves the quaternization of the imidazole ring with organic substituents, particularly alkyl and aryl groups, as well as tertiary nitrogen (N3), resulting in a permanent positive charge. This enables the imidazole ring to accept and donate protons during substitution reactions. Furthermore, secondary amine (N1) exhibits various reactions that enhance its amphoteric behavior, allowing it to both receive and donate protons, as well as its tunable properties in imidazolium [27, 28]. Imidazolium-based ionic liquids provide numerous applications in catalysis [29], sensors [30], adsorption [31-33], and biomass pretreatment [34].

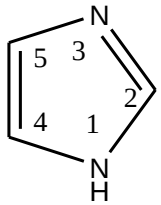

Figure.I.3: *The imidazole ring with numbered position.*

The synthesis of imidazolium-based ionic liquids can be conducted using several preparation methods, including diverse chemical reagents and reaction conditions, as indicated in the existing literature. Nonetheless, the synthesis process utilising standard thermal heating and instrument-assisted procedures, including alkylation, quaternization, and anion exchange reactions, typically involves distinct reaction pathways. The traditional thermal heating method for the preparation of ionic liquids (ILs) requires extended reaction times at temperatures exceeding 70 °C. The instrument-assisted method commonly employs radiation energy from ultrasound, microwave, and microreactor for the synthesis of ILs. This technique enhances reaction rate and conversion efficiency, resulting in increased yield of ILs products. This technique demonstrates low solvent consumption, high energy efficiency, and milder operating conditions [35, 36]. Although conventional techniques may require longer reaction times to produce ILs products, they remain more prevalent in the literature compared to instrument-assisted techniques, which entail higher capital and operational costs. Table 1 summarizes the various preparation methods for imidazolium-based ionic liquids.

Cation	*R_1*	*R_2*	*Anions (X^-)*	*Method*	*Findings*	*Application*	*Ref.*
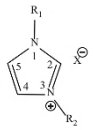	CH_3	2-phenoxyethyl and 3-phenoxypropyl	Br^-	Microwave-assisted (Scheme 1)	3-phenoxypropyl increased the hydrophobicity of ILs, rendering them highly selective	Toxicity and antibacterial activities	[1]
	C_n (n = 8, 10, 12, 16)	$CH_2{=}CH_2$	Br^-	Conventional heating	ILs with C_{12} exhibit small particle size (32 nm) compared to others (n = 8, 10, 16)	Antibacterial activities	[37]
	C_nCH_3 where (n=1,2,3,4 and 5) and benzyl CnCH3 where (n=2,3,4,6,8,10, and 12), 1,2-dimethyl, methylcyclohexyl, isopropyl, and sec-butyl	$CH_2{=}CH_2$	Tf_2N^-	Conventional heating	Styrene-functional ILs polymerized rapidly in neat formulations or with non-polymerizable $[C_2mim][Tf_2N]$	Polymerization behavior study	[38]
	$CH_2{=}CH_2$	C_8H_{18}	Br^-	Ultrasonic irradiation (Scheme 2)	Ultrasound technique affected surface morphology, shape, and size of ILs	Comparative analysis with conventional techniques	[35]
	1-CH_2-1-OH-2-alkyl-imidazolium iodide (IM-E-C_n-ImI), n = 13, 15, 17	—	I^-	Conventional heating	ILs showed high dispersibility and stabilization of double-walled carbon nanotubes in water	Stabilization and dispersion study	[39]
	C_7H_{16}	CH_3	Br^-	Ultrasound-, microwave-, microreactor-assisted, and conventional heating	Ultrasound technique promoted productivity; microwave-assisted was least favorable	Comparative analysis of methods	[40]
	CH_3	C_4H_{10}	BF_4^-, PF_6^-, $CF_3SO_3^-$, BPh_4^-, $RCOO^-$, $(CF_3SO_2)_2N^-$	Ultrasound-assisted and mechanical stirring (Scheme 3)	BMIM with BF_4^- anion showed higher yield (94%) than others under low-frequency ultrasound	Comparative analysis of methods	[41]
	CH_3	$C_{16}H_{33}$	Br^-	Conventional heating (Scheme 4)	Increasing alkyl chain length enhanced hydrophobicity and IL–Montmorillonite performance	Removal of amaranth dye	[42]
	C_n (n = 8, 10, 12)	CH_3	BF_4^-	Conventional heating	Surface tension and micelle compactness decreased with longer alkyl chains	Surface properties and micellization study	[43]
	$CH_2{=}CH_2$	C_n (n = ethyl, pentyl, benzyl, naphthyl)	Br^-	Conventional heating (Scheme 5)	Only ethyl, pentyl, and naphthy exhibited stable solid membrane with high CO2 and N2 permeability	CO_2 and N_2 separation	[44]
	C_n (n = 4, 8, 16)	CH_3	Br^-, OH^-, BF_4^-	Conventional heating	Interlayer spacing of MMT clay increased with longer alkyl chain; BF_4^- improved thermal stability	Organic composites	[45]
	C_4H_{10}	C_4H_{10}	Br^-, BF_4^-, SO_3^-, Tos^-, TfO^-	Ultrasound-assisted (Scheme 6)	Br^- promoted higher IL yield (95%) and faster reaction (2.5 h) with higher conductivity (0.23 S/m)	Comparative analysis with conventional methods	[46]

TableI.1 *Summary of various methods to synthesize imidazolium-based ionic liquids.*

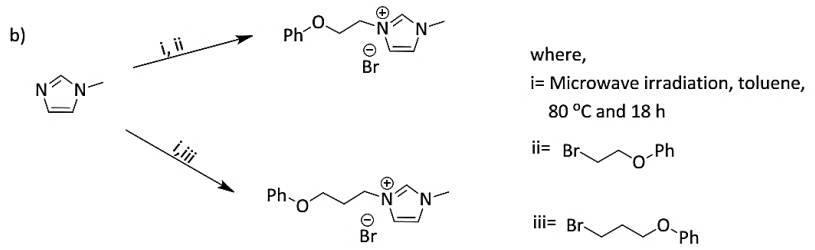

Scheme.I.1. *Synthesis of imidazolium-based ILs with different cation's substituents. Reprinted from Ref. [2], Copyright (2018), with permission from Elsevier.*

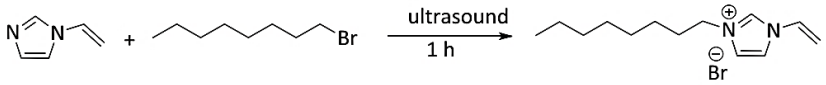

Scheme.I.2. *Synthesis of 3-octyl-1-vinylimidazolium bromide. Reprinted from Ref. [52], Copyright (2019), with permission from Elsevier.*

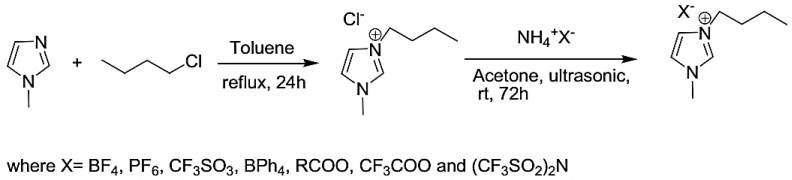

Scheme.I.3. *Synthesis of 1-butyl-3- methylimidazolium with various counter anions. Reprinted from Ref. [61], Copyright (2006), with permission from Elsevier.*

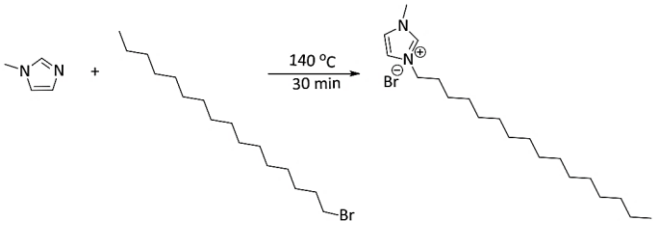

Scheme.I.4. *Synthesis of 1-methyl-3-decahexylimidazolium bromide. Republish from Ref. [62]. Copyright (2015), with permission from Royal Society of Chemistry.*

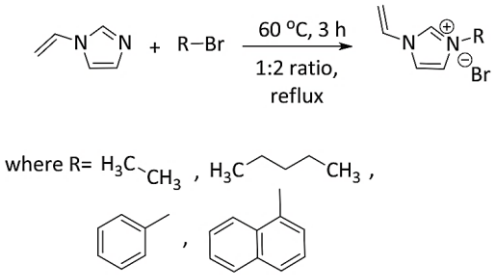

Scheme.I.5. *Synthesis of ILs with different side chain groups. Reprinted (adapted) with permission from Ref. [64]. Copyright (2019) American Chemical Society.*

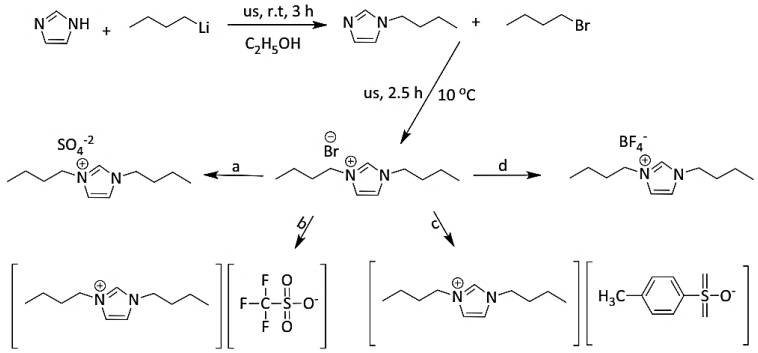

where,

d= Sodium tetrafluoroborate, us, r.t, dry acetone

b= Sodium trifluoromethylsulphonate, us, 50 °C, dry acetone

c= p-Toluenesulphonic acid monohydrate, us, 50 °C, dry acetone

a= Silver sulphate, us, r.t, dry acetone

us= ultrasound radiation

r.t= room temperatur

Scheme.I.6. *Synthesis of imidazolium-based ILs with various anion. Reprinted from Ref. [66], Copyright (2015), with permission from Elsevier.*

I.3 The application of imidazolium-based ILs in polymer preparation

In recent years, the polymerisation of ILs monomers through the use of polymeric ionic liquids or poly(ionic liquids) (PILs) has been found to yield ILs that exhibit distinctive characteristics and adaptability. To enhance processability and mechanical stability, favourable macromolecular architectural properties with improved durability and spatial control were achieved in the ionic liquids [47, 48]. The synthesis of ILs monomers typically involves the desired starting material under controlled conditions, including temperature, stirring rate, and duration. The production of PILs proceeds via a polymerization process using an initiator and a specific solvent [47].

Imidazolium-based ionic liquids have garnered significant scientific interest. They are extensively studied as monomer units for polymerisation due to the distinctive features of aromatic rings that exhibit a positive charge in a quaternary amine state [5, 49, 50].

Imidazolium-based PILs can be synthesised using appropriate procedures and reagents, offering numerous advantages for diverse applications and industrial processes. [51-53].

Three primary methods can be utilised to produce imidazolium-based poly(ionic liquids) (PILs): i) pre-polymerisation of IL monomer, ii) post-polymerisation modification, and iii) step-growth polymerisation.

I.3.1 The Pre-Polymerisation of ILs Monomer

Pre-polymerisation (direct polymerisation) refers to the transformation of monomers into a partly polymerised state or pre-polymer during the first phase of synthesis.

Maksym et al. reported the effect of different alkyl groups on the homopolymer-type PILs prepared through RAFT direct polymerisation in 2,2'-azobisisobutyronitrile (AIBN) and trithiocarbonate RAFT agent as initiators (Scheme 7). Poly(1-ethyl-3-vinylimidazolium bis(trifluoromethanesulfonyl)imide) (p[EVIM][NTf_2]) was found to have a higher molecular weight, dispersity, and thermal stability, with longer chains producing a lower glass transition temperatures, indicating the influence of alkyl chain length on the physical and thermal properties of PILs [54].

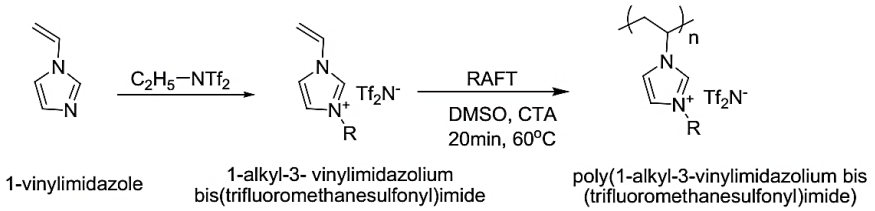

where R= -CH_3 or -CH_2CH_3

Scheme.I.7. *Pre-polymerization technique for the synthesis of homopolymer-type PILs [54].*

At the same time, Zhang et al. demonstrated that polyimidazolium chloride salts (PImCl) synthesized via direct polymerisation could be chelated with palladium chloride in 3-chloropyridine (Pd) to form N-hetericyclic carbenes-Pd (NHC-Pd) polymer. Adding PImCl to NHC-Pd polymer improves catalytic activity surface contact with the substrate by creating a mesoporous structure (fig. 4) [55].

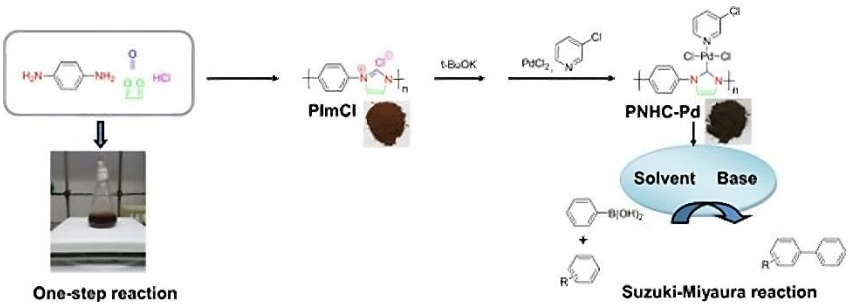

Figure.I.4. *Schematic illustration of the synthesis of polyimidazolium chloride salts (PImCl) via direct polymerisation, followed by chelation with palladium chloride in 3-chloropyridine to form N-heterocyclic carbene–palladium (NHC–Pd) polymer complexes, which serve as efficient catalysts for the Suzuki–Miyaura reaction [55].*

Jacinto et al. achieved direct photopolymerisation of poly (1–vinyl-3-ethyl imidazolium bis(trifluoromethylsulfonyl)imide) (poly(VEIM-TFSI)) using 2-hydroxy- 2 methylpropiophenone as photoinitiator (fig. 5), which enabled bacteriophage purification through electrostatic interactions. The proposed mechanism relies on a predominant anion exchange process [56].

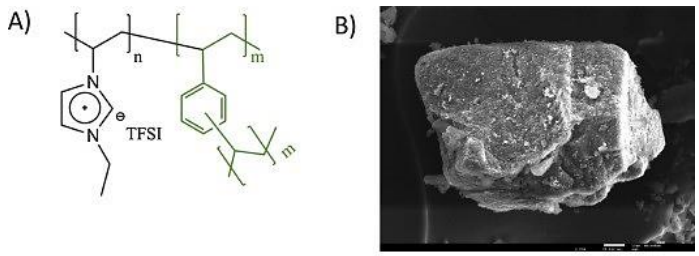

Figure.I.5. *(A) Chemical structure of poly(1–vinyl-3-ethylimidazolium bis(trifluoromethylsulfonyl)imide) (poly(VEIM–TFSI)). (B) Scanning electron microscopy (SEM) image showing the morphology of poly(VEIM–TFSI) [56].*

By investigating how the amount of 1-ethyl-3-methylimidazolium bistriflimide ([C_2mim][Tf_2N]) monomers affecting the interaction on the polymerization process, Whitley et al. highlighted that intermolecular interactions, such as π–π stacking and IL aggregation, influence polymerisation behaviour [38]. Figure 6 (vinyl C–H bending data and C=C stretching frequency), demonstrates that substituent size directly influences the electronic environment and vibrational characteristics of the polymerizable ionic liquid monomers. Both C–H and C=C vibrational shifts reflect changes in intermolecular π–π interactions and ionic liquid aggregation behavior, which ultimately affect polymerization dynamics.

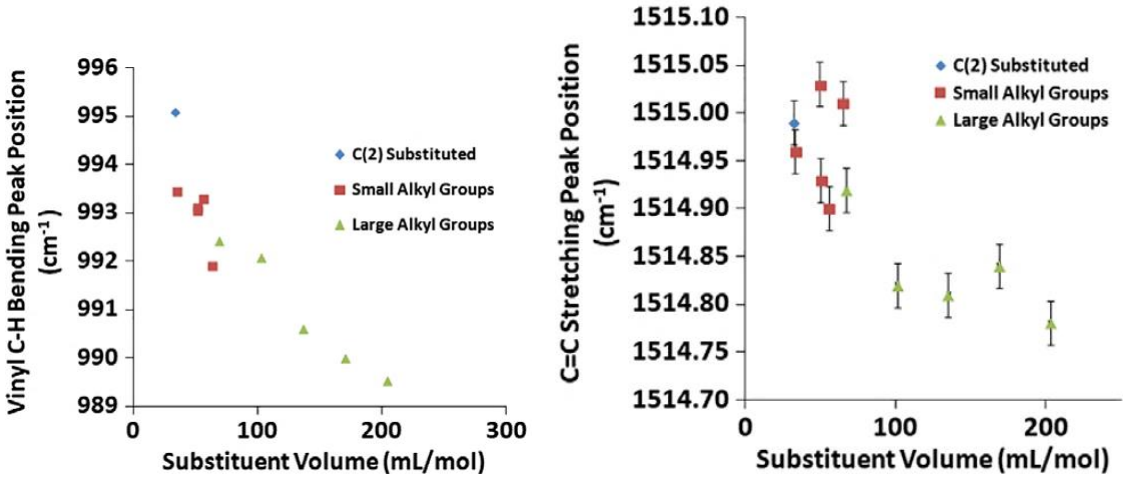

Figure.I.6*. (A) Plot displaying variation of the position of the infrared band (± 0.048 cm^{-1}) corresponding to the vinyl C–H out-of-plane deformation for Sim PIL monomers. (B) Plot displaying position of infrared bands corresponding to aromatic C=C stretching (bordered markers; ± 0.023 cm^{-1}) of Sim PILs [38].*

Similarly, Zaoui et al. developed a nanoscale, permanently porous poly(3-octyl-1-vinylimidazolium) bromide (PVIM-Oct-Br) via ultrasound-assisted direct polymerisation (Scheme 8) [35].

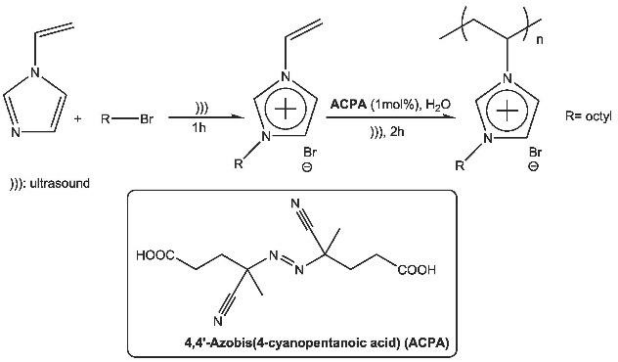

Scheme.I.8. *Synthetic route to obtain the PVIM-Oct-Br by an ultrasound irradiation [35].*

Yin et al. proposed a three-step method for poly(1-ethyl-3-vinylimidazolium bis(trifluoromethanesulfonylimide)) (P(EtVIm-TFSI)), starting with the direct radical polymerisation of 1-vinylimidazole monomer, followed by the quaternisation reaction, and finally undergoing an anion exchange process (Scheme 9), improving the electrochemical performance of polymer electrolytes in lithium-ion batteries [53].

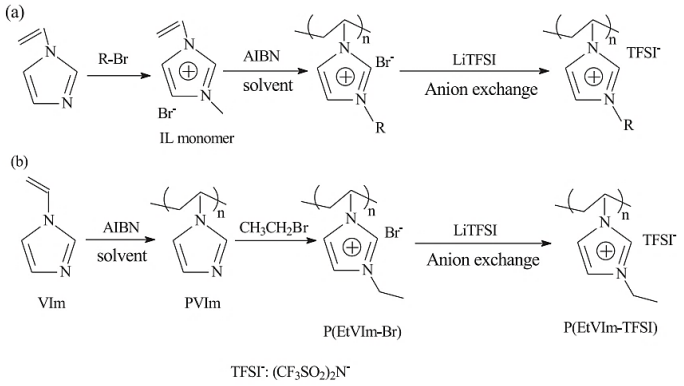

Scheme.I.9. *(a) The conventional synthetic route of the imidazolium-based PIL and (b) new synthetic route of the imidazolium-based PIL [53].*

Furthermore, Liu et al. demonstrated that the length of alkyl spacers in bis-vinylimidazolium-based PILs significantly affects ion transport dynamics and interfacial polarisation, as confirmed by dielectric spectroscopy and WAXS analysis (Fig. **7**) [53].

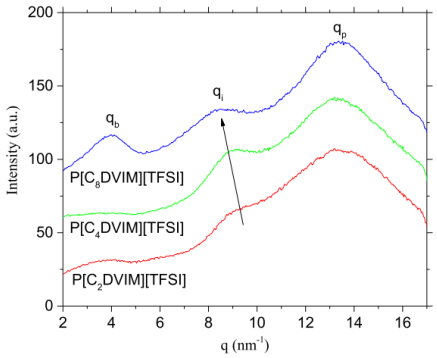

Figure.I.7. *Wide-angle X-ray scattering spectra for P[C_nDVIM][TFSI]. Three scattering peaks corresponding to the main chain correlation length for the lowest q, q_b, the anion-anion correlation length for the interm[57]ediate q, q_i, and the alkyl group correlation length for the highest q, q_p [53] .*

I.3.2 The Post-Polymerisation Modification

The post-polymerisation modification of imidazolium-based PILs provides an effective route to tailor functional groups and develop 'smart polymers' with application-specific properties, inspiring potential real-world applications [27, 28, 58].

Tseng et al. synthesised co-poly(ionic liquids) (co-PILs) via the free radical copolymerisation using a combination of 1-(nbutylimidazole)-based ILs monomer (MEBIm-I), poly(ethylene glycol) methyl ether methacrylate (POEM), and acrylonitrile. The resulting co-PILs exhibited improved ionic conductivity and diffusion efficiency, achieving a maximum short-circuit current density of 16.0 mA cm^{-2} in DSSCs. This enhancement was attributed to the formation of ion transport channels between adjacent imidazolium cations and ethylene oxide segments in the co-PILs (fig. 8) [59].

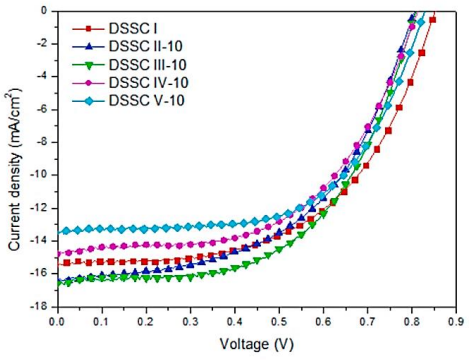

Figure.I.8. *Current density–voltage characteristics measured under AM 1.5G illu-mination (100 mW cm− 2) for DSSCs incorporating solution electrolytes based on ionic liquid copolymers. A higher value of JSC (16.6 mA cm- 2) and a higher PCE (7.5%) were observed for the ILPA431-based DSSC III-10 (copolymers ILPA431 was synthesized through co-polymerizations of MEBIm-I with POEM and acrylonitrile at various molar ratios) [59].*

While Thomas and Rajiv developed poly (ethylene oxide) (PEO) nanocomposites incorporating tungsten oxide nanoparticles (WO_3NPs), which exhibited superior photovoltaic performance in quasi-solid-state dye-sensitised solar cells (QSS-DSSC), the Poly (ethylene oxide–vinylimidazoliummethyl methacrylate iodide) (PVIM) membrane was consisted of uniform and beadless nanofiber, making it a promising functional electrolyte for QSS-DSSC [60].

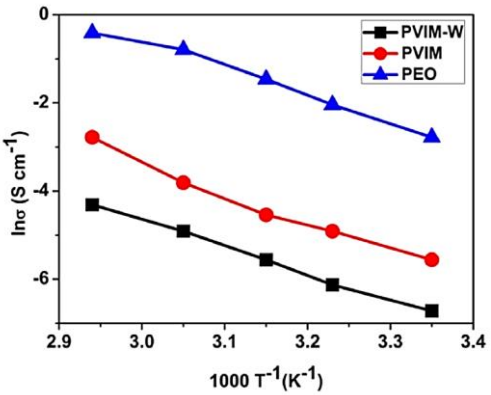

Figure.I.9. *Arrhenius plot of PEO, PVIM and PVIM-W membranes, the linear increase in ionic conductivity with temperature was observed for all the membranes according to the Arrhenius conduction mechanism. As shown, NPs incorporated PVIM-W exhibited higher ionic conductivity among all the three samples. This clearly pointed out that PVIM-W introduced conducting channels into the membrane for efficient ionic transport [60].*

Further advancements include grafting poly(vinylimidazolium) bromide (PVImBr) and poly(4,4'-diphenylether-5,5'-bibenzimidazole) (OPPBI) onto the surface of silica nanoparticles (SiNP) via the RAFT technique, to enhance crystallinity, mechanical strength, and proton conductivity. An XRD analysis revealed that the PVImBr exhibited an ordered crystalline matrix in the 2θ range of 5 – 25°, due to the interactions of hydrogen bonding between the nitrogen from PVImBr and the hydrogen in amine from OPPBI (fig. 10) [61].

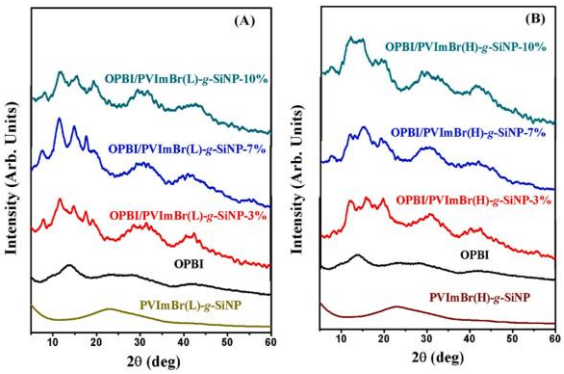

Figure.I.10. PXRD of (A) PVImBr(L)-g-SiNP and (B) PVImBr(H)-g-SiNP incorporated OPBI nanocomposite membranes at their indicated compositions [61].

Green et al. have made a significant breakthrough in the field of polymer chemistry by synthesising ABA triblock copolymers, specifically poly(1-(4-vinylbenzyl)imidazole-co-n-butyl acrylate). Their work resulted in a reduction of the T_g value from 345 K to 261 K, and an increase in ionic conductivity from 0.271 to 1.750 S/cm (fig. 11). This remarkable improvement was primarily attributed to the innovative quaternization of imidazole, which led to the generation of additional IL monomer within the copolymer [62].

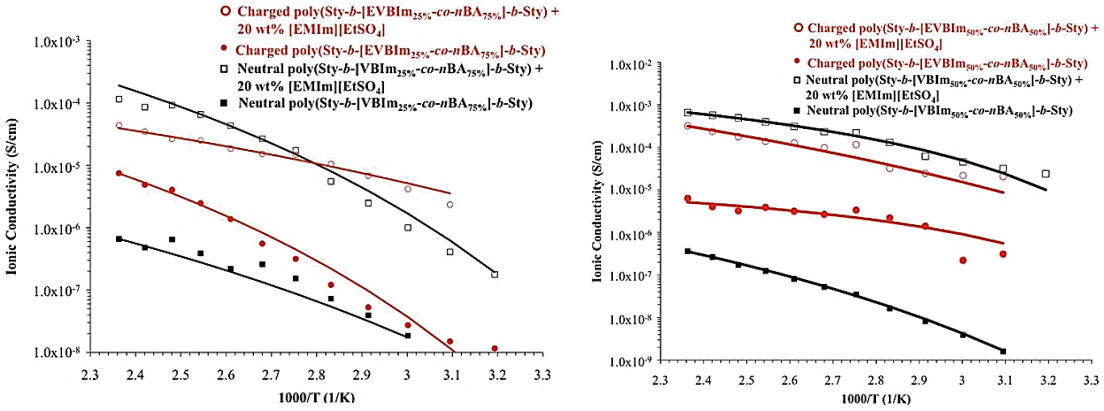

Figure.I.11: *(A) Ionic conductivity for neutral poly(Sty-b-[VBIm25%-conBA75%]-b-Sty) and charged poly(Sty-b-[EVBIm25%-co-nBA75%]-b-Sty) triblock copolymers in the presence and absence of added IL. Solid lines indicate analysis using the VFT equation. (B) Ionic conductivity for neutral poly(Sty-b-[VBIm50%-conBA50%]-b-Sty) and charged poly(Sty-b-[EVBIm50%-co-nBA50%]-b-Sty) triblock copolymers in the presence and absence of added IL, solid lines indicate analysis using the VFT equation [62].*

I.3.3 Step-Growth Polymerisation

Step-growth polymerisation has been explored as an alternative route for synthesising imidazolium-based PILs, though its use is limited due to poor control over chain length and dispersity [63, 64].

Roeleveld et al. successfully applied this method to produce poly(C3Im$^+$NTf$_2^-$), which exhibited higher thermal stability (325 °C) (Scheme 10). They demonstrated effective performance as a stationary phase in gas chromatography due to enhanced accessibility of imidazolium groups and favorable interactions with analytes [65].

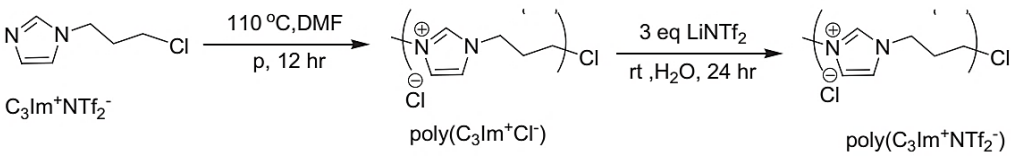

Scheme.I.10. *Synthesis route of poly(propylimidazolium-bis(trifluoromethane)sulfonamide)) via step-growth polymerisation method. Reprinted from [65].*

Moreover, Martin et al. developed step-growth synthesised PILs from N, N′-bis(hydroxyalkyl)imidazolium [Tf2N] and DABCO catalyst via alcohol–isocyanate polymerization (Scheme 11). These PILs served as protective coatings for industrial surfaces, with mechanical properties and curing times tunable by the structure and ratio of monomers used [66].

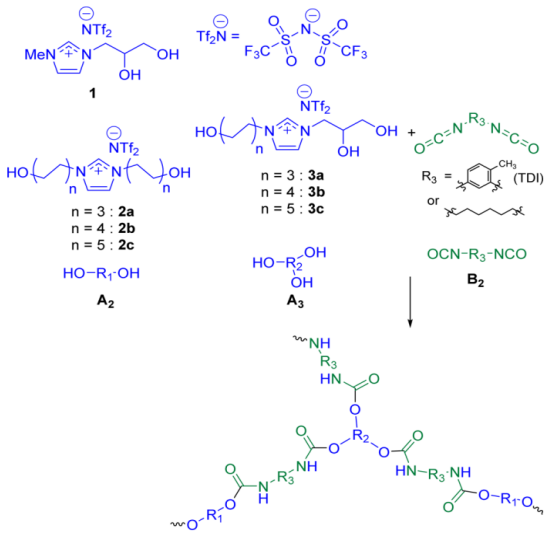

Scheme.I.11. *Structures of the Step-Growth Monomers and Resulting RTIL-Based Polymer Network. This New Spreadable Coating Material Is a Two-Component System That Consists of an Imidazolium-Based Polymer Network and Free RTIL [66].*

I.4 Presentation of binary ionic liquids

The appealing feature of ionic liquids lies in the ability to act as “designer solvents,” with tunable properties achieved by varying cation–anion combinations. More recently, this design concept has expanded to binary ionic liquids BILs [67], offering new opportunities to tailor physicochemical properties beyond those of individual components [68-70].

I.4.1 Nomenclature

The nomenclature of ionic liquid (IL) mixtures remains a subject of debate, as systems such as [A][X] + [B][X] or [A][X] + [A][Y] can be classified either by constituents (ions and molecules present) or by components (chemically independent species) [71]. For example, while NaCl in water contains three constituents (Na^+, Cl^-, H_2O), it has only two components (NaCl and H_2O). Similarly, IL mixtures may be considered ternary or quaternary in terms of constituents, but often remain binary when classified by components. Thus, mixtures such as

[A][B][X] or [A][X][Y] are referred to as binary ionic liquids, and [A][B][X][Y] are referred to as Reciprocal Binary ionic liquids (Table I.2) [72].

MIXTURE	ABBREVIATION	NO. OF COMPONENTS	NO. OF CONSTITUENTS	NAME
NONE	[A][X]	1	2	Simple
[A][X] + [A][Y] OU [A][X] +[B][X]	[A][X][Y] or [A][B][X]	2	3	Binary
[A][X] + [B][Y]	[A][B][X][Y]	2	4	Reciprocal Binary
[A][X] + [B][X] + [B][Y] OR [A][X] + [A][Y] + [B]	[A][B][X][Y]	3	4	Reciprocal Ternary
[A][X] + [A][Y] + [A][Z] OR [A][X] + [B][X] + [C][X]	[A][X][Y][Z] or [A][B][C][X]	3	4	Ternary

Table I.2: Nomenclature of Ionic Liquid Mixtures

I.4.2 Mixtures of ionic liquids

I.4.2.1 Raoult's Law and Ideal Solutions

The concept of an ideal solution, originating from Raoult's observations, describes a mixture in which the partial vapour pressure of each component is proportional to its mole fraction in the liquid phase [71]. Thermodynamically, the chemical potential of a component in an ideal solution is expressed in terms of its pure state as:

$$\mu_A^{id} = \mu_A^* + RT \ln X_A \qquad (I.1)$$

μ_A^{id} ***:*** *Chemical potential of component A in an ideal solution (the "effective" potential per mole of A in the mixture).*

μ_a^****:*** *Chemical potential of pure component A (when X_A=1). It represents the reference state.*

R: *Universal gas constant (8.314 $J \cdot mol^{-1} \cdot K^{-1}$).*

T: *Absolute temperature in kelvins (K).*

X_a***:*** *Mole fraction of component A in the solution (ratio of moles of A to total moles).*

ln X_a***:*** *Natural logarithm of the mole fraction — accounts for the entropy of mixing.*

Consequently, the Gibbs free energy and entropy of mixing are entirely governed by entropy, with no enthalpy contribution to the mixing process (I.2).

$$\Delta G_{mix}^{id} = nRT\,(X_A\, lnX_A + X_B \ln X_B) \qquad (I.2)$$

ΔG_{mix}^{id} *: Gibbs free energy change of mixing for an ideal binary solution.*

n: *Total number of moles of the mixture ($n = n_a + n_b$).*

R: *Universal gas constant.*

T: *Absolute temperature (K).*

X_a, X_b: *Mole fractions of components A and B, respectively.*

In binary ionic liquids, these relations imply that interionic interactions cancel, leaving entropy as the main driving force. However, not all properties vary linearly with composition; only those directly tied to Raoult's law must follow this trend, while others, such as spectroscopic properties, may show nonlinear behaviour [73-75].

I.4.2.2 Thermodynamics of an ionic liquid mixture

Direct thermodynamic data for ionic liquid (IL) mixtures are limited, so insights are often drawn from molten salt studies. In such systems, nearly ideal behaviour is sometimes observed, with minor deviations attributed mainly to ion size effects on Coulombic interactions. These typically yield small negative enthalpies of mixing (ΔH_{mix}), while positive ΔH_{mix} values arise from dispersion force contributions in size-similar ions [76-80].

Entropy of mixing (ΔS_{mix}) was initially assumed to be ideal [81], but small negative values have been reported, reflecting non-random ion distributions. These deviations were modelled using conformational ion-solution theory, incorporating non-random mixing terms [80, 82-84].

Experimental studies by Navia et al. [85] using microcalorimetry revealed small positive excess enthalpies (HE) for mixtures of different cations with a common anion, attributed to disruption of cation–cation dispersion interactions. Conversely, negative HE values were found for mixtures of different anions with a common cation, suggesting enhanced cation–anion bonding. Figure 3 illustrates these enthalpic trends across varying compositions.

Molecular dynamics simulations by Castejón and Lashock [86] supported these findings, showing nearly ideal mixing with small HE values. Systems with small, symmetrical ions exhibited negative, symmetric enthalpy–composition curves typical of regular solutions. In contrast, mixtures containing bulkier cations, such as $[C_4C_1im]^+$, showed slightly positive, asymmetric HE values, reflecting structural changes driven by steric effects. Nonetheless, imidazolium-based mixtures studied by Navia et al. [85] generally followed symmetric trends consistent with near-ideal behavior.

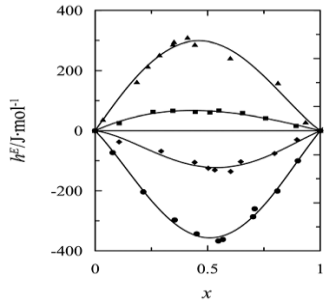

Fig.I.12. *Excess molar enthalpies based on composition at T = 303.15 K: ▲, X [C_6C_1im] [BF_4] + (1-X) [C_2C_1im] (BF_4); ■, X [C_4C_1im] [BF_4] + (1-X) [C_6C_1im] [BF_4]; ♦, X [C_4 C_1im] [PF_6] + (1-X) [C_4C_1im] [BF_4]; ●, X [C_5C_1im] [BF_4] + (1 - X) [C_4C_1im] [$MeSO_4$]. [85]*

I.5 Physicochemical Properties

I.5.1 Polarity

Ionic liquids are capable of interacting with both polar and nonpolar solutes. Because of this dual affinity, they are often described as organic salts with a distinctive polar character, sometimes exhibiting extreme polarity. Several studies provide useful data on the polarity of ionic liquids. Studies have shown that [BMIM][PF_6] has a polarity comparable to that of 1-butanol [87], whereas [BMIM][BF_4] demonstrates a polarity similar to methanol [88].

Generally, ionic liquids are considered polar yet weakly coordinating solvents, with polarity levels close to those of acetonitrile, N, N-dimethylformamide, short-chain alcohols [89], or dichloromethane [90]. Overall, due to the Coulombic interactions between their ions, the dipolar effects and polarisability of ionic liquids are stronger than those of conventional molecular solvents.

The significant polarity and the ability to dissolve a wide variety of organic and ionic compounds to a notable degree make ionic liquids attractive solvents for ionic polymerization processes. These properties significantly influence polymerization reactions, where serve as effective solvents or media that enhance reaction rates, facilitate product separation, and allow solvent recyclability, as shown in various cationic and ring-opening polymerizations [91-94].

In contrast, binary ionic liquids (BILs), formed by mixing two distinct ILs, exhibit complex polarity behaviour arising from microheterogeneities and preferential solvation effects. Experimental and solvatochromic analyses reveal that deviations from ideal mixing often occur, leading to nonlinear trends in polarity, hydrogen-bonding acidity and basicity,

and viscosity. Such effects depend strongly on ionic composition, specific ion–probe interactions, and localised solvation environments rather than bulk composition [95-99].

Pandey et al. have reiterated the importance of this for ionic liquid mixtures, in which unexpected behaviour could either be induced by the probe molecule itself, by either specific or non-specific interaction between it and the different solvent ions, thus enriching its solvation shell in a way that is not representative of the bulk liquid, or the ionic liquid mixture itself could form "micro-heterogeneities" which the probe molecule detects, but does not cause [96]. A notable deviation from simple linear behaviour upon mixing was observed for solutions of pyrene in all possible binary mixtures of the ionic liquids $[C_4C_1im][PF_6]$, $[C_4C_1im][NTf_2]$, and $[C_2C_1im][NTf_2]$ [97].

In general, conventional ILs have clear and predictable polarities. PILs use high polarity to improve polymerization control, and BILs have tunable solvation properties that depend on the composition of the solution and the interactions between ions and solutes.

I.5.2 Thermal stability

The thermal stability of ionic, polyionic, and binary ionic liquids exhibit distinct yet interconnected characteristics shaped by their molecular architectures.

Ionic liquids exhibit significant chemical stability; however, some exhibit super acidic behaviour [100]. Although it is recognised that the imidazolium ion is more chemically stable when substituted at the C2 position [101], nevertheless, ionic liquids composed of this ion can cause parasitic reactions [102, 103]. The anion's stability against hydrolysis is essential for handling ionic liquids. In contrast, the dealkylation of the cation can occur at high temperatures or according to the Hoffman elimination in sonochemistry [104]. Furthermore, ionic liquids exhibit high electrochemical stability, ranging from 5 to 6 Volts [105]. In these environments, electrolytic deposits of metals such as aluminium can form [106].

Polyionic liquids (PILs) exhibit a remarkable tolerance to various chemical environments; however, their stability is generally lower than that of monomeric ILs. This reduced stability primarily arises from the potential degradation and rearrangement of the polymer backbone under heat or irradiation. Specific examples demonstrate degradation via ring-opening and chain scission reactions, particularly in strongly alkaline or microwave environments. It is worth noting that PIL stability is significantly influenced not only by the

composition of the polymer backbone but also by the type of cation used, providing a comprehensive understanding of the factors that affect it.

For instance, Tang et al. demonstrated that the distinctive dielectric characteristics, including high dielectric constants and significant dielectric loss factors, of imidazolium- and tetraalkylammonium-based PILs render them potentially useful as transparent microwave-absorbing materials [107]. However, it is essential to recognise that not all PILs are appropriate for this purpose. Amajjahe and Ritter reported that poly(1-vinyl-3-tert-butoxycarbonylmethylene imidazolium) PILs release isoprene gas within seconds when exposed to microwave radiation [108]. This observation explained why a transparent film of this PIL could rapidly transition to an opaque state under microwave conditions. The microwave radiation appeared to act with remarkable specificity, promoting the structural rearrangement within bulk PILs.

In contrast, binary ionic liquids (BILs) exhibit thermal stability largely dictated by the behavior of their individual ionic components. Thermogravimetric studies show that mixtures often decompose in stepwise patterns corresponding to each constituent IL, though at certain compositions, cooperative stabilization can occur, yielding a unified decomposition profile [109].

In order to analyse the decomposition behaviour of mixes of [C4C1pyrr][NTf2] and [C3C1pyrr][FSI] containing 0.3 M LiX, thermogravimetric heating traces were acquired. The breakdown proceeds in two independent phases for X = [PF6]-, with onset temperatures that are about the same as those of the pure compounds (fig.13). These are probably the two ionic liquids that are breaking down independently. Only one standard decomposition temperature was discovered for X = [NTf2]-mixtures containing up to 13.2% (n/n) [C3C1pyrr][FSI], but at larger concentrations, each ionic liquid undergoes the exact step-wise breakdown [109].

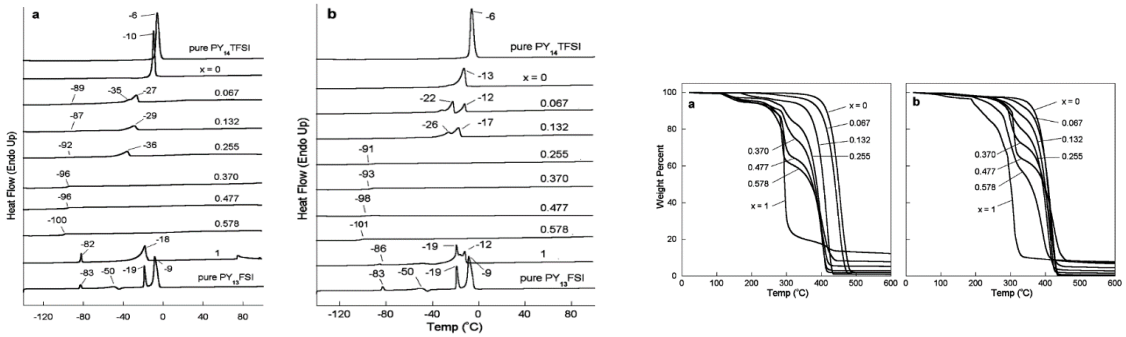

Figure.I.13. ** DSC heating traces (5 °C min-1) of (1-x) PY14TFSI-(x) PY13FSI-0.3 M LiX mixtures: (a) X) TFSI- and (b) X) PF6-. * Variable-temperature TGA heating traces (5 °C min-1) of (1-x) $PY_{14}TFSI$-(x) $PY_{13}FSI$-0.3 M LiX mixtures: (a) X) $TFSI^-$ and (b) X) PF_6^- (N_2 atmosphere).[109]*

Collectively, while ILs maintain the highest intrinsic thermal and electrochemical stability, PILs require structural optimization for thermal endurance, and BILs display composition-dependent stability governed by the interplay between their ionic species.

I.5.3 Density

The density of ionic liquids varies considerably with molecular architecture and composition, showing distinct trends across conventional, binary, and polymeric systems.

Ionic liquids (ILs) are generally denser than water, with values ranging from 1.0 to 1.6 $g \cdot cm^{-3}$, primarily governed by ionic packing and the size of the alkyl chains attached to the cation. An increase in alkyl chain length typically decreases density due to reduced packing efficiency, while density increases linearly with decreasing temperature [110-112].

Polyionic liquids (PILs), on the other hand, exhibit densities dependent on polymer chain structure and charge distribution. Although high charge density might suggest compact ion packing, PILs often exhibit moderate densities (around 1.6 $g \cdot cm^{-3}$) due to electrostatic shielding within the polymer matrix. Their tunable density arises from structural flexibility, the type of counterion, and the degree of crosslinking, allowing the synthesis of low-Tg, low-density materials suitable for functional and hybrid applications [113-116].

In binary ionic liquids (BILs), the mixing of two ionic components usually produces nearly ideal behavior, where molar volumes and densities vary linearly with composition. Most systems exhibit small positive or negative excess molar volumes (V^E), indicating only minor deviations from ideality, often attributed to slight ion size differences, dispersion interactions, or structural heterogeneities such as polar–nonpolar domain formation. Deviations become more pronounced when distinct ionic species or hydrogen-bonding interactions are involved, but overall, BILs tend to maintain additive density behavior close to that of their parent ILs [85, 117-121].

In the first comprehensive study on the excess volumes of ionic liquid mixes, Rebelo et al.[122] examined the mixing volumes of the mixtures $[C_nC_1im][C_mC_1im][NTf_2]$, $[C_4C_1im][PF_6][NTf_2]$, $[C_4C_1im][BF_4][NTf_2]$, and $[C_4C_1im][BF_4][PF_6]$. All of these mixes had almost linear mixing behaviour. The V^E for these combinations consistently measured low, remaining below 0.1% of the total volume and under 1.5% of the disparity in the molar volumes of the pure components. These observations were later supported by density

measurements conducted by Stoppa et al. and Larriba et al. indicated that the volumetric expansion (V^E) for $[C_2C_1im][N(CN)_2][BF_4]$ and $[C_4C_1pyrr][BF_4][NTf_2]$ were minimal and positive (less than 0.1%), consistent with the findings of Rebelo et al. for $[C_4C_1im][BF_4][PF_6]$.

Overall, BILs show almost perfect compositional dependency, PILs provide more tunability because of their macromolecular structure and less restrictive ionic packing, and ILs show high and consistent densities controlled by ionic size and temperature.

I.5.4 Viscosity

On initial view, any liquid medium that exhibits a degree of resistance to flow can be characterised as viscous. At the microscopic level, specific phenomena define this characteristic; the Van der Waals interaction forces and the capacity to form hydrogen bonds are the primary factors influencing the viscosity of ionic liquids [123]. Therefore, ionic liquids (ILs) exhibit viscosities one to three orders of magnitude higher than those of common organic solvents, typically ranging from 0.7 to 257,000 mPa·s at temperatures between 290–370 K [124]. The viscosity of ionic liquids is mainly related to the selection of the anion. Thus, low viscosity can be observed in the case of certain ionic liquids composed of anions that have a high charge delocalisation or weak hydrogen bonds [125]. The cation, in turn, plays a considerable role in changes in its value; as the carbon chains of the cations lengthen, the viscosity of the ionic liquid that constitutes them increases. On the other hand, by slightly increasing the temperature or adding small amounts of an organic cosolvent to ionic liquids, their viscosities can be reduced.

For binary ionic liquids (BILs), viscosity follows complex but predictable mixing behaviour. Studies show that most mixtures exhibit nearly ideal trends described by the Katti–Chaudhri (I.6) and Grunberg–Nissan mixing laws [126-130], with minor deviations attributed to molecular size disparities, ion aggregation, or entropic effects [85, 126, 131]

$$\log(\eta V) = X \log\,(\,\eta_1 V_1) + (\,1 - X) \log\,(\eta_2 V_2\,) + \frac{\Delta g^E}{RT} \qquad (I.3)$$

$$\log(\eta) = X \log\,(\,\eta_1\,) + (1 - X) \log(\eta_2) \qquad (I.4)$$

Generally, viscosity varies logarithmically with component ratio, increasing with higher salt content (e.g., $Li[BF_4]$ or Cl^- impurities) and displaying Vogel–Fulcher–Tamman temperature dependence typical of glass-forming liquids [131, 132].

$$\eta(T) = \eta_0 e^{\frac{B}{T-T_0}} \qquad (I.5)$$

Slightly non-ideal mixtures may exhibit positive or negative excess Gibbs energies of mixing (Δg^E), which correlate with changes in free volume and enthalpy [85, 126].

Polyionic liquids (PILs) demonstrate much higher and more tunable viscosities due to macromolecular architecture and ion confinement within polymer backbones. The viscosity of PIL-based electrolytes or gels depends strongly on molecular weight, polymer flexibility, and side-chain length, with longer alkyl groups increasing viscosity while reducing density [133, 134].

The viscosity of the polymerisation medium plays a crucial role in determining the kinetics of free-radical polymerisation in ionic liquids. As reported by Harrison et al. [133, 135], increasing medium viscosity decreases the termination rate constant (kt). This reduction is attributed to the restricted mobility of growing polymer radicals in a more viscous environment, which hinders their diffusion-controlled termination reactions.

I.5.5 Conductivity

Electrical conductivity in ionic systems is closely linked to ion mobility, viscosity, and structural organisation, displaying distinct patterns across conventional, binary, and polymeric ionic liquids.

The experimental electrical conductivity of ionic liquids documented in the literature ranges from 7×10^{-3} and 7 $S\cdot m^{-1}$ [136, 137]. It has a substantial correlation with transport parameters, including viscosity and self-diffusion coefficient, indicating that ion mobility governs this characteristic.

On the whole, the specific conductivities of imidazolium ILs are larger than those based on pyridinium, pyrrolidinium, and acyclic quaternary ammonium cations. However, all are considerably lower than those of concentrated aqueous electrolytes used in batteries, as shown by Galinski et al. [138].

In classical salt solutions, ions are separated by solvent molecules, leading to thermodynamic properties governed by ion-solvent, ion-ion, and solvent-solvent interactions. In ionic liquids, ions are always in contact with one another, with their thermodynamic properties determined by ion-ion interactions, London dispersion forces, and hydrogen

bonding. The 'free space model' or 'hole model' is the most efficient way to describe ionic liquids' conductivity. The idea is based on the fact that salts show a significant fusion volume (20-30% by volume) during melting. This model assumes that within the molten salt, there are empty spaces that constantly fluctuate due to thermal motion. To quantify a model, the chance of discovering a hole in IL is computed, yielding the diffusion coefficient and conductivity.

The diffusion coefficient and conductivity are expressed using the Vogel-Tammann-Fulcher (VTF) equation, which depends on the glass transition temperature (T_g) and the reference temperature (T_0). The VTF equation can be expressed in various modified forms, with the most common modification assuming temperature-dependent pre-exponential factors [138].

$$\sigma = \sigma_{\infty} \exp\left[\frac{-B}{(T - T0)}\right] \qquad (I.6)$$

$$\ln \sigma = \ln \sigma_{\infty} - \frac{B}{T - T_0} \qquad (I.7)$$

σ_{RT} *:Conductivity at room temperature*

T_g*: The glass transition temperature,*

σ_{∞}*: Logarithm of conductivity at* ∞*,*

B: *Describes the dependence of sigma as a function of temperature in the high-temperature limit and* T_0*,*

T_o*: The temperature at which the conductivity (σ) approaches zero is the Vogel temperature*.

For the conductivity of mixtures, there is no clear description of what would constitute ideal behaviour and therefore excess conductivity. MacFarlane et al. found positive deviation of the molar conductivity from a simple linear mixing rule for mixtures of $[C_2C_1im][NTf_2]$ and $[C_2C_1im][OTf]$ exceeding the value of the higher conducting simple liquid for all of the compositions studied [139]. The authors point out that this could be explained by either a larger number of charge carriers or their facilitated movement.

For mixtures of $[C_2C_1im][BF_4]$ and $[C_3C_1im]Br$, the conductivity was found to be less than expected from simple linear mixing, but not less than for the least conducting pure component, with no minima or maxima being identified [140]. For mixtures of $[C_2C_1im][BF4]$ and $[C_2C_1im][NTf_2]$, a negative deviation was found as well, with the conductivities of both of the mixtures studied being less than that of the least conducting pure component.

As one would expect from the viscosity results above, the temperature dependences of the conductivities of ionic liquid mixtures follow Vogel Fulcher–Tamman behaviour (eqn (I.7)), as do simple ionic liquids.[131] This is very typical of glass-forming materials. It is likely that a number of the observations above also result from ionic liquid mixtures forming glasses.

Unlike conventional ionic liquids (ILs), which allow both cations and anions to move freely, PILs typically behave as single-ion conductors. In these systems, one ionic species (either the anion or cation) becomes part of the polymer backbone, restricting its mobility. As a result, ionic conductivity significantly decreases after polymerisation, mainly due to an increase in glass transition temperature (T_g) and a reduction in mobile ions once covalent bonds form between ionic units [141].

For example, Colby et al. studied imidazolium-based PILs with varying spacer lengths and found that longer flexible spacers (containing alkylene or oxyethylene units) lower T_g and increase ionic conductivity [142]. This improvement arises from greater ion mobility and enhanced polymer polarizability.

Furthermore, Ohno and co-workers observed that extending the spacer between the polymerisable group and imidazolium cation—while simultaneously enlarging the anion—boosted conductivity by two orders of magnitude and reduced T_g by approximately 50 K [143].

Morphology also plays a significant role. Madsen et al. investigated block copolymers such as PS-b-PVBn(alkyl)IMTFSI and showed that defects and grain boundaries in lamellar and cylindrical microphases drastically lower ionic conductivity compared to homopolymers. Conductivity in ordered lamellar structures dropped by roughly one order of magnitude compared to their amorphous counterparts [114, 144].

The molecular weight of PILs affects multiple physical properties, including Tg, viscosity, and ionic conductivity. Studies by Fan et al. demonstrated that, as molecular weight increases, conductivity initially decreases (from monomer to trimer) but then plateaus beyond ~10^5 Da [145]. This is attributed to the decoupling of ion transport from segmental dynamics as the polymer becomes longer; ions move through a more frustrated, less cooperative matrix.

Tg correspondingly rises with molecular weight but stabilises when the polymerisation degree exceeds about n = 70, resembling the behaviour of flexible non-ionic polymers. Overall, higher molecular weights tend to suppress ionic conductivity while improving mechanical stability.

The glass transition temperature plays a central role in determining ionic conductivity. In general, a lower T_g enhances ionic mobility, leading to higher conductivity [146]. PILs often display lower T_g values than conventional polyelectrolytes because their ionic interactions are weaker and more delocalized.

For example, Elabd and co-workers showed that substituting the BF_4^- anion with the more flexible $TFSI^-$ anion in a poly(1-butyl-3-vinylbenzylimidazolium) system reduced T_g dramatically, which in turn improved ionic conductivity [147].

Overall, the trend in conductivity decreases in the order IL > BIL > PIL, reflecting the transition from freely mobile ions in simple ionic liquids to increasingly constrained ionic motion in binary mixtures and polymeric networks.

I.6 Applications of ionic liquids

1.6.1 Catalysis and Functionalization of Ionic Liquids

Ionic liquids (ILs) and their derivatives exhibit complementary catalytic properties that can be tailored for various chemical processes.

Mono-ionic liquids (ILs) can be chemically modified to stabilise homogeneous or heterogeneous catalysts, thereby enhancing catalytic performance and enabling catalyst recovery and recycling. Ionic liquids (ILs) are suitable for reactions that require harsh conditions because of their low vapour pressure and high thermal stability. Imidazolium-based ionic liquids modified with acidic groups exhibit improved catalytic efficiency in phase-transfer and acid-catalysed transformations, since these groups stabilise intermediates and boost activity [148]. Their modularity enables diverse reactions, such as hydrogenation and alkylation, while reducing environmental impact compared to traditional solvents.

Binary ionic liquids (BILs) function as adaptable solvent–catalyst systems, in which the combination of different ions precisely adjusts acidity, polarity, and coordination behaviour, thereby enhancing catalytic conditions. They have shown benefits in procedures

such as difasolt olefin dimerisation [149, 150], Ru-catalysed hydroformylation, and the production of metal-organic frameworks (MOFs) [151].

Poly-ionic liquids (PILs) function as solid or quasi-solid catalysts and supports, exceeding monomeric ionic liquids in mechanical stability, porosity, and reusability. Their catalytic performance can be modified by selecting cations and anions, as well as polymerisation methods. This is shown by PIL-supported metal nanoparticles used for dye degradation, recyclable Fenton-like oxidation catalysts [152], and pyridine-based PILs demonstrating high enantioselectivity in heterogeneous catalysis [153].

1.6.2 Electrochemical Applications of Ionic Liquids

Room-temperature ionic liquids (RTILs) have gained considerable attention in electrochemical technologies due to their intrinsic properties; notably high ionic conductivity, wide electrochemical windows, negligible volatility, and exceptional thermal and electrochemical stability [154]. They are used in batteries, capacitors, fuel cells, sensors, and solar systems, functioning as both solvents and electrolytes. However, limitations such as instability at highly negative potentials, particularly when in contact with lithium or graphite anodes, and poorly understood electrode–electrolyte interfacial chemistry remain barriers to their widespread commercialisation [155]. Takaya et al. [156] reported that ammonium-based RTILs with methoxyethyl substituents and BF_4^- or $TFSI^-$ anions exhibit excellent electrochemical performance, showing oxidation–reduction potentials up to 6.0 V and conductivities of 4.8 mS cm^{-1} at 25 °C, highlighting their suitability as electrolytes for high-voltage capacitors.

The applications of binary ionic liquids (BILs) are expanding because they enable fine-tuning of the electrochemical performance of the system by forming ionic mixtures. BILs improve iodide transport and diffusion in dye-sensitised solar cells (DSSCs) by mixing high-iodide-content ILs with low-viscosity components. Both charge transfer and electrolyte mobility are optimised by this combination [157-159]. Further, eutectic mixtures of iodide-based ILs, which are solid individually, can form low-melting, high-conductivity electrolytes when mixed [160, 161]. In lithium-ion battery systems, the addition of lithium salts to BILs expands their electrochemical window and enables stable solid–electrolyte interface formation [161, 162]. Multiple binary ionic liquid (BIL) systems have shown improved performance in metal-ion batteries [163].

Polyionic liquids (PILs) represent a relatively recent, structurally advanced class of ionic materials that exhibit solid-state ion transport and multifunctionality. Their polymeric backbones confer enhanced mechanical stability, tunable glass transition temperatures, and suppressed volatility, making them ideal candidates for non-spillable, solid-state electrolytes in fuel cells, DSSCs, Li-ion batteries, and supercapacitors [164-166]. Recent studies highlight the versatility of polymeric ionic liquids (PILs) in electrochemical applications. Sulfonated imidazolium-based copolymers demonstrated proton conductivities of 10^{-3}–10^{-2} S cm^{-1} for fuel cells [164], hybrid PMMA/PIL/polyindole membranes achieved 5.96% efficiency and long-term stability in DSSCs [165], and PIL-based blends exhibited ionic conductivities up to 2.09×10^{-3} S cm^{-1} with excellent capacitance retention in supercapacitors. These results emphasise the ability of PILs to enable efficient ion transport while maintaining strong electrochemical and mechanical stability.

Collectively, ILs, BILs, and PILs define a continuum in electrochemical electrolyte design; progressing from highly conductive molecular ILs, through compositionally tunable BILs, to structurally robust, polymeric PILs. The transition from liquid to polymeric architectures enables enhanced electrode compatibility, broader operating voltages, and greater environmental and operational safety, thus positioning these ionic systems as the next generation of materials for sustainable electrochemical energy storage and conversion.

CONCLUSION

This chapter began with an overview of the evolution and nomenclature of ionic liquids (ILs), followed by a detailed examination of the synthesis of imidazolium-based ILs, which continue to dominate the field due to their chemical stability, structural modularity, and functional versatility. The discussion then extended to the polymerization of imidazolium-based ionic liquids, leading to the formation of polymeric ionic liquids (PILs) that successfully merge the tunable ionic characteristics of ILs with the mechanical robustness and thermal stability of polymers.

The chapter further introduced the concept of binary ionic liquids (BILs), emphasizing how the combination of different ions provides a powerful approach for tailoring key physicochemical parameters such as acidity, polarity, and coordination behavior. The nomenclature, miscibility behavior, and thermodynamic treatment of ionic liquid mixtures were presented, including discussions of Raoult's law and ideal solution models, to highlight non-ideal behaviors and the energetic interactions governing IL mixtures.

Subsequent sections examined the physical properties of monomeric, binary, and polymeric ionic liquids, with particular focus on how viscosity, polarity, and glass transition temperature (Tg) influence their performance, tunability, and application potential.

Finally, the chapter summarized the diverse applications of ionic liquids, placing special emphasis on their use in electrochemical systems, where ILs and PILs act as durable and efficient electrolytes, and in catalysis, where they serve as recyclable reaction media that enhance selectivity, efficiency, and sustainability.

In summary, this chapter demonstrated that ionic liquids—from monomeric to polymeric and binary systems—constitute a continuum of highly tunable materials whose structure, composition, and intermolecular interactions can be precisely engineered. Their combination of design flexibility, thermodynamic complexity, and environmental compatibility establishes ionic liquids as key materials for next-generation catalytic, electrochemical, and green chemical technologies.

BIBLIOGRAPHY

1. Aljuhani, A., et al., Microwave-assisted synthesis of novel imidazolium, pyridinium and pyridazinium-based ionic liquids and/or salts and prediction of physico-chemical properties for their toxicity and antibacterial activity. Journal of Molecular Liquids, 2018. **249**: p. 747-753.
2. Soares, B.G., et al., Synthesis and characterization of epoxy/MCDEA networks modified with imidazolium-based ionic liquids. 2011. **296**(9): p. 826-834.
3. Kawai, R., S. Yada, and T. Yoshimura, Characterization and solution properties of adamantane-containing quaternary-ammonium-salt-type amphiphilic ionic liquids. Journal of Molecular Liquids, 2019. **294**: p. 111586.
4. Eftekhari, A. and T.J.E.P.J. Saito, Synthesis and properties of polymerized ionic liquids. 2017. **90**: p. 245-272.
5. Azaceta, E., et al., Synthesis and characterization of poly(1-vinyl-3-alkylimidazolium) iodide polymers for quasi-solid electrolytes in dye sensitized solar cells. Electrochimica Acta, 2010. **56**(1): p. 42-46.
6. Ikeda, T., S. Moriyama, and J. Kim, Imidazolium-based poly(ionic liquid)s with poly(ethylene oxide) main chains: Effects of spacer and tail structures on ionic conductivity. Journal of Polymer Science Part A: Polymer Chemistry, 2016. **54**(18): p. 2896-2906.
7. Nie, J., et al., New insights on the fast response of poly (ionic liquid) s to humidity: the effect of free-ion concentration. 2019. **9**(5): p. 749.
8. Hutchings, J.W., et al., Surprisingly high solubility of the ionic liquid trihexyltetradecylphosphonium chloride in dense carbon dioxide. Green Chemistry, 2005. **7**(6): p. 475-478.
9. Ponkratov, D.O., A.S. Shaplov, and Y.S. Vygodskii, Metathesis Polymerization in Ionic Media. Polymer Science, Series C, 2019. **61**(1): p. 2-16.
10. Walden, P.J.B.A.I.S., Molecular weights and electrical conductivity of several fused salts. 1914. **1800**.
11. Welton, T.J.B.r., Ionic liquids: a brief history. 2018. **10**(3): p. 691-706.
12. Gale, R. and R.J.I.C. Osteryoung, Potentiometric investigation of dialuminum heptachloride formation in aluminum chloride-1-butylpyridinium chloride mixtures. 1979. **18**(6): p. 1603-1605.
13. Wilkes, J.S. and M.J. Zaworotko, Air and water stable 1-ethyl-3-methylimidazolium based ionic liquids. Journal of the Chemical Society, Chemical Communications, 1992(13): p. 965-967.
14. Cooper, E.I. and E.J.J.E.P.V. O'Sullivan, New, stable, ambient-temperature molten salts. 1992. **1992**(1): p. 386.
15. Earle, M.J., et al., The distillation and volatility of ionic liquids. 2006. **439**(7078): p. 831-834.
16. Seddon, K.R.J.J.o.C.T., E. Biotechnology: International Research in Process, and C. Technology, Ionic liquids for clean technology. 1997. **68**(4): p. 351-356.
17. Welton, T.J.C.r., Room-temperature ionic liquids. Solvents for synthesis and catalysis. 1999. **99**(8): p. 2071-2084.
18. Freemantle, M.J.C.E.N., Mimicking natural photosynthesis. 1998. **76**: p. 37-46.
19. Zhou, T., et al., Energy applications of ionic liquids: recent developments and future prospects. 2023. **123**(21): p. 12170-12253.
20. MacFarlane, D.R., et al., Energy applications of ionic liquids. 2014. **7**(1): p. 232-250.

21. Watanabe, M., et al., Application of ionic liquids to energy storage and conversion materials and devices. 2017. **117**(10): p. 7190-7239.
22. Estager, J., J. Holbrey, and M.J.C.S.R. Swadźba-Kwaśny, Halometallate ionic liquids–revisited. 2014. **43**(3): p. 847-886.
23. Hayes, R., G.G. Warr, and R. Atkin, Structure and Nanostructure in Ionic Liquids. Chemical Reviews, 2015. **115**(13): p. 6357-6426.
24. Kaur, N., V.S. Mithu, and S. Kumar, A review on (eco)toxicity of ionic liquids and their interaction with phospholipid membranes. Journal of Molecular Liquids, 2024. **397**: p. 124095.
25. Sadanandhan, A.M., P.K. Khatri, and S.L.J.J.o.M.L. Jain, A novel series of cyclophosphazene derivatives containing imidazolium ionic liquids with variable alkyl groups and their physicochemical properties. 2019. **295**: p. 111722.
26. Anderson, E.B. and T.E. Long, Imidazole- and imidazolium-containing polymers for biology and material science applications. Polymer, 2010. **51**(12): p. 2447-2454.
27. Green, M.D. and T.E. Long, Designing Imidazole-Based Ionic Liquids and Ionic Liquid Monomers for Emerging Technologies. Polymer Reviews, 2009. **49**(4): p. 291-314.
28. Vraneš, M., et al., Thermophysical and electrochemical properties of 1–alkyl–3–(3–butenyl) imidazolium bromide ionic liquids. 2019. **139**: p. 105871.
29. Wan, H., et al., Heterogenization of ionic liquid based on mesoporous material as magnetically recyclable catalyst for biodiesel production. Journal of Molecular Catalysis A: Chemical, 2015. **398**: p. 127-132.
30. Gao, R., et al., Imidazolium sulfonate-containing pentablock copolymer–ionic liquid membranes for electroactive actuators. Journal of Materials Chemistry, 2012. **22**(27): p. 13473-13476.
31. Kassaye, S., K.K. Pant, and S. Jain, Hydrolysis of cellulosic bamboo biomass into reducing sugars via a combined alkaline solution and ionic liquid pretreament steps. Renewable Energy, 2017. **104**: p. 177-184.
32. Zhijun, Z. and D.J.C.J.o.C.E. Haifeng, The research progress of CO2 capture with ionic liquids. 2012. **20**(1): p. 120-129.
33. Pacheco-Fernández, I., et al., Utilization of highly robust and selective crosslinked polymeric ionic liquid-based sorbent coatings in direct-immersion solid-phase microextraction and high-performance liquid chromatography for determining polar organic pollutants in waters. Talanta, 2016. **158**: p. 125-133.
34. Singh, S.K. and P.L. Dhepe, Novel Synthesis of Immobilized Brønsted- Acidic Ionic Liquid: Application in Lignin Depolymerization. 2018. **3**(19): p. 5461-5470.
35. Zaoui, A., Z. Cherifi, and M. Belbachir, Ultrasound-induced synthesis of an imidazolium based poly(ionic liquid) in an aqueous media: A structural, thermal and morphological study. Ultrason Sonochem, 2019. **55**: p. 149-156.
36. Yang, H., et al., Synthesis, structure and properties of imidazolium-based energetic ionic liquids. 2017. **7**(53): p. 33231-33240.
37. Fang, C., et al., Antibacterial activities of N-alkyl imidazolium-based poly (ionic liquid) nanoparticles. 2019. **10**(2): p. 209-218.
38. Whitley, J.W., et al., Systematic Investigation of the Photopolymerization of Imidazolium-Based Ionic Liquid Styrene and Vinyl Monomers. 2018. **56**(20): p. 2364-2375.
39. Raiah, K., et al., Influence of the hydrocarbon chain length of imidazolium-based ionic liquid on the dispersion and stabilization of double-walled carbon nanotubes in water. 2015. **469**: p. 107-116.

40. Bubalo, M.C., et al., A comparative study of ultrasound-, microwave-, and microreactor-assisted imidazolium-based ionic liquid synthesis. 2013. **2**(6): p. 579-590.
41. Lévêque, J.-M., et al., A general ultrasound-assisted access to room-temperature ionic liquids. 2006. **13**(2): p. 189-193.
42. Lawal, I.A. and B.J.R.A. Moodley, Synthesis, characterisation and application of imidazolium based ionic liquid modified montmorillonite sorbents for the removal of amaranth dye. 2015. **5**(76): p. 61913-61924.
43. Pillai, P., et al., Synthesis, characterization, surface properties and micellization behaviour of imidazolium-based ionic liquids. 2017. **20**(6): p. 1321-1335.
44. Nellepalli, P., et al., Imidazolium-Based Copoly (Ionic Liquid) Membranes for CO_2/N_2 Separation. 2019.
45. Montaño, D.F., et al., Functionalization of montmorillonite with ionic liquids based on 1-alkyl-3-methylimidazolium: Effect of anion and length chain. 2017. **198**: p. 386-392.
46. Ameta, G., et al., Sonochemical synthesis and characterization of imidazolium based ionic liquids: A green pathway. 2015. **211**: p. 934-937.
47. Feng, X., et al., Pore structure controllable synthesis of mesoporous poly(ionic liquid)s by copolymerization of alkylvinylimidazolium salts and divinylbenzene. RSC Advances, 2014. **4**(45): p. 23389-23395.
48. Zhou, D., et al., In Situ Synthesis of a Hierarchical All-Solid-State Electrolyte Based on Nitrile Materials for High-Performance Lithium-Ion Batteries. 2015. **5**(15): p. 1500353.
49. Steinkoenig, J., et al., Controlled radical polymerization and in-depth mass-spectrometric characterization of poly(ionic liquid)s and their photopatterning on surfaces. Polymer Chemistry, 2016. **7**(2): p. 451-461.
50. Sang, Y. and J. Huang, Benzimidazole-based hyper-cross-linked poly(ionic liquid)s for efficient CO2 capture and conversion. Chemical Engineering Journal, 2020. **385**: p. 123973.
51. Bi, W., B. Tang, and K.H. Row, Adsorption of alcohol from water by poly(ionic liquid)s. Bioprocess and Biosystems Engineering, 2013. **36**(6): p. 651-658.
52. Ríos-Gómez, J., et al., Polymeric ionic liquid immobilized onto paper as sorptive phase in microextraction. 2020. **1094**: p. 47-56.
53. Yin, K., et al., An imidazolium-based polymerized ionic liquid via novel synthetic strategy as polymer electrolytes for lithium ion batteries. Journal of Power Sources, 2014. **258**: p. 150-154.
54. Maksym, P., et al., A facile route to well-defined imidazolium-based poly(ionic liquid)s of enhanced conductivity via RAFT. Polymer Chemistry, 2017. **8**(35): p. 5433-5443.
55. Zhang, W., et al., A simple method for preparing imidazolium-based polymer as solid catalyst for Suzuki-Miyaura reaction. Molecular Catalysis, 2018. **445**: p. 170-178.
56. Jacinto, M.J., et al., M13 bacteriophage purification using poly(ionic liquids) as alternative separation matrices. Journal of Chromatography A, 2018. **1532**: p. 246-250.
57. Jonscher, A.K.J.J.o.P.D.A.P., Dielectric relaxation in solids. 1999. **32**(14): p. R57.
58. Reese, C.M., et al., Sequential and one-pot post-polymerization modification reactions of thiolactone-containing polymer brushes. Polymer Chemistry, 2019. **10**(36): p. 4935-4943.
59. Tseng, S.-K., et al., Synthesis of a series of novel imidazolium-containing ionic liquid copolymers for dye-sensitized solar cells. 2020. **210**: p. 123074.
60. Thomas, M. and S. Rajiv, Grafted PEO polymeric ionic liquid nanocomposite electrospun membrane for efficient and stable dye sensitized solar cell. Electrochimica Acta, 2020. **341**: p. 136040.

61. Koyilapu, R., et al., Grafting of vinylimidazolium-type poly (ionic liquid) on silica nanoparticle through RAFT polymerization for constructing nanocomposite based PEM. 2020. **195**: p. 122458.
62. Green, M.D., et al., Synthesis of imidazolium-containing ABA triblock copolymers: role of charge placement, charge density, and ionic liquid incorporation. 2012. **45**(11): p. 4749-4757.
63. Zhang, Y., et al., Colloidal poly-imidazolium salts and derivatives. Nano Today, 2009. **4**(1): p. 13-20.
64. Li, F., et al., Novel quasi-solid electrolyte for dye-sensitized solar cells. 2007. **165**(2): p. 911-915.
65. Roeleveld, K., F. David, and F.J.J.o.C.A. Lynen, Comparison between polymerized ionic liquids synthesized using chain-growth and step-growth mechanisms used as stationary phase in gas chromatography. 2016. **1451**: p. 135-144.
66. Martin, R.M., et al., Curable imidazolium poly (ionic liquid)/ionic liquid coating for containment and decontamination of toxic industrial chemical-contacted substrates. 2016. **55**(22): p. 6547-6550.
67. Gond, D., et al., Hierarchical matrix completion for the prediction of properties of binary mixtures. 2025: p. 109122.
68. Dhakal, P., J.K.J.C.O.i.G. Shah, and S. Chemistry, Recent advances in molecular simulations of ionic liquid–ionic liquid mixtures. 2019. **18**: p. 90-97.
69. Yao, P., X. Yu, and X. Huang, Effect of the physicochemical properties of binary ionic liquids on lipase activity and stability. Int J Biol Macromol, 2015. **77**: p. 243-9.
70. Mancarella, F., et al., Binary mixtures of menthol and alkanoic acids as green solvents for efficient astaxanthin recovery from Aristaeomorpha foliacea shrimp shells. 2025: p. 133261.
71. Atkins, P.W., J. De Paula, and J. Keeler, Atkins' physical chemistry. 2023: Oxford university press.
72. Niedermeyer, H., et al., Mixtures of ionic liquids. Chem Soc Rev, 2012. **41**(23): p. 7780-802.
73. Onsager, L.J.J.o.t.A.C.S., Electric moments of molecules in liquids. 1936. **58**(8): p. 1486-1493.
74. Tasic, A.Z., et al., Use of mixing rules in predicting refractive indexes and specific refractivities for some binary liquid mixtures. 1992. **37**(3): p. 310-313.
75. Gohres, J.L., et al., A spectroscopic and computational exploration of the cybotactic region of gas-expanded liquids: methanol and acetone. 2008. **112**(15): p. 4666-4673.
76. Kleppa, O.J., Thermodynamics of Molten Salt Mixtures, in Molten Salt Chemistry: An Introduction and Selected Applications, G. Mamantov and R. Marassi, Editors. 1987, Springer Netherlands: Dordrecht. p. 79-122.
77. Papatheodorou, G.N. and O.J. Kleppa, Enthalpies of mixing in the liquid mixtures of the alkali chlorides with MnCl2, FeCl2 and CoCl2. Journal of Inorganic and Nuclear Chemistry, 1971. **33**(5): p. 1249-1278.
78. Kleppa, O.J. and L.S. Hersh, Heats of Mixing in Liquid Alkali Nitrate Systems. The Journal of Chemical Physics, 1961. **34**(2): p. 351-358.
79. Kleppa, O.J. and S.V. Meschel, THERMOCHEMISTRY OF ANION MIXTURES IN SIMPLE FUSED SALT SYSTEMS. II. SOLUTIONS OF SOME SALTS OF MO4- AND MO4-2 ANIONS IN THE CORRESPONDING ALKALI NITRATES. The Journal of Physical Chemistry, 1963. **67**(12): p. 2750-2753.

80. Kleppa, O.J.A.R.o.P.C., The solution chemistry of simple fused salts. 1965. **16**(1): p. 187-212.
81. Hildebrand, J.H. and E.J.J.J.o.t.A.C.S. Salstrom, Thermodynamic properties of liquid solutions of silver bromide with alkali bromides. 1932. **54**(11): p. 4257-4261.
82. Saboungi, M., C. Vallet, and Y.J.T.J.o.P.C. Doucet, Thermodynamic properties of the reciprocal system (potassium (+), silver (+)//nitrate (-), sulfate (2-)) from its phase diagram. 1973. **77**(13): p. 1699-1704.
83. Saboungi, M., et al., Phase diagrams of reciprocal molten salt systems. Calculations of liquid-liquid miscibility gaps. 1974. **78**(11): p. 1091-1096.
84. Flor, G., et al., Liquid-liquid equilibriums in the reciprocal ternary system cesium, lithium. dblvert. chloride, fluoride. 1978. **23**(4): p. 336-338.
85. Navia, P., et al., Excess magnitudes for ionic liquid binary mixtures with a common ion. 2007. **52**(4): p. 1369-1374.
86. Castejón, H.J. and R.J.J.J.o.M.L. Lashock, Mixtures of ionic liquids with similar molar volumes form regular solutions and obey the cross-square rules for electrolyte mixtures. 2012. **167**: p. 1-4.
87. Carmichael, A.J. and K.R.J.J.o.P.O.C. Seddon, Polarity study of some 1-alkyl-3-methylimidazolium ambient-temperature ionic liquids with the solvatochromic dye, Nile Red. 2000. **13**(10): p. 591-595.
88. van den Broeke, J., et al., Designing Ionic Liquids: 1-Butyl-3-Methylimidazolium Cations with Substituted Tetraphenylborate Counterions. 2003. **2003**(15): p. 2798-2811.
89. Baker, S.N., G.A. Baker, and F.V.J.G.C. Bright, Temperature-dependent microscopic solvent properties of 'dry'and 'wet'1-butyl-3-methylimidazolium hexafluorophosphate: correlation with ET (30) and Kamlet–Taft polarity scales. 2002. **4**(2): p. 165-169.
90. Poole, C.F.J.J.o.c.A., Chromatographic and spectroscopic methods for the determination of solvent properties of room temperature ionic liquids. 2004. **1037**(1-2): p. 49-82.
91. Vijayaraghavan, R. and D.R.J.M. Macfarlane, Organoborate acids as initiators for cationic polymerization of styrene in an ionic liquid medium. 2007. **40**(18): p. 6515-6520.
92. Guerrero-Sanchez, C., R. Hoogenboom, and U.S.J.C.C. Schubert, Fast and "green" living cationic ring opening polymerization of 2-ethyl-2-oxazoline in ionic liquids under microwave irradiation. 2006(36): p. 3797-3799.
93. Liao, L., C. Zhang, and S.J.J.o.P.S.P.A.P.C. Gong, Microwave-assisted ring-opening polymerization of trimethylene carbonate in the presence of ionic liquid. 2007. **45**(24): p. 5857-5863.
94. Vijayaraghavan, R. and D.R.J.C.C. Macfarlane, Living cationic polymerisation of styrene in an ionic liquid. 2004(6): p. 700-701.
95. Tada, E.B., L.P. Novaki, and O.A.J.J.o.P.O.C. El Seoud, Solvatochromism in pure and binary solvent mixtures: effects of the molecular structure of the zwitterionic probe. 2000. **13**(11): p. 679-687.
96. Fletcher, K.A., et al., Probing solute and solvent interactions within binary ionic liquid mixtures. 2003. **27**(12): p. 1706-1712.
97. Weber, C.C., A.F. Masters, and T.J.T.J.o.P.C.B. Maschmeyer, Controlling hydrolysis reaction rates with binary ionic liquid mixtures by tuning hydrogen-bonding interactions. 2012. **116**(6): p. 1858-1864.
98. Kagimoto, J., et al., Polar and low viscosity ionic liquid mixtures from amino acids. 2008. **37**(10): p. 1026-1027.

99. Chiappe, C. and D.J.T.J.o.P.C.A. Pieraccini, Determination of Ionic Liquids Solvent Properties Using an Unusual Probe: The Electron Donor− Acceptor Complex between 4, 4 '-bis (Dimethylamino)-benzophenone and Tetracyanoethene. 2006. **110**(14): p. 4937-4941.
100. Smith, G., et al., Broensted superacidity of hydrochloric acid in a liquid chloroaluminate. Aluminum chloride-1-ethyl-3-methyl-1H-imidazolium chloride (55. O m/o AlCl3). 1989. **111**(2): p. 525-530.
101. Hunt, P.A.J.T.J.o.P.C.B., Why does a reduction in hydrogen bonding lead to an increase in viscosity for the 1-butyl-2, 3-dimethyl-imidazolium-based ionic liquids? 2007. **111**(18): p. 4844-4853.
102. Thomazeau, C., et al., Determination of an acidic scale in room temperature ionic liquids. 2003. **125**(18): p. 5264-5265.
103. Arduengo, A.J.J.A.o.C.R., Looking for stable carbenes: the difficulty in starting anew. 1999. **32**(11): p. 913-921.
104. Oxley, J.D., T. Prozorov, and K.S.J.J.o.t.A.C.S. Suslick, Sonochemistry and sonoluminescence of room-temperature ionic liquids. 2003. **125**(37): p. 11138-11139.
105. Endres, F., et al., Electrodeposition of nanocrystalline metals and alloys from ionic liquids. 2003. **42**(29): p. 3428-3430.
106. Moustafa, E., et al., Electrodeposition of al in 1-butyl-1-methylpyrrolidinium bis (trifluoromethylsulfonyl) amide and 1-ethyl-3-methylimidazolium bis (trifluoromethylsulfonyl) amide ionic liquids: In situ STM and EQCM studies. 2007. **111**(18): p. 4693-4704.
107. Tang, J., M. Radosz, and Y. Shen, Optically transparent microwave-absorbing materials. 2008.
108. Amajjahe, S. and H.J.M.r.c. Ritter, Microwave-Sensitive Foamable Poly (ionic liquids) Bearing tert-Butyl Ester Groups: Influence of Counterions on the Ester Pyrolysis. 2009. **30**(2): p. 94-98.
109. Zhou, Q., et al., Phase Behavior and Thermal Properties of Ternary Ionic Liquid− Lithium Salt (IL− IL− LiX) Electrolytes. 2010. **114**(13): p. 6201-6204.
110. Bouchardy, L., Elaboration de liquides ioniques (chiraux) réversibles et applications en catalyse organique et en glycochimie. Carbènes N-hétérocycliques chiraux: synthèse et application dans la réaction d'addition conjuguée. 2016, Université Paris Saclay (COmUE).
111. Endres, F. and S.Z.J.P.c.c.p. El Abedin, Air and water stable ionic liquids in physical chemistry. 2006. **8**(18): p. 2101-2116.
112. Dzyuba, S.V. and R.A.J.C. Bartsch, Influence of structural variations in 1-alkyl (aralkyl)-3-methylimidazolium hexafluorophosphates and bis (trifluoromethylsulfonyl) imides on physical properties of the ionic liquids. 2002. **3**(2): p. 161-166.
113. Ye, Q., et al., Grafting poly (ionic liquid) brushes for anti-bacterial and anti-biofouling applications. 2012. **22**(26): p. 13123-13131.
114. Ricks-Laskoski, H.L. and A.W.J.J.o.t.A.C.S. Snow, Synthesis and electric field actuation of an ionic liquid polymer. 2006. **128**(38): p. 12402-12403.
115. Prescher, S., et al., Polyelectrolyte as solvent and reaction medium. 2014. **136**(1): p. 12-15.
116. Dong, Y., J. Yin, and X.J.J.o.M.C.A. Zhao, Microwave-synthesized poly (ionic liquid) particles: a new material with high electrorheological activity. 2014. **2**(25): p. 9812-9819.
117. Ab Rani, M.A., et al., Understanding the polarity of ionic liquids. 2011. **13**(37): p. 16831-16840.
118. Aparicio, S. and M.J.T.J.o.P.C.B. Atilhan, Mixed ionic liquids: the case of pyridinium-based fluids. 2012. **116**(8): p. 2526-2537.

119. Fox, E.T., J.E. Weaver, and W.A.J.T.J.o.P.C.C. Henderson, Tuning binary ionic liquid mixtures: linking alkyl chain length to phase behavior and ionic conductivity. 2012. **116**(8): p. 5270-5274.
120. Fannin Jr, A.A., et al., Properties of 1, 3-dialkylimidazolium chloride-aluminum chloride ionic liquids. 2. Phase transitions, densities, electrical conductivities, and viscosities. 1984. **88**(12): p. 2614-2621.
121. Pereiro, A.B., et al., Inorganic salts in purely ionic liquid media: the development of high ionicity ionic liquids (HIILs). 2012. **48**(30): p. 3656-3658.
122. Canongia Lopes, J.N., et al., Deviations from ideality in mixtures of two ionic liquids containing a common ion. 2005. **109**(8): p. 3519-3525.
123. Marsh, K.N., J.A. Boxall, and R.J.F.p.e. Lichtenthaler, Room temperature ionic liquids and their mixtures—a review. 2004. **219**(1): p. 93-98.
124. Paduszyński, K., Extensive Databases and Group Contribution QSPRs of Ionic Liquids Properties. 2. Viscosity. Industrial & Engineering Chemistry Research, 2019. **58**(36): p. 17049-17066.
125. Gordon, C.M.J.A.C.A.G., New developments in catalysis using ionic liquids. 2001. **222**(1-2): p. 101-117.
126. Navia, P., J. Troncoso, and L.J.J.o.s.c. Romaní, Viscosities for ionic liquid binary mixtures with a common ion. 2008. **37**(5): p. 677-688.
127. Grunberg, L. and A.H.J.N. Nissan, Mixture law for viscosity. 1949. **164**(4175): p. 799-800.
128. Katti, P., M.J.J.o.C. Chaudhri, and E. Data, Viscosities of Binary Mixtures of Benzyl Acetate with Dioxane, Aniline, and m-Cresol. 1964. **9**(3): p. 442-443.
129. Glasstone, S., K. Laidler, and H.J.N.Y. Eyring, The Theory of Rate Processes MacGraw-Hill Book Co. 1941. **477**.
130. Powell, R., et al., Diffusion, thermal conductivity, and viscous flow of liquids. 1941. **33**(4): p. 430-435.
131. Hayamizu, K., et al., Ionic conduction and ion diffusion in binary room-temperature ionic liquids composed of [emim][BF4] and LiBF4. 2004. **108**(50): p. 19527-19532.
132. Castiglione, F., et al., Blending ionic liquids: how physico-chemical properties change. 2010. **12**(8): p. 1784-1792.
133. Harrisson, S., S.R. Mackenzie, and D.M.J.M. Haddleton, Pulsed laser polymerization in an ionic liquid: strong solvent effects on propagation and termination of methyl methacrylate. 2003. **36**(14): p. 5072-5075.
134. Barth, J., et al., Termination kinetics of free-radical polymerization in ionic liquids. 2009. **50**(24): p. 5708-5712.
135. Harrisson, S., S.R. Mackenzie, and D.M.J.C.C. Haddleton, Unprecedented solvent-induced acceleration of free-radical propagation of methyl methacrylate in ionic liquids. 2002(23): p. 2850-2851.
136. Nancarrow, P., et al., Comprehensive analysis and correlation of ionic liquid conductivity data for energy applications. Energy, 2021. **220**: p. 119761.
137. Chen, Z., et al., Prediction of Electrical Conductivity of Ionic Liquids: From COSMO-RS Derived QSPR Evaluation to Boosting Machine Learning. ACS Sustainable Chemistry & Engineering, 2024. **12**(17): p. 6648-6658.
138. Galiński, M., A. Lewandowski, and I. Stępniak, Ionic liquids as electrolytes. Electrochimica Acta, 2006. **51**(26): p. 5567-5580.
139. Every, H., et al., Ion diffusion in molten salt mixtures. 2000. **45**(8-9): p. 1279-1284.
140. Jarosik, A., et al., Conductivity of ionic liquids in mixtures. 2006. **123**(1): p. 43-50.

141. Döbbelin, M., et al., Synthesis of pyrrolidinium-based poly (ionic liquid) electrolytes with poly (ethylene glycol) side chains. 2012. **24**(9): p. 1583-1590.
142. Choi, U.H., et al., Polymerized ionic liquids with enhanced static dielectric constants. 2013. **46**(3): p. 1175-1186.
143. Yoshizawa, M. and H.J.E.A. Ohno, Synthesis of molten salt-type polymer brush and effect of brush structure on the ionic conductivity. 2001. **46**(10-11): p. 1723-1728.
144. Weber, R.L., et al., Effect of nanoscale morphology on the conductivity of polymerized ionic liquid block copolymers. 2011. **44**(14): p. 5727-5735.
145. Fan, F., et al., Effect of molecular weight on the ion transport mechanism in polymerized ionic liquids. 2016. **49**(12): p. 4557-4570.
146. Green, O., et al., The design of polymeric ionic liquids for the preparation of functional materials. 2009. **49**(4): p. 339-360.
147. Chen, H., et al., Polymerized ionic liquids: the effect of random copolymer composition on ion conduction. 2009. **42**(13): p. 4809-4816.
148. Plechkova, N.V. and K.R.J.C.S.R. Seddon, Applications of ionic liquids in the chemical industry. 2008. **37**(1): p. 123-150.
149. Gilbert, B., et al., Chloroaluminate ionic liquids: from their structural properties to their applications in process intensification. 2007. **62**(6): p. 745-759.
150. Chauvin, Y., et al., Catalytic dimerization of propene by nickel-phosphine complexes in 1-butyl-3-methylimidazolium chloride/AlEtxCl3-x (x= 0, 1) ionic liquids. 1995. **34**(4): p. 1149-1155.
151. Lin, Z., et al., Anion control in the ionothermal synthesis of coordination polymers. 2007. **129**(34): p. 10334-10335.
152. Qian, W., et al., Condiment-derived 3D architecture porous carbon for electrochemical supercapacitors. 2015. **11**(37): p. 4959-4969.
153. Mascotto, S., et al., Poly (ionic liquid)-derived nanoporous carbon analyzed by combination of gas physisorption and small-angle neutron scattering. 2015. **82**: p. 425-435.
154. Wei, D. and A. Ivaska, Applications of ionic liquids in electrochemical sensors. Analytica Chimica Acta, 2008. **607**(2): p. 126-135.
155. Matsumi, N., et al., Liquid imidazole–borane complex. Chemical Communications, 2005(36): p. 4557-4559.
156. Sato, T., G. Masuda, and K. Takagi, Electrochemical properties of novel ionic liquids for electric double layer capacitor applications. Electrochimica Acta, 2004. **49**(21): p. 3603-3611.
157. Gorlov, M. and L.J.D.T. Kloo, Ionic liquid electrolytes for dye-sensitized solar cells. 2008(20): p. 2655-2666.
158. Fredin, K., et al., On the influence of anions in binary ionic liquid electrolytes for monolithic dye-sensitized solar cells. 2007. **111**(35): p. 13261-13266.
159. Xi, C., et al., Tetrahydrothiophenium-based ionic liquids for high efficiency dye-sensitized solar cells. 2008. **112**(29): p. 11063-11067.
160. Bai, Y., et al., High-performance dye-sensitized solar cells based on solvent-free electrolytes produced from eutectic melts. 2008. **7**(8): p. 626-630.
161. Cao, Y., et al., Dye-sensitized solar cells with solvent-free ionic liquid electrolytes. 2008. **112**(35): p. 13775-13781.
162. Lane, G.H., et al., An Azo-Spiro Mixed Ionic Liquid Electrolyte for Lithium Metal–LiFePO4 Batteries. 2010. **157**(7): p. A876.

163. Wang, P., et al., Mixed ionic liquids as electrolyte for reversible deposition and dissolution of magnesium. 2006. **201**(6): p. 3783-3787.
164. Ortiz-Martínez, V.M., et al., Fuel cell electrolyte membranes based on copolymers of protic ionic liquid [HSO3-BVIm][TfO] with MMA and hPFSVE. 2019. **179**: p. 121583.
165. Thomas, M., S.J.J.o.P. Rajiv, and P.A. Chemistry, Porous membrane of polyindole and polymeric ionic liquid incorporated PMMA for efficient quasi-solid state dye sensitized solar cell. 2020. **394**: p. 112464.
166. Zhang, D.-Z., et al., Ionic liquid/poly (ionic liquid)-based semi-solid state electrolytes for lithium-ion batteries. 2020. **38**(5): p. 506-513.

CHAPTER II

POLARIZATION AND DIELECTRIC RELAXATION PHENOMENA

INTRODUCTION

The electrical behaviours observed in electronic and dielectric materials originate from the intrinsic physico-chemical properties of the constituent substances. These properties; such as atomic composition, crystalline structure, and the nature of chemical bonds; determine how charge carriers and dipoles respond to an external electric field. The interactions at the microscopic scale, therefore, play a decisive role in defining the material's macroscopic electrical characteristics. Understanding these behaviours requires a thorough knowledge of the nature, structure, and interactions of the materials involved, as well as the physical mechanisms that govern charge distribution and motion within them.

The objective of this chapter is to present and analyze the main physical phenomena that occur in dielectric materials, which are fundamental in determining their electrical characteristics and performance in various technological applications.

In the first part, we will examine the phenomenon of polarisation, describing the different polarisation mechanisms that can arise in dielectrics: namely, electric, ionic, orientational (dipolar), and interfacial polarisation. Particular emphasis will be placed on the microscopic origins of each mechanism and on the mathematical formulation of permittivity, including both its linear and non-linear components, which describe the material's response to an applied electric field.

The second part of the chapter will be devoted to dielectric relaxation, which describes the temporal delay between the variation of the applied electric field and the resulting polarisation within the material. This behaviour will be analysed based on experimental observations of the variation of the dielectric permittivity and dielectric losses as a function of frequency. Furthermore, we will present and discuss the main models of dielectric relaxation proposed in the literature, such as the Debye, Cole-Cole, Cole-Davidson, and Havriliak-Negami models, which provide theoretical descriptions of the frequency-dependent dielectric response observed in real materials.

In summary, this chapter provides the theoretical foundations for understanding polarisation and dielectric relaxation mechanisms in dielectrics. These concepts are essential for interpreting the experimental results and discussions presented in the following chapters of this work.

II.1 Description of the Dielectric Polarization Phenomenon

II.1.1 Polarization, Susceptibility, and Permittivity [1]

A dielectric material is a substance that is a poor conductor of electricity. On the basis of band structure, the dielectric materials have an energy gap of 3 eV or more. This large magnitude of energy gap precludes the possibility of electrons being excited from the valence band to the conduction band by thermal means. In electromagnetism, a dielectric (or dielectric material or dielectric medium) is an electrical insulator that can be polarized by an applied electric field. When a dielectric material is placed in an electric field, electric charges do not flow through the material as they do in an electrical conductor, but instead only slightly shift from their average equilibrium positions, causing dielectric polarization (Figure II.1). Because of dielectric polarization, positive charges are displaced in the direction of the field and negative charges shift in the direction opposite to the field (e.g. if the field is moving parallel to the positive x-axis, the negative charges will shift in the negative x-direction). This creates an internal electric field that reduces the overall field within the dielectric itself. If a dielectric is composed of weakly bonded molecules, those molecules not only become polarized but also reorient so that their symmetry axes align to the field.

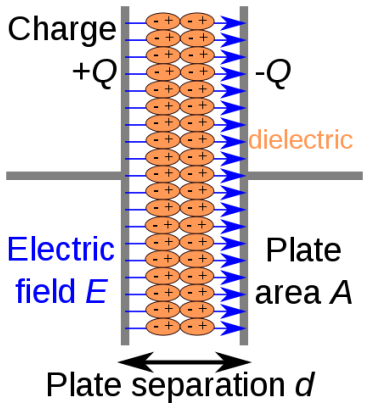

Figure II.1 *A polarized dielectric material.*

Based on the fundamental principle that no material can respond instantaneously to an external stimulus (only the vacuum can react instantaneously), it follows that the response of a dielectric medium necessarily depends on time and, consequently, on frequency. Indeed, any material subjected to an excitation, whether electrical, mechanical, or of another nature, exhibits a certain degree of inertia that delays its response.

Applying this principle to a system composed of two parallel electrodes separated by a distance d, with a dielectric material between them, we consider the case where a time-dependent voltage V(t) is applied across the electrodes. The total charge induced on the electrodes consists of two contributions: the first corresponds to the instantaneous response of the vacuum, while the second arises from the dielectric material's time-dependent polarisation. The relationship between these quantities can therefore be expressed as follows:

$$\overrightarrow{D(t)} = \varepsilon_0 \vec{E} + \overrightarrow{P(t)} \qquad (II.1)$$

Where, D denotes the dielectric displacement, which represents the total surface charge density induced on the electrodes per unit area; E is the electric field applied between the electrodes; P is the polarisation of the dielectric material; and ε_0 is the permittivity of free space (vacuum).

To determine the polarisation P(t), the dielectric response function, f(t), is introduced. This function characterises the time-dependent response of the dielectric material to an applied electric excitation. By performing the convolution (integration) of this response function with the applied electric field E(t), the polarisation can be expressed as:

$$P(t) = \varepsilon_0 \int_0^{\infty} f\,(t).E(t - \tau).d\tau \qquad (II.2)$$

Calculating the Fourier transform of the previous time-domain expression allows us to express the polarization as a function of frequency. This transformation yields:

$$P(\omega) = \varepsilon_0.\chi^*(\omega).E(\omega) \qquad (II.3)$$

Where $\chi^*(\omega)$ is the complex electric susceptibility, a frequency-dependent function that characterises the dielectric response of the material, this quantity provides both the amplitude and phase shift (argument) of the polarisation with respect to the applied electric field.

The complex susceptibility can be expressed as:

$$\chi^*(\omega) = \chi'(\omega) - i.\chi''(\omega) = \int_0^{\infty} f\,(t).\, e^{-i.\omega.t}\, dt \qquad (II.4)$$

Where $\chi'(\omega)$ represents the real part of the susceptibility, corresponding to the stored (reversible) polarisation energy, and $\chi''(\omega)$ represents the imaginary part, which is associated with the energy losses due to dielectric relaxation processes.

The real and imaginary components of the complex susceptibility can be expressed as the Fourier transforms of the dielectric response function f(t):

$$\chi'(\omega)=\int_0^\infty f\ (t).cos(\omega t)\ dt \qquad (II.5)$$

$$\chi\ ''(w)=\int_0^\infty f\ (t).sin(\omega t)\ dt \qquad (II.6)$$

It is therefore possible to re-evaluate the total charge density D(ω) induced on the electrodes as a function of frequency. This relationship can be written as:

$$D(\omega) = \varepsilon_0.\{1+\chi'(\omega) - i.\chi\ ''(\omega)\}E(\omega) \qquad (II.7)$$

By introducing the complex permittivity ε*(ω), defined as the ratio between the dielectric displacement and the applied electric field, we obtain:

$$\varepsilon^*\ (\omega) = \frac{D(\omega)}{E(\omega)} \qquad (II.8)$$

By considering the contribution of the various polarization mechanisms that may occur within a dielectric material, the total complex permittivity can be expressed as:

$$\varepsilon^*\ (\omega)= \varepsilon_0.\ \{1 + \sum_n \chi'(\omega\ ) - i \sum_n \chi\ ''(\omega\ )\} \qquad (II.9)$$

The amounts come from the fact that several types of polarization can appear in a dielectric.

It is therefore possible to define the complex relative permittivity, which expresses the dielectric response of the material normalised with respect to the vacuum permittivity:

$$\varepsilon_r^*\ (\omega) = \frac{\varepsilon^*\ (\omega\ )}{\varepsilon 0} = \left\{1 + \sum_n \chi'_n(\omega\ ) - i \sum_n \chi''_n(\omega\ )\right\} \qquad (II.10)$$

By decomposing the complex relative permittivity into its real and imaginary components, we obtain:

$$\varepsilon_r^*\ (\omega) = \varepsilon\ '(\omega) - i.\varepsilon\ ''\ (\omega) \qquad (II.11)$$

Where

$$\varepsilon'(\omega) = 1 + \sum_n \chi'_n(\omega) \qquad (II.12)$$

and

$$\varepsilon''(\omega) = \sum_n \chi''_n(\omega) \qquad (II.13)$$

In the remainder of this thesis, ε′(ω) will be referred to as the real part of the permittivity (also known as the dielectric constant or relative permittivity), representing the ability of the material to store electrical energy. Conversely, ε″(ω) will denote the imaginary part of the permittivity, associated with dielectric losses that reflect the energy dissipated within the material due to polarisation mechanisms and relaxation processes.

At this stage, it is appropriate to introduce the loss angle δ, illustrated in Figure II.2, which represents the phase difference between the applied electric field E and the resulting dielectric displacement D. The tangent of this angle, tan δ = ε″/ε′, is commonly referred to as the dielectric loss factor, and provides a quantitative measure of the dissipative processes occurring in the dielectric medium.

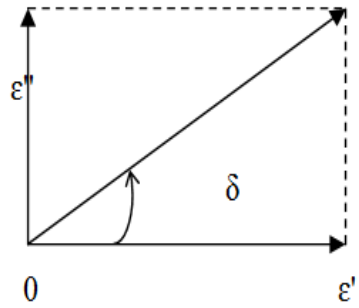

***Figure II.2**: Visualization of the loss angle δ according to ε' and ε".*

The loss angle δ is defined as:

$$Tan\delta = \frac{\varepsilon''}{\varepsilon'} \qquad (II.14)$$

This parameter provides a simple means to compare dielectric losses with the real part of the permittivity. Physically, it represents the ratio between the energy dissipated per radian within the dielectric and the energy stored in the material. It is also worth noting that, in the high-frequency domain, tan δ is equal to the inverse of the quality factor (Q) commonly used to characterise resonant systems.

We can now define the capacitance of a capacitor as the ratio between the charge Q induced on the electrodes and the voltage V applied across them:

$$C = \frac{dQ}{dV} \qquad (II.15)$$

From the equation (II.7) the charge Q can be expressed as:

$$Q = S.D = S.\varepsilon^*.E = S.\varepsilon^*.\frac{V}{d} \qquad (II.16)$$

where S is the surface area of the electrodes and d is the thickness of the dielectric layer. Hence, the capacitance can be written as:

$$C = \frac{\varepsilon^*.S}{d} \qquad (II.17)$$

By expanding the complex permittivity, we obtain the frequency-dependent complex capacitance:

$$C(\omega) = \frac{\varepsilon.[\varepsilon'(\omega) - i.\varepsilon''(\omega)].S}{d} = C'(\omega) - i.C''(\omega) \qquad (II.18)$$

These relations allow us to establish the fundamental relationships among permittivity, susceptibility, and polarisation. They provide the theoretical basis for the analysis presented throughout this manuscript, in which the physical mechanisms responsible for dielectric relaxation phenomena will be examined in detail.

II.1.2 Types of Polarisation

In general terms, polarization is a fundamental reaction of dielectric materials to an external electric field, intricately linked to the microscopic mechanics that dictate charge displacement and redistribution.

In this section, we will examine the four principal polarisation mechanisms that may occur in dielectric media, each associated with distinct physical origins and characteristic time scales. These mechanisms are:

1. Electronic polarization
2. ionic polarization
3. dipolar polarization
4. Space charge polarization

Each of these polarisation types contributes differently to the material's overall dielectric behaviour and exhibits characteristic frequency dependence, which will be discussed in the following subsections.

II.1.2.1 Electronic polarization

Let us consider the spherical orbital of an electron. Under the influence of an external electric field $\vec{E}$: the electrons are subject to a force -e$\vec{E}$ and the orbital gets distorted (figure. II.3). Consequently, the centers of gravity of the positive and negative charges which were initially merged, no longer are: this is electric polarization, and this leads to the formation of an electrostatic dipole; therefore, a dipole moment internal to the atom is characterized by:

$$\vec{P}_{elect} = \varepsilon_0 \alpha_{elect} \vec{E} \qquad (II.19)$$

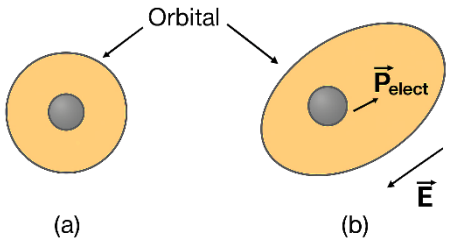

Figure. II.3: *(a) orbital in the absence of electric field; (b) distortion of the orbital and appearance of electronic polarisation $\vec{P}_{elect}$ in the presence of an electric field $\vec{E}$.*

which opposes itself to the field $\vec{E}$. α_{elec} is called electronic polarisability. The polarisation disappears if the field is removed. This polarisation occurs for frequencies higher than optical [1].

II.1.2.2 Ionic polarization

This process is characterised by the relative motion of cations and anions under the influence of an electric field. The application of an electric field to a dielectric induces a displacement of positive ions with respect to negative ions [1]

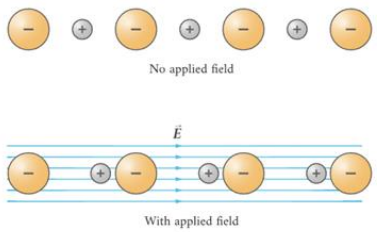

Figure. II.4: *(a) the absence of an electric field; (b) the application of an electric field on a dielectric induces a displacement of positive ions relative to negative ions.*

Let's assume the ion is perfectly rigid throughout. The action of the electric field will be to move it by an amount $\vec{l}$ relative to a fixed reference point centred at O; hence, a variation in the dipole moment:

$$\vec{P}_{ion} = q\vec{l} \; - \; \varepsilon_0 \alpha_{ion} \vec{E} \qquad (II.20)$$

This is the induced ionic polarisation, proportional to the electric field (elastic deformations), with α_{ion} being the ionic polarisability.

The total dipole moment attached to the ion displacement and the deformation of the electronic orbitals is, to a first approximation, the sum of two (II.19) and (II.20), namely:

$$\vec{P}_t = \vec{P}_{ion} + \vec{P}_{elect} \qquad (II.21)$$

Ionic polarisation is slower than electronic polarisation, as the displacement involved here is that of a much heavier ion as compared to the electron cloud.

II.1.2.3 Dipolar Polarisation

It is slower than ionic polarization. Dipolar polarisation arises from the presence of permanent electric dipole moments that exist even in the absence of an external electric field. Particles or molecular entities possessing such permanent moments are often referred to as orientation dipoles. When an external electric field is applied, these dipoles partially align with it, thereby generating a net polarisation. A medium containing such orientation dipoles is therefore referred to as a polar dielectric.

Polar environments can take different forms depending on the material's molecular structure and bonding. In many solid dielectrics, whether crystalline or amorphous, various extrinsic sources of permanent dipole moments can also be present. For instance, the break in periodicity in crystalline or polycrystalline structures can lead to the formation of local dipoles. Similarly, dangling bonds or unsatisfied valences may give rise to permanent dipole moments within the lattice.

In real dielectric materials, other types of structural or chemical defects can also contribute to dipolar polarisation. For example, molecular agglomerates (often called clusters) with a permanent dipole moment may form within the material. The size and stability of these clusters

can increase as the temperature decreases, thereby enhancing the medium's overall dipolar polarisation [2].

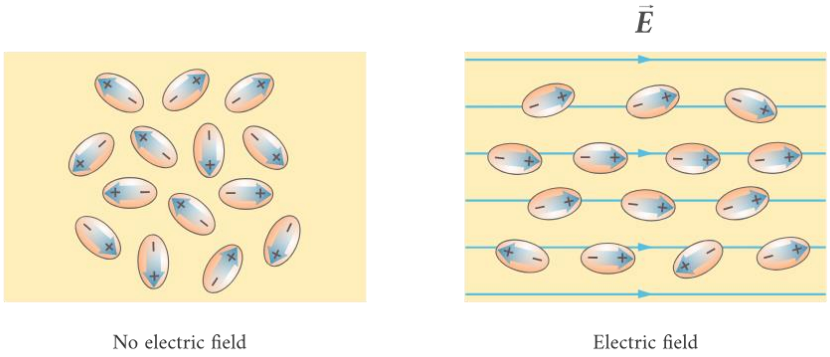

Figure II.5: *(a) dipoles in the absence of an electric field; (b) the orientation of the dipoles towards the electric field* $\vec{E}$ *.*

As with space load polarisation, the frequency response of dipolar polarisation is characterised by a decrease in effective permittivity and the appearance of a loss peak. Dipolar polarisation occurs when the frequency of the applied voltage is in the audio range.

II.1.2.4 Space Charge Polarization

Space-charge polarisation refers to the polarisation effects arising from the motion of charge carriers under an applied electric field. The species involved in this type of polarisation can be trapped electrons (within the dielectric or at interfaces) or ions that diffuse within the dielectric [3]. We observe the formation of a "macroscopic dipole" in a sample that, initially homogeneous, becomes heterogeneous under the action of the electric field (see figure II.6).

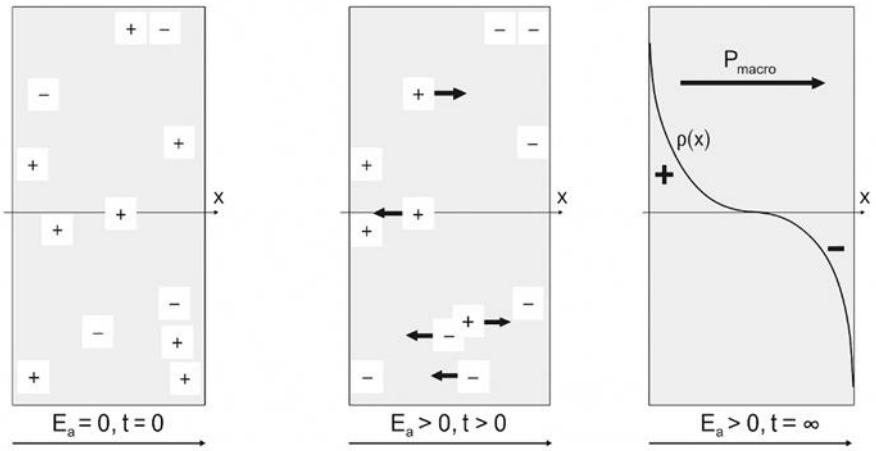

Figure. II.6: *Formation of a "macroscopic dipole" due to the migration of charged species in the dielectric subjected to an external electric field.*

Generally, the effects of space charge polarisation are very slow to establish, and are observed in frequency ranges between millihertz and hundreds of Hertz.

II.1.3 Frequency Dependence of Dielectric Polarization

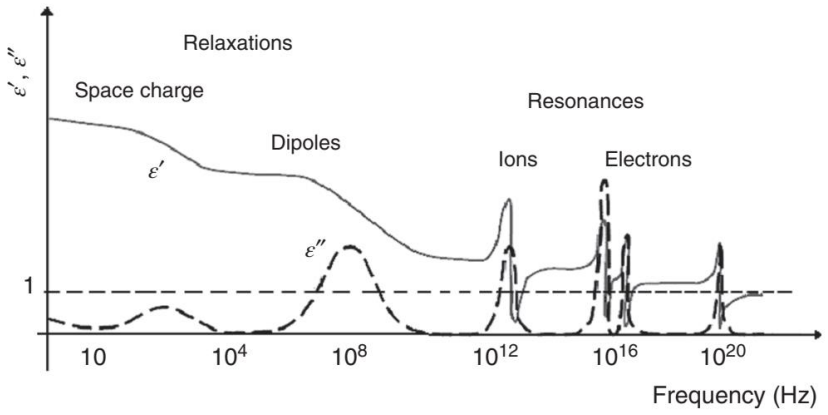

Figure. II.7: *Presentation of the different effects on permittivity and dielectric losses of relaxation and resonance modes. [1]*

Referring to Figure II.3, all the four types of polarization are present at machine frequencies. As the frequency increases, space charge, orientation, and ionic polarization become inoperative in that order. When several polarization processes occur in a material, it follows that the dielectric constant will decrease with increasing frequency of the applied voltage. When the period of the applied voltage is much larger than the relaxation time of a polarization process, the polarization is completed at any instant during each cycle, and when the period of the applied voltage is much shorter than the relaxation time for a polarization process, the polarization does not occur at all. But when the period of the applied voltage is in the same range as the relaxation time, resonance occurs.

At high frequencies, usually microwave and beyond – the processes that take place are undamped and are called “resonances.” Real dielectric materials have several such resonances due to ionic and electronic polarization. At frequencies below microwaves, the polarization processes are heavily damped and are called “relaxations.” In physics, dielectric dispersion is the dependence of the permittivity of a dielectric material on the frequency of an applied electric field. This is because there is a lag between changes in polarization and changes in the electric field. The permittivity of the dielectric is a complicated function of frequency of the electric field.

Dielectric dispersion is very important for the applications of dielectric materials and for the analysis of polarization systems.

This is one instance of a general phenomenon known as material dispersion: a frequency-dependent response of a medium for wave propagation. When the frequency becomes higher:

dipolar polarization can no longer follow the oscillations of the electric field in the microwave region around 10^{10} Hz

ionic polarization and molecular distortion polarization can no longer track the electric field past the infrared or far-infrared region around 10^{13} Hz

electronic polarization loses its response in the ultraviolet region around 10^{15} Hz. In the frequency region above ultraviolet, permittivity approaches the constant $\varepsilon 0$ in every substance, where $\varepsilon 0$ is the permittivity of the free space. Because permittivity indicates the strength of the relation between an electric field and polarization, if a polarization process loses its response, permittivity decreases.

The effect of temperature on the relative permittivity of a material can be twofold. In orientation polarization, the randomizing action of thermal energy decreases the tendency for the permanent dipoles to align themselves in the applied field. This results in a decrease in the relative permittivity with increasing temperature. The other effect of temperature is to facilitate the diffusion of ions in space charge polarization. Thermal energy may aid in overcoming the activation barrier for the orientation of relatively large polar molecules in the direction of the field.

II.2 Description of the Dielectric Relaxation Phenomenon and Its Characterization Methods

II.2.1 Dielectric Relaxation

Dielectric relaxation is the momentary delay (or lag) in the dielectric constant of a material. This is usually caused by the delay in molecular polarization with respect to a changing electric field in a dielectric medium (e.g. inside capacitors or between two large conducting surfaces). Dielectric relaxation in changing electric fields could be considered analogous to hysteresis in changing magnetic fields (e.g. in inductor or transformer cores).

Relaxation in general is a delay or lag in the response of a linear system, and therefore, dielectric relaxation is measured relative to the expected linear steady state (equilibrium) dielectric values. The time lag between electrical field and polarization implies an irreversible degradation of Gibbs free energy. In physics, dielectric relaxation refers to the relaxation response of a dielectric medium to an external, oscillating electric field. This relaxation is often described in terms of permittivity as a function of frequency, which can, for ideal systems, be described by the Debye equation. On the other hand, the distortion related to ionic and electronic polarization shows behavior of the resonance or oscillator type. The character of the distortion process depends on the structure, composition, and surroundings of the sample.

II.2.2 Debye-type Relaxations

As we have already mentioned in the previous section, permittivity is due to dipoles present in the dielectric, which will orient themselves under the action of an electric field. At the beginning of the 20th century, inspired by liquid dielectrics, Debye observed that if all the dipoles have the same orientation time τ and do not interact with each other [4], the complex permittivity ε^* as a function of frequency follows the following law:

$$\varepsilon^* = \varepsilon_\infty + \frac{\Delta\varepsilon}{1 + i\,\omega\,\tau} \qquad (II.22)$$

Avec $\Delta\varepsilon = \varepsilon_{BF} - \varepsilon_{HF}$

ε_{BF} is the low-frequency permittivity, ε_{HF} is the high-frequency permittivity, τ is the characteristic relaxation time, and ω is the pulsation (in rad/s).

This response is said to be ideal because all the dipoles participating in the relaxation phenomenon have the same relaxation time τ. This behavior has been mainly observed in liquid dielectrics such as water [1]. In practice, it is quite rare to observe such relaxation in solid dielectrics. Indeed, interactions between dipoles cannot generally be neglected in these materials, leading to dispersion in the relaxation time τ.

II.2.3 Distribution of relaxation times

In the case where all the dipoles do not have the same relaxation time but a relaxation peak is visible, we speak of the distribution of relaxation times DRT (Distribution of Relaxation

Time). There are several empirical models that can accurately describe these types of relaxation. These models are all derived from the Debye equation.

II.2.3.1 Cole-Cole relation

This relationship is written:

$$\varepsilon^* = \varepsilon_\infty + \frac{\Delta\varepsilon}{1+(i\,\omega\,\tau)^{\alpha}} \qquad (II.23)$$

With $0 < \alpha \leq 1$

This empirical relationship yields a symmetrical but flatter frequency response than the Debye model and is mostly used in amorphous solid dielectrics. [5]

II.2.3.2 Davidson-Cole relation

This relationship is written:

$$\varepsilon^* = \varepsilon_\infty + \frac{\Delta\varepsilon}{[1+i\,\omega\,\tau]^{\beta}} \qquad (II.24)$$

With $0 < \beta \leq 1$

This empirical relationship produces an asymmetrical frequency response that follows the Debye curve at low frequencies but exhibits a gentler slope at high frequencies. It is frequently used for liquid dielectrics [6].

II.2.3.3 Havriliak-Negami relation

This relationship is written:

$$\varepsilon^* = \varepsilon_\infty + \frac{\Delta\varepsilon}{[1+(i\,\omega\,\tau)^{\alpha}]^{\beta}} \qquad (II.25)$$

With $0 < \alpha \leq 1$ et $\alpha\beta \leq 1$

This empirical relationship allows for an asymmetrical frequency response, with a and b adjusting the slopes at high and low frequencies, respectively. It can be noted that for a = b = 1, we obtain a Debye-type response [7].

Let's also mention the empirical models of Fuoss-Kirkwood [8] and Jonscher [1], which are slightly more complex and allow for independent parameterisation of high-frequency behaviour from low-frequency behaviour.

II.2.3.4 Comparison of the three presented models with the Debye model

The three models were simulated in the frequency domain to characterize their individual behaviors. The results, shown in Figure II.8.a.b, illustrate the variations in the real permittivity (ε′), dielectric losses (ε″), and loss tangent (tan δ).

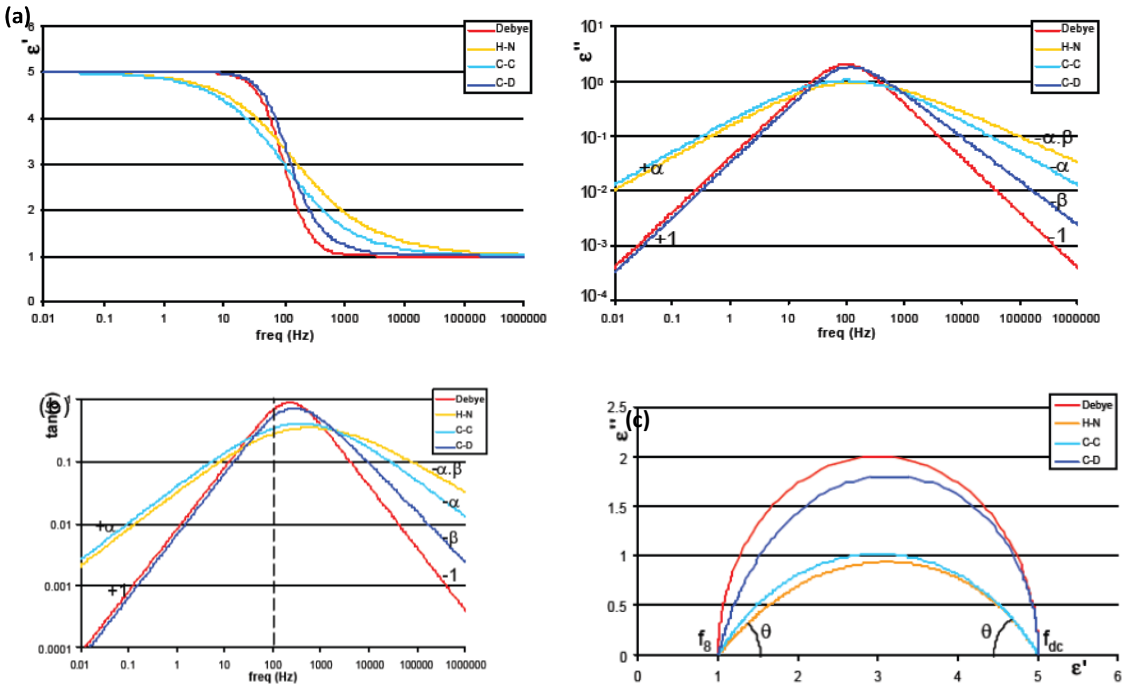

Figure. II.8: ***(a)*** *Variation of the real permittivity and dielectric losses as a function of frequency for the different models.* ε_{HF} *=1,* ε_{BF} *= 5, t =* $10^{-2}/(2*\pi)$ *in seconds,* α *= 0.6, and* β *= 0.8.* ***(b)*** *Variation of the loss angle tangent as a function of frequency for the different models.* ε_{HF} *= 1,* ε_{BF} *= 5, t =* $10^{-2}/(2*\pi)$ *in seconds,* α *= 0.6, and* β *= 0.8.* ***(c)*** *Cole–Cole plot ε″(ε′).*

We can observe in figure II.8.a that empirical models allow for variations in real permittivity over a wider frequency range than in the case of a pure Debye response.

In Figure II.8.b, the slopes in the low- and high-frequency domains (on a log–log plot) are presented. As observed, the Havriliak–Negami model enables independent adjustment of each slope—high-frequency and low-frequency—providing greater flexibility in fitting experimental data.

Another important aspect to note is the behavior of tan (δ) as a function of frequency, which closely follows that of the dielectric losses (ε″). However, it can be clearly seen that the peak does not occur at 100Hz, i.e., at 1/(τ.2π).

By calculating tan (δ) from the Debye model, we obtain:

$$tan(\delta) = \frac{\varepsilon''}{\varepsilon'} = \frac{(\varepsilon_{BF} - \varepsilon_{HF}).\tau.\omega}{\varepsilon_{BF} + \varepsilon_{HF}(\tau\omega)^2} \quad (II.26)$$

The frequency corresponding to the maximum of tan (δ) is then given by:

$$\omega_{MAX} = \frac{1}{2\pi\tau} \cdot \sqrt{\frac{\varepsilon_{BF}}{\varepsilon_{HF}}} \quad (II.27)$$

It follows that the frequency of the tan (δ) peak depends not only on τ, but also on ε_{BF} and ε_{HF}. For the other empirical models, the peak frequency depends on the same parameters, with the addition of the coefficients α and β.

Therefore, any reasoning based on the frequency of the relaxation peak observed in tan (δ) must be made with great caution. In particular, extracting an activation energy from the tan (δ) peak to infer that of the relaxation process is valid only if the parameters ε_{BF}, ε_{HF}, α, and β remain constant with temperature.

Figure II.8.c presents the Cole–Cole plot, which shows dielectric losses (ε″) as a function of the real permittivity (ε′) for the models discussed above.

For the Debye model, the Cole–Cole representation forms a semicircle with a diameter of $\varepsilon_{BF} - \varepsilon_{HF}$, centered at $1/2(\varepsilon_{BF}+\varepsilon_{HF})$ on the ε' axis. The maximum dielectric loss equals the radius and occurs at a frequency of $1 / (2\pi\tau)$.

The angle θ, corresponding to the angle between the curve and the x-axis when the losses approach zero, is equal to π/2. In general—and therefore for the other models—this angle is expressed as:

$$\theta = 2.\pi.p \quad (II.28)$$

where p represents the slope of the ε″ curve at that frequency on a log–log scale. This representation clearly demonstrates that the maximum of dielectric losses is always correlated with the maximum variation in permittivity.

II.2.4 Effect of temperature on relaxation time τ

The relaxation time (τ) associated with dipole moments is temperature-dependent. It is generally observed that τ varies logarithmically with the inverse of temperature, exhibiting two characteristic behaviours: Arrhenius behaviour, typical of most dielectrics, and Vogel–Fulcher–Tammann (VFT) behaviour, often observed in relaxation processes. These two behaviours are briefly described below [9-11].

II.2.4.1 Arrhenius law

This behaviour has been interpreted based on band theory or Eyring's theory [12]. For the band theory, the interaction forces between a molecule and its neighbours can be represented by a potential energy curve. The addition of a sufficient thermal fluctuation to the system allows the molecule to overcome the potential barrier and occupy another equilibrium position [13, 14]. Eyring's theory treats dipole rotation as a chemical reaction, and the reaction's equilibrium state is the one in which the dipole has sufficient energy to overcome the potential barrier. The relaxation time is ultimately determined by:

$$\tau\,(T) = \tau_0\, exp\, \frac{E_a}{k_b\, T} \qquad (II.29)$$

With τ_0 a constant in seconds, E_a the activation energy, and k the Boltzmann constant. The plot of lg τ as a function of 1/T is linear, and the calculation of the slope allows us to obtain E_a.

II.2.4.2 Vogel-Tammann-Fulcher Law

This type of behaviour is often observed when the temperature is above the glass transition temperature T_g, due to changes in the material's free volume. The evolution of the average relaxation time as a function of temperature, following the Vogel-Fulcher-Tamman (VFT) law, is then given by [15]:

$$\tau\,(T) = \tau_0\, exp\, \frac{E_a}{k_b\,(T - T_v)} \qquad (II.30)$$

Where T_V is the Vogel temperature above which the free volume fraction is non-zero.

II.2.5 Origins of dielectric relaxation

Several mechanisms have been reported in the literature as potential origins of the dielectric relaxation phenomenon. In the following sections, we will present and discuss three of them: hopping conduction, electrode polarization, and interfacial relaxation.

II.2.5.1 Hopping conduction

The presence of defects in the dielectric can lead to variations in permittivity with frequency. Indeed, these defects constitute potential wells that can hold charges.

Under certain conditions, these charges can move from one trap to another and thus move within the dielectric. We can find in the figure. II. 9 A representation of this jump transition model.

Without an electric field, the probability of transitions between the wells R_{ij} and R_{ji} are equal, and the barrier height to overcome to move from one trap to the other is ΔH. We can clearly see that the application of an electric field has the effect of decreasing the barrier height to jump from point j to i or increasing the barrier height to jump from point i to j. This has the effect of increasing the jump probability R_{ij} and decreasing R_{ji}. From this model, Jonscher was able to show that when the electric field is sinusoidal, a contribution from "hopping" to polarisation appears.

$$\chi(\omega) = \frac{N\mu^2}{3kT\varepsilon_0}\, r\tau\, \frac{1}{1+i\omega\tau} \qquad (II.31)$$

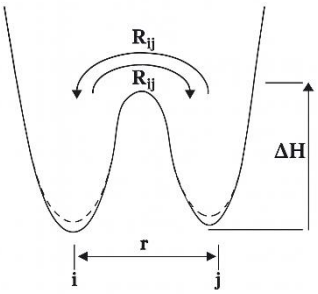

Figure. II.9: *Hopping transition model without electric field (solid line) and with electric field (dashed line).*

We can observe that it is of pure Debye type.

From this transition theory, Jonscher proposed a concept of a "power-law frequency" (PLF) type response that follows the following law:

$$\chi(\omega) \propto \varepsilon(\omega) = B(i\omega)^{c-1} \qquad (II.32)$$

With B a constant and c a coefficient between 0 and 1. By decomposing the permittivity into real and imaginary parts, we obtain:

$$\varepsilon'(\omega) = B \sin\left(\frac{c\pi}{2}\right) \omega^{C-1} \qquad (II.33)$$

$$\varepsilon''(\omega) = B \cos\left(\frac{c\pi}{2}\right) \omega^{C-1} \qquad (II.34)$$

We can observe that the real and imaginary parts of the permittivity both have the same frequency dependencies. This implies that tan(δ) is independent of frequency:

$$Tan(\delta)(\omega) = \cot\left(\frac{c\pi}{2}\right) \qquad (II.35)$$

In the following study, we will make the change of variable n = 1 - c. This allows us to obtain:

$$\chi(\omega) \propto \varepsilon(\omega) = B(i\omega)^{-n} \qquad (II.36)$$

$$Tan(\delta)(\omega) = \tan\left(\frac{n\pi}{2}\right) \qquad (II.37)$$

With n between 0 and 1.

Jonscher also discussed the coefficient n. When it is close to 0 (or c close to 1), the variations in real permittivity and dielectric losses with frequency are very small. This case occurs only in very high-quality dielectrics with few defects. It is called the "flat loss" behaviour (flat dielectric losses).

The introduction of this power-law behaviour is very important in the study of the dielectric relaxation phenomenon. Indeed, until now we have presented the loss peaks as the origin of the variations in permittivity as a function of frequency. Nevertheless, between two dielectric relaxation peaks, the capacitances never being perfect, the dielectric losses are not zero. And as the Kramers-Kronig law stipulates, all dielectric losses induce variations in permittivity as

a function of frequency. That is why when measuring any dielectric at a frequency, we will obtain a non-zero value of tan(δ) even if no relaxation peak is the cause [16].

II.2.5.2 Electrode polarization

On the other hand, in the literature, it has been shown that at the interface between two materials, relaxation mechanisms can occur.

This is precisely the case of electrode polarisation that occurs when a high impedance layer appears between the electrode and the dielectric. This appearance can be due to the accumulation of charges that have migrated into the sample or poor contact between the dielectric and the electrode. This results in a significant increase in the measured capacitance at low frequency (equation II.38) and a dependence of the apparent permittivity on ω^{-2} in the case where the high impedance layer is air [17].

$$\varepsilon'_{app} = \varepsilon' + \frac{\sigma^2 C_0}{\omega^2 \varepsilon_0^2 C_e} \qquad (II.38)$$

With C_0 the capacitance of the layer between the electrode and the dielectric, C_e the capacitance of the sample, and σ the conductivity of the material.

The phenomenon of electrode polarisation has also been attributed to the fractal dimension of the electrode. Indeed, Liu showed that by simulating the roughness of the interface between an electrode and a dielectric using a fractal model, a dielectric relaxation phenomenon was obtained Figure. II.10 [18].

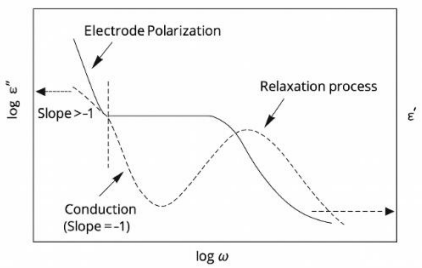

Figure. II.10: *Representative diagram of the real (ε′) and imaginary (ε″) parts of permittivity as a function of frequency.*

II.2.5.3 Interfacial polarization

The same behaviour as electrode polarisation but this time between two dielectrics was presented by Maxwell [19]. This behaviour is called the interfacial polarisation

phenomenon. It can notably appear when species or charges accumulate at an electrode, creating a capacitance composed of two dielectrics of different composition and thus different electrical characteristics.

He showed that this association of two dielectrics with different permittivity and conductivity inevitably induces a Debye-type relaxation. This model is called the Maxwell-Wagner model [20] (also known as dual-capacity operation), it is physically described in the figure. II.11.

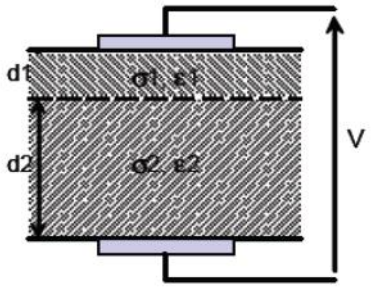

Figure. II.11: *Presentation of the Maxwell-Wagner model from a physical point of view.*

This physical model can be translated into an electrical model presented in figure II.12 This model consists of two impedances in series, where each impedance is composed of a capacitance in parallel with a conductance. The capacitance and conductance can be expressed in terms of physical parameters $C_i=\varepsilon_i.\varepsilon_0.S/d_i$ and the conductance $G_i = s_i/d_i$. With ε_0 the permittivity of free space and S the surface area of the capacitance.

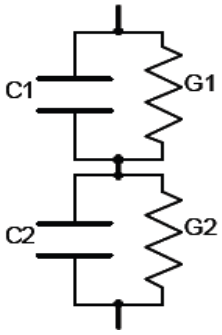

Figure. II.12: *Presentation of the Maxwell-Wagner model from an electrical point of view.*

The low-frequency permittivity, the high-frequency permittivity, the relaxation peak, and the frequency of the relaxation peak are obviously dependent on the system variables. Depending on these variables (ε_i the permittivity, σ_i the conductivity, and d_i the thickness), it can be of very low amplitude and occur at extremely low and unmeasurable frequencies.

Let's also note the Maxwell-Wagner-Sillars model [19, 21] which is directly inspired by that of Maxwell-Wagner, but by working on the behaviour of a dielectric containing impurities of different shapes. These impurities, like the main dielectric, have their own permittivity and conductivity. Sillars showed that depending on the shape of these impurities, the total apparent permittivity can exhibit very strong variations at low frequencies, sometimes much stronger than those of the Maxwell-Wagner model (see figure II.13).

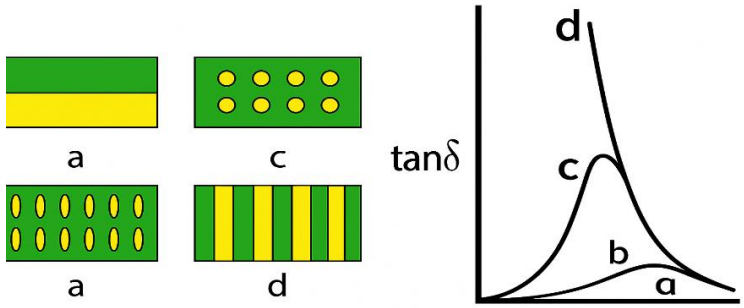

Figure. II.13: *Maxwell-Wagner model (a) and Maxwell-Wagner Sillars (b, c, d).*

II.2.6 Dielectric Relaxation Behavior of Ionic Liquid

The analysis of dielectric properties —namely effective permittivity (ε′), losses, (ε″), and dissipation factor (tan δ)— as a function of temperature provides valuable insight into the molecular dynamics and relaxation processes occurring within ionic liquid-based materials.

The multiple relaxation phenomena observed during frequency- and temperature-dependent measurements can be correlated with the molecular organization and structural state of the materials, whether amorphous, semi-crystalline, or crystalline. These relaxation processes manifest as peaks in the isofrequency or isothermal dielectric loss curves [22, 23]. It is generally observed that these relaxation peaks shift:

- ✓ Towards higher temperatures as the frequency increases (in isofrequency plots), and
- ✓ Towards higher frequencies as the temperature increases (in isothermal plots).

In isofrequency representations, the various relaxation modes are conventionally designated by the symbols α, β, and γ, corresponding to processes occurring in the direction of decreasing temperature (Figure II.14).

The α-relaxation peak is associated with the glass transition phenomenon and reflects the cooperative micro-Brownian motion of the polymer chains. This relaxation is highly sensitive

to frequency, often resulting in an apparent shift of the glass transition temperature with measurement conditions [24].

The β-relaxation peak is generally attributed to local segmental motions of the polymer chains, particularly those involving side or pendant groups, as well as conformational rearrangements within the molecular structure [25].

The γ-relaxation peak is related to the rotational motions of small chemical groups within the amorphous phase of the material [26].

Dielectric relaxation spectra thus provide a powerful means of probing molecular mobility across different temperature and frequency domains. When combined with complementary techniques such as differential scanning calorimetry (DSC), dielectric analysis enables precise determination of key parameters such as the glass transition temperature (T_g).

In this study, we will focus on Chapters IV.2 and IV.4 on the dielectric response of ionic liquids within the frequency range 10^{-2}–10^{6} Hz and the temperature range –80 °C to +20 °C. This range encompasses the glass transition region, the most widely investigated temperature domain for ionic liquids (ILs), where characteristic relaxation processes are most prominent.

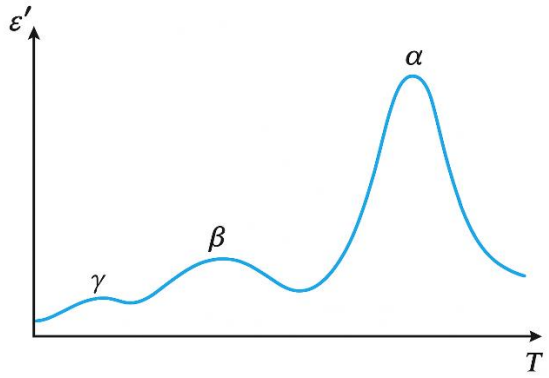

Figure. II.14: *Temperature dependence of the real part of the dielectric permittivity (ε') showing the α, β, and γ relaxation processes. The γ-relaxation corresponds to localized molecular motions at low temperatures, the β-relaxation is associated with the mobility of side groups or chain segments, and the α-relaxation represents the main cooperative molecular motion related to the glass transition (T_g). The increase in temperature activates successive relaxation mechanisms as molecular mobility increases.*

CONCLUSION

In this chapter, we have presented a comprehensive overview of the main relaxation mechanisms occurring in dielectric materials. The discussion was structured into two main parts in order to provide both a fundamental understanding of dielectric behavior and an analytical perspective on relaxation phenomena.

In the first part, the fundamental dielectric properties were introduced, including the key concepts of polarization, electric susceptibility, and permittivity. The different polarization mechanisms were classified into four principal categories: space charge polarization, dipolar polarization, electronic polarization, and ionic polarization. We also analyzed how the dielectric constant and dielectric losses vary with frequency. These variations reveal the occurrence of relaxation phenomena, which manifest when dipoles can no longer follow the rapid alternation of the applied electric field. This frequency-dependent behavior highlights the intrinsic time-dependent response of dielectrics to external excitations.

In the second part, the phenomenon of dielectric relaxation was examined in detail. We discussed the physical origins of relaxation processes, as well as the methods used for their characterization. Particular attention was given to the influence of temperature on the relaxation time (τ), which plays a crucial role in determining the dynamic response of dielectric materials. The observed dependence of τ on temperature provides valuable insights into molecular motion and energy barriers associated with polarization mechanisms.

Overall, this chapter establishes the theoretical foundation necessary for understanding dielectric relaxation and its significance in the electrical and thermal behavior of insulating materials. These principles form the basis for subsequent analysis and experimental investigations aimed at optimizing dielectric performance in practical applications such as capacitors, sensors, and high-frequency devices.

BIBLIOGRAPHY

1. Jonscher, A.K.J.J.o.P.D.A.P., *Dielectric relaxation in solids.* 1999. **32**(14): p. R57.
2. Uwe, H., et al., *Ferroelectric microregions and Raman scattering in KTaO 3.* 1986. **33**(9): p. 6436.
3. Macdonald, J.R.J.P.r., *Theory of ac space-charge polarization effects in photoconductors, semiconductors, and electrolytes.* 1953. **92**(1): p. 4.
4. Debye, P.J.W., *Polar molecules*. 1929: Dover publications.
5. Cole, K.S. and R.H.J.T.J.o.c.p. Cole, *Dispersion and absorption in dielectrics I. Alternating current characteristics.* 1941. **9**(4): p. 341-351.
6. Davidson, D.W. and R.H.J.T.J.o.C.P. Cole, *Dielectric relaxation in glycerol, propylene glycol, and n-propanol.* 1951. **19**(12): p. 1484-1490.
7. Havriliak, S. and S. Negami. *A complex plane analysis of α-dispersions in some polymer systems*. in *Journal of Polymer Science Part C: Polymer Symposia*. 1966. Wiley Online Library.
8. Fuoss, R.M. and J.G.J.J.o.t.A.C.S. Kirkwood, *Electrical properties of solids. VIII. Dipole moments in polyvinyl chloride-diphenyl systems.* 1941. **63**(2): p. 385-394.
9. Block, H., R. Groves, and S.M. Walker, *Dielectric relaxation in polymaleimide and N-substituted polymaleimides.* Polymer, 1972. **13**(11): p. 527-535.
10. Paluch, M., *Dielectric properties of ionic liquids*. 2016: Springer.
11. Kremer, F. and A. Schönhals, *Broadband dielectric spectroscopy*. 2002: Springer Science & Business Media.
12. Eyring, H.J.T.o.t.F.S., *The theory of absolute reaction rates.* 1938. **34**: p. 41-48.
13. Debye, P.J.L.H., *Polare molekeln.* 1929.
14. Frohlich, H., *Theory of Dielectrics: Permittivity and Dielectric Loss*. 1958, Oxford Science Publications, Oxford.
15. Runt, J.P. and J.J.J. Fitzgerald, *Dielectric spectroscopy of polymeric materials: fundamentals and applications.* 1997.
16. Seguin, B., et al. *Calorimetric apparatus for measurement of power losses in capacitors*. in *IMTC/98 Conference Proceedings. IEEE Instrumentation and Measurement Technology Conference. Where Instrumentation is Going (Cat. No. 98CH36222)*. 1998. IEEE.
17. Blythe, A.R. and D. Bloor, *Electrical properties of polymers*. 2005: Cambridge university press.
18. Liu, S.J.P.r.l., *Fractal model for the ac response of a rough interface.* 1985. **55**(5): p. 529.
19. Tuncer, E., S.M. Gubański, and B.J.J.o.A.P. Nettelblad, *Dielectric relaxation in dielectric mixtures: Application of the finite element method and its comparison with dielectric mixture formulas.* 2001. **89**(12): p. 8092-8100.
20. Şentürk, E.J.S.-s.e., *Two relaxation mechanisms in (Sr1− 1.5 xBix) TiO3 (x: 0.0067).* 2005. **49**(6): p. 935-939.
21. Sillars, R.J.I.o.E.E.-P.o.t.W.S., *The properties of a dielectric containing semiconducting particles of various shapes.* 1937. **12**(35): p. 139-155.
22. Coelho, R., B. Aladenize, and A.J.T.d.n.t. Le Méhauté, *Les diélectriques(propriétés diélectriques des matériaux isolants).* 1993.
23. Sutton, L.E., *Dielectric Behavior and Structure. Dielectric Constant and Loss, Dipole Moment and Molecular Structure.* Journal of the American Chemical Society, 1956. **78**(2): p. 507-508.
24. Elias, H.-G., *Electrical Properties*, in *Macromolecules: Volume 1 · Structure and Properties*, H.-G. Elias, Editor. 1977, Springer US: Boston, MA. p. 509-521.
25. Von Hippel, A.R. and M. Sauzade, *Les diélectriques et leurs applications*. 1961: Dunod.

26. Calucci, L., et al., *Unravelling Main- and Side-Chain Motions in Polymers with NMR Spectroscopy and Relaxometry: The Case of Polyvinyl Butyral.* Polymers (Basel), 2021. **13**(16).

CHAPTER III

DATAMINING AND EXPERIMENTAL METHODS

III.1 DATAMINING METHODS

Data mining, also known as Knowledge Discovery in Databases (KDD), is a data exploration technique that aims to extract useful knowledge or insights from large volumes of data through automatic or semi-automatic methods [1]. It is primarily applied in professional and organizational contexts and differs from traditional statistical data analysis in several important ways:

Absence of a prior hypothesis: Unlike classical statistical approaches, data mining does not require the formulation of an initial hypothesis to be tested. Instead, it allows patterns, relationships, and correlations to emerge directly from the data, with algorithms serving as discovery tools rather than hypothesis-verification mechanisms. In this sense, data mining stands at the intersection of statistics and artificial intelligence.

Integration into organizational processes: The knowledge extracted through data mining is designed to be operationally actionable within an organizational framework. The results of analyses must often be implemented rapidly to support timely decision-making, making responsiveness and adaptability essential features of the data mining process.

Nature and origin of data: The data analyzed typically originate from existing storage systems—such as databases, data warehouses, or enterprise resource systems—and are often heterogeneous, multi-source, and semi-structured. Since these data were not initially collected for analytical purposes, their use requires high-performance tools for data preparation, integration, and transformation.

In summary, data mining seeks to transform vast and diverse datasets—whether stored in relational databases or extracted from semi-structured sources such as the Internet—into meaningful and actionable information, thereby supporting knowledge discovery and informed decision-making.

III.1.1 Definition

Data mining encompasses a set of methods and algorithms designed for the exploitation and analysis of data with the objective of discovering hidden rules, associations, and previously unknown trends within that data. It also aims to identify particular structures

that succinctly summarize the essential information required to support decision-making processes.

In other words, data mining represents the acquisition of new knowledge from existing data, transforming already accumulated information into actionable insights that enhance understanding and guide strategic decisions.

III.1.2 Principle

Data mining is an analytical process that adopts a fundamentally different approach from that used in traditional statistics. Statistical analysis typically begins with the formulation of a hypothesis that the data are then used to test or validate. In contrast, data mining follows an empirical and exploratory approach, aiming to uncover hidden patterns and relationships within raw data—patterns that the analyst may not initially anticipate, but whose relevance must subsequently be verified.

Rather than constituting a standardized theoretical framework, data mining is best understood as a knowledge extraction process, which generally follows several main steps:

- *Problem Formalization:* Defining the problem to be solved in terms of available or required data.
- *Data Access:* Identifying and collecting relevant data from various sources.
- *Data Preparation:* Cleaning, transforming, and structuring the data to make it suitable for analysis.
- *Modeling:* Applying appropriate analytical or machine learning algorithms to extract patterns or relationships.
- *Evaluation and Validation:* Assessing the quality, accuracy, and usefulness of the knowledge extracted from the analysis.

This process is inherently iterative rather than linear, allowing for continuous refinement and validation at each stage. Data mining thus contributes to a more systematic and rational management of information, facilitating the capitalization of acquired knowledge in explicit, structured forms that support knowledge engineering.

In essence, data mining integrates techniques from multiple disciplines—including statistics, artificial intelligence, and database systems—to construct models from data and to identify "interesting" or informative patterns according to predefined criteria. Its ultimate goal is to extract the maximum amount of useful knowledge from data to support decision-making and discovery.

III.1.3 Types of Datamining Techniques

Solving a problem using a data mining process generally involves the application of multiple methods and algorithms, each serving a specific analytical purpose. In practice, these methods can be grouped into two main families, depending on the objective of the analysis and the nature of the available data [2]:

III.1.3.1 Descriptive Techniques

Descriptive techniques are used to analyze datasets in which no variable is designated as a target or dependent variable. In such cases, all variables are treated equally, and the objective is to identify patterns, similarities, or structures within the data rather than to predict a specific outcome. These methods aim to extract homogeneous groups or reveal underlying relationships among individuals or variables, thereby achieving information compression and data simplification (see Fig. III.1).

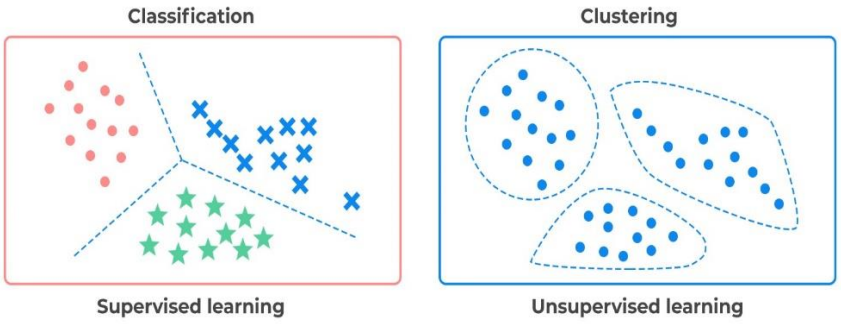

***Fig III.1.1**: Supervised and Unsupervised techniques.*

We can mention some techniques available for these methods:

• Principal Component Analysis (PCA);

• Techniques classically used in the world of statistics: hierarchical clustering, k-means and dynamic clouds (Nearest Neighbour Search), mixed classifications (Birch...), relational classifications.

III.1.3.2 Predictive Techniques

Predictive techniques are methods designed to explain and/or predict one or more observable and measurable phenomena. In practice, they focus on one or more variables in a dataset that are defined as the targets (or response variables) of the analysis. These methods aim to model the relationships between explanatory variables and target variables to enable interpretation, classification, or prediction.

The main existing predictive techniques include:

• Decision trees (Decision tree).

• Neural network;

• Linear and non-linear regressions in the broad sense: (Binary or multinomial logistic regression, linear or quadratic discriminant analysis, generalised linear model, PLS regression, non-parametric regressions, structural equations).

• Genetic algorithms.

• Bayesian inference (Bayesian network).

III.1.4 Partial Least Squares Method (PLS)

Many industrial and engineering problems can be formulated as regression models, where a set of input variables (X) can be controlled or influenced to some extent, while a set of output variables (Y) can only be observed. The main objective is to describe and model the relationships between Y and X in situations where no explicit theoretical model is available.

A major difficulty in such cases is that the number of predictor variables (X) is often much larger than the number of available observations, leading to issues of multicollinearity and model instability. Partial Least Squares Regression (PLSR) is a data analysis method specifically developed to address this type of problem.

It provides a robust framework for modeling complex systems by extracting latent variables that capture the essential relationships between X and Y, even when the predictors are numerous and highly correlated. [3].

III.1.4.1 Presentation

Partial Least Squares (PLS) regression can be viewed as an extension of the multiple linear regression (MLR) model. In its simplest form, a linear model describes the linear relationship between one or more dependent (response) variables, denoted by Y, and a set of independent (predictor) variables, denoted by X, as follows:

$$Y = b_0 + b_1X_1 + b_2X_2 + \cdots + b_pX_p \quad \text{(III.1)}$$

Where the *b*i are the regression coefficients.

A simple example of regression analysis is the estimation (or prediction) of an individual's weight based on their height and gender, where weight (Y) is expressed as a function of height (X_1) and gender (X_2). In such a case, linear regression can be applied to estimate the corresponding regression coefficients from a dataset containing measurements of these variables.

In many data analysis problems, estimating the linear relationship between two variables is sufficient to describe the observed data and to provide reliable predictions for new observations. However, the multiple regression model has been extended in several ways to handle more complex analytical challenges. It serves as the foundation for numerous multivariate statistical methods, such as discriminant analysis, principal component regression (PCR), and canonical correlation analysis.

Partial Least Squares (PLS) regression is a relatively recent technique that generalizes and combines the features of principal component analysis (PCA) and multiple linear regression. It is particularly advantageous when the objective is to predict a set of dependent variables from a large number of highly correlated predictors.

When the predictors are few, not significantly collinear, and have a well-defined relationship with the responses, multiple linear regression remains the most appropriate method. However, when these conditions are not met—particularly in the presence of

multicollinearity or when the number of predictors exceeds the number of observations—multiple linear regression becomes unreliable or even unusable.

The PLS method is therefore well suited for constructing predictive models when the explanatory variables are numerous and strongly correlated. It emphasizes the prediction of the response variable rather than the interpretation of the relationships among variables. Consequently, PLS is not designed to identify variables with negligible effects on the response; rather, it is most valuable when prediction accuracy is the primary goal and there is no strict need to reduce the number of measured variables.

III.1.4.2 Comparison

Compared to other regression methods designed for collinear data, the principal advantage of Partial Least Squares Regression (PLSR) lies in the fact that information from the response variable (Y) is explicitly utilized in the model construction. Although this notion is difficult to demonstrate statistically, a more tangible advantage of PLSR is its ability to simultaneously perform prediction and uncover a joint latent structure between the explanatory variables (X) and the response variables (Y).

As a result, PLSR often requires fewer components than Principal Component Regression (PCR) to achieve comparable predictive performance. Owing to its ease of implementation and interpretability, PLSR has become highly popular in chemistry—particularly in spectroscopy—but is also widely applied across various scientific and engineering disciplines.

III.1.5 Principal Component Analysis (PCA) Method

Principal Component Analysis (PCA) is a descriptive statistical technique whose use dates back to the early 20th century. It is employed for data exploration and analysis, enabling the study of relationships among variables without assuming any predefined structure [4].

The primary objective of PCA is to identify the dependency structure among multivariate observations in order to obtain a compact and informative representation of the data. Traditionally, PCA has been used to project data onto a set of factorial axes, thereby facilitating dimensionality reduction and the visualization of underlying data patterns.

III.1.5.1 Principle of PCA

Principal Component Analysis (PCA) is a linear orthogonal projection technique that transforms multidimensional observations—originally represented in an m-dimensional space (m being the number of observed variables)—into a lower-dimensional subspace of dimension l (l < m), while maximizing the variance of the projected data.

PCA can be interpreted in two equivalent ways: as a method for minimizing the quadratic reconstruction error, or as a method for maximizing the variance of the projections

In practice, PCA is widely used as a tool for modeling the relationships among variables that describe the behavior of a given process, enabling dimensionality reduction and the identification of dominant patterns within the data. The estimation of the parameters of the PCA model is carried out by calculating the eigenvalues and eigenvectors of the correlation matrix of the data. However, determining the structure of the model requires selecting the appropriate number of components to retain. Several criteria exist for this purpose. In our work, we adopt the reconstruction variance criterion for selecting the number of components to retain in the PCA model, as it effectively exploits the redundancies among the variables. The chosen number of components thus defines the structure and identification of the PCA model.

III.1.5.2 Steps of PCA:

Through calculations, an estimate of the parameters of the PCA model is obtained. However, to determine the structure of the model, it is sufficient to decide on the number of components retained. Whatever the model, the main steps of the PCA procedure are generally as follows:

First step: Data standardization — the data must be centered and scaled so that each variable has a mean of zero and a variance of one. This step is crucial if the original variables have different scales.

Second step: The correlation (or covariance) matrix of the standardized data is calculated. It describes the relationships between the variables [5].

Third step: The eigenvalues and eigenvectors of the covariance (or correlation) matrix are computed. The eigenvalues indicate the amount of variance explained by each principal

component, while the eigenvectors (principal axes) define the directions of the principal components in the data space.

Fourth step: The original data is projected onto the eigenvectors to obtain the new variables, known as the principal components [6].

CONCLUSION

Data mining is a discipline that originated outside traditional statistics, emerging from the database management and artificial intelligence communities with the objective of enhancing the value of large databases. It offers new perspectives for analyzing massive datasets and addresses the challenge of processing data at the gigabyte and terabyte scales. Data mining seeks to discover previously unknown but useful model structures directly from data—rather than from pre-established theoretical models—through algorithmic search processes, whether linear or non-linear, explicit or implicit, such as neural networks, genetic algorithms, decision trees, and Bayesian networks [7].

Many of these methods are particularly effective in contexts where there are more predictor variables than observations, and where strong collinearity exists among the predictors. However, once a model has been constructed, it becomes essential to evaluate its quality through validity tests and residual analysis. This evaluation helps determine whether the model provides a reliable representation of the data. Even when coherent models can be built in situations with few observations and many correlated variables, there is no guarantee a priori that such models will exhibit good predictive or explanatory quality.

Another important issue concerns the treatment of outliers, which may result from numerical errors, empirical inaccuracies, or genuine exceptional cases that cannot be handled by conventional methods. A critical question, therefore, is how different modeling techniques manage these atypical observations. While several robust procedures have been developed for linear regression, it remains uncertain whether they can be directly applied to Partial Least Squares (PLS) regression, or whether new approaches are required to address this challenge.
From this perspective, Principal Component Analysis (PCA) emerges as a valuable technique for data compression and classification. Its fundamental goal is to reduce the dimensionality of a dataset by identifying a smaller set of new variables that retain most of the information contained in the original variables. Here, “information” refers to the variance present in the

dataset, typically expressed through the correlations among the original variables. The new variables—called principal components (PCs)—are uncorrelated and ordered according to the amount of total variance they explain:

- The first principal component (PC_1) captures the largest share of the total variation;
- The second principal component (PC_2) captures the second largest share, and so forth.

In precise terms, the principal utility of PCA lies in its ability to reduce data dimensionality while preserving as much relevant information as possible [5, 8].

Despite significant progress, many data mining techniques remain in active development. These methods continue to evolve, with ongoing research aimed at improving their robustness, interpretability, and adaptability to increasingly complex and high-dimensional datasets.

III.2 CALORIMETRIC METHODS

Recent technological advancements have led to significant progress in Differential Scanning Calorimetry (DSC), resulting in the development of new techniques and the expansion of its applications.

In general, thermal analysis involves measuring changes in a physical property of a sample as it is subjected to a controlled temperature program, typically a linear variation of temperature over time under a controlled atmosphere. In some studies, however, experiments are also conducted at constant temperature or under non-linear heating conditions.

This broad field encompasses several analytical techniques—such as calorimetry, thermogravimetry (TGA), and dilatometry—each of which provides complementary information about a material's thermal behavior. Among these methods, Differential Thermal Analysis (DTA) and Differential Scanning Calorimetry (DSC) specifically focus on monitoring the temperature of a sample and the heat flow exchanged between the sample and its surroundings.

The applications of DSC are highly diverse and include:

- ✓ determination of purity and heat capacity,
- ✓ characterization of non-crystalline solids (e.g., glasses, polymers, and elastomers),
- ✓ investigation of polymorphism,
- ✓ construction of binary and ternary phase diagrams for mineral or organic systems,
- ✓ evaluation of thermal stability of organic compounds, and
- ✓ analysis of oxidation, reduction, and cross-linking reactions.

Consequently, DSC is widely employed by researchers and technicians in research and development (R&D) as well as in quality control across numerous industries, including the chemical, petrochemical, pharmaceutical, food, electronic, mining, and metallurgical sectors [9].

Furthermore, DSC, Thermogravimetric Analysis (TGA), and Differential Thermal Analysis (DTA) are among the most widely used characterization techniques in the study of ionic liquids, particularly for investigating their thermal properties [10-13].

III. 2.1 Differential Scanning Calorimetry (DSC)

Differential Scanning Calorimetry (DSC) is a thermal analysis technique widely used to study the behavior of materials under controlled heating or cooling conditions [14, 15]. It enables the determination of key phase transition parameters, including:

- ✓ the glass transition temperature (T_g),
- ✓ melting and crystallization temperatures, and
- ✓ reaction enthalpies, which are used to evaluate the degree of crosslinking in certain polymers.

Analyses are generally conducted under a flow of inert gas (such as nitrogen or argon) to prevent reactions between the sample and the furnace atmosphere.

III.2.1.1 Principle of the measurement

Figure (III.I.1) illustrates the principle diagram of this technique. The system consists of two containers: one holds an aluminium crucible containing the material to be analyzed, while the other contains an empty crucible that serves as a reference. Both containers are placed inside a furnace, where a linear heating rate is maintained by an independent temperature control loop for each container.

The principle of operation is to maintain identical temperatures in both containers throughout the experiment. The power required to compensate for the thermal effects—whether endothermic, exothermic, or non-thermal phenomena—that occur during phase transitions is directly proportional to the measured heat flow.

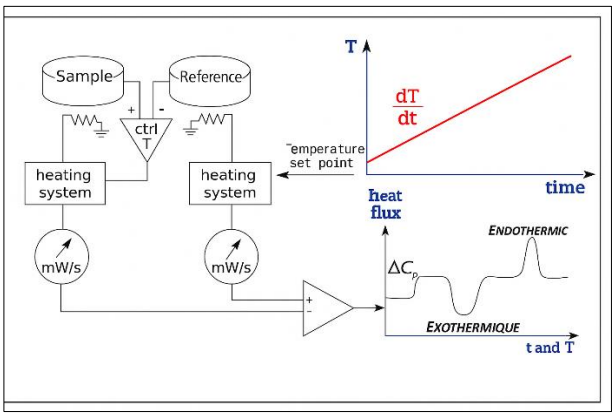

Figure. III.2.1: *Principle of Differential Scanning Calorimetry (DSC) measurement.*

The variation of heat flow is measured when a material is subjected to a controlled temperature change over time. During this analysis, the recorded thermogram represents the variation of dH/dT, which corresponds to the variation of specific heat at constant pressure as a function of temperature, expressed by:

$$\frac{dH}{dT} = mC_P$$

or, in its differential form:

$$\frac{dH}{dT} = C_P\left(\frac{dT}{dt}\right) + f(T.t)$$

The accurate detection of thermal transitions depends strongly on the measurement conditions. Certain transitions—such as evaporation, crystallization, melting, and decomposition—are kinetic phenomena that depend on both temperature and time. Consequently:

1. These transitions shift to lower temperatures during cooling, and
2. To higher temperatures during heating.

According to Equation (III.I.2), the heat flow is proportional to the temperature ramp through the heat capacity of the material under study. For purely thermodynamic transitions such as the glass transition (T_g), the kinetic term is zero, i.e., f(T, t) = 0.

The application of a high temperature ramp will result in a slight shift of the T_g towards higher temperatures. This slight shift is the result of the low thermal conductivity of the material, which leads to a temperature difference between the surface and the volume of the sample [16, 17].

III.2.1.2 Key Parameters derived from the DSC Curve

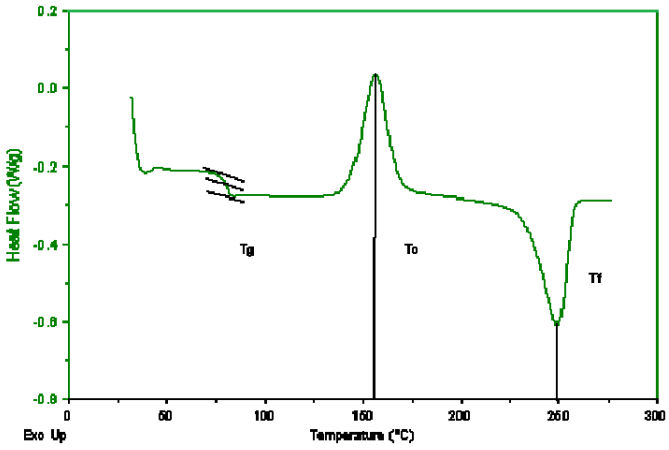

Figure. III.2.2: *The DSC curve*

Figure III.2.2 represents a Differential Scanning Calorimetry (DSC) curve, illustrating the three key parameters that can be extracted to characterize a material's thermal behavior: Melting Temperature (T_f), Crystallisation Temperature (T_c), and Glass Transition Temperature

(T_g).

III.2.1.3 Melting Temperature T_f

Melting is an endothermic transition that, upon heating, transforms a material from a crystalline or amorphous solid state into a liquid state. In calorimetry, the melting temperature (T_f) is determined from the extremum of the melting peak. Figure II.8.

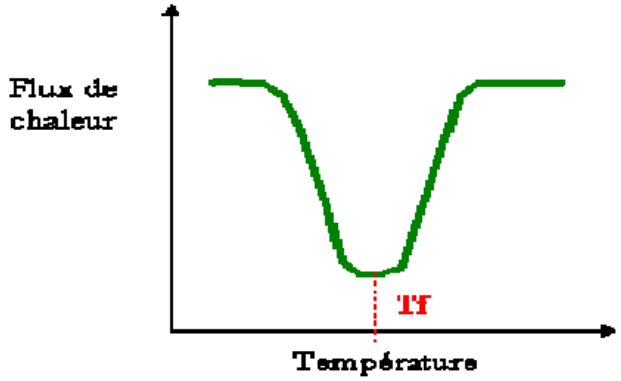

Figure.III.2.3: *Melting temperature peak*

III.2.1.4 Crystalization temperature T_c

Crystallisation is an exothermic transition that, upon heating, transforms a material from an amorphous liquid state into a crystalline state characterized by a highly ordered molecular arrangement.

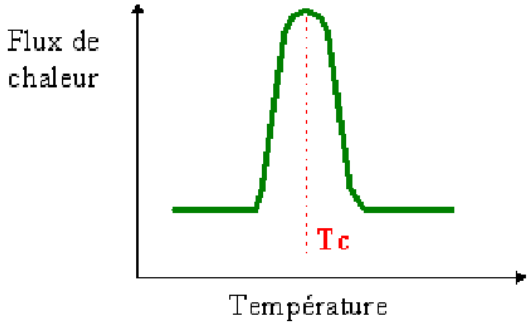

Figure.III.2.4: *Crystallisation temperature peak*

III.2.1.5 Glass transition temperature T_g

The glass transition (characterized by the glass transition temperature, T_g) is defined as the transition from a glassy state to a supercooled liquid state when a material is heated. It is not, strictly speaking, a thermodynamic transition, as it arises from kinetic phenomena. During the transition to the glassy state, all the properties of the material change significantly. The glass transition temperature (T_g) marks a notable variation in several physical properties

of the material, including its mechanical, optical, dielectric, and thermal characteristics. Upon heating, this temperature corresponds to the reversible transformation of the amorphous phase of a material from a hard and relatively brittle form to a viscous or fluid-like state [14]. The transformation is reversible upon cooling.

The value of T_g is influenced by several factors, including:

- ✓ Chain flexibility: In polymers, when chain flexibility decreases, T_g increases.
- ✓ Molecular weight: As the molecular mass increases, T_g also increases.
- ✓ Crystallinity: Generally, an increase in crystallinity leads to a higher T_g, as the crystallites stiffen the structure of the material.
- ✓ Humidity: An increase in moisture content leads to a decrease in T_g.

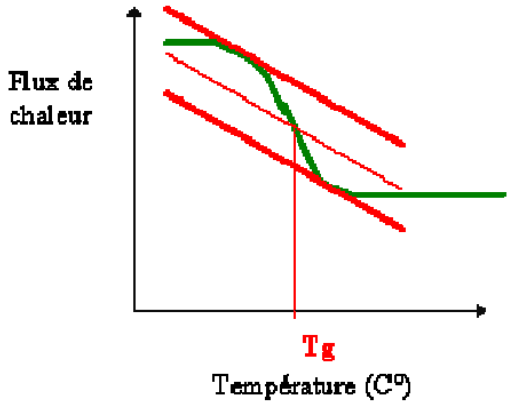

Figure.III.2.5: *Appearance of glass transition temperature*

III.2.2. Thermogravimetric Analysis (TGA)

III.2.2.1. Principle of TGA

Thermogravimetric Analysis (TGA) is a thermal analysis technique that measures the variation in the mass of a sample as a function of temperature or time under a controlled atmosphere. The resulting mass-loss curve provides valuable information on:

Changes in the composition of the sample, Thermal stability, and Kinetic parameters of chemical reactions occurring within the sample.

A derivative thermogravimetric curve (DTG) is often used to indicate the temperature regions where mass loss is most significant, providing enhanced clarity of decomposition or reaction steps.

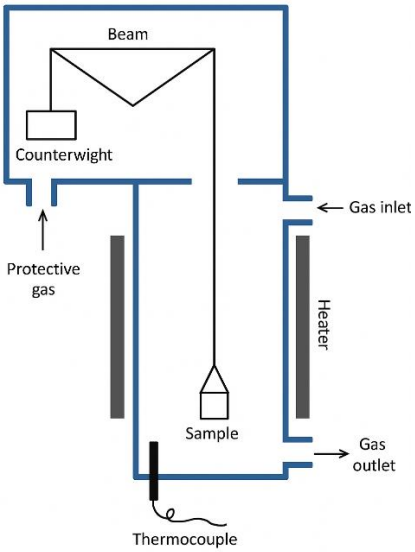

Figure III.2.6: *illustrates the principle of a TGA experimental setup.*

A typical TGA system consists of:

- A sealed chamber that allows control of the sample atmosphere,
- A furnace to regulate the temperature,
- A weighing module (microbalance) for continuous mass measurement,
- A thermocouple for precise temperature monitoring, and
- A computer system to control operations and record data.

The microbalance generally operates under an inert atmosphere (e.g., nitrogen or argon). This inert gas forms a protective "lid" that prevents the reactive gas from entering the weighing module. For this reason, the inert gas must be less dense than the reactive gas.
Additionally, the instrument is equipped with a cooling system, often water-circulated, to limit overheating of the sensitive components.

Depending on the model, the degree of automation varies: some systems require manual control of the vacuum pump and gas flow, while others feature automated solenoid-valve control.

For sample suspension, several methods are commonly used:

- Platinum wire wrapping,
- Hook method, where the sample is drilled and hung with platinum wire, or
- Basket method, where the sample is placed in a woven platinum or alumina basket (alumina being more inert at high temperatures).

In certain configurations, instead of a suspension, an “ATD rod” can be used. This is a small Differential Thermal Analysis (DTA) module that replaces the suspension system,

enabling the simultaneous detection of heat flow and mass changes. Such an integrated instrument is referred to as a combined TGA-DSC or TG-DTA system.

When a corrosive reactive atmosphere is employed, an additional protective "super-enclosure", typically made of silica, may be installed to further minimize the risk of reactive gas backflow into the weighing module.

III.2.3 Experimental conditions

For DSC characterization, a (NETZSCH DSC 204 F1) was used with a speed of heating and cooling of 10 °C /min, performing two heating and cooling cycles to remove traces of water and solvent in a temperature range of -60 °C to 200 °C under Argon.

To determine the degradation of ionic liquids, TGA and DTG experiments were made with NETZSCH STA 449 C (TGA-DSC) system coupled to a mass spectrometer for analysing the gas emitted, in a temperature range of 20 °C to 400 °C at a scan rate of 5 °C/min under a high purity argon flux (60 mL/ min).

Differential Scanning Calorimetry (DSC) and Thermogravimetric Analysis (TGA) are two complementary thermal analysis techniques that provide fundamental information about the thermal behavior and stability of materials.

CONCLUSION

DSC allows the quantitative study of heat flow associated with physical and chemical transformations such as melting, crystallization, glass transition, oxidation, and curing reactions. It provides essential data on transition temperatures, enthalpy changes, and the energetic nature of reactions (endothermic or exothermic). Through DSC, one can determine the purity, thermal capacity, and phase behavior of a wide range of materials, including polymers, pharmaceuticals, and metals.

TGA, on the other hand, measures the mass variation of a material as a function of temperature or time, offering insight into thermal stability, composition, and decomposition mechanisms. It is particularly useful for evaluating moisture content, oxidation resistance, and degradation kinetics of materials.

Together, DSC and TGA provide a comprehensive thermal characterization, allowing researchers to correlate heat flow events with mass changes, thereby achieving a more complete understanding of a material's thermal properties, stability, and reaction behavior. These techniques are indispensable tools in materials science, chemistry, and industry, ensuring the development, optimization, and quality control of diverse materials.

III.3 Dielectric Methods

Dielectric methods are widely employed for the study and characterization of organic and inorganic insulating materials, owing to their ability to cover a broad frequency range with high resolution. These techniques provide valuable insights into the electrical and molecular dynamics of materials.

Dielectric spectroscopy measures the response of a material—in terms of current and voltage—when subjected to a variable electric field. This response reflects the polarization behavior within the sample and is thus directly related to the movement of free charge carriers and permanent or induced dipoles.

The experimental results are typically expressed in terms of the complex dielectric permittivity (ε*), a dimensionless quantity that characterizes the dielectric properties of the material. This parameter depends on several factors, including frequency, temperature, and applied voltage.

With this general framework established, the following sections will present the theoretical background of dielectric phenomena, particularly in the context of alternating electric fields, followed by a detailed description of the measurement principles and the instrumentation used in this study.

III.3.1 Dynamic Dielectric Spectroscopy

Dynamic Dielectric Spectroscopy (DDS) is a general dielectric technique that measures a material's dielectric response (permittivity and impedance) as a function of frequency under isothermal conditions. It usually focuses on a limited frequency range, often within the low to intermediate frequency domain (from a few Hz up to around 1 MHz).

Dielectric measurements of binary ionic liquids were conducted using an GWINSTEK, LCR-821 impedance meter. The measurements were performed at controlled temperatures ranging from 300K to 400K, with adjustments made in 4 – 5 K increments per minute, across a broad spectrum of frequencies (500 Hz to 100 KHz), enabling the observation of polarisation variation as a function of electric field frequency and temperature.

DDS is an isothermal dielectric analysis technique performed under a variable electric field. It enables the measurement of the dielectric properties of materials by analyzing their response to an applied alternating voltage. The primary objective of this method is to determine the complex impedance (Z*) of the material under study.

In this technique, the sample is placed between two electrodes, across which a sinusoidal voltage U(t)—or U* in complex notation—is applied. This voltage has a low amplitude (U_0)

and a defined angular frequency (ω):

$$U^*(\omega) = U_0 e^{i\omega t} \qquad (III.3.1)$$

This applied sinusoidal voltage induces a sinusoidal current I(t) (or I* in complex notation) within the sample. The current oscillates at the same angular frequency (ω) as the voltage but is phase-shifted by an angle Φ:

$$I^*(\omega) = I_0 e^{i(\omega t+\Phi)} \qquad (III.3.2)$$

The complex impedance of the material is then defined as the ratio of the complex voltage to the complex current:

$$z^*(\omega) = \frac{U^*(\omega)}{I^*(\omega)} \qquad (III.3.3)$$

From this relationship, the complex permittivity (ε*) can be expressed as a function of the complex impedance, the sample geometry, and the vacuum permittivity (ε_0):

$$\varepsilon^*(\omega) = \frac{1}{i\omega Z^*(\omega)} \times \frac{\varepsilon_0 S}{d} \qquad (III.3.4)$$

where: **S** is the surface area of the sample, **d** is the sample thickness, and **ε_0** is the vacuum permittivity.

This relationship forms the basis for analyzing the dielectric behavior of materials as a function of frequency, providing insights into their polarization mechanisms and charge transport phenomena.

III.3.2 Broadband Dielectric Spectroscopy (BDS):

BDS is an extended form of DDS that measures the dielectric properties over an extremely wide frequency range, typically from 10^{-6} Hz (microhertz) up to 10^{9}–10^{12} Hz (gigahertz to terahertz). It provides a broader and more detailed picture of the dielectric relaxation processes. Dielectric measurements were performed in the temperature range from 100–400 K and in the frequency range between 10^{-2} and 10^{6} Hz using a Novocontrol Alpha impedance analyzer. All the measurements are carried out isothermally, where the temperature was controlled by a Quatro Novocontrol cryo-system with stability of 0.1 K. The samples were prepared utilising brass spectrometer ground plates. Cylindrical glass fiber spacers with a diameter of 50 μm were employed to achieve a consistent electrode distance and planar geometry. Most samples

utilized top brass electrodes with a 10 mm diameter (fig III.3.1). However, due to the reactivity of the [EtOHVIM][HSO_4] sample, gold electrodes were used instead.

The sample cell was prepared in an open geometry configuration and subsequently annealed according to the specifications. All samples were subjected to a vacuum environment of approximately ~1e^{-6} mbar for 24 h. Most samples underwent an annealing process for 12 h at elevated temperatures, and then the top electrodes were placed on the sample material while still under an inert atmosphere and then transported to the spectrometer. All measurements were conducted under an inert and dry nitrogen atmosphere to maintain consistent conditions during the experiments.

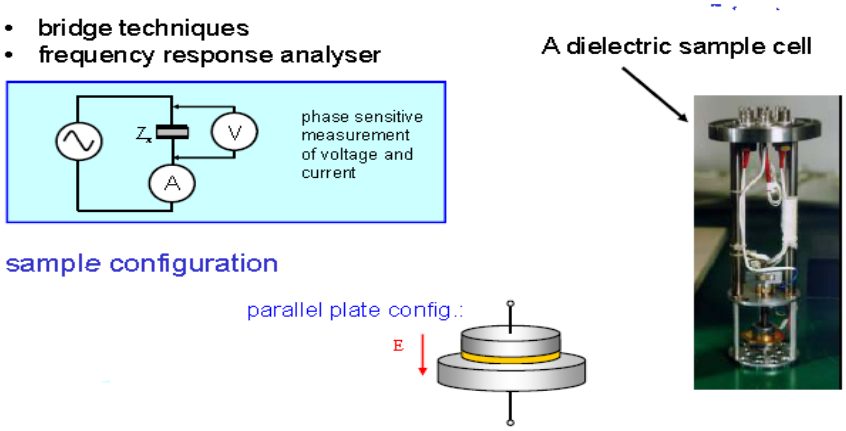

Figure. III.3.1: *Principle of a frequency domain dielectric and conductivity measurement and the dielectric cell structure with two electrodes and separator.*

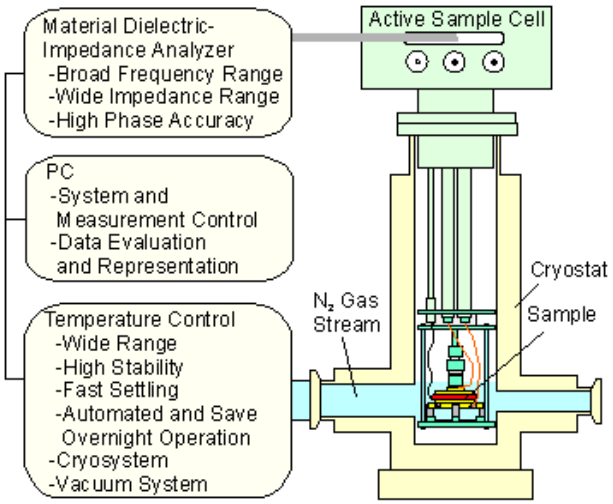

Fig.III.3.2 *Experimental setup of Broadband Dielectric Spectroscopy.*

III.3.4 Principle of Current Conductivity Determination (AC and DC)

The objective of conductivity measurements is to determine the electrical conductivity of

a material and to study the charge transport mechanisms involved. In the analysis of conductivity spectra, only the real part of the complex conductivity, denoted $\sigma'(\omega)$, is considered.

The real part of the complex conductivity can be expressed as:

$$\sigma'(\omega)=\sigma_{DC}+\sigma_{AC} \quad \text{(III.3.6)}$$

where:

- σ_{DC} is the direct current (DC) conductivity corresponding to the zero-frequency limit,
- σ_{AC} is the alternating current (AC) conductivity, representing the frequency-dependent component.

A change in the conduction regime occurs at a critical angular frequency (ωc), with $\omega = 2\pi f$.

For $\omega < \omega_c$, the conductivity is independent of frequency, corresponding to the DC regime, and σ' exhibits a plateau:

$$\sigma'(\omega<\omega_C) = \sigma_{DC} \quad \text{(III.3.7)}$$

For $\omega > \omega_c$, the conductivity becomes frequency-dependent, corresponding to the AC regime, and is expressed as:

$$\sigma'(\omega>\omega_C) = \sigma_{AC}(\omega) \quad \text{(III.3.8)}$$

In this regime, $\sigma_{AC}(\omega)$ follows a power-law dependence on frequency:

$$\sigma_{AC}(\omega) = A\omega^s \quad \text{(III.3.9)}$$

where:

- A is a temperature-dependent constant, and
- s is an exponent ($0 \leq s \leq 1$) that depends on both temperature and frequency.

Thus, the real part of the complex conductivity can be written as:

$$\sigma'(\omega) = \sigma_{DC}+ A\omega^s \quad \text{(III.3.10)}$$

This relationship describes the transition from a DC conduction regime, dominated by long-range charge transport, to an AC regime, where localized hopping or polarization mechanisms contribute to the overall conductivity [18].

CONCLUSION

Dielectric methods constitute powerful tools for investigating the electrical, structural, and dynamic properties of materials. Through the analysis of a material's response to an applied electric field, these techniques provide essential information about polarization mechanisms, charge transport, and molecular mobility.

Among these methods, Dynamic Dielectric Spectroscopy (DDS) and Broadband Dielectric Spectroscopy (BDS) allow for a detailed study of the frequency and temperature dependence of dielectric properties, enabling the identification of various relaxation processes and conductivity behaviors. By determining parameters such as complex permittivity, impedance, and conductivity, dielectric analysis helps to clarify the mechanisms of dipolar relaxation, ion migration, and interfacial polarization.

In conclusion, dielectric methods provide a comprehensive and non-destructive approach to characterizing materials. They are indispensable for understanding electrical conduction, dielectric relaxation, and phase transitions in both organic and inorganic systems, making them valuable in fields such as materials science, electronics, polymer physics, and solid-state chemistry.

BIBLIOGRAPY

1. Larose, D.T., Data mining methods & models. 2006: John Wiley & Sons.
2. Stéphane, T., Data mining et statistique décisionnelle: l'intelligence des données. 2012: Editions Technip.
3. Bastien, P., et al., PLS generalised linear regression. 2005. **48**(1): p. 17-46.
4. Bellman, R.J.P., NJ, Adaptive control processes; a guided tour, princeton univ. 1961.
5. Pearson, K.J.T.L., Edinburgh,, D.p. magazine, and j.o. science, LIII. On lines and planes of closest fit to systems of points in space. 1901. **2**(11): p. 559-572.
6. Hotelling, H.J.J.o.e.p., Analysis of a complex of statistical variables into principal components. 1933. **24**(6): p. 417.
7. Saporta, G., Liaisons entre plusieurs ensembles de variables et codage de données qualitatives. 1975, Université Pierre et Marie Curie-Paris VI.
8. Diamantaras, K., Principal component neural networks theory and applications. 1996.
9. Grenet, J. and B. LEGENDRE, Analyse calorimétrique différentielle à balayage (DSC). 2010.
10. McEwen, A.B., et al., Electrochemical properties of imidazolium salt electrolytes for electrochemical capacitor applications. 1999. **146**(5): p. 1687.
11. Penna, T.C., et al., Pressure and temperature effects on intermolecular vibrational dynamics of ionic liquids. 2013. **138**(10).
12. Sashina, E.S., et al., Thermal properties of 1-alkyl-3-methylpyridinium halide-based ionic liquids. 2013. **568**: p. 185-188.
13. Ngo, H.L., et al., Thermal properties of imidazolium ionic liquids. 2000. **357**: p. 97-102.
14. Wigmans, R., Calorimetry: Energy measurement in particle physics. 2000: Oxford University Press.
15. Marcilla, A., J. Reyes-Labarta, and F.J.P. Sempere, DSC kinetic study of the transitions involved in the thermal treatment of polymers. Methodological considerations. 2001. **42**(12): p. 5343-5350.
16. Thomas, L.C.J.A.L., Use of multiple heating rate DSC and modulated temperature DSC to detect and analyze temperature-time-dependent transitions in materials. 2001. **33**(1): p. 26-31.
17. Gmelin, E., S.M.J.P. Sarge, and a. chemistry, Calibration of differential scanning calorimeters. 1995. **67**(11): p. 1789-1800.
18. Boumediene, H., Nouveaux liquides ioniques Bis-Pipéridinium: Synthèse, Etude des propriétés thermiques et relaxation diélectrique. 2012, UNIVERSITE DJILLALI LIABES (Algérie).

CHAPTER IV

RESULTS AND DISCUSSIONS

This chapter has presented the results derived from the application of data mining techniques, thermal analysis, and dielectric analysis to investigate the dielectric behavior of individual, binary, and polymeric ionic liquids.

In the first stage of this study, advanced data mining approaches—specifically Principal Component Analysis (PCA) and Partial Least Squares (PLS) regression—were employed to predict and classify the dielectric characteristics of ionic liquids and to model the behavior of binary ionic liquid systems. Subsequently, the dielectric properties of a selected ionic liquid were examined in detail using dielectric spectroscopy to gain deeper insight into its relaxation mechanisms and frequency-dependent response.

The second part of this work focused on the thermal and dielectric properties of two distinct ionic liquids and their binary mixture, allowing for comparative evaluation of their interactions and combined effects.

Finally, a comprehensive investigation of a selective mono and polymeric ionic liquids was carried out, emphasizing both their dielectric and thermal behaviors to better understand their potential for advanced solid-acid electrolytes in electrochemical devices or as proton exchange membranes.

IV.1 Prediction and Classification of Binary Ionic Liquids

The recent strategy of combining two ionic liquids to influence thermophysical [1-3], phase equilibrium [4-6], and for mechanical properties [7, 8] has garnered significant interest. Therefore, it is crucial to develop a straightforward and precise model for predicting the physicochemical properties of binary mixtures of ionic liquids.

Data mining tasks can be categorised into two fundamental groups: descriptive and predictive. Several data mining functionalities, such as clustering and classification, can be effectively accomplished through various techniques. [9, 10] This study employs a descriptive data mining approach, focusing on the exploration of patterns and relationships within the data. The core descriptive functions include summarisation, prediction, clustering, association, and discovery. PLS and PCA are suitable methods for executing this data mining task.

Partial least squares (PLS) is a technique that facilitates the numerical fitting of a linear model to elucidate the primary relationships among process variables. This technique is especially effective for simplifying high-dimensional, multivariate systems that contain collinear variables, thereby alleviating the challenges associated with handling poorly conditioned datasets [11]. Hence, it is crucial to identify a clear and accurate model for predicting the electrical conductivity of binary mixtures. Additionally, Principal Component Analysis (PCA) was utilised as a data analysis technique to identify a combination of variables that describes general trends in the predicted database.

The current study builds upon the previous study of Guettaf et al. [12], which investigated the dielectric characteristics of imidazolium-based ionic liquids using dielectric spectroscopy. That earlier study revealed that increasing the anion size enhances electrical conductivity, whereas extending the alkyl chain length of the cation reduces it. The conductivity followed the Vogel–Fulcher–Tammann (VFT) behavior near the glass transition temperature (T_g) and showed Arrhenius-type linearity at higher temperatures. In the second phase, principal component analysis (PCA) was employed to explore the correlation between ionic liquid structure (cation chain length and anion size) and the VFT parameters. The analysis highlighted that the fragility (m) primarily influences room-temperature conductivity for different anions, while T_g is largely governed by the alkyl chain length of the cation.

IV.1.1 DATA MINING METHODS

In data mining, the results obtained from descriptive statistics techniques are examined through various approaches to achieve perspectives that are not provided by other methods. The process of data mining enables the identification of the most effective study techniques, thereby enhancing the overall comprehension of the findings [13].

IV.1.1.1 Description of Partial least square (PLS)

PLS regression is a statistical method used to analyse data from multiple variables, frequently utilised in fields such as chemical engineering, physical chemistry, analytical chemistry, and industrial processes [14]. PLS functions as a technique for minimising dimensionality in datasets. The use of a constrained set of latent variables aids in classification, discrimination, prediction, or illustrating relationships among groups of variables under investigation that are not directly analysed.

IV.1.1.2 Description of principal component analysis (PCA)

PCA is defined as a classification method for projecting spatial data into a set of principal components (PCs) and mapping the data over a dimensionally reduced space [15]. The PC is used to capture information and is linked to the eigenvalue corresponding to the largest eigenvalue of the covariance matrix of the original dataset. The first PC (PC1) explains the maximal variance in the data set as well as its direction, the second (PC2) retains much of the remaining variation in such a way as to be uncorrelated with the first principal components, and so on. Vectors that are the eigenvectors of the variance-covariance matrix [16, 17] define the PCs. The variance along the vector is defined as the eigenvalue of the covariance matrix. All PCs are orthogonal to each other, and therefore each captures unique information. The strong point of PCA is that a few PCs are sufficient to describe a system, and that a data set of n dimensions can be reduced to a smaller number of dimensions with negligible loss of information [18].

IV.1.1.3 Database and XLSTAT

Table IV.1.1 presents the data used for various ionic liquids. The magnitude of the anion increases from the bromine anion to the large FAP anion in the series[19]. The datasets utilized are those that correspond to the parameters of the VFT equation.

$$\sigma = \sigma_{\infty} \; exp\left[\frac{-B}{(T - T0)}\right] \qquad (IV.1)$$

$$\ln \sigma = \ln \sigma_{\infty} - \frac{B}{T - T_0} \qquad (IV.2)$$

σ_{RT} : Conductivity at room temperature,

T_g : The glass transition temperature,

$\ln \sigma_{\infty}$: Logarithm of conductivity at ∞,

B : Describes the dependence of sigma as a function of temperature in the high-temperature limit and T0,

T_0 : The temperature at which the conductivity (σ) approaches zero is the Vogel temperature.

M : Fragility, calculated by the following equation [20].

$$m = \frac{B}{\ln 10} \cdot \frac{T_g}{(T_g - T_0)^2} \qquad (IV.3)$$

	σ_{RT} (S/m)	T_g(K)	$ln\sigma_{\infty}$(S/m)	B	T_0(K)	m
$C_3 mim , BF_4$	0,519	175,1	7,86	1284	139,7	78
$C_4 mim , BF_4$	0,364	177,9	6,89	1160	146,8	93
$C_5 mim , BF_4$	0,163	182,8	6,69	1240	147,1	78
$C_6 mim , BF_4$	0,118	187,6	6,37	1238	148,5	66
$C_7 mim , BF_4$	0,067	186,1	6,03	1291	146,1	68
$C_8 mim , BF_4$	0,059	189,7	6,1	1295	148,3	62
$C_9 mim , BF_4$	0,042	190,5	5,8	1324	145,9	55
$C_6 mim , Br$	0,0074	187,8	7,47	1668	158,4	158
$C_6 mim , Tf_2N$	0,17	187,1	5,59	1057	148,3	57
$C_6 mim , FAP$	0,096	184,7	3,86	965	152,2	73

Table IV.1.1: *Database table.*

In this study, the XLSTAT software package (Addinsoft, 2019) was used for the statistical treatment and multivariate analysis of the experimental data. XLSTAT is an advanced statistical and data analysis tool integrated into Microsoft Excel, allowing for efficient and intuitive manipulation of complex data sets. It provides a wide range of analytical methods, including Principal Component Analysis (PCA) and Partial Least Squares (PLS) regression, which were both applied in this research to explore correlations and identify patterns among the studied variables. The use of XLSTAT facilitated precise data visualization, interpretation, and validation of the developed models. (Addinsoft, 2019. XLSTAT statistical and data analysis solution. Long Island, NY, USA. Available at: https://www.xlstat.com)

IV.1.2 Application of the regression method: Partial Least Squares (PLS) method:

IV.1.2.1 Measures of variable importance:

One of the first results of PLS is the correlation graph (Figure IV.1.1), or more precisely, the correlation circle, which accurately represents the correlations for each group of X and Y variables.

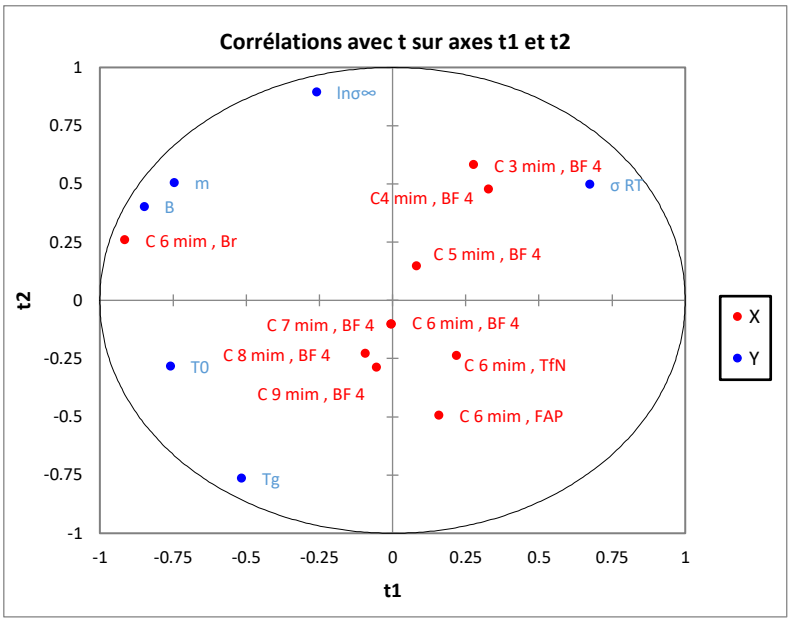

Figure.IV.1.1*Graph of the observations (t_1, t_2) of ionic liquids.*

The PLS correlation circle shows a clear separation between the variables, confirming that ionic liquids significantly influence the model. Certain ionic liquids (notably C_5mim and C_6mim derivatives) have a strong impact on m and B. T_g and T_0 vary inversely with these variables, highlighting distinct thermodynamic behavior depending on the ionic liquid type. The model exhibits good stability and predictive power, as the main relationships are consistent and interpretable.

In the PLS model, a variable X_k can be important for the modelling of Y. The VIP (Variable Importance for the Projection) graph for each explanatory variable on each component gives a summary of the importance of a variable X_k for both X and Y. This allows for a quick identification of which explanatory variables are the most important across all models. (Figure.IV.1.2).

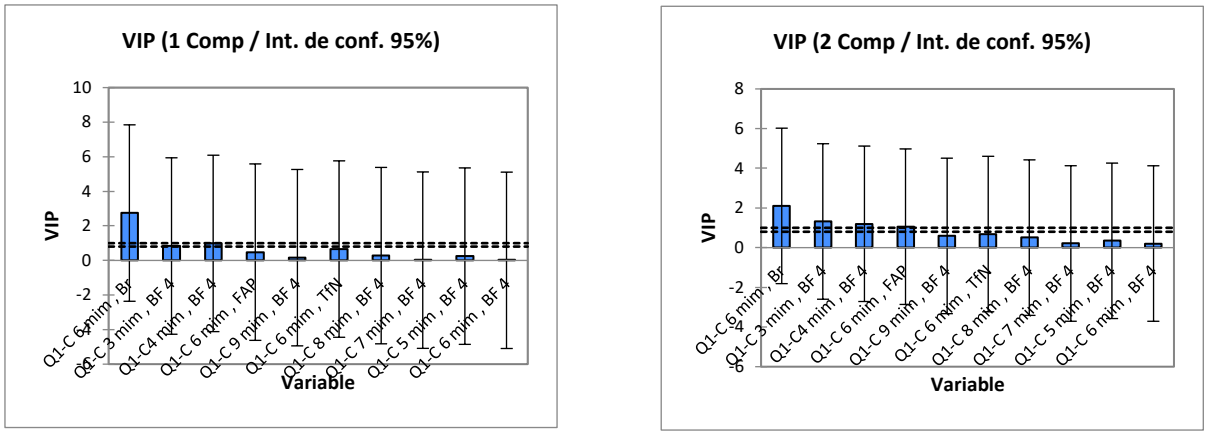

Figure.IV.1.2 *VIP for the first two components of ionic liquids.*

The VIP analysis confirms that C_6mim, Br and, to a lesser extent, C_3mim, BF_4, are the key contributors influencing the model's predictive capacity. These results align with the findings from the correlation circle (Figure IV.1), where these ionic liquids were also located near the most influential Y variables, highlighting their major role in determining the system's behavior.

IV.1.2.2 The residuals and predictions:

The PLS model also allows for the generation of graphs corresponding to the normalized coefficients, as well as graphs of residuals and predictions, enabling the identification of the model's quality. We then obtain richer results by examining the graphs below, which correspond to the normalized coefficients for the model, specifically for the five or six variables (m, T_g, ln, B, T_0, σ_{RT}).

The variable "σ_{RT}":

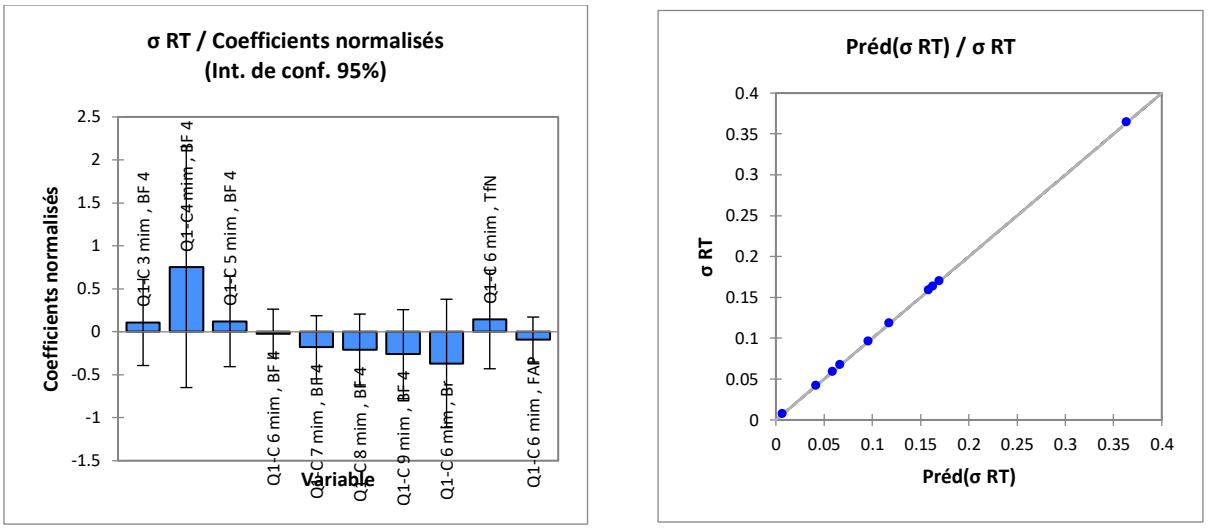

Figure IV.1.3. *Graphs of residuals and predictions corresponding to the variable "σ $_{RT}$"*

The analysis of the model corresponding to the first variable "σ $_{RT}$" allows us to conclude that the set of ionic liquids C_3mim, BF_4, C_4mim, BF_4, C_5mim, BF_4, C_6mim, TFN are significant and influences the model. We notice in the prediction graph that the variation is linear between the predicted values of «σ $_{RT}$ » based on the input values, which indicates the good quality of the model.

The variable "Tg":

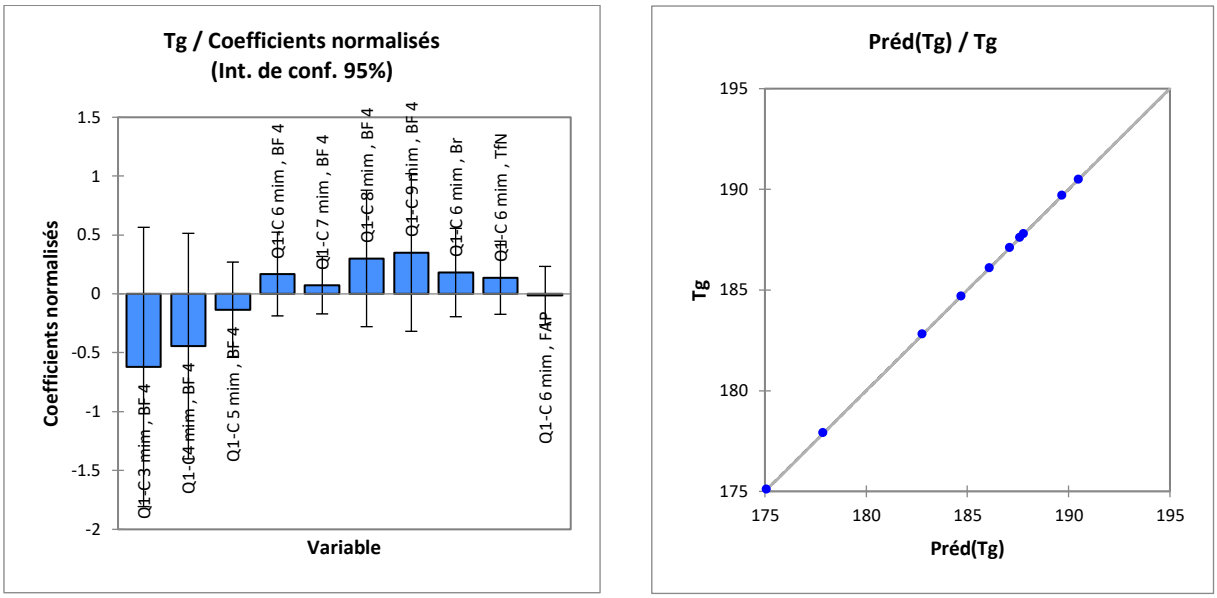

Figure IV.1.4. *Residual and prediction graphs corresponding to the variable "Tg".*

We can say that the ionic liquids C_9 mim, BF_4, C_8 mim, BF_4, C_7 mim, BF_4, C_6 mim, Br, C_6 mim, Tf_2 N, C_6 mim, and BF_4 are important and have an effect on the model by looking at the model for the second variable "T_g" We notice in the prediction graph that the variation is linear between the predicted "T_g" values based on the input values, which allows us to say that the model is good.

The variable "Ln σ∞":

We can say that the ionic liquids C $_3$ mim, BF_4, C $_4$ mim, BF_4, C $_5$ mim, BF_4, C $_6$ mim, Br, and C $_6$ mim, BF_4 are important and have an effect on the model by looking at the model for the variable "Ln σ∞." We notice in the prediction graph that the variation is linear between the predicted values of "ln σ∞" based on the input values, which allows us to say that the model is good.

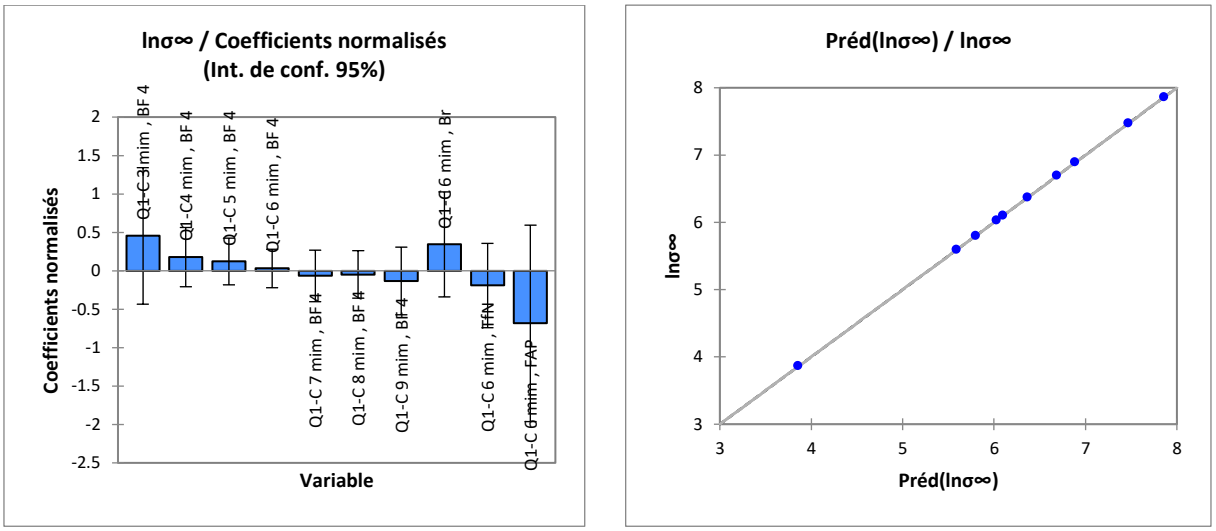

Figure IV.1.4: *Residual and prediction graphs corresponding to the variable "lnσ∞"*

The variable "B":

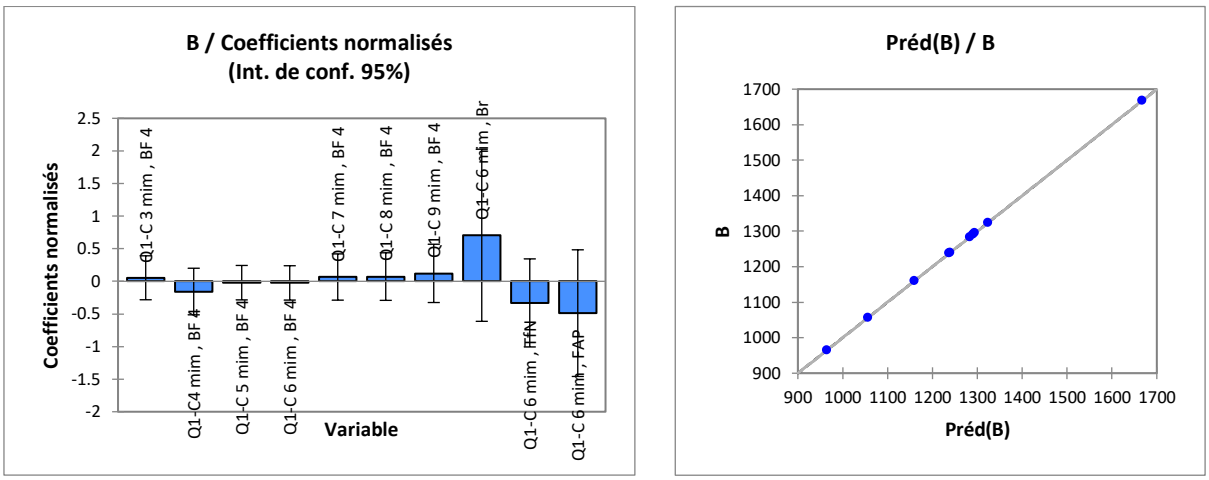

Figure IV.1.5. *Residuals and predictions graphs corresponding to the variable "B".*

Look at the graphs (Figure IV.1.5) of the fourth variable "B." They show that the ionic liquids C_3 mim, BF_4, C_7 mim, BF_4, C_8 mim, BF_4, C_9 mim, BF_4, C_6 mim, and Br are important and have an effect on the model. We also observe that the prediction graph shows a linear variation between the predicted values of "B" based on the input values, indicating the high quality of the model.

The variable "T0":

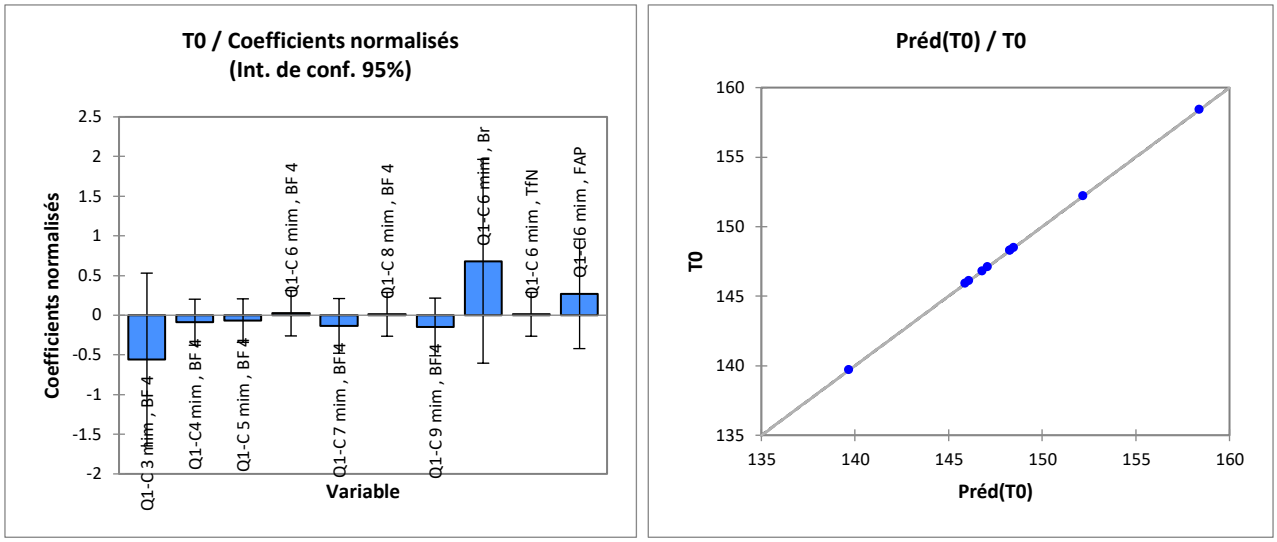

Figure IV.1.6. *Residuals and predictions graphs corresponding to the variable "T0"*

Based on the "T_0" graphs (Figure IV.1.6), we can say that the ionic liquids C_6 mim, BF_4, C_8 mim, BF_4, C_6 mim, FAP, C_6 mim, Br and C_6mim, FAP are important and have an effect on the model. We also observe that the prediction graph shows a linear variation between the predicted values of "T_0" depending on the input used, indicating the high quality of the model.

The variable m:

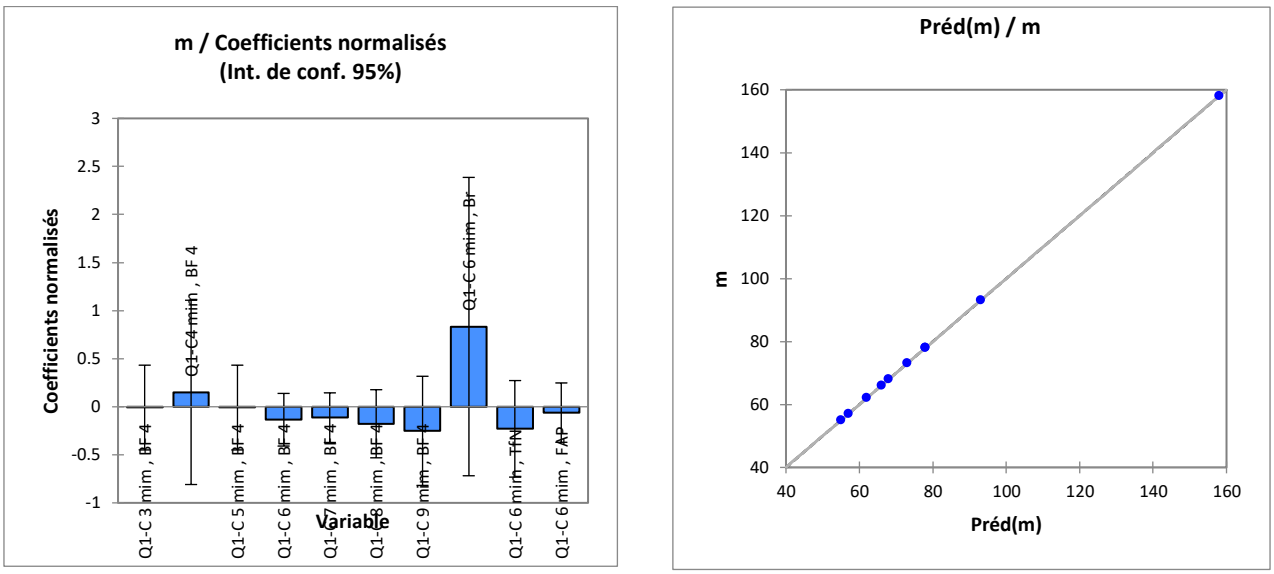

Figure IV. 1.7 *shows the residuals and prediction graphs corresponding to the variable "m".*

The analysis of the model corresponding to the variable "m" allows us to conclude that the ionic liquids C_4 mim BF_4, and C_6 mim Br are significant and influence the model. We notice

in the prediction graph that the variation is linear between the predicted values of "m" based on the input used, which allows us to say that the model is good.

IV.1.2.3 Parameters and equations of the model:

Variable	*σ RT*	*Tg*	*lnσ∞*	*B*	*T_0*	*m*
Constante	0,125	184,930	6,266	1252,200	148,130	78,800
C_3 mim , BF_4	0,034	-9,830	1,594	31,800	-8,430	-0,800
C_4 mim , BF_4	0,239	-7,030	0,624	-92,200	-1,330	14,200
C_5 mim , BF_4	0,038	-2,130	0,424	-12,200	-1,030	-0,800
C_6 mim , BF_4	-0,007	2,670	0,104	-14,200	0,370	-12,800
C_7 mim , BF_4	-0,058	1,170	-0,236	38,800	-2,030	-10,800
C_8 mim , BF_4	-0,066	4,770	-0,166	42,800	0,170	-16,800
C_9 mim , BF_4	-0,083	5,570	-0,466	71,800	-2,230	-23,800
C_6 mim , Br	-0,117	2,870	1,204	415,800	10,270	79,200
C_6 mim , TfN	0,045	2,170	-0,676	-195,200	0,170	-21,800
C_6 mim , FAP	-0,029	-0,230	-2,406	-287,200	4,070	-5,800

Table.IV.1.2: *Parameters of the Ionic Liquid Model*

IV.1.2.4 Prediction of the dielectric properties of binary ionic liquids:

The Partial Least Squares (PLS) method was employed to predict the dielectric properties of binary mixtures of ionic liquids. These mixtures were constructed from individual ionic liquids included in our experimental database. Using the parameters of the model presented in Table.IV.1.2 and applying Raoult's law at different molar fractions (X = 0.25, 0.50, and 0.75), the predicted values of the dielectric properties were calculated. The resulting data are summarized in Table.IV.1.3.

The PLS model integrates experimental data from pure ionic liquids to establish a quantitative relationship between molecular descriptors and dielectric behavior. When combined with Raoult's law, the model allows estimation of the dielectric properties of binary mixtures based on the weighted contribution of each component. This approach effectively captures non-ideal

interactions that may arise between different cation–anion pairs, providing a more realistic representation of the system's behavior.

	x	*σ RT*	*Tg*	*lnσ∞*	*B*	*T0*	*m*
C_3,C_4,BF_4	0.25	0,313	177,200	7,132	1191,000	145,025	89,250
	0.5	0,261	176,500	7,375	1222,000	143,250	85,500
	0.75	0,210	175,800	7,617	1253,000	141,475	81,750
C_3,C_5,BF_4	0.25	0,162	180,875	6,982	1251,000	145,250	78,000
	0.5	0,161	178,950	7,275	1262,000	143,400	78,000
	0.75	0,160	177,025	7,567	1273,000	141,550	78,000
C_3,C_6,BF_4	0.25	0,128	184,475	6,743	1249,500	146,300	69,000
	0.5	0,138	181,350	7,115	1261,000	144,100	72,000
	0.75	0,148	178,220	7,487	1272,500	141,900	75,000
C_3,C_7,BF_4	0.25	0,090	183,350	6,487	1289,250	144,500	70,500
	0.5	0,113	180,600	6,922	1287,500	142,900	73,000
	0.75	0,136	177,820	7,402	1285,750	141,300	75,500
C_3,C_8,BF_4	0.25	0,084	186,050	6,540	1292,250	146,150	66,000
	0.5	0,109	182,400	6,980	1289,500	144,000	70,000
	0.75	0,129	178,750	7,420	1286,750	141,850	74,000
C_3,C_9,BF_4	0.25	0,071	186,650	6,310	1314,000	144,350	60,750
	0.5	0,100	182,800	6,830	1304,000	142,800	66,500
	0.75	0,129	178,950	7,340	1294,000	141,250	72,250
C_4,C_5,BF_4	0.25	0,213	181,570	6,740	1220,000	147,020	81,750
	0.5	0,263	180,350	6,790	1200,000	146,950	85,500
	0.75	0,313	179,125	6,840	1180,000	146,870	89,250
C_4,C_6,BF_4	0.25	0,179	185,170	6,500	1218,500	148,075	72,750
	0.5	0,241	182,750	6,630	1199,000	147,650	79,500
	0.75	0,302	180,325	6,760	1179,800	147,220	86,250
C_4,C_7,BF_4	0.25	0,141	184,050	6,245	1258,250	146,270	74,250
	0.5	0,215	182,200	6,460	1225,500	146,450	80,500
	0.75	0,289	179,950	6,675	1192,750	146,620	86,750
C_4,C_8,BF_4	0.25	0,135	186,750	6,297	1261,250	147,670	69,750
	0.5	0,211	183,800	6,495	1227,500	147,550	77,500
	0.75	0,287	180,850	6,692	1193,750	147,170	85,500
C_4,C_9,BF_4	0.25	0,123	187,350	6,073	1283,000	146,125	64,500
	0.5	0,203	184,200	6,364	1242,000	146,350	74,000
	0.75	0,283	181,050	6,617	1201,000	146,570	83,500
C_5,C_6,BF_4	0.25	0,129	186,600	6,450	1238,500	148,150	69,180
	0.5	0,140	185,200	6,530	1239,000	147,800	72,000
	0.75	0,151	183,970	6,610	1239,500	147,450	75,540
C_5,C_7,BF_4	0.25	0,091	185,270	6,195	1278,250	146,350	70,500
	0.5	0,115	184,450	6,360	1265,500	146,600	73,000
	0.75	0,139	181,620	6,525	1252,750	146,800	75,500
C_5,C_8,BF_4	0.25	0,085	187,975	6,247	1281,250	148,000	66,000
	0.5	0,111	186,250	6,395	1267,500	147,700	70,000
	0.75	0,137	184,520	6,540	1253,750	147,400	74,000
C_5,C_9,BF_4	0.25	0,072	188,570	6,020	1303,000	146,200	60,750

	0.5	0,102	186,650	6,240	1282,000	146,500	66,500
	0.75	0,132	184,720	6,460	1261,000	146,800	72,250
C_6,C_7,BF_4	0.25	0,079	186,470	6,115	1277,750	146,700	67,500
	0.5	0,092	186,850	6,259	1278,700	147,300	67,000
	0.75	0,105	187,220	6,285	1272,550	147,700	66,500
C_6,C_8,BF_4	0.25	0,073	189,170	6,167	1280,750	148,350	63,000
	0.5	0,088	188,650	6,235	1280,700	148,400	64,000
	0.75	0,103	188,120	6,302	1273,550	148,450	65,000
C_6,C_9,BF_4	0.25	0,061	189,770	5,942	1302,500	146,550	57,750
	0.5	0,080	189,050	6,085	1295,200	147,200	60,500
	0.75	0,099	188,320	6,227	1280,800	147,850	63,250
C_7,C_8,BF_4	0.25	0,061	188,800	6,082	1294,000	147,750	63,500
	0.5	0,063	187,900	6,065	1293,000	147,200	65,000
	0.75	0,068	187,000	6,041	1292,000	146,650	66,500
C_7,C_9,BF_4	0.25	0,060	189,400	5,857	1315,750	145,950	58,250
	0.5	0,054	188,300	5,915	1307,500	146,000	61,500
	0.75	0,063	187,200	5,966	1299,250	146,050	64,750
C_8,C_9,BF_4	0.25	0,046	190,300	5,875	1316,750	146,500	56,750
	0.5	0,050	190,100	5,950	1309,500	147,100	58,500
	0.75	0,054	189,900	6,025	1302,250	147,700	60,250
C_6,BF_4,BR	0.25	0,035	187,750	7,195	1560,500	155,920	135,000
	0.5	0,063	187,700	6,920	1467,200	153,450	112,000
	0.75	0,090	187,650	6,645	1366,800	150,970	89,000
C_6,BF_4,TF_2N	0.25	0,157	187,220	5,785	1102,250	148,350	59,250
	0.5	0,144	187,350	5,980	1161,700	148,400	61,500
	0.75	0,131	187,470	6,175	1067,650	148,450	63,750
C_6,BF_4,FAP	0.25	0,101	185,420	4,487	1033,250	151,275	71,250
	0.5	0,107	186,150	5,115	1118,700	150,350	69,500
	0.75	0,112	186,870	5,742	975,650	149,420	67,750
C_6,BR,TF_2N	0.25	0,130	187,270	6,060	1209,750	150,820	82,250
	0.5	0,089	187,450	6,530	1362,500	153,350	107,500
	0.75	0,049	187,620	7,000	1515,250	155,870	132,750
C_6,BR,FAP	0.25	0,074	185,475	4,762	1140,750	153,750	94,250
	0.5	0,052	186,250	5,665	1316,500	155,300	115,500
	0.75	0,030	187,020	6,567	1492,250	156,850	136,750
C_6,TF_2N,FAP	0.25	0,114	185,300	4,292	988,000	151,220	69,000
	0.5	0,133	185,900	4,725	1011,000	150,250	65,000
	0.75	0,151	186,500	5,157	1034,000	149,270	61,000

Table.IV.1.3: *Predicted values of the properties of mixed binary ionic liquids and data table used in principal component analysis.*

IV.1.3 Application of the principal component analysis method

The descriptive method principal component analysis (PCA) lets you look at the connections between variables and the structure of dependencies between observations. This is done by

projecting the data onto different axes, which are called principal axes, and making a description or representation of the data.

Among the results obtained by the principal component analysis (PCA) are the correlation matrix, the observation graph, and the variable graph.

We carried out this work by performing PCA using numerical data structured into 81 observations related to 6 variables.

The variable graph represents the most important variables, and the observation graph shows the similarities and differences between the samples (the binary ionic liquids in our case) [21]. Table 3 contains the data used for different binary ionic liquids.

IV.1.3.1 Choice of axes:

PCA generates a set of new orthogonal axes or variables, called principal components (PCs), from the original variables. The generated axes are orthogonal and uncorrelated with each other. The first component (PC1) explains the maximum deviation (variance) in the entire dataset as well as its direction, and so on. The PCs are defined by vectors that are the eigenvectors of the variance-covariance matrix. The deviation (the variance) along the vector is defined as the eigenvalue. We obtain the observations (or variables) corresponding to the PCs from the correlation matrix. Each variable reveals the contribution of the original variable with respect to the principal components. Neglecting the directions where the sample variance is insignificant leads to variance reduction [21].

The main idea of the PCA technique is to reduce the dimensionality of a dataset that contains a large number of interdependent variables while preserving as much as possible the variation found in the dataset. This makes visualization, as well as forecasting and classification, easier [22, 23].

IV.1.3.2 Data interpretation:

The principal component analysis yielded the first noteworthy outcome. The figure presents the graph of observations (scores plot) from this analysis. (Figure.IV.1.8). we examine how much of the initial cloud's information a given factorial plan captures. Thus, an axis explaining less than 10% will rarely be interesting. We arrange the axes in descending order, ensuring that the first factorial plane—consisting of the first two factorial axes—consists of the richest information about the properties of the studied cloud. In our examples, the axes F1 (PC1) and F2 (PC2) are the richest in information. In this work, principal component analysis defines two principal components that together represent 74.52% of the total variance in the database. PC1

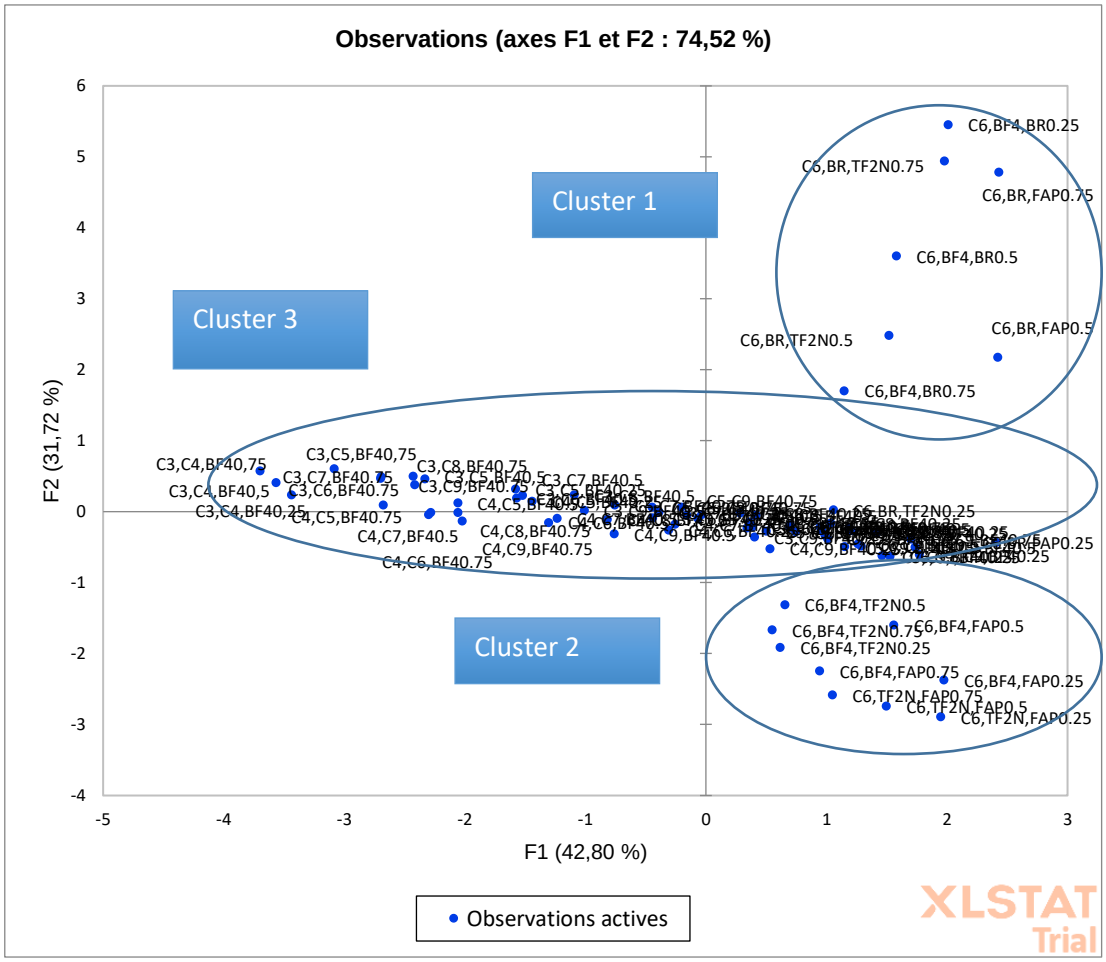

Figure IV.1.8: *graph of the observations (scores plot)*

captures 31.72% of the variance in the entire dataset, and PC2 captures 42.80% of the variance, as indicated in Figure IV.1.8.

According to the loading plot graph, several properties already correlated can dominate a grouping of LIBs in the score plot, not just one. The two-dimensional score plot displays the dispersion of the LIBs we studied along the F1 and F2 axes. The analysis is primarily visual; from Figure IV.1.8, we can distinguish three clusters of binary ionic liquids.

For this analysis, the sign of each principal component (positive or negative) is irrelevant; what matters is its positioning (or grouping).

Note that cluster 1 contains the binary ionic liquids that have the same cation C_6 mim, but two different anions, with one anion being Br. We comment on molar fractions X = 0.25, 0.5, and 0.75. We have observed that these ionic liquids exhibit low conductivity.

C_6 mim, Br is an exception in this series. Its fragility is much greater than that of ionic liquids with fluorinated anions. The bromide ion's ability to form strong hydrogen bonds with

the hydrogen atoms of the imidazolium cation explains this anomaly. The interionic forces will lead to the formation of a hydrogen bond and, consequently, to greater fragility. The presence of this network also makes it more difficult for ions to move through the sample, resulting in much lower conductivity. Because the negative charge spreads over a much larger volume, fluorinated anions have a lower charge density. The interaction of these anions with the imidazolium cation is much weaker than the interaction between the bromide anion and the cation. Therefore, this ionic liquid influences the mixing of ionic liquids, even when combined with ILs that have high conductivity.

Cluster 2 contains binary ionic liquids that have the same cation, C_6 mim, but two different anions, except for the Br anion. The conductivity of these ionic liquids is intermediate.

Observe that cluster 3 encompasses all binary ionic liquids with the same anion, BF4, but with two distinct cations, and their compounds are present in various molecular fractions. The conductivity of these ionic liquids is high.

We can directly compare the information in these two graphs because the graph representing the variables or descriptors (loadings plot) corresponds to the axis representing the observations (scores plot). The figure (Figure IV.1.9) represents the arrangement of variables corresponding to the observations shown in the figure. (Figure IV.1.8). Table 4 illustrates the properties in each cluster.

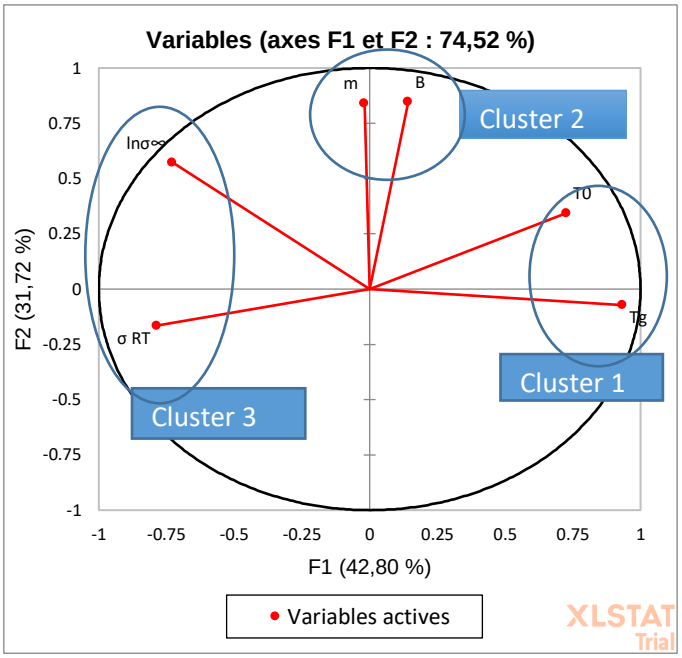

Figure.IV.1.9 *Graph of the variables (loading plot).*

Cluster 1	T_0, T_g
Cluster 2	**m, B**,
Cluster 3	**ln σ_∞, σ_{RT}**

Table 4: *The properties in each cluster.*

Clusters 1 and 2 contribute to the PC1 axis values of the score plot. They are strongly correlated because they have similar values on the same principal component axis.

Whereas the inverse values on the PC axis indicate inverse correlations. Therefore, the properties in cluster 1 are inversely correlated with the properties in cluster 3. Binary ionic liquids are systems with glassy behavior (the glass transition temperature (T_g) increases, and the conductivity at room temperature decreases since they are inversely correlated).

We also note that the fragility m is strongly correlated with B, which describes the temperature dependence of σ in the high-temperature limit (they appear in the same cluster).

To better examine the properties, we will analyze the predicted values of binary mixed ionic liquids with the same anion (Table 5) for LIBs with X = 0.5.

LIBs X= 0,5	σ_{RT}	T_g	$ln\sigma_\infty$	*B*	T_0	*m*
C_3,C_4,BF_4	0,261	176,500	7,375	1222,000	143,250	85,500
C_3,C_5,BF_4	0,161	178,950	7,275	1262,000	143,400	78,000
C_3,C_6,BF_4	0,138	181,350	7,115	1261,000	144,100	72,000
C_3,C_7,BF_4	0,113	180,600	6,922	1287,500	142,900	73,000
C_3,C_8,BF_4	0,109	182,400	6,980	1289,500	144,000	70,000
C_3,C_9,BF_4	0,100	182,800	6,830	1304,000	142,800	66,500
C_4,C_5,BF_4	0,263	180,350	6,790	1200,000	146,950	85,500
C_4,C_6,BF_4	0,241	182,750	6,630	1199,000	147,650	79,500
C_4,C_7,BF_4	0,215	182,200	6,460	1225,500	146,450	80,500
C_4,C_8,BF_4	0,211	183,800	6,495	1227,500	147,550	77,500
C_4,C_9,BF_4	0,203	184,200	6,364	1242,000	146,350	74,000
C_5,C_6,BF_4	0,140	185,200	6,530	1239,000	147,800	72,000
C_5,C_7,BF_4	0,115	184,450	6,360	1265,500	146,600	73,000
C_5,C_8,BF_4	0,111	186,250	6,395	1267,500	147,700	70,000
C_5,C_9,BF_4	0,102	186,650	6,240	1282,000	146,500	66,500
C_6,C_7,BF_4	0,092	186,850	6,259	1278,700	147,300	67,000
C_6,C_8,BF_4	0,088	188,650	6,235	1280,700	148,400	64,000
$C_6,C9,BF_4$	0,080	189,050	6,085	1295,200	147,200	60,500
C_7,C_8,BF_4	0,063	187,900	6,065	1293,000	147,200	65,000
C_7,C_9,BF_4	0,054	188,300	5,915	1307,500	146,000	61,500
C_8,C_9,BF_4	0,050	190,100	5,950	1309,500	147,100	58,500

Table.IV. 4: *Predicted values of the properties of binary mixed ionic liquids with the same anion.*

The PCA graph, which represents the entire dataset, shows the predicted values of the properties of binary mixed ionic liquids with the same anion (Figure IV.1.10). It is noteworthy that the two most significant PCs, PC1 and PC2, account for 69.80% and 27.33% of the total variability in the dataset, respectively. We observe three groups: Groups 2 and 3 consist of binary ionic liquids with intermediate conductivity. Group 1 contains binary ionic liquids with high conductivity. We observe a strong correlation between the conductivity and the fragility. Therefore, we conclude that fragility significantly influences the conductivity of binary mixed ionic liquids that contain the same anion, particularly in the case of a binary mixture that includes the ionic liquid Bmim, BF_4.

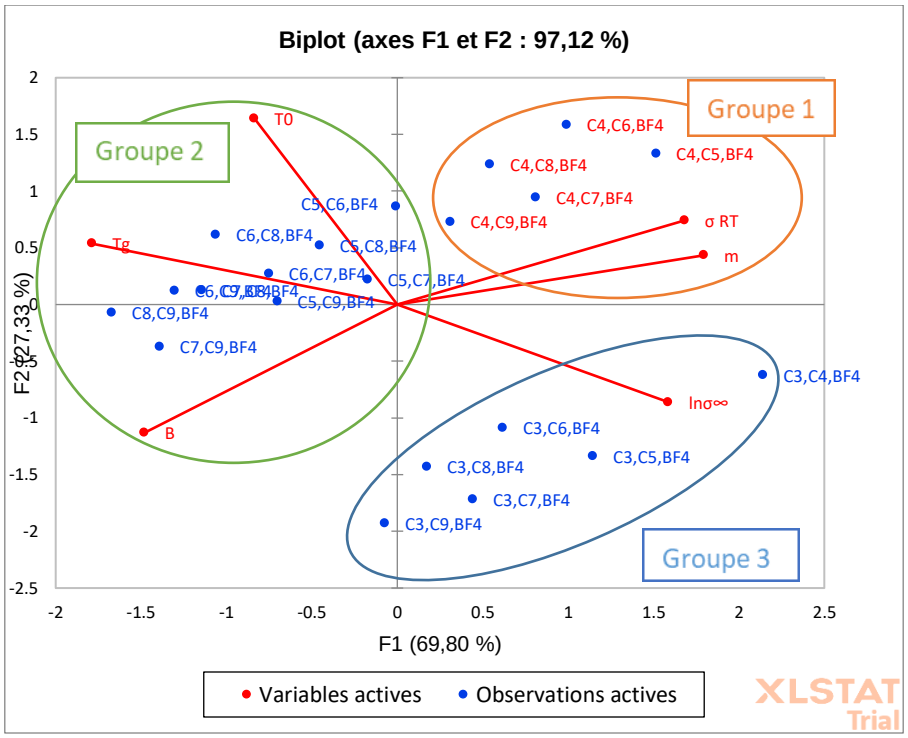

Figure V.1.10: *graph of observations (scores plot) for the predicted values of the properties of binary mixed ionic liquids with the same anion.*

The comparison between the two ionic liquids, C_3mim BF_4 and C_4mim BF_4, reveals the following: The conductivity of C_3mim BF_4 is higher than that of C_4mim BF_4, but in a binary mixture, C_4mim BF_4 is a good candidate for having a binary ionic liquid with high conductivity.

IV.1.4 Description of the dielectric relaxation phenomenon of (1-butyl-3-methylimidazolium) tetrafluoroborate [Bmim][Bf4]

The present part examines the dielectric properties of (1-butyl-3-methylimidazolium) tetrafluoroborate [BMIM][BF4] over a wide range of frequencies and temperatures. We explore the charge transport mechanism in detail and also study the secondary dielectric relaxation processes associated with the reorientation and release of dipoles.

IV.1.4.1 Synthesis of 1-butyl-3-methylimidazolium tetrafluoroborate [BMIM][BF_4]:

The compound [BMIM][Br] (2.30 g, 10.08 mmol) is ground into small grains using a spatula. In a flask, ammonium tetrafluoroborate (1.04 g, 9.91 mmol) and [BMIM][Br] are mixed together. The resulting powder is irradiated at 90 watts for 30 seconds. A yellow liquid and a white precipitate are formed. After returning to room temperature, the mixture is filtered to remove the precipitate. The ionic liquid is obtained quantitatively.

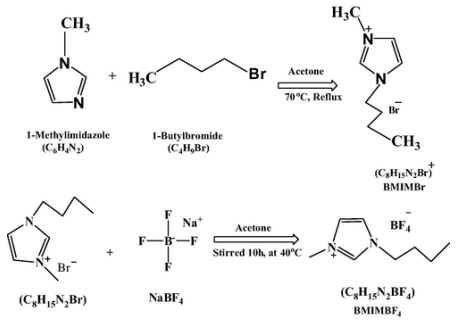

Scheme IV.1.1*: Synthesis of 1-butyl-3-methylimidazolium tetrafluoroborate [BMIM][BF_4]*

IV.1.4.2. Measurement of dielectric properties

Dielectric measurements were carried out using a high-resolution alpha analyzer (BDS 4000 Novocontrol spectrometer), assisted by a Quatro temperature controller. The samples were measured in a parallel plate geometry with a separation distance using platinum electrodes and Teflon spacers. The applied voltage was 0.1 V. Before starting the measurements, the samples were annealed for several hours at 160 °C under a flow of pure nitrogen, in the cryostat of the dielectric spectrometer. After that, dielectric measurements were performed as a function of frequency (typically in the range between 10 MHz and 0.1 Hz) with a temperature variation from -75 to -5 °C. The temperature was controlled by heating the sample with a jet of pure nitrogen, which leads to stabilization conditions better than 0.1 °C. This range allows for an in-

depth analysis of conductivity and reorientation modes in the glassy and liquid phases of these systems.

At low applied electric fields, linear response theory holds, and the complex dielectric function ε* (ω, T) as well as the complex conductivity σ * (ω, T) are related by σ * (ω, T) = iε$_0$ωε * (ω, T), where ε$_0$, ω, and T denote the dielectric permittivity of free space, the radial frequency, and the temperature, respectively.

Thus, complex conductivity is defined as:

$\sigma^* = \sigma' + i\sigma'' = \varepsilon_0\omega\varepsilon'' + i\,\varepsilon_0\omega\varepsilon'$

Therefore, the following formula determines the loss factor:

$$\tan(\delta(\omega)) = \frac{\varepsilon''(\omega)}{\varepsilon'(\omega)}$$

Furthermore, the relation expresses the dielectric modulus, which represents the actual process of dielectric relaxation.

$$M^* = \frac{1}{\varepsilon^*(\omega)} = M' + i\,M''$$

V.1.4.3. Dielectric Spectroscopy 1-butyl-3-imidazolium tetrafluoroborate

Figure.IV.1.11. presents the typical dielectric spectra of the ionic liquid [BMIM] [BF_4]. We measured the dielectric response of this IL, covering frequencies from approximately 10^{-1} to 10^6 Hz and a wide temperature range, extending deep into the liquid regime and approaching the glass transition temperature T_g at low temperatures. This range allows for an in-depth analysis of conductivity, fragility, and reorientation modes in the glassy and liquid phases of these systems. The real and imaginary parts of this ionic liquid's dielectric permittivity (ε′ and ε″), its conductivity (σ′), and its imaginary part of the dielectric modulus (M″) are shown in Figure.IV.1.11.d. The temperatures used were chosen.

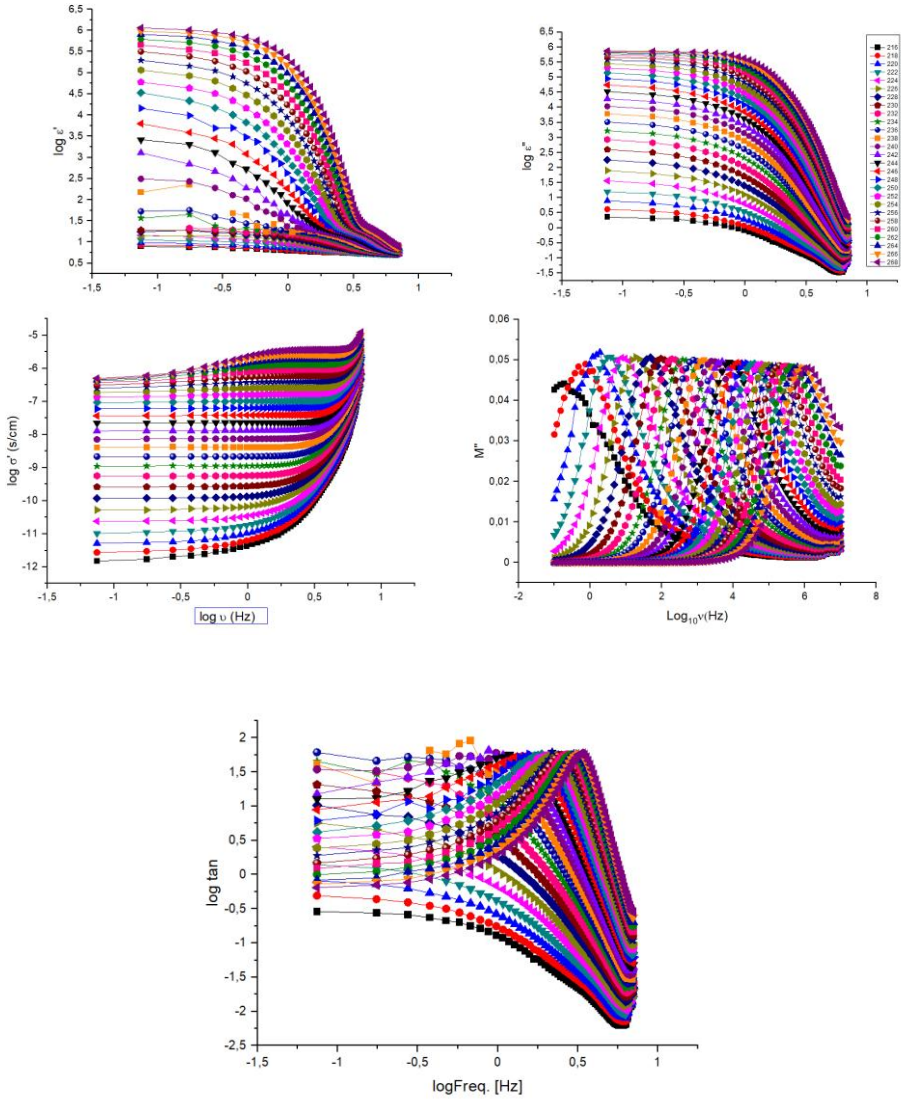

Figure.IV.1.11. *Dielectric spectra of [BMIM][BF_4] The spectra are included for a variety of temperatures. The indicated quantities are: the dielectric constant (a), the dielectric loss (b), the conductivity (c), the imaginary part of the dielectric modulus (d), and the loss factor. (e).*

In ε′(ν) (Figure.IV.1.11.a), the huge rise and the approach of a plateau at low frequencies are caused by the polarization of the electrodes or the blocking of the electrodes, which happens because ions can't get through the metal capacitor plates [24].The steep slope—the increase in low-frequency loss, ε″(ν), up to about 10^5, which is generally found in many ionic conductors, including ionic liquids [24, 25] (Figure.IV.1.11. b)—is caused by the dc conductivity σ_{dc} and corresponds to the plateau observed in σ′(ν). (Figure.IV.1.11.c). The stabilization of ε"(ν) at the lowest frequencies and the corresponding decrease in σ′(ν) also result from electrode blocking. Curiously, in ionic conductors, AC (alternating current) measurements are necessary to determine the dc conductivity.

We provide a more comprehensive assessment of these dipolar modes. In the high-frequency range, the experiment results show the dielectric properties of ionic conductors in the bulk, with the interfaces not making a difference. When the frequency goes down, the electrode polarization effect starts to show up at $f = f_{on}$. This causes big changes in the measured dielectric response. These effects are manifested by a significant increase in the measured permittivity values $\varepsilon'(\omega)$. As the frequency decreases, the complete development of the electrode polarization effects appears at $f = f_{max}$. These changes can be seen by the fact that the measured permittivity values reach a plateau at the same frequency where the conductivity values start to drop sharply ($\sigma'(\omega)$). Recent studies have systematically studied the characteristic frequencies f_{on} and f_{max}, defining the relevant frequency range for electrode polarization effects and their corresponding scaling laws with respect to various physical parameters [26, 27] As the temperature increases, these characteristic frequencies shift to higher values, an obvious consequence of the increase in conductivity.

The M″ spectra, as shown in Fig. 1.d, are often used to define a conductivity relaxation time (τ_σ) to characterize ionic dynamics. The main peak of M″(ν) is attributed to translational ionic movements, and τ_σ is determined from the peak frequency ν_σ via $\tau_\sigma = 1 / (2 \pi \nu_\sigma)$. The representation of the modulus eliminates the effects of blocking electrodes appearing at low frequencies in the other quantities. It should be noted that this main peak in M ″ (ν) is the conductivity relaxation peak. Any significant charge transport in a material generates a prominent peak in M'(ν) [28].

V.1.4.4. Relaxation and conductivity dynamics.

For various temperatures, the relaxation time, τ, is found by using the resonance condition, which is shown in Figure.IV.1.12. (a.b) and is given by $\tau = 1$ from the highest point of log M "(ω) and tan (δ).

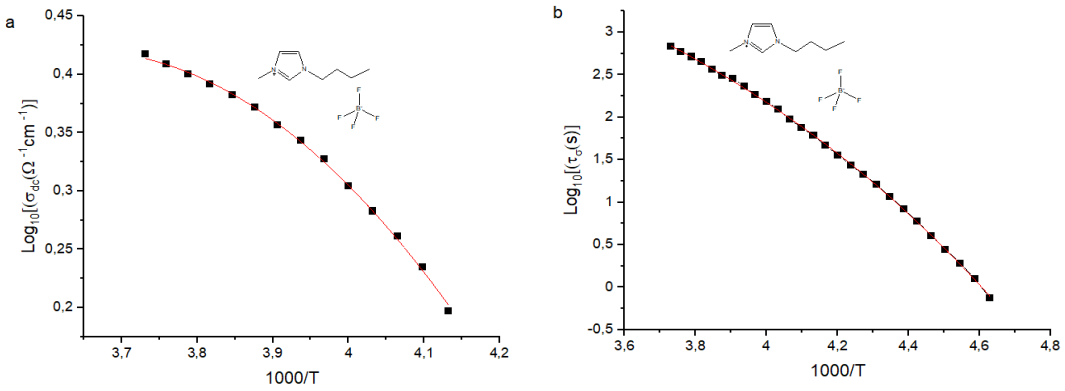

Figure.IV.1.12: *Temperature dependence in ionic dynamics.*

The dc-conductivities from the loss factor tang tan (δ) (a). In (b), we deduce the conductivity relaxation time from M "(v)." The solid lines in (a, b) correspond respectively to the VFT formulas and equations (V.4, 5).

We fitted the data in Figure 2a using the empirical Vogel-Fulcher-Tammann (VFT) formula, which is widely known in glass physics and generally expressed in the modified form 11:

$$\sigma_{dc} = \sigma_0 \exp\left[-\frac{\mathrm{DT}_0}{T - T_0}\right]$$

We fitted the data (Fig. 2b) with the corresponding VFT formula for the relaxation time:

$$\tau = \tau_0 \exp\left[\frac{\mathrm{DT}_0}{T - T_0}\right]$$

At high temperatures, the module peaks start to move out of the available frequency window (Figure.IV.1.12. d), making it impossible to determine the peak frequency uniquely. Therefore, we calculated m using D, which we obtained from the dc fittings. We relate D and m by m = 16 + 590 / D. Figure.IV.1.12. shows an Arrhenius representation of the temperature dependencies of σ_{dc} and τ_σ for [BMIM] [BF_4] LI that we studied. The nonlinear behavior found reveals different degrees of deviations from the Arrhenius law. From τ_σ, the glass transition temperature can be determined using τ_σ (Tg) = 100 s (sometimes 250 or 1000 s are assumed, leading to a shift in T_g of only a few K). Table. IV. 5. lists the obtained values. Note that this establishes the glass transition temperature of the ionic subsystem. It must correspond to the defined structural glass transition temperature.

T_g (K)	T_0(K)	D	m
244	164.61	9.56	78.10

Table.IV. 5. *Parameters of the ionic liquid [BMIM] [BF4].*

CONCLUSION

The current work has enabled us to explore an original and innovative field of physicochemical ionic liquids, which is rapidly developing. We are primarily interested in studying the dielectric properties of imidazolium-based ionic liquids. This study employs the VTF equation, PLS and PCA data mining techniques to utilize informatics in identifying necessary and valuable information for the design of new materials. Thus, we used the PLS method, which is based on the VTF dielectric equation parameters of individual ionic liquids in our database, to predict the properties of binary ionic liquid mixtures. The PCA method

enabled us to classify the properties and elements, which helped visualize the position of the elements relative to one another, as well as the existing relationships between their properties. It is challenging for scientists to comprehend the relationships between numerous variables, so we employed PCA and PLS as tools to identify existing structures in a dataset, as well as for screening and extracting useful information from the data.

Broadband dielectric spectroscopy has been used to study the dielectric properties of the ionic liquid systematically -butyl-3-methylimidazolium tetrafluoroborate [BMIM][BF_4] as a function of frequency and temperature. We determined the characteristic frequencies of the electrode polarization effects and their corresponding scaling laws by analyzing the experimental results. We have demonstrated that we can directly select the complex dielectric function of ionic liquids at the interface with a metallic electrode by utilizing electrode polarization effects. We observed a relaxation peak in the dielectric loss of the interfacial layers. We attribute the relaxation peak, which displays Vogel-Fulcher-Tammann temperature dependence, to an ion exchange process between the interfacial layers and the bulk ionic liquid. Therefore, our method enables the study of electrical and dielectric properties of ionic liquids at metallic interfaces in a more organized manner. This could lead to a better understanding of how charges move across solid interfaces.

IV.2. Studies of Thermal and Dielectric Properties of Binary Ionic Liquids

Ionic liquids are promising candidates for electrolytes in energy storage systems. For this study, we conducted detailed investigations using broadband dielectric spectroscopy and differential scanning calorimetry on individual and binary ionic liquids. We demonstrate that the mixture of two ionic liquids allows for precise adjustment of their physical properties, such as continuous conductivity. From a chemical standpoint, adjusting ionic liquids through blending is a simple and, therefore, economical method.

In the present work, we conduct an in-depth study of two ionic liquids, 1-(2-hydroxyethyl)-3-vinylimidazolium chloride [EtOHVIM]Cl and 1-(hydroxyethyl)-3-methylimidazoliumdihydrogenophosphate [EtOHMIM][H_2PO_4], using broadband dielectric spectroscopy (BDS). Subsequently, these two ionic liquids were mixed to form a binary ionic liquid, which was also examined by BDS to evaluate its dielectric behavior and conductivity characteristics.

IV.2.1 Sample definitions

IV.2.1.1 1-(hydroxyethyl)-3-vinylimidazolium chloride [EtOHVIM]Cl

The chemical reaction of 2-chloroethanol with 1-vinylimidazol as precursor led to the corresponding compound 1-hydroxyethyl-3-vinylimidazolium chloride [ETOHVIM]CL. The structure of these compounds was identified by ^{1}H NMR, ^{13}C NMR as preliminary spectroscopic characterization. To obtain information on the structure and vibrational behavior in these compounds, vibrational spectroscopy measurements were investigated by Fourier Transform-Infrared-Attenuated Total Reflectance and Fourier Transform Raman spectroscopy in the spectral range 600–4000 cm^{-1} and 4000–500 cm^{-1}, respectively. Scheme IV.1.[29]

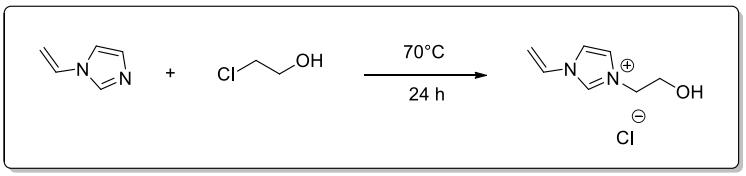

Scheme IV.1 *Réaction de quaternisation d'amine.*

IV.2.1.2 1-(hydroxyethyl)-3-methylimidazoliumdihydrogenophosphate ionic liquid [EtOHMIM][H_2PO_4]

Very recently, the hydroxyl-functionalized ionic liquids have gained immense interest and were developed for a number of interesting applications.

In this work and for the first-time new hydroxyl-functionalized namely; 1-(hydroxyethyl)-3-methylimidazolium dihydrogenophosphate ionic liquid [EtOHMIM][H_2PO_4] was synthesized in our laboratory. The synthesis is based on an alkylation reaction of 1-methylimidazole followed by anion exchange (Scheme IV.2). The obtained IL is characterized by 1H-NMR, ^{13}C-NMR spectroscopy. This experimental vibrational spectroscopy have been investigated using Infrared and Raman spectroscopy, based on the infrared (IR) and Raman spectroscopies results, complete vibrational assignments have been performed. [30]

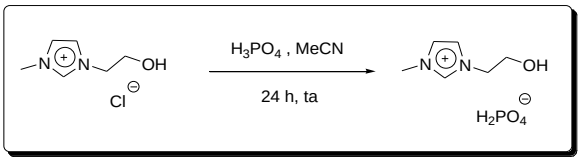

Scheme IV.2 *Réaction de métathèse anionique.*

IV.2.2 Thermal measurements

Thermal properties of this hydroxyl-functionalized ILs were investigated by using following techniques, (i) differential scanning calorimetry (DSC) from -100 °C to 200 °C. (ii) Thermogravimetric Analysis (TGA) and Derivative Thermogravimetry (DTG) in the temperature range from 20 to 600 C°, The thermogravimetry analysis was coupled with mass spectrometry in order to assess the influence of anion on the measured property. [19, 21]

IV.2.2.1 Chloride 1- (hydroxyethyl) -3-vinylimidazolium [ETOHVIM]CL

The DSC thermogram revealed an endothermic peak onset at -44 °C, corresponding to the melting point.

Thermal stability analysis showed that [EtOHVIM]Cl remained steady below 50 °C, with degradation occurring in two stages. The first stage began at 50 °C and ended at 184 °C, resulting in a mass loss of 6.46%, attributed to the release of H_2O gas as identified by mass spectrometry. The second stage occurred between 182 °C and 390 °C, with a mass loss of 66.68%, corresponding to the release of CH_3OH/CH_3CH_2OH or CH_3CH_2OH/O_2, also identified by mass spectrometry. At 400 °C, the sample left a reddish residue of 13.52% of its initial mass.

The compound is thermally stable below 50 °C, as indicated by the TGA and DTG analyses. It begins to degrade at 50 °C, with the degradation occurring in two distinct stages. This

demonstrates that while [EtOHVIM]Cl has a defined thermal stability range, it starts to decompose beyond this temperature threshold.

IV.2.2.2 Dihydrogen phosphate 3-(2-hydroxyethyl) -1-methylimidazolium [EtOHMIM][H_2PO_4]

The thermal properties of [EtOHMIM][H_2PO_4] were characterized using DSC, TGA, and DTG techniques.

The DSC thermogram showed no glass transition during the heating scan. An exothermic peak onset was observed at 77 °C, followed by an endothermic peak onset at 84 °C, corresponding to the melting point. Another endothermic peak at 117 °C likely represents the melting point of a second morphology of the same compound.

Thermal stability analysis revealed that [EtOHMIM][H_2PO_4] is stable below 50 °C and degrades in three stages, leaving a reddish residue of 26.19% at 600 °C. The first stage, occurring between 50 °C and 200 °C, showed a mass loss of 14.81%, attributed to the release of H_2O gas. The second stage, between 200 °C and 360 °C, resulted in a mass loss of 37.08%, corresponding to the release of H_2O, CH_3, OH, and other fragments. The third stage, between 360 °C and 600 °C, showed a mass loss of 21.92%, further confirming the influence of the dihydrogen phosphate anion on the compound's thermal properties.

The compound remains thermally stable below 50 °C, as indicated by the TGA and DTG analyses. Beyond this temperature, it undergoes degradation in three distinct stages, leaving a residue of 26.19% of its initial mass at 600 °C. This indicates that [EtOHMIM][H_2PO_4] has relatively good thermal stability, with the dihydrogen phosphate anion contributing to its enhanced thermal properties compared to other ionic liquids.

IONIC LIQUIDS	T_G(°C)	T_C (°C)	T_F (°C)	T_D(°C)	T_{DT}(°C)
[ETOHVIM]CL	--	--	-44 °C	294.1	405
[ETOHMIM][H_2PO_4]	--	77	84	264	365

Table IV.2.1: *Thermal properties of [EtOHVIM]Cl and [EtOHMIM][H_2PO_4]*

Among the two ionic liquids, [EtOHMIM][H_2PO_4] exhibits greater thermal stability compared to [EtOHVIM]Cl. [EtOHMIM][H_2PO_4] remains stable below 50 °C and undergoes degradation in three stages, leaving a higher residual mass of 26.19% at 600 °C. In contrast, [EtOHVIM]Cl begins to degrade at a similar temperature but decomposes in two stages, leaving a lower residue of 10.54% at 400 °C. This enhanced stability of [EtOHMIM][H_2PO_4] is

attributed to the influence of the dihydrogen phosphate anion ([$H_2PO_4^-$]), which provides better thermal properties than the chloride anion ([Cl^-]).

[EtOHMIM][H_2PO_4] is more stable than [EtOHVIM]Cl due to the nature of the anion. The dihydrogen phosphate anion ([$H_2PO_4^-$]) has stronger hydrogen bonding and more complex interactions with the cation compared to the chloride anion [Cl]. These interactions contribute to a more robust ionic network, requiring more energy to break, which enhances the thermal stability of the compound. Additionally, the larger size and greater delocalization of charge in [$H_2PO_4^-$] reduce the ionic liquid's volatility and susceptibility to thermal decomposition, further stabilizing the structure at higher temperatures.

IV.2.3. Dielectric measurements

Dielectric measurements were conducted using an GWINSTEK, LCR-821 impedance meter. The measurements were performed at controlled temperatures ranging from 300K to 400K, with adjustments made in 4 – 5 K increments per minute, across a broad spectrum of frequencies (500 Hz to 100 KHz), enabling the observation of polarisation variation as a function of electric field frequency and temperature. Through these observations, we may ascertain the values of ε' (actual relative permittivity) and ε" (imaginary relative permittivity), which together constitute the complex permittivity ε*.

IV.2.3.1 Chloride 1-(hydroxyethyl) 3-vinylimidazolium [ETOHVIM]Cl

Figures IV.2.7, IV.2.8, and IV.2.9, respectively, represent the variations of the real relative permittivity (ε'), imaginary permittivity (ε"), and the variation of the logarithm of the conductivity log(σ ($\Omega^{-1}m^{-1}$)) as a function of temperature for a series of five frequencies: 100 Hz, 500 Hz, 1 kHz, 10 kHz, and 100 kHz for the ionic liquid chloride 1-(hydroxyethyl)-3 vinylimidazolium [ETOHVIM] Cl.

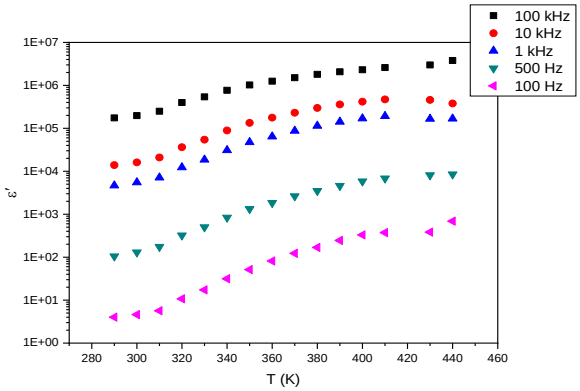

Figure.IV.2.7 *Variation of permittivity (ε') as a function of temperature for different frequencies [ETOHVIM]Cl.*

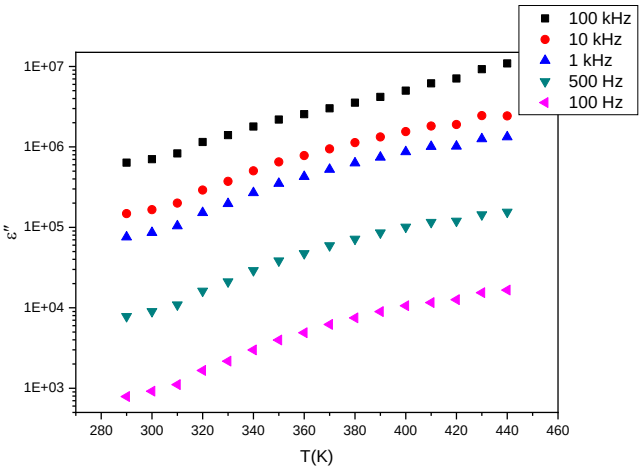

Figure.IV.2.8 *Variation of permittivity (ε") as a function of temperature for different frequencies [ETOHVIM]Cl.*

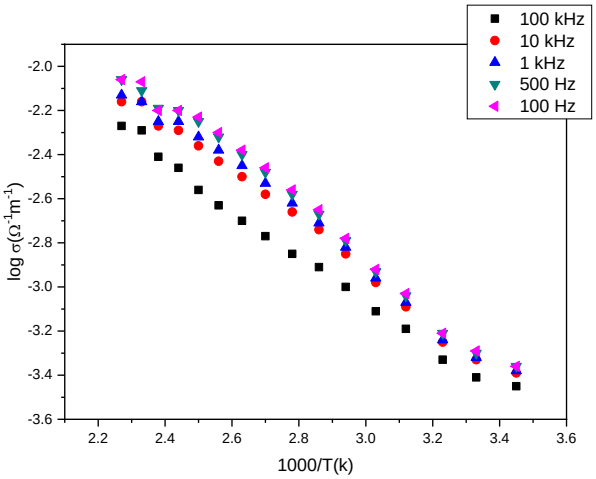

Figure. IV.2.9: *The variation of the logarithm of conductivity as a function of the inverse of the temperature and for different frequencies [ETOHVIM]Cl.*

From the two figures (Fig. IV.2.8) and (Fig. IV.2.9), we notice a significant increase in the real relative permittivity (ε') and imaginary permittivity (ε") for the frequencies 100 kHz, 10 kHz, and 1 kHz, and a lesser increase for the frequencies 500 Hz and 100 Hz.

The conductivity of 1-(hydroxyethyl)-3-vinyl imidazolium chloride for the 5 frequencies (Fig. IV.2. 9) is very high between room temperature and T_f = 320 K for the 5 frequencies.

Fréquence (HZ)	**100**	**500**	**1000**	**10000**	**100000**
E_a (eV)	9.68×10^{-2}	9.83×10^{-2}	9.01×10^{-2}	1.01×10^{-1}	1.03×10^{-1}

Tableau (IV.2.2) : *L'énergie d'activation pour différentes fréquences de liquide ionique de [ETOHVIM]Cl.*

From the table (IV.2.1), the activation energy for different frequencies of ionic liquid [ETOHVIM]CL measured from conductivity is for the five frequencies determined by the Arrhenius equation.

The average activation energy: $E_{amoy} = 9.784 \times 10^{-2}$ eV.

IV.2.3.2 1-(hydroxyethyl)-3-methylimidazolium dihydrogenophosphate [EtOHMIM][H2PO4]

The (Figs. IV.2.10; IV.2.11, and IV.2.12) respectively represent the variations of the real relative permittivity (ε'), imaginary permittivity (ε"), and the variation of the logarithm of the conductivity $\log(\sigma(\Omega^{-1}m^{-1})$ as a function of temperature for a series of five frequencies: 100 Hz, 500 Hz, 1 kHz, 10 kHz, and 100 kHz for the -(hydroxyethyl)-3-methylimidazolium dihydrogenophosphate ionic liquid $[ETOHMIM][H_2PO_4]$.

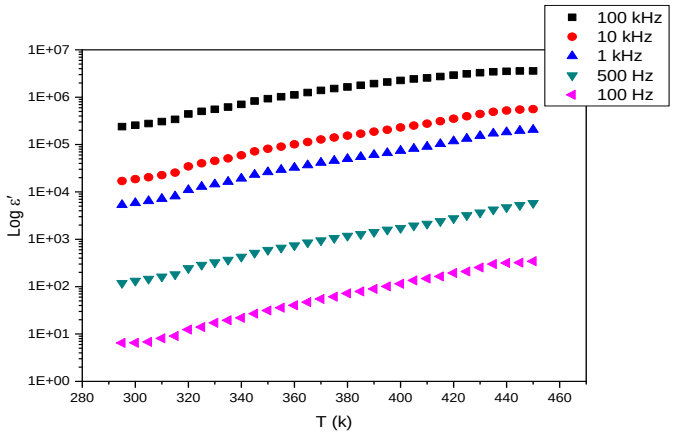

Figure IV.2.10: *The variation of permittivity (ε') as a function of temperature for different frequencies [ETOHMIM][H_2PO_4].*

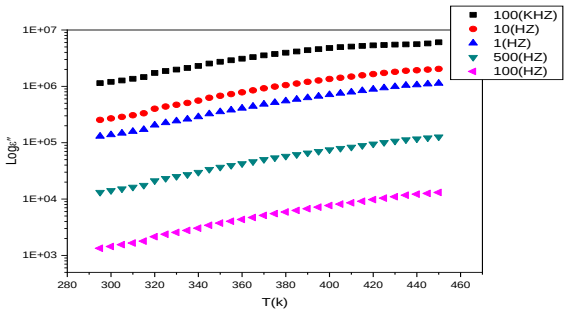

Figure.IV.2.11: *The variation of permittivity (ε") as a function of temperature for different frequencies [ETOHMIM][H_2PO_4].*

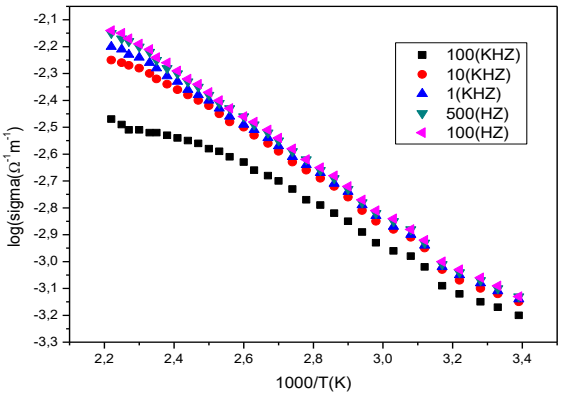

Figure.IV.2.12 : *The variation of conductivity as a function of temperature for different frequencies [ETOHMIM][H_2PO_4].*

From these three figures, we notice that the real relative permittivity (ε'), imaginary (ε"), and the variation of the conductivity log (σ ($\Omega^{-1}m^{-1}$)) exhibit two regions.

The real relative permittivity, (ε'), and imaginary permittivity, (ε"), increase with temperature after the melting onset temperature T_f = 92.8°C and shift towards higher temperatures as the frequency increases.

A significant increase in the real relative permittivity (ε') and imaginary permittivity (ε") for temperatures above the melting onset temperature. This increase is associated with the phenomenon of electrode polarization.

The conductivity of [ETOHMIM][H_2PO_4] is very high between room temperature and T_f = 365.8 K for the 5 frequencies. (Fig. IV. 2.12).

Fréquence (Hz)	**100**	**500**	**1000**	**10000**	**100000**
E_a(eV)	7.10×10^{-2}	7.33×10^{-2}	5.68×10^{-2}	7.95×10^{-2}	7.62×10^{-2}

Tableau (IV.2.3): *The activation energy for different frequencies of [ETOHMIM][H_2PO_4] ionic liquid.*

From Table (IV.2), the activation energy for different frequencies of [ETOHMIM][H2PO4] ionic liquid was measured from the conductivity log (σ($\Omega^{-1}m^{-1}$) for the five frequencies and determined by the Arrhenius equation.

The average activation energy: $E_{a\,moy} = 7.136 \times 10^{-2}$eV.

IV.2.3.3 The binary ionic liquid 75% [EtOHVIM]Cl 25% [ETOHMIM][H2PO4]

Figures IV.2.13, IV.2.14, and IV.2.15 respectively represent the variations of the real relative permittivity (ε'), imaginary (ε"), and the variation of the logarithm of the conductivity

log (σ ($\Omega^{-1}m^{-1}$)) as a function of temperature for a series of five frequencies: 100 Hz, 500 Hz, 1 kHz, 10 kHz, and 100 kHz for the binary ionic liquid 75% [EtOHVIM]Cl and 25% [ETOHMIM][H_2PO_4].

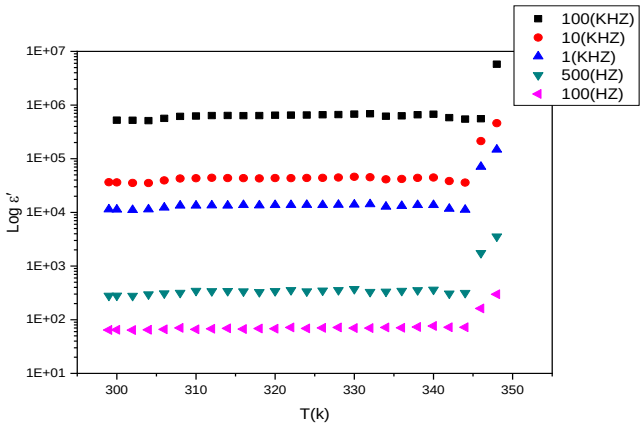

Figure.V.2.13: The variation of permittivity (ε') as a function of temperature for different frequencies of binary ionic liquid for 75% [EtOHVIM]Cl 25% [ETOHMIM][H_2PO_4].

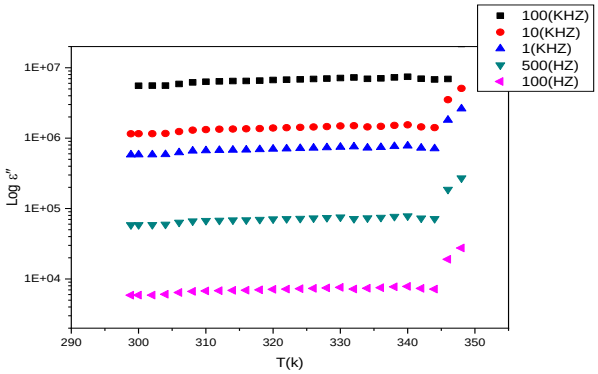

Figure. (IV.2.14) : The variation of permittivity (ε") as a function of temperature for different frequencies of binary ionic liquid for 75% [EtOHVIM]Cl 25% [ETOHMIM][H2PO4].

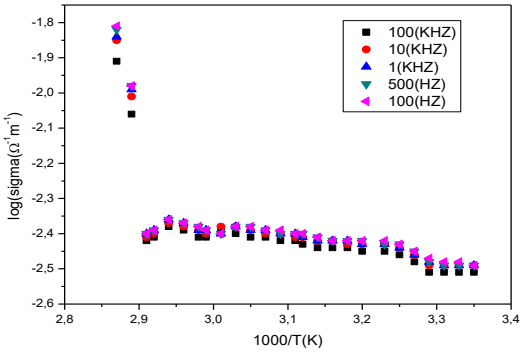

Figure.IV.2.15 : The variation of the logarithm of conductivity as a function of the inverse of temperature for different frequencies of the binary IL 75% [EtOHVIM]Cl 25% [ETOHMIM][H_2PO_4].

A significant increase in the real relative permittivity (ε') and imaginary permittivity (ε") for temperatures above the melting onset temperature. This increase is associated with the phenomenon of electrode polarization.

From Table (IV.2. 4), the activation energy for different frequencies of the binary ionic liquid 75% [EtOHVIM]Cl 25% [ETOHMIM][H_2PO_4] is measured from the conductivity for the five frequencies and determined by the Arrhenius equation.

Frequencies (HZ)	**100**	**500**	**1000**	**10000**	**100000**
E_a(eV)	5.45×10^{-2}	5.44×10^{-2}	5.38×10^{-2}	5.22×10^{-2}	5.10×10^{-2}

Table (IV.2.4): *the activation energy for different frequencies of the binary ionic liquid 75% [EtOHVIM]Cl 25% [ETOHMIM][H_2PO_4].*

The average activation energy: $E_{a\ moy} = 5.316 \times 10^{-2}$eV.

IV.2.3.4 The binary ionic liquid 50% [EtOHVIM]Cl 50% [ETOHMIM][H2PO4]

Figures IV.2.16, IV.2.17, and IV.2.18 respectively represent the variations of the real relative permittivity (ε'), imaginary permittivity (ε"), and the variation of the logarithm of the conductivity log (σ (Ω^{-1} m^{-1})) as a function of temperature for a series of five frequencies: 100 Hz, 500 Hz, 1 kHz, 10 kHz, and 100 kHz for the binary ionic liquid 50% [EtOHVIM]Cl and 50% [ETOHMIM][H_2PO_4].

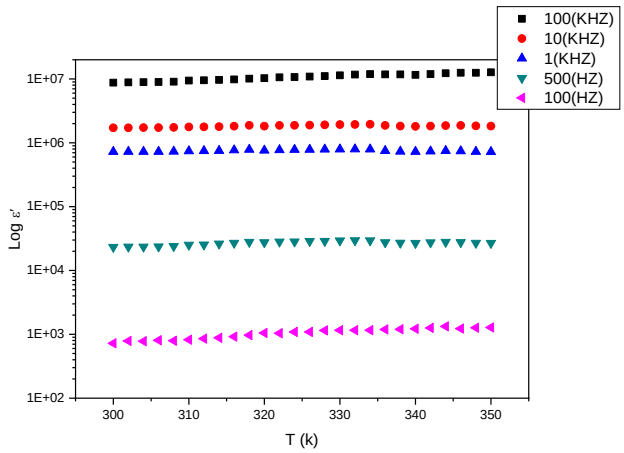

Figure.V.2.16: *the variation of the permittivity (ε') as a function of the temperature of 50% [ETOHMIM][H_2PO_4] and 50% [EtOHVIM]Cl.*

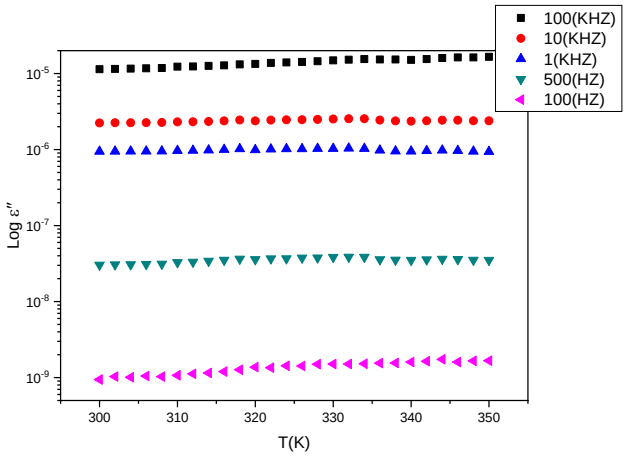

Figure. (IV.2.17): *the variation of permittivity (ε'') as a function of temperature for 50% [EtOHVIM]Cl and 50% [ETOHMIM][H_2PO_4].*

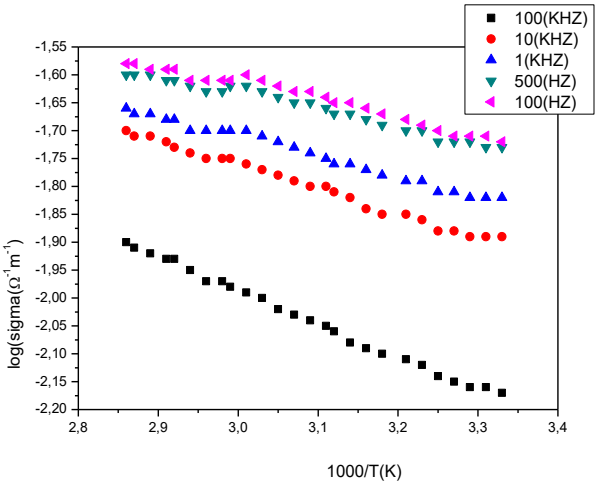

Figure IV.2.18: *The variation of conductivity as a function of temperature for 50% [EtOHVIM]Cl and 50% [ETOHMIM][H_2PO_4].*

From the two figures (Fig. IV.2.16) and (Fig. IV.2.17), we notice a significant and remarkable increase in the figures of the real relative permittivity (ε') and imaginary permittivity (ε") predominant for the frequencies 100 kHz, 10 kHz, 1 kHz and less significant for the frequencies 500 Hz, 100 Hz. This increase is associated with the phenomenon of electrode polarization.

From Table (IV.2. 4), the activation energy for different frequencies of the binary ionic liquid 50% [EtOHVIM] 50% [ETOHMIM][H_2PO_4] is measured from the conductivity for the five frequencies. Determined by the Arrhenius equation.

Table (IV.2.5): *the activation energy for different frequencies of ionic liquid 50% [EtOHVIM]Cl and 50% [ETOHMIM][H_2PO_4].*

Fréquence (HZ)	**100**	**500**	**1000**	**10000**	**100000**
Ea(eV)	2.64×10^{-2}	2.59×10^{-2}	3.11×10^{-2}	3.71×10^{-2}	5.12×10^{-2}

The average activation energy: $E_{amoy} = 3.434\times 10^{-2}$eV.

IV.2.3.5 The binary ionic liquid 25% [EtOHVIM]Cl and 75% [ETOHMIM][H_2PO_4]:

Figures IV.2.19, IV.2.20, andI IV.2.21 respectively represent the variations of the real relative permittivity (ε'), imaginary permittivity (ε"), and the variation of the logarithm of the conductivity log (σ (Ω_{-1} m_{-1})) as a function of temperature for a series of five frequencies: 100 Hz, 500 Hz, 1 kHz, 10 kHz, and 100 kHz for the binary ionic liquid 25% [EtOHVIM]Cl 75% [ETOHMIM][H_2PO_4].

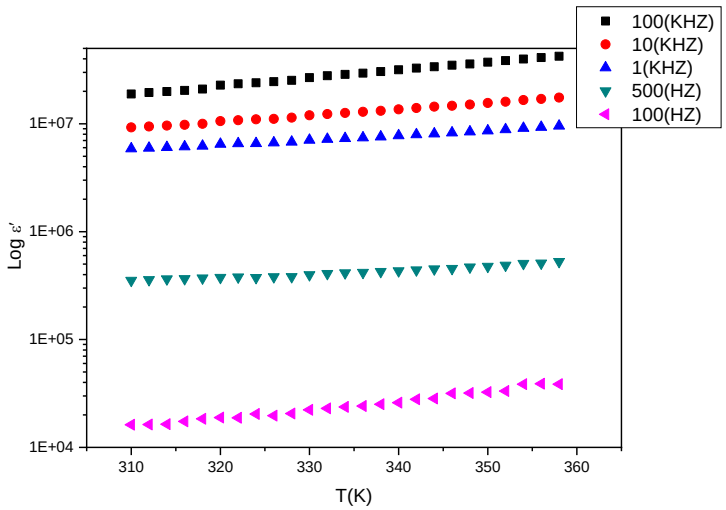

Figure.IV.2.19: *the variation of the permittivity (ε') as a function of the temperature of 75% [ETOHMIM][H_2PO_4] and 25% [EtOHVIM]Cl.*

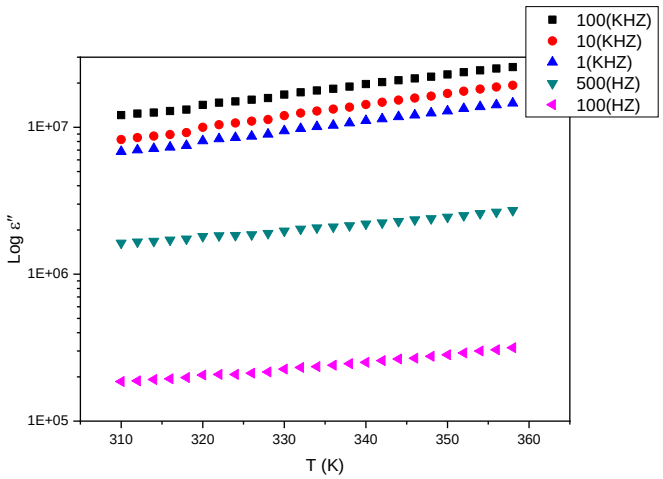

Figure.IV.2.20: *The variation of permittivity (ε") as a function of temperature for 25% [EtOHVIM]Cl and 75% [ETOHMIM][H_2PO_4].*

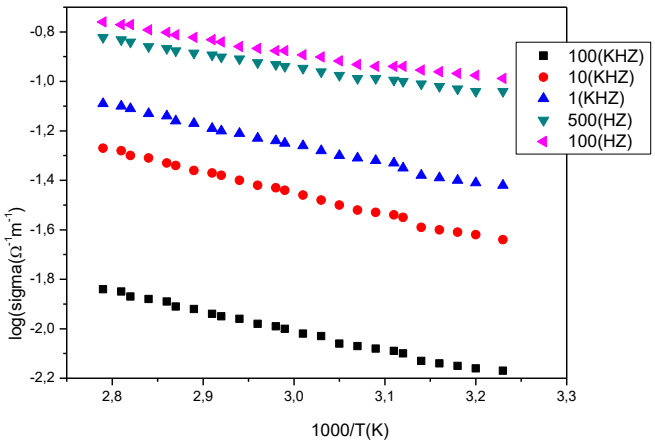

Figure.IV.2. 21: *The variation of conductivity as a function of temperature for 25% [EtOHVIM] and 75% [[ETOHMIM][H_2PO_4]].*

From the two figures (Fig.IV.2.19) and (Fig.IV.2.20), we observe a significant and remarkable increase in the real (ε') and imaginary (ε") relative permittivity figures for frequencies of 100 kHz, 10 kHz, and 1 kHz, and a lesser increase for frequencies of 500 Hz and 100 Hz. This increase is associated with the phenomenon of electrode polarization.

From table (IV.2.6), the activation energy for different frequencies of the binary ionic liquid 25% [EtOHVIM] 75% [ETOHMIM][H_2PO_4] is measured from the conductivity for the five frequencies. Determined by the Arrhenius equation.

Fréquence (HZ)	**100**	**500**	**1000**	**10000**	**100000**
Ea(eV)	4.57×10^{-2}	4.42×10^{-2}	6.74×10^{-2}	7.49×10^{-2}	6.77×10^{-2}

Table (IV.2.6): *the activation energy for different frequencies of ionic liquid 25% [EtOHVIM]Cl and 75% [ETOHMIM][H2PO4].*

The average activation energy: $E_{amoy} = 5.998\times 10^{-2}$eV.

IV.2.3.6 Comparison of individual and binary ionic liquids

The comparison of the logarithmic conductivity as a function of the inverse temperature and for a single frequency (100 KHz) showed that a binary liquid is always better than an individual liquid, regardless of the proportion of either liquid. This is shown in the figure. IV.2.22.

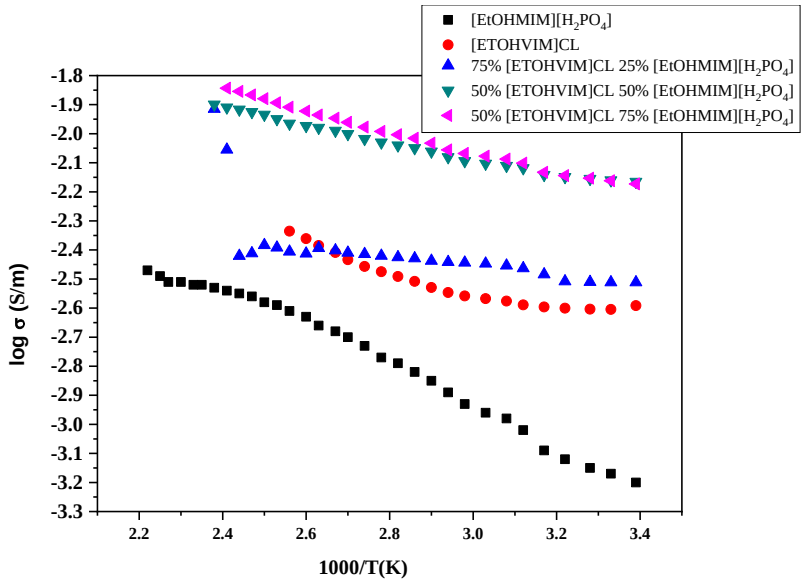

Figure.IV.2.22 : *The comparison of the variation in conductivity as a function of temperature LI and LI Binary 100 KHz.*

LI ou LI binaire	*[ETOHMIM][H₂PO₄]*	*[ETOHVIM]Cl*	*25% [ETOHMIM][H₂PO₄]*	*50 % [ETOHMIM][H₂PO₄]*	*75 % [ETOHMIM][H₂PO₄]*
E_a *(eV)*	1.03×10^{-1}	7.62×10^{-2}	5.10×10^{-2}	5.12×10^{-2}	6.77×10^{-2}

Table (IV.2.7): *The activation energy of the comparison between ionic liquid and binary ionic liquid.*

The comparison of activation energies confirms our observation, and it is deduced that binary ionic liquids possess the lowest activation energy and, therefore, a high electrical conductivity.

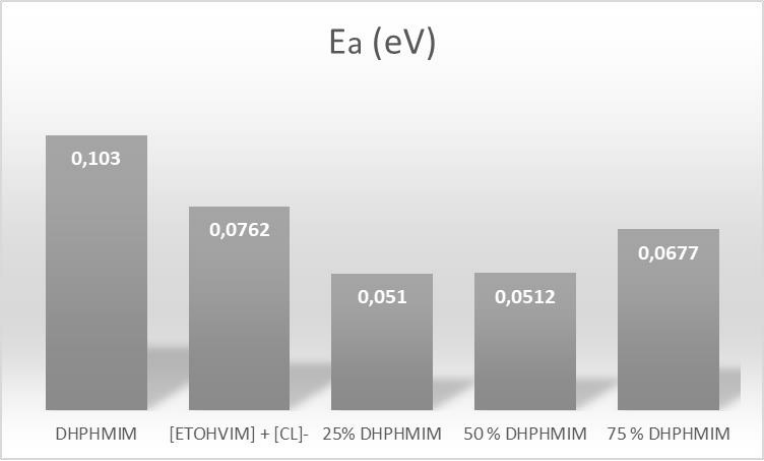

Figure.IV.2.21: *Comparison diagram of the activation energy of ionic liquids and binary ionic liquids.*

CONCLUSION

The relaxation dynamics and direct current conductivities of all the mixtures studied in this work lie between those of the original ionic liquids. The analysis of the glass transition, temperatures, and in-depth evaluations of the measured dielectric permittivity and conductivity spectra reveal that the dynamics in the ionic liquid mixtures are well-defined by the fractions of their composed parent molecules.

We provide the activation energy revealed by dielectric spectroscopy of the two individual ionic liquids [EtOHVIM]Cl and [ETOHMIM][H_2PO_4] and their binary mixture [EtOHVIM]Cl + [ETOHMIM][H_2PO_4], corresponding to the weighted average of their parent compounds. Moreover, the dielectric properties of the mixture mimic those of the parent compounds, exhibiting relaxation dynamics and conductivities exactly between them. It is observed in all cases that the conductivity of a binary mixture is higher than that of an individual ionic liquid.

IV.3 High ionic conductivity for ionic and poly ionic liquids based on 1-(hydroxyethyl)-3-vinylimidazolium cation

For the purpose of this study, our previous research reviewed the chemical and thermal properties of poly(1-hydroxyethyl-3-vinylimidazolium) chloride [P-EtOHVIM]Cl, poly(1-hydroxyethyl-3-vinylimidazolium) hydrogen sulfate [P-EtOHVIM][HSO_4], and 1-hydroxyethyl-3-vinylimidazolium chloride [EtOHVIM]Cl, focusing on their synthesis, thermal behavior, and vibrational characteristics [29]. The findings revealed that the [P-EtOHVIM][HSO_4] as a PIL with an asymmetric acidic anion exhibits notable thermal characteristics, including a high degradation temperature, good thermal stability, and a low glass transition temperature compared to [P-EtOHVIM]Cl. It is worth mentioning that the anion's contribution significantly affects both the compound's vibrational behavior and thermal stability. However, their dielectric properties' broader impact has not been previously documented. In addition, a new ionic liquid, 1-(hydroxyethyl)-3-methylimidazolium dihydrogen phosphate [EtOHMIM][H_2PO_4], was synthesized and characterized by Zaoui et al. [31]. The study demonstrated that the [H_2PO_4] anion plays a crucial role in enhancing the thermal stability of the compound, while also contributing to its distinctive vibrational and thermal properties. To further explore the role of [H_2PO_4] as an asymmetric acidic anion in poly(1-hydroxyethyl-3-vinylimidazolium)-based PILs, as well as the influence of the [HSO_4] asymmetric acidic anion in 1-hydroxyethyl-3-vinylimidazolium monomeric ionic liquids MILs, the present study was conducted. Firstly, an anion exchange reaction was performed on poly(1-hydroxyethyl-3-vinylimidazolium) chloride [P-EtOHVIM]Cl, resulting in the formation of poly(1-hydroxyethyl-3-vinylimidazolium) dihydrogen phosphate [P-EtOHVIM][H_2PO_4]—a second polymeric ionic liquid (PIL) containing an asymmetric acidic anion. Secondly, an anion exchange reaction on 1-hydroxyethyl-3-vinylimidazolium chloride [EtOHVIM]Cl yielded 1-hydroxyethyl-3-vinylimidazolium hydrogen sulfate [EtOHVIM][HSO_4].

IV.3.1. Synthesis of [EtOHVIM][HSO_4]

According to (Scheme. IV.3.1.a), Synthesis and characterisation of [EtOHVIM]Cl followed prior protocols [29].

With an anion exchange reaction, [EtOHVIM][HSO_4] was synthesized by combining sulfuric acid H_2SO_4 (0.56 mL, 10 mmol) and [EtOHVIM]Cl (5.0 g, 10 mmol); a slow addition was maintained to prevent excessive heat generation and unwanted side reactions. The mixture was stirred vigorously in 30 mL of acetonitrile at room temperature for 24 h (Scheme IV.3. 1.b).

After that, acetonitrile was removed under reduced pressure, and the crude product was rinsed with diethyl ether (3 x 30 mL) to eliminate unreacted components and byproducts. The final ionic liquid was obtained by vacuum drying at reduced pressure for 3 hours to remove residual solvents.

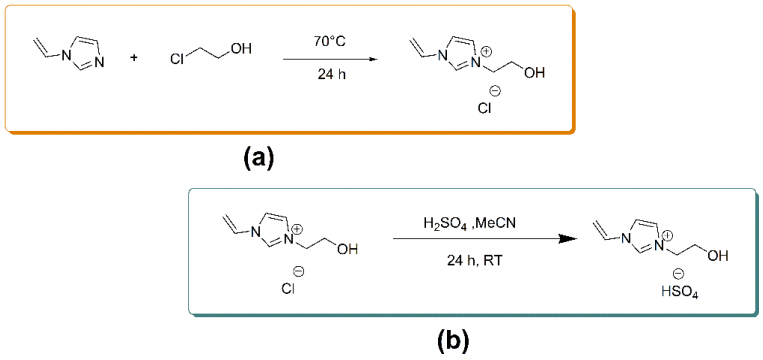

Scheme.IV.3.1. *(a) Amine quaternization and (b) Anion exchange reactions.*

IV.3.2. Polymerization of [P-EtOHVIM][H_2PO_4]

According to scheme (2.a.b) , [P-EtOHVIM]Cl and [P-EtOHVIM][HSO_4] were synthesized and characterized according to procedures reported previously [29] .

For the preparation of [P-EtOHVIM][H_2PO_4] (Scheme IV.3.2.a.b) via an anion exchange reaction, a combination of [P-EtOHVIM]Cl (10 mmol, 1.82 g) and concentrated phosphoric acid (10 mmol, 0.53 mL), was vigorously agitated at room temperature for 48 hours. After completion of the reaction, contaminants were removed by washing the crude product with acetone.

To minimize water continuous agitation under vacuum conditions (≈10) at 70 °C for several hours.

For optimal preparation and complete drying, the product was further dried under a high vacuum (pressure < 10^{-5} bar) and approximately 40 °C for two days. Finally, any residual moisture was removed using phosphorus pentoxide (P_2O_5) as a drying agent.

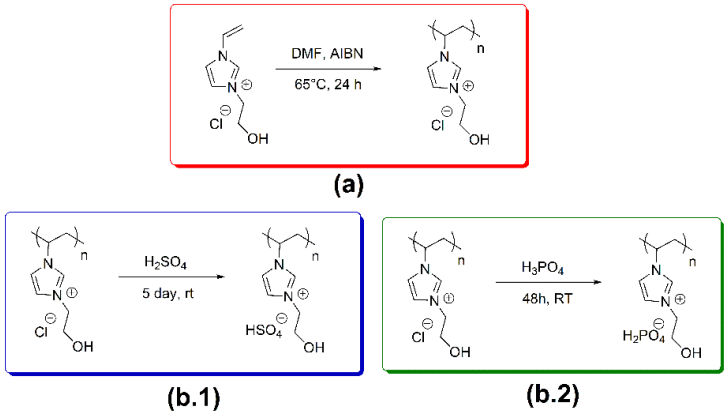

Scheme IV.3. 2. *(a) Polymerization and (b.1) (b.2) anion exchange reactions.*

IV.3.3 Thermal Behavior of [EtOHVIM][HSO_4] and [P-EtOHVIM][H_2PO_4]

The thermal properties of the synthesized ionic liquids were investigated using Differential Scanning Calorimetry (DSC) and Thermogravimetric Analysis (TGA/DTG).

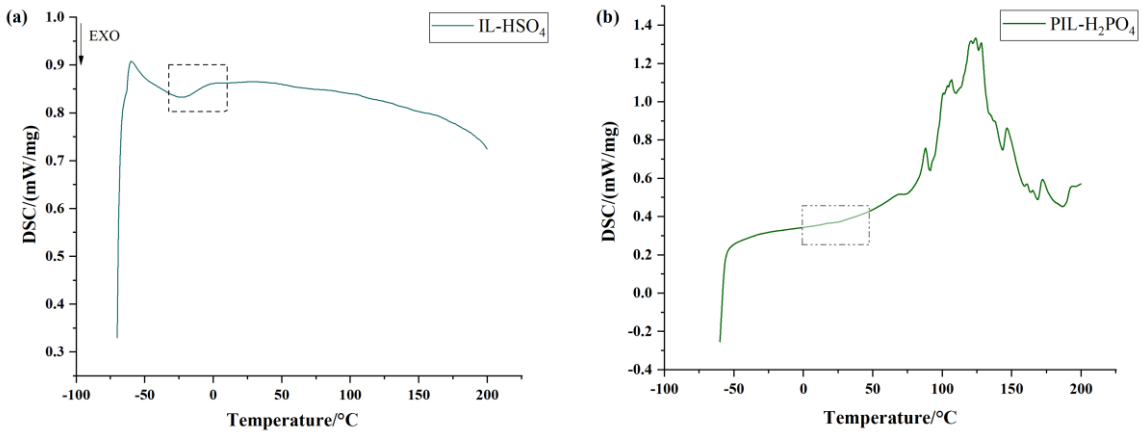

Figure IV.3.2. *(a) DSC thermogram of [EtOHVIM][HSO_4] and (b) [P-EtOHVIM][H_2PO_4] from -60 °C to 200* °C.

For [EtOHVIM][HSO_4] (Fig. IV.3. 2.a) showed a step change in heat flow corresponding to a glass transition temperature T_g = -8.5 °C, with no corresponding endothermic peak, indicating the absence of a defined melting point.

In the case of [P-EtOHVIM][H_2PO_4] (Fig. IV.3.2.b), T_g was detected at approximately 20 °C. Notably, the glass transition temperatures (T_g) for both compounds were determined from the second heating scan in the DSC measurements, which eliminated the effects of thermal history to ensure reliable data. Furthermore, [P-EtOHVIM][H_2PO_4] decomposition is characterized by a peak at 124 °C observed in the heating phase corresponding to the melting point (T_m). A similar peak at 146 °C marks a significant step in its decomposition process. However, an additional endothermic peak at 172 °C, observed in the DSC curve, indicates the

complete decomposition of this poly ionic liquid. Finally, an exothermic peak was observed at 186 °C.

Fig IV.3.3. displays the TGA and DTG curves of [EtOHVIM][HSO_4] and [P-EtOHVIM][H_2PO_4].

Fig IV.3.3.a, [EtOHVIM][HSO_4]. This IL degrades in two phases between 20 °C and 400 °C, with decomposition starting at 50 °C remaining stable below this temperature. The first degradation stage, which proximately began at 50 °C and ended at 150 °C, resulted in a 3.53% mass loss, corresponding to the removal of H_2O gas. The IL imidazolium cation decomposed in the second step, which began at 163 °C and finished at around 390 °C, resulting in a mass loss of 61.92% due to dealkylation and degradation.

Fig IV.3.3.b, [P-EtOHVIM][H_2PO_4]. This PIL remains stable below 50 °C, and the degradation process started after this temperature and progressed in four phases until 600 °C. The first stage, begins at approximately 50 °C with a mass loss of 15.58 %, concluding at 150 °C, corresponding to the release of H_2O gas recognized from the TG mass spectrometry curve (fig. S4) due to dehydration processes or volatile solvents [32]. The decomposition of organic functional groups (loss of 4.91%) started at 180 °C and finished around 260 °C. The third stage, which occurred between 250 and 350 °C, with a loss of 11.63% associated with the dealkylation degradation of the IL imidazolium cation. Final decomposition is the major decomposition of dihydrogen phosphate anion at 350 °C. In addition, temperatures greater than 600 °C are required for the poly ionic liquid (H_2PO_4) to completely decompose thermally. Ultimately, the [P-EtOHVIM][H_2PO_4] demonstrated initial thermal stability up to approximately 50 °C, beyond which weight loss begins with a residual weight of ~ 35% was observed, and multiple degradation steps that suggest complex thermal decomposition behavior, which is characteristic of polyionic liquids with interact molecular architecture.

The water loss can be attributed to the hydrophilic characteristic of this PIL [33]. This hydrophilicity depends on its constituent ions' nature and ability to interact with water molecules [34, 35]. In more detail for this case, the dihydrogen phosphate anion [H_2PO_4] anion contains two -OH groups, allowing extensive hydrogen bonding with both water and polymer side chains [36, 37]. This capability often indicates higher water retention, more hydrated structure and, certain level of hydrophilicity. Therefore, [P-EtOHVIM][H_2PO_4] can be considered as a hydrophilic ionic liquid.

At high temperatures, the [P-EtOHVIM][H_2PO_4] ability to decompose is limited by the development of a robust P–O···H–O–P network. Additionally, [P-EtOHVIM][H_2PO_4] and

[EtOHVIM][HSO_4] with hydrogen bonding networks have greater decomposition temperatures and superior mechanical stability as compared to those that mainly depend on van der Waals interactions [38].

DSC and Thermogravimetric analysis showed that [EtOHVIM][HSO_4] and [P-EtOHVIM][H_2PO_4] compared with MILs and PILS investigated in this study possess low glass transition temperature, a good thermal stability, and decomposition at higher temperatures. Furthermore, it must be noted that the chain polymerization and the type of anion significantly impacted thermal stability [39, 40].

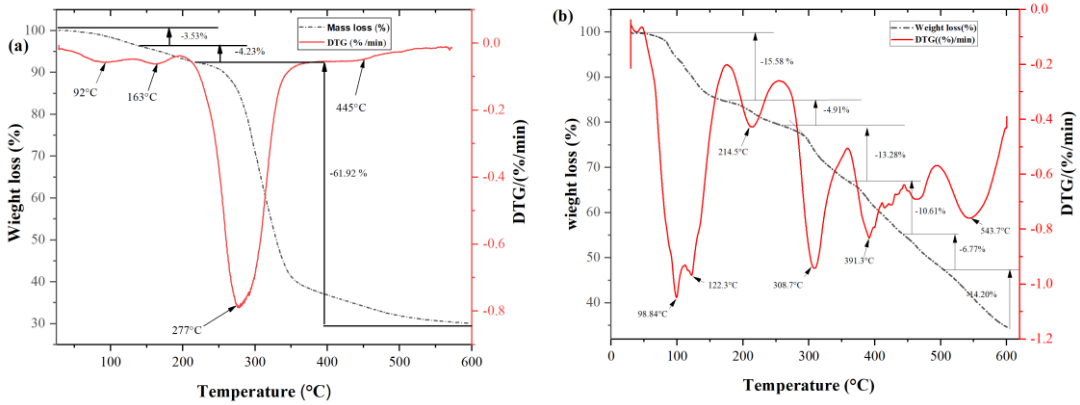

Figure IV.3.3. *(a) TGA and DTG curves of [EtOHVIM][HSO_4] and (b) [P-EtOHVIM][H_2PO_4] from 20°C to 600* °C.

IV.3.4. Dielectric and Conductivity Behavior of Polymeric and Monomeric Ionic Liquids

Broadband dielectric spectroscopy (BDS) is ideally suited to compare and examine the dielectric properties of three polymeric ionic liquids [P-EtOHVIM][H_2PO_4], [P-EtOHVIM]Cl, [P-EtOHVIM][HSO_4] and two monomeric ionic liquids [EtOHVIM][HSO_4], [EtOHVIM]Cl with systematically varied anion composition. The research is centered on analysing of conductivity and dielectric relaxation processes in the frequency range of 10^{-2} to 10^{6} Hz.

The molecular dynamics and charge transport mechanism of the MILs and PILs under study are investigated using BDS spectroscopy. The BDS spectrum is characterised by a superposition of the real and imaginary components of the complex dielectric function ($\varepsilon^* = \varepsilon' - i\varepsilon''$) and the complex conductivity ($\sigma^* = \sigma' + \sigma''$), as shown in Fig. IV.3.4.

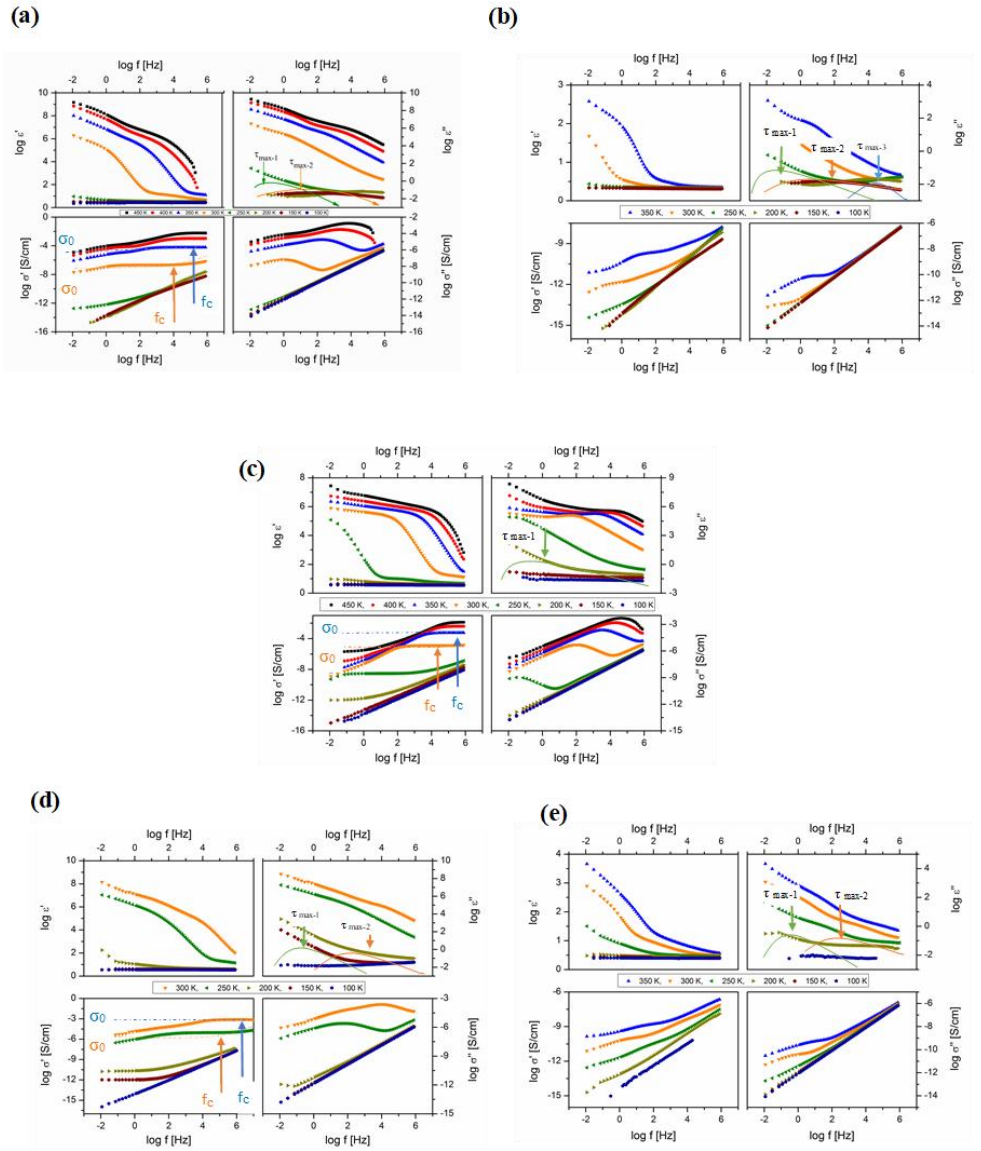

Figure IV.3. 4. *Complex dielectric function (ε*=ε'(f)-iε''(f)) and complex conductivity function (σ*= σ'(f) + iσ''(f)) of (a) [EtOHVIM]Cl, (b) [P-EtOHVIM]Cl, (c) [P-EtOHVIM][H_2PO_4] (d) [EtOHVIM][HSO_4] and (e) [P-EtOHVIM][HSO_4], at different temperatures as indicated. Havriliak-Negami-function analysis using mean relaxation durations* τ_{max-1} *(green line),* τ_{max-2} *(orange line), and* τ_{max-3} *(blue line) reveals dielectrically active relaxation processes reflecting molecular dynamics in ε'' vs. f. Charge transfer is defined by DC-conductivity* σ_0 *and critical frequency* $\omega_c = 2\pi fc$. *The first is a plateau in* σ_0 *vs. f, whereas the second is the frequency necessary to overcome the highest DC-conductivity barrier, indicating a power law dependency* $\sigma_0 \sim \omega_\chi$. *The Dyre-function (dashed-dotted lines) analyzes* σ_0 *and* ω_c *in* σ_0 *vs. f.*

This analysis identified and described a combination of phenomena, including (i) electrode polarization (EP), (ii) conductivity or charge transport, and (iii) molecular relaxation processes [41-46].

Particularly remarkable at elevated temperatures and low frequencies, electrode polarization

(EP) is identified by a significant rise in ε' or σ" versus frequency. This surge indicates the gathering of mobile charges, whether ionic or polaronic, at the interface connecting the sample and the electrode. Therefore, the surge mentioned above may reflect the contribution of both

ionic and polaronic carriers to the overall charge accumulation at the electrode interface in the case of polyionic liquids [41, 47, 48]. In contrast, for monomeric ionic liquids (MILs), electrode polarization arises solely from the accumulation of ionic charge carriers. The distinct elevation in low-frequency behavior, especially in MILs, highlights the intricate nature of polymeric ionic liquids. The rationale behind this observation is rooted in the notion that the movement of charge carriers is considerably impeded or slowed down at the interface between the metal and the ionic conductor due to coulombic interactions [49].This phenomenon is characteristic of polar dielectrics, as the temperature rise facilitates dipole orientation, leading to an augmentation in permittivity [50]. Although electrode polarization (EP) is generally more prominent in monomeric ionic liquids (MILs) than in polymeric ionic liquids (PILs), [EtOHVIM]Cl exhibits strong EP, particularly at elevated temperatures, due to the small and highly mobile Cl anion, which facilitates interfacial charge accumulation. In contrast, [P-EtOHVIM]Cl shows reduced EP, as polymerization restricts ion mobility and space charge formation. A similar trend is observed for [P-EtOHVIM][HSO_4] (Fig. IV.3.4c), while its monomeric counterpart [EtOHVIM][HSO_4] (Fig. IV.3.4d) displays pronounced and rapid EP. Interestingly, [P-EtOHVIM][H_2PO_4], despite being a PIL, exhibits strong EP comparable to the monomeric ILs, likely due to enhanced ion transport associated with its hydrophilic character.

Concerning charge transport (ii), the dielectric spectra revealed one or more relaxation processes characterized by a distinct plateau in σ' versus frequency. This plateau represents the DC-conductivity σ_0 and the critical frequency ω_c, which marks the onest of a power-law relationship $\sigma' \sim \omega^x$. The frequency ω_c is interpreted as the crucial hopping rate of mobile charge carriers that contribute to σ_0 to overcome the highest potential barrier [41, 51]. (iii) Dielectric active relaxation processes provide information on the dynamics of molecules. The mean structural relaxation times $\omega_{max} = \tau_{max}^{-1}$ could be precisely found by examining ε"(f). Energy dissipation is shown by the graph's characteristic peaks, which must be analysed using the empirical Havriliak–Negami formula [52], which builds upon the Debye formula by incorporating two extra shape parameters, β, and γ [53].

Plotting the latter as a function of the inverse temperature 1000/T (Fig IV.3.5) allows us to find the temperature dependency of two somewhat separated, hence independent, processes. For all MILs and PILs, one observes a transition of σ_0 and τ_{max-1} in its thermal activation from VFT-like eq (1) to an Arrhenius-law by decreasing temperatures eq (IV.3.2)

$$\tau = \tau_\infty \, exp\left(\frac{DT_0}{T - T_0}\right) \qquad (IV.3.1)$$

Where, τ_∞ represents the relaxation time at high temperatures, D is a shape constant commonly known as the fragility index, and T_0 is the Vogel temperature.

$$\tau = \tau_0 exp\left(\frac{E_a}{k_b T}\right) \qquad (IV.3.2)$$

Where, τ_0 pre- exponential factor, E_a activation energy, R gas constant, and T absolute temperature.

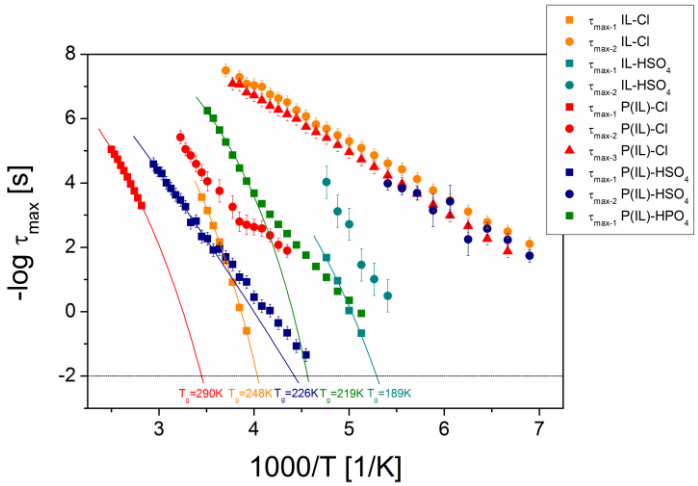

Figure. *IV.3.5.* Activation plot for all investigated samples. The presumably α-relaxations (τ_{max-1}) are depicted in squares, the secondary ones in circles and for [P-EtOHVIM]Cl one additional in triangles. The first ones are fitted with Vogel-Fulcher-Tammann functions; the extrapolated glass transition temperatures are indicated. The error-bars are comparable to the size of the symbols, if not explicitly indicated otherwise. The logarithm is to base 10.

The calorimetric glass transition temperature T_g, calculated by conventional DSC, scales well with the average structural relaxation time τ_{max-1} associated with the dynamic glass transition, as measured by BDS (Table IV.3.3). The sample [P-EtOHVIM][H_2PO_4] exhibits a glass transition temperature (T_{g-BDS}) of 219 by almost 7 K less than the value of [P-EtOHVIM][HSO_4] and 81 K less than [P-EtOHVIM][Cl].

These differences in T_{g-DSC} so T_{g-BDS} values can be attributed to several factors: (i) Reduced segmental mobility in the polymer, due to its maximal involvement in hydrogen bonding, increases the glass transition temperature (T_g) [54]. The Kamlet–Taft β parameter indicates the hydrogen-bonding capabilities of various anions and can be used to understand their effects on the T_g of polymers. Chloride anion (Cl^-), as a small monatomic halide anion with high charge density, with a high β (0.84–0.95) value exhibits strong hydrogen-bonding accepting ability [55-57], leading to strong interactions with cations, which restrict ion mobility and segmental motion, thereby raising T_g. On the other hand, hydrogen sulfate [HSO_4] and dihydrogen phosphate [H_2PO_4] function as asymmetric acidic anions with a moderate β value (~0.30–0.60)

[58-60]. Their ability to interact with multiple but distant H-bond donor sites within the same cation results in a qualitative change in the H-bonding structures [61]. Such moderate hydrogen-bond basicity allows partial interaction with the cation, while their acidic hydrogen atoms can simultaneously act as hydrogen-bond donors [62], facilitating interionic cross-linking [63]. This dual donor–acceptor character reduces polymer chain mobility, leading to low-to-intermediate T_g values compared to the Cl^- anion. (ii) differences in hydrophilicity degree - reflected in the residual water contents as determined by DSC and DTG analysis, (iii) and potentially different molecular weights which can influence segmental dynamics.

Moreover, the other mean relaxation rates are thermally Arrhenius-like activated, where the τ_{max-2} for [EtOHVIM]Cl and [P-EtOHVIM][HSO_4], as well as τ_{max-3} for [P-EtOHVIM]Cl, are similar, which indicates the same molecular origin, which is attributed to the liberation of the imidazolium ion with a mean activation energy E_a = 0.064 eV. The absence of secondary relaxation processes in [P-EtOHVIM][H_2PO_4], combined with a fragility index (D=13.38), indicates that the polymer exhibits relatively strong glass-forming behavior. Besides the structural relaxation processes, the charge transport follows the Barton-Namikawa-Nakajima (BNN) relation, which relates the DC-conductivity σ_0 with the charge carrier hopping rate ω_0. This correlation holds accurate for all MILs and PILs over up to 9 orders of magnitudes (Fig. 6). Additionally, there is a correlation between the charge carrier hopping rate ω_c and the mean structural relaxation time τ_{max-1}, this indicates a 'dynamic glass transition assisted hopping' conduction [43, 45, 64-68].

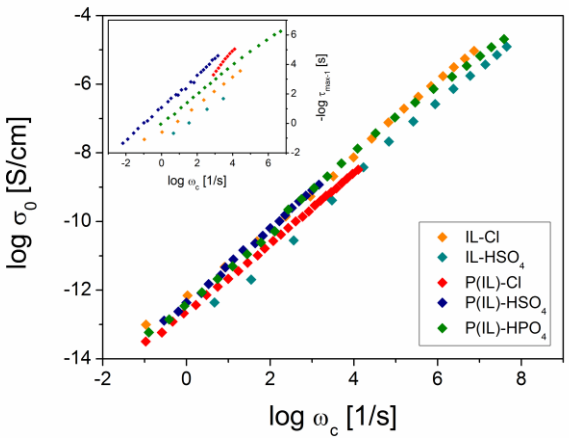

Figure. *IV.3.6.* Barton-Namikawa-Nakajima (BNN)-relation of the DC-conductivity σ0 and the charge carrier hopping rate ωc for all samples as indicated. Inset: correlation between the latter and the structural mean relaxation rate that is presumably assigned to the fluctuation of transient ion-pairs. The error-bars are comparable to the size of the symbols, if not explicitly indicated otherwise. The logarithm is to base 10.

On the one hand, the thermal activation of [P-EtOHVIM]Cl and [P-EtOHVIM][HSO_4] tends to be lower than their monomeric counterparts at absolute temperatures. This difference is evident in the higher values of T_g observed at a macroscopic level (Fig. IV.3.7). As was anticipated, [EtOHVIM][HSO_4] as a MIL with an asymmetric acidic anion shows an a VFT-type thermal activation above T_g with the highest direct current (DC) conductivity (σ_{RT} = 5.53 x 10^{-4} S·cm^{-1}) among the investigated ionic liquids in this study (Table 3). For [P-EtOHVIM][H_2PO_4], the only investigated poly ionic that shows a noticeable shift in the thermal activation of σ_0 ($T_{\sigma 0}$). This shift can be observed in Fig. IV.3.7, where the dependence changes from a VFT-like behavior to an Arrhenius-law. $T_{\sigma 0}$ = 263 K was found to be close to the calorimetric glass transition T_g= 253 K.

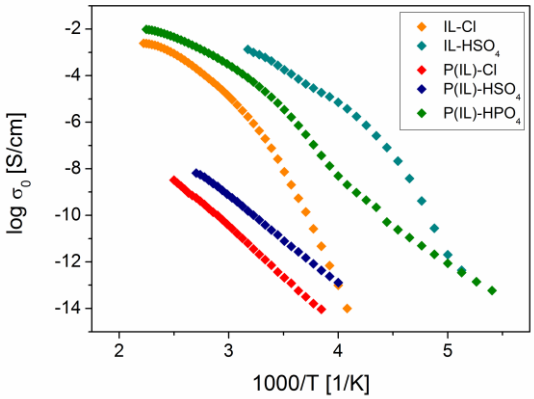

Figure IV.3. 7. Temperature-dependence of the DC-conductivity. For MILs and PILs one observes a transition at which its thermal activation changes from a VFT-law to an Arrhenius one. The error-bars are comparable to the size of the symbols, if not explicitly indicated otherwise. The logarithm is to base 10.

Furthermore, [P-EtOHVIM][H_2PO_4] shows a comparably high DC-conductivity, which exhibits an ionic conductivity of σ_{RT} = 1.99 x10^{-5} S·cm^{-1} (approaching the highest possible polymer ionic liquid conductivity of approximately ≈10^{-5} S·cm^{-1} at 25 °C, as reported by [69]), this is remarkable for such an asymmetric acidic anion poly ionic liquid.

Temperature	$T_{g\text{-}DSC}$ *(K)*	$T_{g\text{-}BDS}$ *(K)*	σ_{RT} *(S·cm^{-1})*	E_a *(eV)*	T_0 *(K)*	*D*
[P-EtOHVIM]Cl	355[29]	290	1.46E–12	0.371	-------	--------
[P-EtOHVIM][HSO_4]	260[29]	226	3.54E–11	0.331	--------	--------
[EtOHVIM][Cl]	---------	248	2.04E–07	0.076	188.51	10.81
[P-EtOHVIM][H_2PO_4]	293	219	1.99E–05	0.077	154.53	13.38
[EtOHVIM][HSO_4]	265	189	5.53E–04	0.038	163.61	6.18

Table. IV.3.3 Comparison of the glass transition temperatures T_g as measured by DSC and extrapolated by BDS. VFT and Arrhenius-law equation regression values of temperature-dependent conductivity data of all MILs and PILs under study.

CONCLUSION

The anionic contribution of asymmetric hydrogen sulfate and dihydrogen phosphate for novel acidic ionic and polyionic liquids based on 1-(hydroxyethyl)-3-vinylimidazolium cation was comprehensively studied. The synthesis of [P-EtOHVIM][H_2PO_4], a polymeric ionic liquid and [EtOHVIM][HSO_4] as a monomeric ionic liquid were investigated using a range of techniques, including ^{1}H ^{13}C NMR, FTIR/ATR, DSC, and TGA, DTG.

These compounds exhibited interesting thermal and dielectric properties. (i) Thermal analysis revealed that both ionic liquids possess a good thermal stability and low glass transition temperature. [P-EtOHVIM][H_2PO_4] was identified as a hydrophilic polymeric ionic liquid with decomposition at higher temperatures. Furthermore, it must be noted that both chain polymerization, the type of acidic anion, leads to strong hydrogen bonds and a level of hydrophilicity; these effects significantly impact thermal stability. (ii) Dielectric analysis showed that [EtOHVIM][HSO_4], a MIL with an asymmetric acidic anion, exhibits a significant direct current (DC) conductivity and follows a VFT-type thermal activation behavior above Tg. The notable behaviors of the [P-EtOHVIM][H_2PO_4], such as hydrophilicity, a moderate thermal stability, the substantial impact of anion structure on glass transition temperature, and the hydrogen bonding networks, a transition from Vogel-Fulcher-Tammann to Arrhenius-type conductivity dependence at a characteristic temperature $T_{\sigma 0}$ all this proprieties alongside a significantly high ionic conductivity. In conclusion, [P-EtOHVIM][H_2PO_4] and [EtOHVIM][HSO_4] displayed, comparatively within the studied monomeric and polymeric ionic liquids, the highest ionic conductivity, making them good candidates for solid-acid electrolytes in electrochemical devices or as proton exchange membranes.

BIBLIOGRAPY

1. Clough, M.T., et al., A physicochemical investigation of ionic liquid mixtures. 2015. **6**(2): p. 1101-1114.
2. Castiglione, F., et al., Blending ionic liquids: how physico-chemical properties change. 2010. **12**(8): p. 1784-1792.
3. Huang, Y., et al., New models for predicting thermophysical properties of ionic liquid mixtures. 2015. **17**(40): p. 26918-26929.
4. Karakatsani, E.K., et al., Equation of state modeling of the phase equilibria of ionic liquid mixtures at low and high pressure. 2008. **10**(40): p. 6160-6168.
5. Bandlamudi, S.R., et al., Understanding liquid–liquid equilibria in binary mixtures of hydrocarbons with a thermally robust perarylphosphonium-based ionic liquid. 2021. **11**(50): p. 31328-31338.
6. Wang, R. and Z.-G.J.T.J.o.c.p. Wang, Effects of ion solvation on phase equilibrium and interfacial tension of liquid mixtures. 2011. **135**(1).
7. Niedermeyer, H., et al., Mixtures of ionic liquids. 2012. **41**(23): p. 7780-7802.
8. Bostwick, J.E., et al., Ionic interactions control the modulus and mechanical properties of molecular ionic composite electrolytes. 2022. **10**(3): p. 947-957.
9. Özekes, S., O.J.I.-J.o.E. Osman, and E. Engineering, Classification and prediction in data mining with neural networks. 2003. **3**(1): p. 707-712.
10. Agyapong, K.B., et al., An overview of data mining models (Descriptive and predictive). 2016. **4**(5): p. 53-60.
11. Vicente-Gonzalez, L. and J.L.J.M. Vicente-Villardon, Partial least squares regression for binary responses and its associated biplot representation. 2022. **10**(15): p. 2580.
12. Guettaf, H., et al., The study of dielectric properties of some ionic liquids based on imidazolium by dielectric spectroscopy and data mining. 2016. **83**: p. 1044-1049.
13. Sehgal, S., et al. Data analysis using principal component analysis. in 2014 International Conference on Medical Imaging, m-Health and Emerging Communication Systems (MedCom). 2014. IEEE.
14. Geladi, P. and B.R.J.A.c.a. Kowalski, Partial least-squares regression: a tutorial. 1986. **185**: p. 1-17.
15. Saidi, F., et al., Structural and mechanical properties of Laves phases YCu2 and YZn2: First principles calculation analyzed with data mining approach. 2014. **89**: p. 176-181.
16. Saidi, F., et al., Structural electronic and mechanical properties of YM2 (M= Mn, Fe, Co) laves phase compounds: first principle calculations analyzed with datamining approach. 2018. **274**: p. 9-20.
17. Sekkal, A., et al., Structural and physical properties of DyCu, NdAg, LaCd, YIn, ErCu, ErAg, and ErAu rare-earth intermetallic compounds: ab initio investigations analyzed by data mining technique. 2020. **62**: p. 2305-2317.
18. Ouadah, O., et al., Influence of alloying transition metals on structural, elastic, electronic and optical behaviors of γ-TiAl based alloys: a comparative DFT study combined with data mining technique. 2020. **242**: p. 122455.
19. Leys, J., et al., Temperature dependence of the electrical conductivity of imidazolium ionic liquids. 2008. **128**(6).
20. Wu, J., et al., Progress on the electrolytes for dye-sensitized solar cells. 2008. **80**(11): p. 2241-2258.
21. Shin, E.-C., et al., Chemometric approach to fatty acid profiles in Runner-type peanut cultivars by principal component analysis (PCA). 2010. **119**(3): p. 1262-1270.

22. Rajan, K.J.M.T., Materials informatics. 2005. **8**(10): p. 38-45.
23. Jolliffe, I., Principal component analysis, in International encyclopedia of statistical science. 2011, Springer. p. 1094-1096.
24. Emmert, S., et al., Electrode polarization effects in broadband dielectric spectroscopy. 2011. **83**(2): p. 157.
25. MacDonald, J.R.J.J.o.e.c. and i. electrochemistry, Comparison and discussion of some theories of the equilibrium electrical double layer in liquid electrolytes. 1987. **223**(1-2): p. 1-23.
26. Serghei, A., et al., Broadband dielectric spectroscopy on electrode polarization and its scaling. 2012: p. 241-273.
27. Macedo, P., M. CT, and R. Bose, The role of ionic diffusion in polarisation in vitreous ionic conductors. 1972.
28. Ito, N. and R.J.T.J.o.c.p. Richert, Effect of dispersion on the relaxation-retardation time scale ratio. 2005. **123**(10).
29. Chaker, Y., et al., The influence of chloride and hydrogen sulfate anions in two polymerised ionic liquids based on the poly(1-(hydroxyethyl)-3-vinylimidazolium cation, synthesis, thermal and vibrational studies. European Polymer Journal, 2018. **108**: p. 138-149.
30. Paluch, M., Dielectric properties of ionic liquids. 2016: Springer.
31. Zaoui, T., et al., Synthesis, vibrational and thermal properties of new functionalized 1- (2-hydroxyethyl) -3-methylimidazolium dihydrogenophosphate ionic liquid. Journal of Molecular Structure, 2021. **1236**: p. 130264.
32. Ping, Z., et al., States of water in different hydrophilic polymers—DSC and FTIR studies. 2001. **42**(20): p. 8461-8467.
33. Fernandes, L.C., et al., Ionic-liquid-based printable materials for thermochromic and thermoresistive applications. 2019. **11**(22): p. 20316-20324.
34. Mikkelsen, R.L.J.F.r., Using hydrophilic polymers to control nutrient release. 1994. **38**: p. 53-59.
35. Bayliss, N. and B.V.K.J. Schmidt, Hydrophilic polymers: Current trends and visions for the future. Progress in Polymer Science, 2023. **147**: p. 101753.
36. Rodrigues, R.F., et al., Ionic Liquids and Water: Hydrophobicity vs. Hydrophilicity. Molecules, 2021. **26**(23).
37. Yousefi, M., et al., Synthesis and characterization of physicochemical properties of hydrophilic imidazolium-based ionic liquids. 2017. **34**: p. 2527-2535.
38. Yankova, R. and I. Tankov, Hydrogen bonding effect on the thermal behavior of acidic ionic liquids. Journal of Molecular Structure, 2021. **1238**.
39. Casimiro, A. and K. Nijmeijer, On the impact of the type of anion on the properties of solid-state electrolytes. Polymer, 2022. **262**: p. 125443.
40. Cao, Y. and T. Mu, Comprehensive Investigation on the Thermal Stability of 66 Ionic Liquids by Thermogravimetric Analysis. Industrial & Engineering Chemistry Research, 2014. **53**(20): p. 8651-8664.
41. Kremer, F. and A. Schönhals, Broadband dielectric spectroscopy. 2002: Springer Science & Business Media.
42. Anton, A.M., et al., Hydrogen bonding and charge transport in a protic polymerized ionic liquid. Soft Matter, 2020. **16**(26): p. 6091-6101.
43. Frenzel, F., et al., Charge transport and glassy dynamics in polymeric ionic liquids as reflected by their inter- and intramolecular interactions. Soft Matter, 2019. **15**(7): p. 1605-1618.
44. Chen, S., et al., Gating effects of conductive polymeric ionic liquids. Journal of Materials Chemistry C, 2018. **6**(30): p. 8242-8250.

45. Frenzel, F., et al., Molecular Dynamics and Charge Transport in Highly Conductive Polymeric Ionic Liquids. Macromolecules, 2017. **50**(10): p. 4022-4029.
46. Frenzel, F., et al., Molecular Dynamics and Charge Transport in Polymeric Polyisobutylene-Based Ionic Liquids. Macromolecules, 2016. **49**(7): p. 2868-2875.
47. Gao, T., et al., Polarization of ionic liquid and polymer and its implications for polymerized ionic liquids: An overview towards a new theory and simulation. 2021. **59**(21): p. 2434-2457.
48. Emin, D., Polarons. 2013: Cambridge University Press.
49. Serghei, A., et al., Electrode polarization and charge transport at solid interfaces. Physical Review B, 2009. **80**(18).
50. Mohan, V., et al., Electrical properties of poly (vinyl alcohol)(PVA) based on LiFePO 4 complex polymer electrolyte films. 2010. **17**: p. 143-150.
51. Dyre, J.C. and T.B.J.R.o.M.P. Schrøder, Universality of ac conduction in disordered solids. 2000. **72**(3): p. 873.
52. Havriliak, S. and S.J.P. Negami, A complex plane representation of dielectric and mechanical relaxation processes in some polymers. 1967. **8**: p. 161-210.
53. Debye, P.J.L.H., Polare molekeln. 1929.
54. Kuo, S.-W.J.J.o.P.R., Hydrogen-bonding in polymer blends. 2008. **15**(6): p. 459-486.
55. Fukaya, Y., A. Sugimoto, and H. Ohno, Superior Solubility of Polysaccharides in Low Viscosity, Polar, and Halogen-Free 1,3-Dialkylimidazolium Formates. Biomacromolecules, 2006. **7**(12): p. 3295-3297.
56. Spange, S., R. Lungwitz, and A. Schade, Correlation of molecular structure and polarity of ionic liquids. Journal of Molecular Liquids, 2014. **192**: p. 137-143.
57. Sappl, M., et al., Decomposition, interpretation and prediction of various ionic liquid solvation parameters: Kamlet-Taft, Catalán and Reichardt's ETN. Journal of Molecular Liquids, 2025. **417**: p. 126646.
58. Debeljuh, N.J., et al., Phase Transition of Poly(N-isopropylacrylamide) in Aqueous Protic Ionic Liquids: Kosmotropic versus Chaotropic Anions and Their Interaction with Water. The Journal of Physical Chemistry B, 2013. **117**(28): p. 8430-8435.
59. Shukla, S.K., N.D. Khupse, and A.J.P.C.C.P. Kumar, Do anions influence the polarity of protic ionic liquids? 2012. **14**(8): p. 2754-2761.
60. Sulaimon, A.A., et al., Synthesis of dihydrogen phosphate-based ionic liquids: Experimental and COSMO-RS based investigation for methane hydrate inhibition. 2020. **319**: p. 114092.
61. Hunt, P.A., C.R. Ashworth, and R.P.J.C.S.R. Matthews, Hydrogen bonding in ionic liquids. 2015. **44**(5): p. 1257-1288.
62. Joshi, R. and T.K. Ghanty, Hydrogen bonding interaction between HO2 radical and selected organic acids, RCOOH (R=CH3, H, Cl and F). Chemical Physics Letters, 2013. **584**: p. 43-48.
63. Song, P. and H.J.A.M. Wang, High-performance polymeric materials through hydrogen-bond cross-linking. 2020. **32**(18): p. 1901244.
64. Frenzel, F., et al., Glassy Dynamics and Charge Transport in Polymeric Ionic Liquids, in Dielectric Properties of Ionic Liquids. 2016. p. 115-129.
65. Barton, J. and M.J.J.o.N.-C.S. Morain, Hydrogen diffusion in silicate glasses. 1970. **3**(1): p. 115-126.
66. Turton, D.A., et al., Structure and dynamics in protic ionic liquids: A combined optical Kerr-effect and dielectric relaxation spectroscopy study. 2012. **154**: p. 145-153.
67. Frenzel, F., et al., Molecular dynamics and charge transport in polymeric polyisobutylene-based ionic liquids. 2016. **49**(7): p. 2868-2875.
68. Sangoro, J., et al., Universal scaling of charge transport in glass-forming ionic liquids. 2009. **11**(6): p. 913-916.

69. Nosov, D.R., et al., Design of Highly Conductive PILs by Simple Modification of Poly (epichlorohydrin-co-ethylene oxide) with Monosubstituted Imidazoles. 2024. **4**(6): p. 512-526.

GENERAL CONCLUSION

GENERAL CONCLUSION

The present work has explored an original and innovative field of physicochemical research focused on imidazolium-based ionic liquids, materials that have attracted growing attention due to their unique thermal, electrical, and structural properties. Our study combined experimental dielectric analysis and data mining approaches to provide a comprehensive understanding of the dielectric behavior, charge transport mechanisms, and structure–property relationships of these materials.

In the first part, we employed data-driven modeling techniques, notably the Vogel–Fulcher–Tammann (VFT) equation, Partial Least Squares (PLS) regression, and Principal Component Analysis (PCA), to extract and interpret key information from experimental data. The PLS method, based on the VFT dielectric parameters of individual ionic liquids in our database, was successfully applied to predict the properties of binary ionic liquid mixtures, demonstrating its usefulness as a predictive tool for material design. Meanwhile, PCA enabled the classification and visualization of the relationships among physicochemical properties, facilitating the identification of structural correlations and trends that would otherwise be difficult to discern. These data mining techniques thus proved to be valuable tools for screening, interpreting, and organizing complex datasets, contributing to the rational design of new ionic materials.

The second part of the work employed Broadband Dielectric Spectroscopy (BDS) to systematically investigate the dielectric properties of 1-butyl-3-methylimidazolium tetrafluoroborate ([BMIM][BF_4]) as a function of frequency and temperature. Analysis of the experimental data revealed characteristic electrode polarization effects, relaxation dynamics, and associated scaling laws. The presence of a relaxation peak in the dielectric loss spectra, attributed to ion exchange processes between interfacial layers and the bulk liquid, confirmed the role of interfacial polarization in charge transport. These findings offer new insights into the dielectric and electrical behavior of ionic liquids at metallic interfaces, thereby contributing to a deeper understanding of charge transfer mechanisms across solid–liquid boundaries.

Furthermore, the relaxation dynamics and DC conductivities of the studied binary mixtures were found to lie between those of their parent ionic liquids, confirming that the fractional composition of the constituents governs the properties of the mix.

The dielectric analysis also revealed that the activation energies, determined via BDS for [EtOHVIM]Cl, [ETOHMIM][H_2PO_4], and their binary mixture, correspond to

weighted averages of the parent compounds, emphasizing the predictable nature of their relaxation behavior. Significantly, in all cases, the conductivity of the binary mixtures exceeded that of the individual ionic liquids, highlighting a synergistic enhancement of ion transport in mixed systems.

In addition, we investigated the thermal and dielectric properties of two newly synthesized ionic liquids: the monomeric [EtOHVIM][HSO_4] and the polymeric [P-EtOHVIM][H_2PO_4], both based on the 1-(hydroxyethyl)-3-vinylimidazolium cation. Characterization by NMR, FTIR/ATR, DSC, TGA, and DTG revealed that these compounds exhibit good thermal stability and low glass transition temperatures. The polymeric ionic liquid [P-EtOHVIM][H_2PO_4] displayed higher decomposition temperatures and greater hydrophilicity due to the presence of strong hydrogen bonding networks associated with the acidic anion and polymeric backbone. The dielectric analysis further demonstrated that [EtOHVIM][HSO_4] shows significant DC conductivity following a VFT-type temperature dependence above Tg, whereas [P-EtOHVIM][H_2PO_4] exhibited a transition from VFT to Arrhenius-type conductivity behavior at a characteristic temperature ($T\sigma_0$).

Overall, both ionic liquids exhibited remarkably high ionic conductivities and well-defined dielectric relaxation dynamics. Their combined features—high proton conductivity, hydrophilicity, moderate thermal stability, and strong hydrogen bonding—make them promising candidates for solid-acid electrolytes and proton exchange membranes in electrochemical applications.

In summary, this study demonstrates that integrating data mining (PCA and PLS) with thermal and dielectric characterization (DSC, TGA, and BDS) provides a comprehensive framework for understanding and predicting the physicochemical properties of ionic liquids. The obtained results not only deepen our understanding of charge transport and relaxation mechanisms in imidazolium-based systems but also pave the way for designing new functional ionic liquids with tailored properties for energy storage, electrochemical devices, and advanced materials engineering.

APPENDIX

NMR results

1H and 13C NMR spectra were acquired using a 400 MHz Avance spectrometer. The chemical shifts (δ) are stated in ppm and referred to the internal signal solvent D2O.

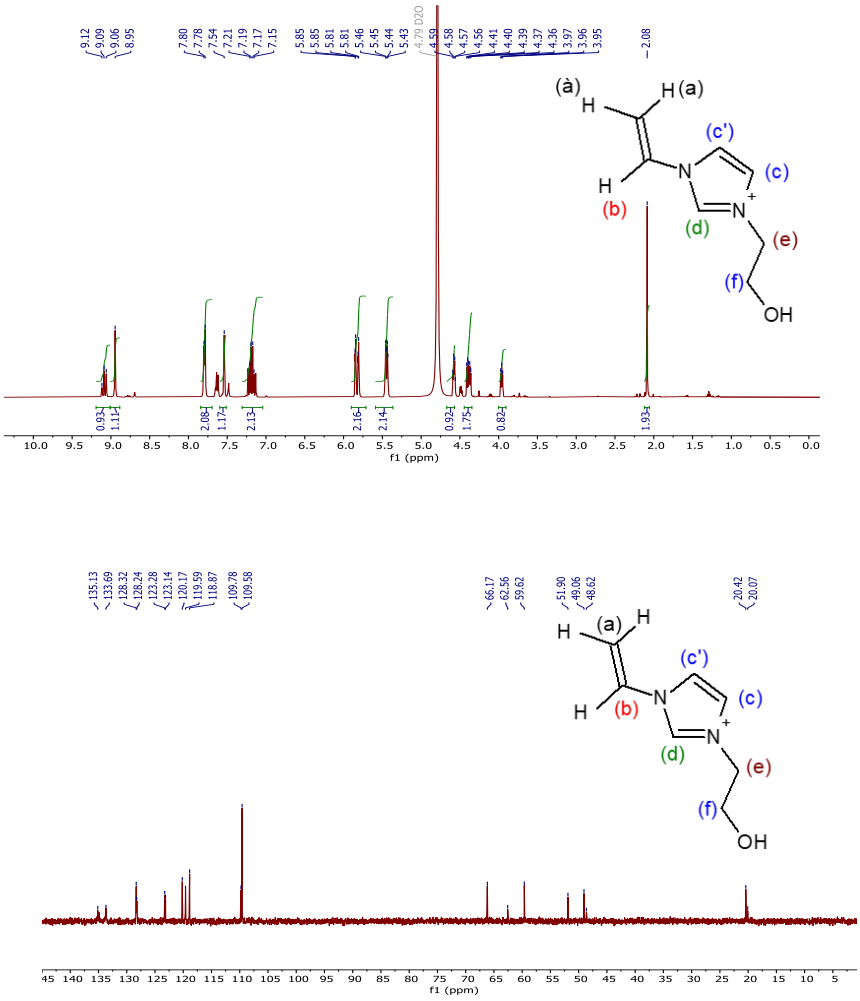

Figure A1. ^{1}H NMR (400 MHz) (a) and ^{13}C NMR (100 MHz) (b) of EtOHVim (HSO_4).

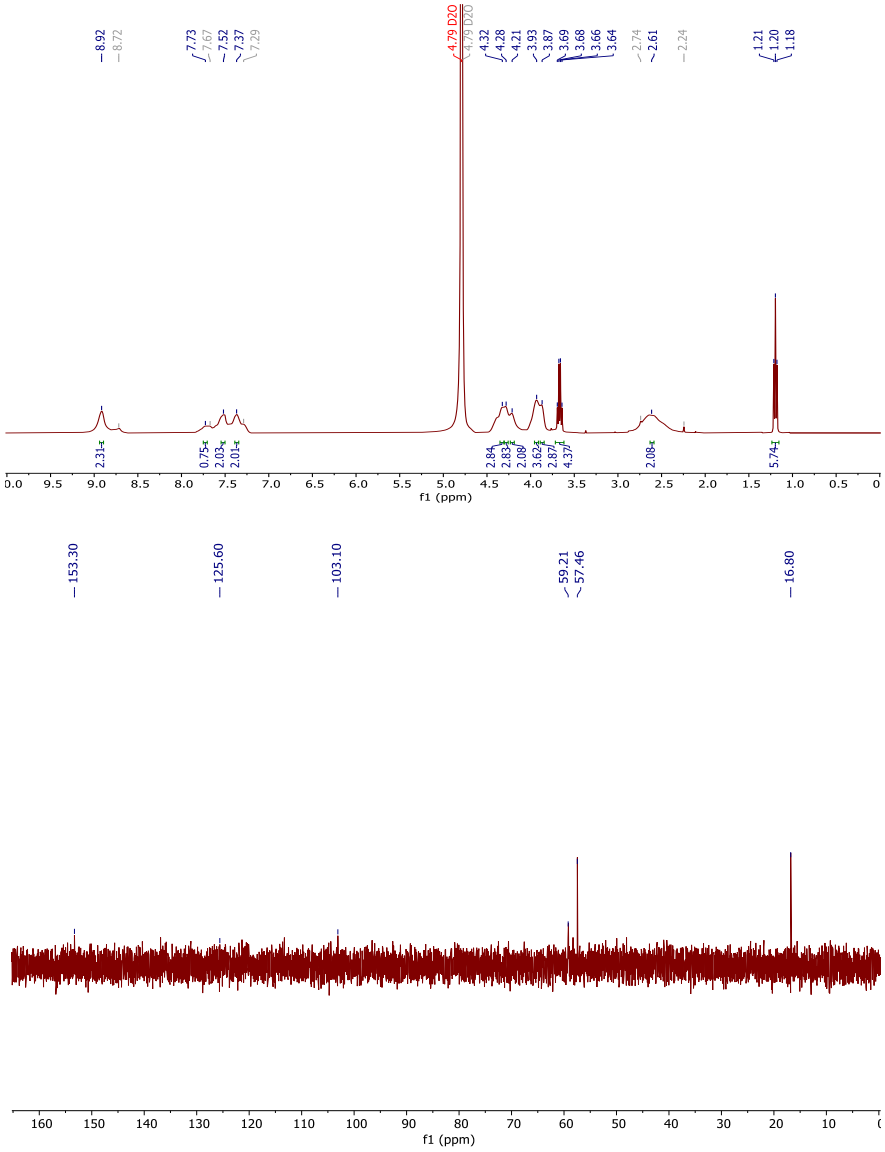

Figure A2. ^{1}H NMR (400 MHz) (a) and ^{13}C NMR (100 MHz) (b) of P-EtOHVim (H_2PO_4).

NMR of [BMIM][BF4]

The ^{1}H NMR spectrum ($CDCl_3$, δ in ppm) showed a singlet at δ = 8.65 ppm (1H, s) corresponding to the imidazolium proton H(a) of the NCH=CH group. Another singlet at δ = 8.07 ppm (1H, s) was assigned to the proton H(b) of the CH=CH–NCH_3 moiety, while the singlet observed at δ = 7.85 ppm (1H, s) was attributed to the proton H(c) of the NCH=N fragment.

The resonance at δ = 4.16 ppm (3H, s) was assigned to the N–CH_3 protons. The multiplet signals at δ = 1.95 ppm (2H, m) and δ = 1.64 ppm (2H, m, J = 6.8 Hz) correspond to the methylene protons of the $CH_3CH_2CH_2$ and NCH_2CH_2 groups, respectively. The multiplet at δ = 1.03 ppm (2H, m, J = 2.8 Hz) was attributed to the $CH_2CH_2CH_2$ protons. Finally, the triplet at δ = 0.99 ppm (3H, t, J = 8.2 Hz) was assigned to the terminal methyl group $N(CH_2)_3CH_3$.

The ^{19}F NMR spectrum ($CDCl_3$, δ in ppm) exhibited a singlet at δ = –149.44 ppm, which was assigned to the fluorine atoms of the tetrafluoroborate anion (BF_4^-).

NMR of [EtOHVIM][HSO4] and [P-EtOHVIM][H_2PO_4]

The ^1H NMR spectrum of [EtOHVIM][HSO_4] (Fig S.2) showed distinct signals corresponding to its structural features. The resonance at δ = 9.09 ppm (t, 1H) was assigned to the proton of the hydrogen sulfate group (HSO_4), while the singlet at δ = 8.95 ppm corresponded to the imidazolium proton H(d). The aromatic protons H (c) and H (c') appears as singlets at δ = 7.8 ppm and δ = 7.54 ppm, respectively. The multiplet observed at δ = 7.19 ppm was attributed to the proton H(b). The vinyl protons (-CH=CH_2) were represented by double doublets at δ = 5.81 ppm (J = 15.6, 2.6 Hz) and δ = 5.44 ppm (J = 8.7, 2.7 Hz), corresponding to H(a) and H (a'). the signal at δ = 4.79 ppm (m, 4H) was assigned to the methylene protons (2H(e) and 2H(f)), while the hydroxyl group proton (-OH) appeared as a multiplet at δ = 4.37 ppm.

The ^{13}C NMR spectrum revealed resonances consistent with the structural framework of the [EtOHVIM][HSO_4] ionic liquid. Both the carbons of the imidazolium nucleus and the vinyl carbons were observed in the unshielded part. Conversely, tow methylene carbons displayed chemical shifts between 50 and 60 ppm in the aliphatic section.

The only difference between [EtOHVIM][HSO_4] and [EtOHVIM][Cl] [43] is the appearance of the peak at 9.09 ppm corresponding to the hydrogen sulfate group [HSO_4] anion.

Regarding poly ionic liquids (PILs), no significant difference appears between the ^1H NMR spectra of [P-EtOHVIM]Cl [43] and [P-EtOHVIM][H_2PO_4] (Fig. A.2).

Similarly, the 13C NMR spectrum shows the disappearance of two peaks in the more shielded region. These spectral changes provide strong evidence of polymerization, leading to the formation of [P-EtOHVIM]Cl and [P-EtOHVIM][H2PO4] (Fig. A.2). For [P-EtOHVIM][HSO_4], NMR characterization was not included in the study by Y. Chaker et al.; however, the structure of the polymer was confirmed through comprehensive vibrational analysis.

FTIR/ATR of investigated ILs

Fig.1 illustrates the FTIR/ATR spectra [4000-600 cm^{-1}] of the five synthesized ionic liquids, while Table 1 summarizes the observed IR absorption bands and their corresponding vibrational assignments. These data confirm the successful synthesis and anion exchange processes, consistent with previous reports.[43-45]

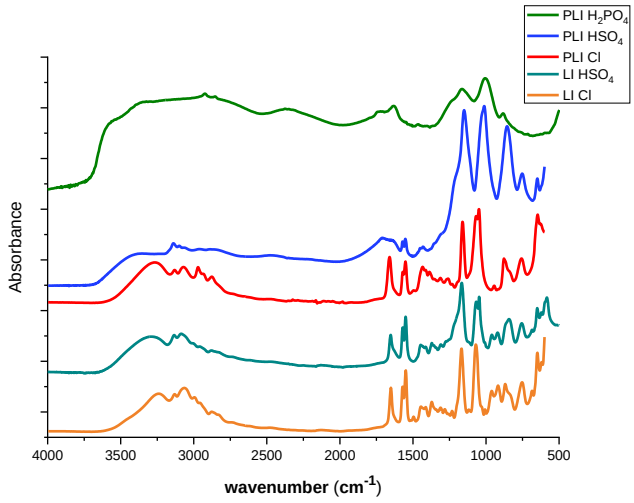

Fig A3. FTIR spectra of [EtOHVIM]Cl, [EtOHVIM][HSO_4], [P-EtOHVIM]Cl, [P-EtOHVIM][H_2PO_4] and [P-EtOHVIM][HSO_4].

Table A1. Observed FTIR/ATR bands and their assignment of 1-(hydroxyethyl)-3-vinylimidazolium chloride, poly1-(hydroxyethyl)-3-vinylimidazolium chlorideand poly1- (hydroxyethyl)-3-vinylimidazolium sulfate (vw = very weak, w = weak, m = medium, s = strong, sh = shoulder, ν = Str = stretching, δ = deformation, bend = bending deformation, ω = wagging, ρ = rocking, s = symmetric, as = asymmetric).

[EtOHVIM]Cl [43]	*[EtOHVIM][HSO_4]*	*[P-EtOHVIM]Cl*	*[P-EtOHVIM][HSO_4]*	*[P-EtOHVIM][H_2PO_4]*	*Assignment*	*Refs*
	584 (m)		611 (vw)	587 (vw)	δ(S–O), δ(P–O)	[43-45]
619 (w)		627 (sh)	622 (vw)		ω (N-H)/CH_3(N) CN Str	[43, 44]
647 (m)	647 (m)	647 (m)	647 (m)		ω (N-H)/CH_3(N) CN Str	[43, 44]
684 (vw)	684 (vw)		698 (m)	706 (vw)	ω (C-H) + ω (N-H)	[43, 44]

752 (m)	757 (m)	752(m)	753(m)		ω (C-H)	[43, 44]
833 (w)	848 (w)	835 (w)			$\rho_{as}(CH_2)$	[43, 44]
869 (w)		877 (sh)	854 (s)	879 (w)	$\rho_{as}(CH_2)$	[43, 44]
916 (w)	921 (w)				$\rho_{as}(CH_2)$	[43, 44]
960 (w)		944(vw)	945(sh)		ω (C-H)	[43, 44]
	966 (w)		968 (sh)		ν (S-O)	[43, 44]
	1039(s)		1004(s)		S-OH CH_3N Str/CH_2N Str	[43, 44]
				1016(s)	ν(C–O), ν(P–OH)	[43, 44]
1027 (w)		1048(s)	1044(sh)		CH_3N Str/CH_2N Str	[43, 44]
1069(s)	1067(s)	1069 (s)	1061		ν (C-O)	[43, 44]
1118 (vw)			1094(sh)		CC Str	[43, 44]
1167 (s)	1167 (s)	1161(s)	1157(s)	1161(s)	Rings CH_2(N) and CH_3(N)CN Str	[43, 44]
			1216(sh)		Ring ip as strstr	[43, 44]
1232 (vw)		1228(vw)		1243 (sh)	Ring ip as strstr	[43, 44]
1282 (vw)		1266 (vw)	1265		Ring ip as strstr	[43, 44]
1310 (vw)	1313 (vw)	1310(vw)	1312(vw)		ν (C-C)	[43, 44]
			1357 (w)		ν (C-C)	[43, 44]
1371 (w)	1367 (w)	1386 (w)	1380 (vw)		ρ(N-H)	[43, 44]
1431 (sh)	1413 (w)	1410 (m)			ρ(N-H)	[43, 44]
1447 (m)		1435 (sh)	1431 (m)		δ (CH_2)/CCH HCH as bend	[43, 44]
	1452 (w)		1452 (m)	14-2 (w)	δ (CH_2)/CCH HCH as bend	[43, 44]
1495 (w)		1495 (vw)	1492 (vw)		δ (CH_2)/CCH HCH as bend	[43, 44]
1549(s)	1550(s)	1550 (s)	1550 (s)		as Str CH_2(N)/CH_3(N)CNStr	[43, 44]
1570 (sh)	1577 (s)	1570 (sh)	1570(s)		as Str CH_2(N)/CH_3(N)CNStr	[43, 44]
1650 (m)	1659 (m)	1659 (s)	1646 (m)	1626 (w)	Ring C=C str, N=C-N str	[43, 44]
				1736 (w)	ν(C=N), ν(C=C)	[43, 44]
2737 (sh)	2729 (w)	2732 (sh)			Ring C=C str, N=C-N str	[43, 44]
2822 (sh)	2822 (w)	2822 (sh)	2852		Ring C=C str, N=C-N str	[43, 44]
2875 (m)	2885 (w)	2875 (m)		2854 (w)	ν_s (CH_2)	[43, 44]
2951 (m)	2952 (w)	2937 (sh)	2921 (m)	2927 (w)	ν_{as} (CH_2)	[43, 44]
		2973 (m)	2955 (vw)		ν_{as} (CH_2)	[43, 44]
2992 (m)	3003 (w)	2969 (vw)			ν (C-H)	[43, 44]
			3027 (sh)		ν (C-H)	[43, 44]
3067 (m)	3088 (m)	3071 (m)	3092 (s)		ν (C-H)	[43, 44]
3128 (m)	3135 (m)	3132 (m)			=C-H Str	[43, 44]
3240 (s)	3292 (s)	3267 (s)	3269(sh)		ν (C-OH)	[43, 44]

	3381 (m)	3376 (m)	ν (C-OH)	[43, 44]

Mass spectrometry diagram of gas escaped

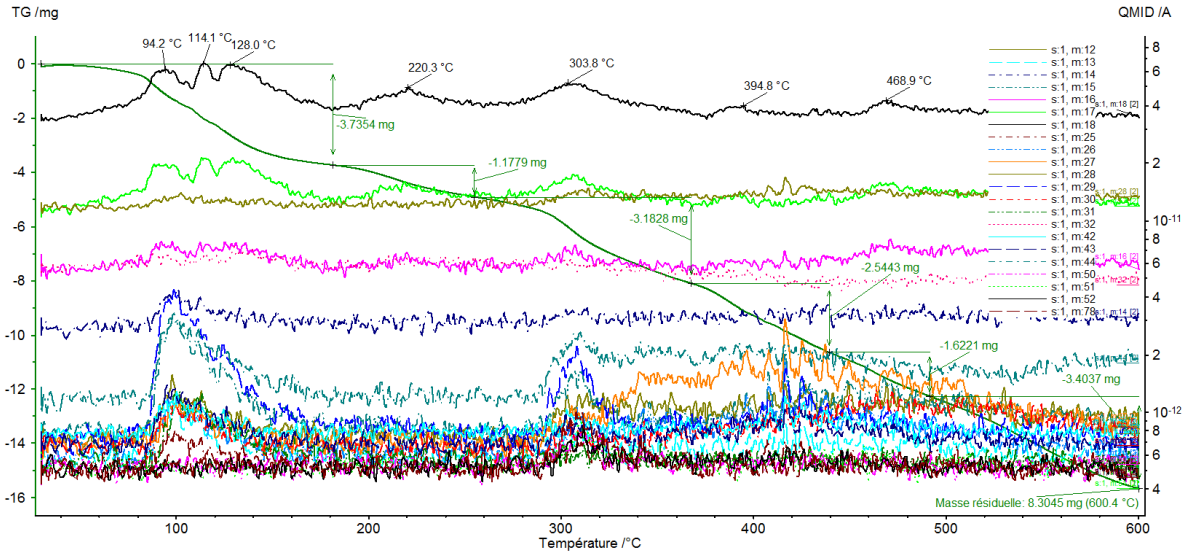

Figure A4. Mass spectrometry diagram of gas escaped from P-EtOHVim(H_2PO_4).

SUMMARY OF THE THESIS

This work focuses on the physicochemical study and dielectric characterization of imidazolium-based ionic liquids, combining experimental analysis and data-driven modeling better to understand their structural, thermal, and electrical behaviors. The study integrates data mining techniques, including Principal Component Analysis (PCA) and Partial Least Squares Regression (PLS), with Broadband Dielectric Spectroscopy (BDS) and thermal analysis methods such as Differential Scanning Calorimetry (DSC) and Thermogravimetric Analysis (TGA).

Using the Vogel–Fulcher–Tammann (VFT) dielectric equation, the PLS approach was applied to predict the dielectric properties of binary ionic liquid mixtures based on the known parameters of their individual components. The PCA method enabled the classification and visualization of property relationships, facilitating the identification of correlations and trends within complex datasets. These techniques provided valuable insight into the structure–property relationships governing ionic liquid behavior.

Experimentally, BDS measurements were performed on 1-butyl-3-methylimidazolium tetrafluoroborate ([BMIM][BF_4]) and other imidazolium-based systems to investigate frequency- and temperature-dependent dielectric properties. The results revealed electrode polarization effects, relaxation dynamics, and scaling laws characteristic of ion exchange processes between interfacial layers and the bulk liquid. The relaxation peaks followed a Vogel–Fulcher–Tammann temperature dependence, confirming the kinetic nature of charge transport mechanisms.

Furthermore, the thermal and dielectric behaviors of two newly synthesized ionic liquids, [EtOHVIM][HSO_4] (monomeric) and [P-EtOHVIM][H_2PO_4] (polymeric), were investigated using NMR, FTIR, DSC, and TGA. Both materials exhibited good thermal stability, low glass transition temperatures, and strong hydrogen bonding networks that influence their hydrophilicity and conductivity. Dielectric analysis showed high ionic conductivities with temperature-dependent transitions from VFT to Arrhenius-type behavior.

Overall, this study demonstrates that combining data mining methods with dielectric and thermal analyses offers a comprehensive and predictive framework for understanding and designing ionic liquids. The results highlight the potential of [EtOHVIM][HSO_4] and [P-EtOHVIM][H_2PO_4] as promising candidates for solid-acid electrolytes and proton exchange membranes, contributing to the development of next-generation electrochemical and energy storage materials.

Key words: Ionic liquids; Imidazolium-based compounds; Dielectric spectroscopy; Broadband Dielectric Spectroscopy (BDS); Dynamic Dielectric Spectroscopy (DDS); Principal Component Analysis (PCA); Partial Least Squares Regression (PLS); Data mining; Vogel–Fulcher–Tammann (VFT) equation; Thermal analysis; Differential Scanning Calorimetry (DSC); Thermogravimetric Analysis (TGA); Glass transition; Electrical conductivity; Charge transport.

RESUME DE LA THESE

Ce travail porte sur l'étude physico-chimique et diélectrique des liquides ioniques à base d'imidazolium, en combinant des analyses expérimentales et des méthodes de modélisation fondées sur les données afin de mieux comprendre leurs comportements structuraux, thermiques et électriques. L'étude intègre des techniques d'extraction de connaissances telles que l'Analyse en Composantes Principales (ACP) et la Régression par Moindres Carrés Partiels (PLS), ainsi que des méthodes d'analyse thermique – la Calorimétrie Différentielle à Balayage (DSC) et l'Analyse Thermogravimétrique (ATG) – et la Spectroscopie Diélectrique à Large Bande (BDS).

En utilisant l'équation diélectrique de Vogel–Fulcher–Tammann (VFT), la méthode PLS a permis de prédire les propriétés diélectriques des mélanges binaires à partir des paramètres des liquides ioniques individuels contenus dans la base de données. L'ACP a servi à classer et visualiser les relations entre les propriétés, mettant en évidence les corrélations et tendances existantes au sein de données complexes. Ces approches ont permis d'établir des relations structure–propriété essentielles à la conception de nouveaux matériaux ioniques.

Sur le plan expérimental, la spectroscopie diélectrique à large bande (BDS) a été utilisée pour étudier les propriétés diélectriques du 1-butyl-3-méthylimidazolium tétrafluoroborate ([BMIM][BF_4]) en fonction de la fréquence et de la température. L'analyse des résultats a révélé des effets de polarisation d'électrode, des dynamiques de relaxation et des lois d'échelle caractéristiques d'un échange d'ions entre les couches interfaciales et le liquide ionique massif. Les pics de relaxation observés suivent une dépendance en température de type VFT, confirmant la nature cinétique du transport de charge.

De plus, les comportements thermiques et diélectriques de deux nouveaux liquides ioniques – le [EtOHVIM][HSO_4] (monomérique) et le [P-EtOHVIM][H_2PO_4] (polymérique) – ont été étudiés à l'aide de la RMN, de la FTIR, de la DSC et de l'ATG. Ces composés présentent une bonne stabilité thermique, de faibles températures de transition vitreuse, et des liaisons hydrogène fortes influençant leur hydrophilie et leur conductivité. L'analyse diélectrique a mis en évidence des conductivités ioniques élevées, avec une transition de comportement de type VFT vers un modèle d'Arrhenius à une température caractéristique ($T\sigma_0$).

En conclusion, ce travail démontre que la combinaison des méthodes de fouille de données avec les analyses thermiques et diélectriques constitue un cadre d'étude complet et prédictif pour comprendre et concevoir de nouveaux liquides ioniques fonctionnels. Les résultats obtenus mettent en évidence le potentiel des composés [EtOHVIM][HSO_4] et [P-EtOHVIM][H_2PO_4] en tant que bons candidats pour les électrolytes solides acides et les membranes échangeuses de protons, contribuant ainsi au développement de matériaux avancés pour les dispositifs électrochimiques et de stockage d'énergie.

Mots-clés : *Liquides ioniques ; Composés à base d'imidazolium ; Spectroscopie diélectrique ; Spectroscopie diélectrique à large bande (BDS) ; Analyse en composantes principales (ACP) ; Régression par moindres carrés partiels (PLS) ; Fouille de données ; Équation de Vogel–Fulcher–Tammann (VFT) ; Analyse thermique ; Calorimétrie différentielle à balayage (DSC) ; Analyse thermogravimétrique (ATG) ; Transition vitreuse ; Conductivité électrique ; Transport de charge.*

ملخّص الأطروحة

يهدف هذا العمل إلى دراسة الخصائص الفيزيائية والكيميائية والعازلية لمجموعة من السوائل الأيونية القائمة على الإيميدازوليوم، وذلك من خلال الجمع بين التحليل التجريبي وأساليب النمذجة المعتمدة على تحليل البيانات، بهدف فهمٍ أعمق للبنية الداخلية والسلوك الحراري والكهربائي لهذه المواد.

تدمج هذه الدراسة بين تقنيات التنقيب في البيانات مثل تحليل المكوّنات الرئيسية (PCA) والانحدار بالمتوسطات الصغرى الجزئية(PLS) ، وبين طرق التحليل الحراري كـ التحليل الحراري الوزني (TGA) والمسح الحراري التفاضلي(DSC) ، بالإضافة إلى التحليل الطيفي العازل واسع النطاق.(BDS)

باستخدام معادلة فوغل–فولخر–تامان (VFT) الخاصة بالسلوك العازل، تم توظيف طريقة PLS للتنبؤ بالخصائص العازلية لخليطين أيونيين ثنائيين اعتماداً على المعطيات الخاصة بكل مركب أيوني منفرد. أما طريقة PCA فقد استُخدمت لتصنيف وتمثيل العلاقات بين الخصائص الفيزيائية والكيميائية، وكشف الترابطات والأنماط العامة في قواعد البيانات المعقدة، مما أتاح فهماً أدق لعلاقات البنية–الخاصية في هذه المواد.

وقد استخدمت تقنية التحليل الطيفي العازل واسع النطاق (BDS) لدراسة الخصائص العازلية لمركب 1-بيوتيل-3-ميثيل إيميدازوليوم تترافلورو بورات ([BMIM][BF_4]) عند ترددات ودرجات حرارة مختلفة. وأظهرت النتائج وجود تأثيرات استقطاب عند الأقطاب المعدنية، وقمم استرخاء تتبع سلوكاً حرارياً من نوع VFT ، ناتجاً عن تبادل الأيونات بين الطبقات البينية والسائل الأيوني الكتلي، مما يوضح آلية انتقال الشحنات عبر الواجهات الصلبة–السائلة.

كما جرى تحليل الخصائص الحرارية والعازلية لسائلين أيونيين جديدين هما [EtOHVIM][HSO_4] (أحادي الوحدات) و**[P-EtOHVIM][H_2PO_4]**(بوليمري). وأظهرت القياسات باستخدام تقنيات NMR و FTIR و DSC وTGA أن المركبين يتميزان بـ ثباتٍ حراري جيد ودرجات انتقال زجاجي منخفضة. كما بين التحليل العازل أن لهما توصيلاً أيونياً مرتفعاً، وأن سلوك النقل الأيوني ينتقل من نموذج VFT إلى نموذج أرينيوس عند درجة حرارة مميزة.($T\sigma_0$)

تؤكد هذه النتائج أن دمج تقنيات التنقيب في البيانات مع التحليل الحراري والعازل يوفر إطاراً متكاملاً وتنبؤياً لفهم وتصميم السوائل الأيونية الوظيفية الجديدة. كما تُظهر أن المركبين [EtOHVIM][HSO_4] و-P]** **[EtOHVIM][H_2PO_4] يتمتعان بخصائص تجعل منهما مرشحين واعدين للاستخدام كـ إلكتروليتات صلبة حمضية وأغشية تبادل بروتوني في التطبيقات الكهروكيميائية وأنظمة تخزين الطاقة.

الكلمات المفتاحية

السوائل الأيونية؛ مركّبات الإيميدازوليوم؛ التحليل الطيفي العازل؛ التحليل الطيفي العازل واسع النطاق (BDS)؛ تحليل المكوّنات الرئيسية (PCA)؛ الانحدار بالمتوسطات الصغرى الجزئية (PLS)؛ التنقيب في البيانات؛ معادلة فوغل–فولخر–تامان (VFT)؛ التحليل الحراري؛ المسح الحراري التفاضلي (DSC)؛ التحليل الحراري الوزني (TGA)؛ الانتقال الزجاجي؛ التوصيلية الكهربائية؛ نقل الشحنة.

Available online at www.sciencedirect.com

ScienceDirect

Procedia Computer Science 83 (2016) 1044 – 1049

Procedia Computer Science

International Workshop on Data Mining for Decision Making Support (DMDMS 2016)

The study of dielectric properties of some ionic liquids based on imidazolium by dielectric spectroscopy and data mining.

HADJER GUETTAF [a]*, EL HABIB BELARBI [a], NOUREDDINE BENKHETTOU[b], BOUMEDIENE HADDAD[a,c]

[a] *Synthesis and Catalysis Laboratory LSCT, Univ Tiaret, Tiaret 14000, Algérie.*
[b]*Laboratoire des MatériauxMagnétiques, Faculté des Sciences, Univ Sidi Bel-Abbès, Sidi Bel-Abbès 22000, Algeria.* [c]*Department of Chemistry, Dr Moulay Tahar Univ Saida ,Saida 2000, Algeria*

Abstract

Ionic liquids (ILs) are liquid salts of differentiating to all molten salts with temperature below 100 ° C (arbitrarily set with reference to the boiling point of water), but a large number of them are liquids at room temperature. The properties of ionic liquids such as their wide field of electro activity, their high conductivity, and high thermal stability have made them new prime candidates in searching for a new energy systems (photovoltaic cell, battery, solar concentrator ...). The present work objective is to study the physicochemical properties of some ionic liquids based on imidazolium ($[BMIM]^+$ $[BF_4]^-$ · $[BMIM]^+[PF_6]^-$ · $[HMIM]^+$ $[Br]^-$ · $[BMIM]^+$ $[Br]^-$) and more particularly the dielectric properties. We performed measurements by dielectric spectroscopy to see the influence of the size of the anion and the length of the alkyl chain of the cation on the conductivity of ionic liquids at different temperatures. We made also theoretical study by using data mining techniques such as the analytical method principal components (PCA), that help us to study the relationships between variables (σ_{RT} (S / m), T_g (K) $\ln\sigma_\infty$ (S / m), B, T_0 (K), m) and their relation with ionic liquids structure.

Peer-review under responsibility of the Conference Program Chairs

Keywords: Ionic liquids (IL), dielectric spectroscopy, electrical conductivity, Data mining, principal component analysis method (PCA).

* Corresponding author. Tel.: +213 46 42 22 15;.
E-mail address: hadjer_07@yahoo.fr

Peer-review under responsibility of the Conference Program Chairs
doi:10.1016/j.procs.2016.04.221

1. Introduction

Ionic liquids have been in recent years the subject of growing research activities because of their interesting physical properties high electrical conductivity and very low vapour pressure and their potential as designer solvents for catalytic and chemical applications. By definition, ionic liquids are organic salts with a melting temperature below 100 ° C. The polarity, dielectric constant, electrochemical window, and electrical conductivity are important physical properties that determine whether an ionic liquid is suitable for a given application.

Due to the large number of possible cation-anion combinations, it is of great interest to understand how the properties of newly synthesized ILs can be predicted from the structure of the molecule, in order to choose suitable candidates for a given application.[1]

From the applied point of view, there are many proposed applications for ILs in the field of green chemistry. Among them we can name those of replacement of organic solvents, charge transport in energy generators, batteries and electrolytic medium in aluminium electrodeposition processes[2,3]. In fact important advances have been achieved recently in the application of ionic liquids to Li batteries[4], as electrolyte in electrochemical processes and devices[5], and even in solar power applications[6].

To develop these proposed applications with the most adequate IL it is first necessary to know the value of their physical magnitudes, and their behaviour with temperature. Experimental data of the different physical magnitudes are also necessary to develop a theoretical model to explain and to predict them in the different ionic liquids (which does not exist nowadays up to our knowledge), and to extend the molecular dynamic simulations reported until now[7,8].

Experimental data or databases are traditionally viewed as ‘‘static’’ documents that are used in a ‘‘search and retrieval’’ mode. These static data can be transformed by informatics and data mining tools into a dynamic dataset for analysis of the properties of the materials and for making predictions.

2. Experimental

2.1. Materials and Methods

To make our experimental conductivity measurements, we used an LCR meter (L for inductance, C for capacitance and R for resistance). The functional role of an LCR bridge is based on measuring the electrical impedance Z of the compound under test. The electrical impedance is defined as the opposition that presents a compound or a circuit against the flux of an alternating electric current for a given frequency. This impedance is a complex quantity, the real part corresponds to the resistor R and the imaginary part to the reactance X that is written as:

$$Z = Z' + iZ'' = R + iX \quad (1)$$

The ionic conductivity measurements were taken using a conductivity cell with coaxial cylindrical copper electrodes manufactured locally; in this case, the cell constant was calculated by:

$$k = \frac{1}{2\pi h} ln \frac{R_1}{R_2} \quad (2)$$

h, R_1, R_2 respectively represent the height of the electrodes (cm), rayons of the two electrodes from small to large (cm) and constant k of the cell (cm^{-1}).

The dielectric measurements were performed on pellets processed by applying uniaxial pressure on powder. Dielectric spectra were recorded by using BDS-4000 Novocontrol spectrometer, which was coupled with the quarto system to ensure the temperature variation from -80 to 20°C for the frequency range (10^{-2} to 10^{6}Hz). For conductivity data analysis, the complex conductivity is defined as:

$$\sigma^* = \sigma' + i\sigma'' = \varepsilon_0 \omega \varepsilon'' + i\varepsilon_0 \omega \varepsilon' \quad (3)$$

Where ε_0 and ω refer to the permittivity of free space and angular frequency ($\omega = 2\pi f$), respectively.

2.2. Results and Discussion

2.2.1. Conductivity:

The conductivity value (σ) has been determined from the electrolyte resistance (R_e) drawn from the diagram impedance by the following relationship:

$$\sigma = \frac{k}{R_e} \quad (4)$$

In this paper we present experimental data on the temperature dependence of the electrical conductivity σ, in four different imidazolium based ionic liquids $[C_nMIM]^+[Br]^-$ with C_n representing butyl and hexyl chains, to study the dependence of σ with the cation length. Moreover, to study the influence of the anion size in the electrical conductivity, we measured three different $[BMIM]^+[X]^-$ with X being, from smaller to bigger sizes, Br^-, BF_4^-, PF_6^-. The influence of the anion size on the electrical conductivity was also studied.

According to the Nyquist diagram and by applying equation (4), conductivity (σ) and the resistance of the electrolyte (R_e) of the two ionic liquids are mentioned in the following table (Table 1).

Table.1. The values of (R_e) electrolyte resistance, (V) volume, (σ) conductivity of LIs of $[BMIM]^+[Br]^-$,$[BMIM]^+[BF_4]^-$, $[BMIM]^+[PF_6]^-$ and $[HMIM]^+[Br]^-$.

LI	$[BMIM]^+[Br]^-$	$[HMIM]^+[Br]^-$	$[BMIM]^+[BF_4]^-$	$[BMIM]^+[PF_6]^-$
R_e (Ω)	6,49	28 ,55	30,58	30,18
V(ml)	1,2	2	0,5	1
σ($mS.cm^{-1}$)	3,75	0,5	1,9	0,96

If we analyse the table (1), we observe, as expected, when the length of the cation $[C_nMIM]^+$ increases the electrical conductivity of the liquid decreases. The long alkyl chains make the movement of cations difficult and thus LIs with longer chains contribute weakly in the electrical conductivity.

Discussing the influence of anion size on the electrical conductivity, we observe in the table that when size of the anion increases (Br^-<$BF4^-$<$PF6^-$) electrical conductivity decreases, because of the external electrical charge density that decreases with the increasing of the anion size.

From a theoretical point of view, a detailed knowledge of the molecular interactions responsible of the ionic character of ionic liquids is to be known. In particular, although it is clear that the large size of the cation is the primary cause of their liquid state, the exact influence of the size in the transport properties is not known.

2.2.2. Dipolar relaxations :

Physically, the dielectric modulus corresponding to the relaxation of the electric current in the material become constant when the electric displacement, so the electric modulus presents the real process of the dielectric relaxation, which is expressed by the relation

$$M^* = \frac{1}{\varepsilon^*(\omega)} = M' + iM'' \quad (5)$$

The imaginary part M "(ω) of the complex spectra of dielectric modulus in frequency was determined.

Secondary relaxation processes were observed in this liquid at high frequencies and low temperatures. These are the β relaxations which are modelled by the empirical function Havriliak-Negami.

$$M^* = M_\infty + \frac{\Delta M}{\left(1+(i\omega\tau_{HN})^\beta\right)^\gamma} \quad (6)$$

τ_{HN} is the relaxation time Havriliak-Negami and β, γ are the parameters of the complex dielectric function and the module M.

The temperature evolution of the relaxation time is adequately fitted using the phenomenological Vogel-Fulcher-

Tammann (VFT) model.

The relaxation time is defined by the equation:

$$\tau = \tau_0 \exp\left[\frac{DT_0}{T-T_0}\right] \quad (7)$$

Equation is commonly adopted to describe the relaxation dynamics of glass formers. In this equation, τ_0 is the high temperature limit of the fast relaxation and T_0 represents the temperature at which the average value of the relaxation time diverges. The coefficient D can be regarded as a measure of the system fragility. The lower its value is, the larger the departure from Arrhenius behaviour.[9]

So we conclude that the conductivity of the ionic liquids often presents a classical linear of Arrhenius behaviour above ambient temperature. However, when the temperature of these ionic liquids approach their glass transition temperature (T_g) , the conductivity displays a significant negative deviation from linear behaviour.

$$\sigma = A^{-1/2}\exp\left[-B / (T - Tg)\right] \quad (8)$$

When A, B, and T_g are adjusted parameters. Comparing the Arrhenius equation with the VFT equation (8), we can observe that the second is equal to the first if $T_g = 0$. Thus, we can connect the fitting parameters the VFT-type equation with the physical parameters of the Arrhenius equation: $A = B = \sigma_\infty$ and E_a / k_B.

Equation (9) is the modified version of the Vogel-Tamman-Fulcher (VFT) equation (9) [10]:

$$\sigma = \sigma_\infty^{-1/2}\exp\left[-Ea / k_B (T - T_g)\right] \quad (9)$$

3. Theoretical Study.

Application of the principal component analysis method.

The objective of this part is to search the correlations between the parameters of the VFT equation (m: fragility, T_g: glass transition temperature, $\ln\sigma_\infty$: logarithm of the conductivity to ∞, B: constant, T_o: the temperature at which the conductivity (σ) tends to zero, σ_{RT}, the conductivity at room temperature) on the one hand and the length of the cation and the size anion of the other hand using the Principal component analysis technique (PCA).

Principal components analysis,(PCA), which is a descriptive technique permitting to study the relationships between variables and identify the dependence of the structure among the observations to obtain a description or representation, in a projection data on different axes, called principal axes.

Table .2. Table of data used in the principal component analysis[1].

Ionic liquid	σ_{RT} *(S/m)*	T_g*(K)*	$\ln\sigma_\infty$*(S/m)*	B	T_0*(K)*	m
C_3mim, BF_4	0,159	175,1	7,86	1284	139,7	78
C_4mim , BF_4	0,364	177,9	6,89	1160	146,8	93
C_5mim , BF_4	0,163	182,8	6,69	1240	147,1	78
C_6mim , BF_4	0,118	187,6	6,37	1238	148,5	66
C_7mim , BF_4	0,067	186,1	6,03	1291	146,1	68
C_8mim , BF_4	0,059	189,7	6,1	1295	148,3	62
C_9mim , BF_4	0,042	190,5	5,8	1324	145,9	55
C_6mim , Br	0,0074	187,8	7,47	1668	158,4	158
C_6mim , Tf_2N	0,17	187,1	5,59	1057	148,3	57
C_6mim , FAP	0,096	184,7	3,86	965	152,2	73

(For simplification we have omitted the charges + and – and the brackets in the representation of ionic liquids)

The first analysis is to examine differences between the 10 different ionic liquids. The observations of the graph (plot scores) of this analysis is given in fig.1. For this analysis, the sign of each principal component has no signification. The principal axis PC1 of variance for the data set, and the principal axis PC2 are the capture of the variance. No other principal axis (PC) is included because they do not provide significant information.

By observing the fig.1 it appears that the principal axis PC1 is strongly related to the variation in the size of the anion, when the value of the PC1 axis increases the size of the anion decreases (C_6mim, FAP; C_6mim, Br; C_6mim, Tf_2N; C_6mim, BF_4). The same observations for the PC2 axis that captures the change in size of the cations, when the value of the PC2 axis increases the size of the cations decreases (C_6mim BF_4, C_4mim BF_4; C_5 mim BF; C_7mim, BF_4; C_8mim, BF_4; C_9mim, BF_4; C_3mim, BF_4). The results can be classified into three clusters, and properties in each cluster are shown in the table 3.

Table.3. the properties in each cluster.

Cluster 1	m, ln σ_{∞}, B
Cluster 2	T_0, T_g
Cluster 3	σ_{RT}

The principal axes are the same for graph observations (plot scores) and the graph of the variables (plot loadings) so the information in these two graphs can be compared directly.

Clusters 1 and 3 contribute to the PC1 axes values of the scores plot; these are highly correlated because they have similar values in the same principal axes PC.

While the inverted values in the PC axes indicate inverted correlations. Therefore, the properties in the cluster 2 are inversely correlated with the properties in the cluster 3 (σ_{RT}, T_0, T_g). It seems that the ionic liquids $C_n$mim BF_4 are glassy systems behaviour at the glass transition temperature (T_g) increases when the room temperature conductivity decreases because they are inversely related).

We also note that the fragility m is strongly correlated with B which describes the temperature dependence of the conductivity at a higher temperature (they belong to the same cluster).

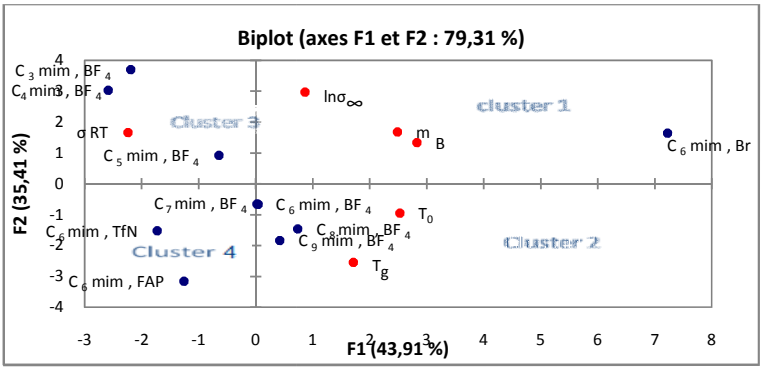

Fig .1. Representation and Score Plot PCA ionic liquids.

From the cluster 3 and 2 we found out that the values of σ_{RT} decrease when length of the alkyl chain increases. As the conductivity is related to the electron mobility, it can be explained by the increase of the viscosity induced by the strong interactions of Van der Waals forces between the alkyl chains and the large cations.

On the other hand, the homologous series shows a relatively small decrease in fragility in terms of the growth of the length of the alkyl chain. The relationship between molecular parameters and fragility is not yet well understood. However, it is known that LI fragility is closely linked to the morphology of the cooperativeness and network

rearrangement. It depends heavily on local inter-ionic Coulomb forces. C_6mim, Br is an exception in this series. Its fragility is much larger than the fragility of ionic liquids with the fluorinated anions. This anomaly can be explained by the fact that the bromide ion is capable of forming strong hydrogen bonds with the hydrogen atoms of cation imidazolium. Inter ionic forces lead to the formation of hydrogen bonding and therefore greater fragility. The presence of this network also makes it more difficult for ions to travel through the sample, causing much lower conductivity. Fluorinated anions have a lower charge density, because the negative charge is distributed over a much larger volume. The interaction of these anions with the imidazolium cation is much weaker than the interaction between the bromide anion and the cation.

The cluster in Figure (1) shows that C_6 mim, FAP and C_6 mim, Tf_2N could be good candidates for high electrical conductivity at room temperature.

So we concluded that:

If we change the nature of the anion the most influencing parameter on the conductivity of the ionic liquid at room temperature is the fragility m.

If changing the length of the alkyl chain of the cation the most influencing parameter on the conductivity of the ionic liquid at room temperature is the glass transition temperature T_g.

4. Conclusion

We focused mainly on the study of physicochemical properties of ionic liquids based on imidazolium.
In this paper, we studied the influence of the size of the anions and cations on the dielectric properties of ionic liquids based on imidazolium at different temperatures.

The experimental work presented in this paper aimed to make physical measurements by dielectric spectroscopy. We observed that when the size of the anion increases the electrical conductivity increases also and the observed electrical conductivity decreases with increasing length of the alkyl chain of the cation C_nMIM. The conductivity as a function of the observed temperature is consistent with the behaviour of the vitreous compounds and it is explained by the Vogel-Fulcher-Tammann equation (VFT).

The objective of the theoretical study is to look for correlations between the parameters of the VFT equation and the length of the alkyl chain of the cation and the anion size by using data mining analysis in particular the PCA method.

The use of PCA shows that data can be used to determine some useful correlations, and then we use this knowledge to develop new materials.

Acknowledgments The authors thank the ATRST-DGRSDT (Algeria) for financial support.

References

1. Leys J, Wübbenhorst M, Menon CP, Rajesh R, Thoen J, Glorieux C, et al. Temperature dependence of the electrical conductivity of imidazolium ionic liquids. The Journal of chemical physics. 2008;128(6):064509.
2. Endres F. Ionic liquids: solvents for the electrodeposition of metals and semiconductors. ChemPhysChem. 2002;3(2):144−54.
3. Wasserscheid P, Welton T. Ionic liquids in synthesis Wiley-VCH, Verlag, Weinheim, 2003
4. Ishikawa M, Sugimoto T, Kikuta M, Ishiko E, Kono M. Pure ionic liquid electrolytes compatible with a graphitized carbon negative electrode in rechargeable lithium-ion batteries. Journal of power sources. 2006;162(1):658−62.
5. Galiński M, Lewandowski A, Stępniak I. Ionic liquids as electrolytes. Electrochimica Acta. 2006;51(26):5567−80.
6. Van Valkenburg ME, Vaughn RL, Williams M, Wilkes JS. Thermochemistry of ionic liquid heat-transfer fluids. Thermochimica Acta. 2005;425(1):181−8.
7. Lee SU, Jung J, Han Y-K. Molecular dynamics study of the ionic conductivity of 1-n-butyl-3-methylimidazolium salts as ionic liquids. Chemical physics letters. 2005;406(4):332−40.
8. Rey-Castro C, Vega LF. Transport properties of the ionic liquid 1-ethyl-3-methylimidazolium chloride from equilibrium molecular dynamics simulation. The effect of temperature. The Journal of Physical Chemistry B. 2006;110(29):14426−35.
9. Pochylski M, Aliotta F, Ponterio RC, Saija F, Gapinski J. Some Evidence of Scaling Behavior in the Relaxation Dynamics of Aqueous Polymer Solutions. The Journal of Physical Chemistry B. 2010;114(4):1614−20.
10. Vila J, Franjo C, Pico JM, Varela LM, Cabeza O. Temperature behavior of the electrical conductivity of emim-based ionic liquids in liquid and solid states. Portugaliae Electrochimica Acta. 2007;25(1):163- 72.

Journal of Ionic Liquids 5 (2025) 100175

Contents lists available at ScienceDirect

Journal of Ionic Liquids

journal homepage: www.elsevier.com/locate/jil

High ionic conductivity for ionic and poly ionic liquids based on 1-(hydroxyethyl)-3-vinylimidazolium cation: Asymmetric acidic anion contribution of hydrogen sulfate and dihydrogen phosphate

Hadjer Guettaf [a,*], Yassine Chaker [a,b], El Habib Belarbi [a], Mansour Debdab [a], Taqiyeddine Moumene [a], Abdelkader Benabdellah [a], Serge Bresson [c]

[a] Synthesis and catalysis laboratory, University IBN KHALDOUN Tiaret, 14000 Tiaret, Algeria
[b] Materials Chemistry and Applications Laboratory, Tissemsilt University- AHMED BEN YAHIA ELWANCHARISSI, 38000, Algeria
[c] UP Transformations & Agro-Ressources, Institut Polytechnique Uni La Salle, SFR Condorcet 3417, BP 30313 F-60026 Beauvais, France

ARTICLE INFO

Keywords:
Monomeric ionic liquids
Polymeric ionic liquids
Asymmetric acidic anion
TGA- DTG
BDS
High ionic conductivity

ABSTRACT

The outstanding characteristics of ionic liquids (ILs), combined with the mechanical stability of polymeric systems, give rise to a novel class of materials known as polymeric ionic liquids (PILs) with transformative potential applications. The study aimed to investigate the influence of asymmetric acidic anions on the ionic conductivity of monomeric ionic liquid MILs and PILs. Therefore, an anion exchange reaction was carried out on 1-hydroxyethyl-3-vinylimidazolium chloride [EtOHVIM]Cl, resulting in the formation of 1-hydroxyethyl-3-vinylimidazolium hydrogen sulfate [EtOHVIM][HSO_4]. Since a previous investigations highlighted the intriguing characteristics of dihydrogen phosphate anion, an additional anion exchange reaction was performed on Poly(1-hydroxyethyl-3-vinylimidazolium) chloride [P-EtOHVIM]Cl, which gave rise to the formation of Poly(1-hydroxyethyl-3-vinylimidazolium) dihydrogen phosphate [P-EtOHVIM][H_2PO_4], resulting in the formation of Poly (1-hydroxyethyl-3-vinylimidazolium) dihydrogen phosphate [P-EtOHVIM][H_2PO_4]. The molecular structures were confirmed using ^{1}H NMR, ^{13}C NMR, and Infrared (ATR/FTIR) spectroscopy. The obtained ionic liquids were analysed using Differential Scanning Calorimetry (DSC), Thermogravimetric Analysis (TGA), and Derivative Thermogravimetry (DTG). The findings revealed that these compounds have intriguing thermal properties, including a low glass transition temperature and good thermal stability. Furthermore, Broadband Dielectric Spectroscopy (BDS) analysis and thermal characterisations were combined to unravel the interplay between charge transport and glassy dynamics.

1. Introduction

Ionic liquids (ILs), recognized for their environmentally friendly characteristics (Zhu, 2025; Welton, 2011; Stark et al., 2010), exhibit exceptional physico-chemical properties, including thermal stability (Kosmulski et al., 2004), low vapor pressure (Aschenbrenner et al., 2009), and high ionic conductivity (Singh and Savoy, 2020; Picálek and Kolafa, 2007). These unique characteristics have made them a mainstay in various applications in diverse areas such as organic synthesis (Zhang et al., 2025), catalysis (Cai et al., 2025), Batteries and Supercapacitors (Mirzaei-Saatlo et al., 2024; Ray and Saruhan, 2021), and extraction processes (Su et al., 2024). Notably, the ability to modify the combinations of cations and anions to set the characteristics of ionic liquids emphasis their versatility for specific uses, underscoring their potential as valuable contributors in various applications (Singh and Savoy, 2020; Welton, 1999; Dupont et al., 2002; Lu et al., 2009; Pârvulescu and Hardacre, 2007; Vekariya, 2017; Matuszek et al., 2024; Morawska and Wardak, 2024).

Over time, ionic liquids have rapidly advanced in polymer science, shifting from solvents to potentially functional additives in polymer chains or hybrid materials (Lu et al., 2009; Salas et al., 2025). Polymerization of ionic liquids yields ionic polymers, also known as polyionic liquids or polymerized ionic liquids (PILs) (Namazi, 2017; Zhu and Yang, 2024). Ionic polymers have a long history in polyelectrolytes and ionomers (Dobrynin and Rubinstein, 2005), whereas PILs are a novel type of ionicity in polymer chains (Eftekhari and Saito, 2017; Nosov

* Corresponding author.
E-mail address: hadjer.guettaf@univ-tiaret.dz (H. Guettaf).

https://doi.org/10.1016/j.jil.2025.100175
Received 3 February 2025; Received in revised form 18 August 2025; Accepted 31 August 2025
Available online 1 September 2025

et al., 2024).

In fact, high ionic conductivity for a novel poly(ionic liquid)s, are gaining attention due to their thermal and electrochemical stability, processability, and potential applications in safe, flexible, all-solid-state electrochemical devices, including electrolytes (Shin et al., 2003), supercapacitors (Mohapatra and Barick, 2025), lithium metal batteries (Zhang et al., 2025), transistors (Dickson et al., 2024), and memory devices (Zhang et al., 2020), in addition to fuel cells (Pan et al., 2025) and Dye-sensitized solar cells (Pan et al., 2025). Nonetheless, the working temperature and operational regime of these electrochemical devices were profoundly influenced by PIL's bulk ionic conductivity (σ_{DC}), thereby constraining the practical application of the latter. Consequently, the advancement of innovative PILs exhibiting enhanced ionic conductivity holds significant importance and embodies a competitive arena among diverse scientific partisanship (Singh and Savoy, 2020; Nosov et al., 2024; Shaplov et al., 2015; Meek and Elabd, 2015; Forsyth et al., 2019; Kiriy et al., 2024). Although the impact of anion substituents is frequently discussed (Ye and Elabd, 2011; Chen et al., 2018; Ogihara et al., 2006; Zhang et al., 2025). However, certain asymmetric anions recently developed for high conductivity for ionic and polyionic liquids (Nosov et al., 2024; Zhao et al., 2019; Verevkin et al., 2024). To the best of our knowledge, the influence of asymmetric acidic anions on the ionic conductivity of ILs and PILs hasn't been discussed. Consequently, it is essential to be examined and assessed.

For the purpose of this study, our previous research reviewed the chemical and thermal properties of poly(1-hydroxyethyl-3-vinylimidazolium) chloride [P-EtOHVIM]Cl, poly(1-hydroxyethyl-3-vinylimidazolium) hydrogen sulfate [P-EtOHVIM][HSO_4], and 1-hydroxyethyl-3-vinylimidazolium chloride [EtOHVIM]Cl, focusing on their synthesis, thermal behavior, and vibrational characteristics (Chaker et al., 2018). The findings revealed that the [P-EtOHVIM][HSO_4] as a PIL with an asymmetric acidic anion exhibits notable thermal characteristics, including a high degradation temperature, good thermal stability, and a low glass transition temperature compared to [P-EtOHVIM]Cl. It is worth mentioning that the anion's contribution significantly affects both the compound's vibrational behavior and thermal stability. However, their dielectric properties' broader impact has not been previously documented. In addition, a new ionic liquid, 1-(hydroxyethyl)-3-methylimidazolium dihydrogen phosphate [EtOHMIM][H_2PO_4], was synthesized and characterized by Zaoui et al. (Zaoui et al., 2021). The study demonstrated that the [H_2PO_4] anion plays a crucial role in enhancing the thermal stability of the compound, while also contributing to its distinctive vibrational and thermal properties. To further explore the role of [H_2PO_4] as an asymmetric acidic anion in poly (1-hydroxyethyl-3-vinylimidazolium)-based PILS, as well as the influence of the [HSO_4] asymmetric acidic anion in 1-hydroxyethyl-3-vinylimidazolium monomeric ionic liquids MILs, the present study was conducted. Firstly, an anion exchange reaction was performed on poly (1-hydroxyethyl-3-vinylimidazolium) chloride [P-EtOHVIM]Cl, resulting in the formation of poly(1-hydroxyethyl-3-vinylimidazolium) dihydrogen phosphate [P-EtOHVIM][H_2PO_4]—a second polymeric ionic liquid (PIL) containing an asymmetric acidic anion. Secondly, an anion exchange reaction on 1-hydroxyethyl-3-vinylimidazolium chloride [EtOHVIM]Cl yielded 1-hydroxyethyl-3-vinylimidazolium hydrogen sulfate [EtOHVIM][HSO_4]. The influence of the asymmetric acidic anion and the absence and presence of the polymeric chain on the structural, thermal, and dielectric properties were examined through various structural and thermal experimental techniques, including NMR ^1H, ^{13}C analyses, Infrared (ATR/FTIR) spectroscopy, thermogravimetric analysis (TGA), Derivative Thermogravimetry (DTG), differential scanning calorimetry (DSC). However, measurements using broadband dielectric spectroscopy (BDS) were carried out to provide further insight into the impact of each previous factors on the ionic conductivity of the five ionic liquids [EtOHVIM]Cl, [EtOHVIM][HSO_4], [P-EtOHVIM]Cl, P-EtOHVIM][HSO_4] and [P-EtOHVIM][H_2PO_4].

2. Materials and methods

2.1. Reagents and materials

1-vinylimidazole (99 %), 2-chloroethanole (99 %), dichloromethane and diethyl ether (99 %), 2-azobisisobutyronitrile (AIBN 98 %), Sulfuric acid (99 %) and Phosphoric acid (99 %) were used as reagents, in this study, without any further purification.

2.2. Synthesis of [EtOHVIM][HSO_4]

According to (Scheme 1.a), Synthesis and characterisation of [EtOHVIM]Cl followed prior protocols (Chaker et al., 2018).

With an anion exchange reaction, [EtOHVIM][HSO_4] was synthesized by combining sulfuric acid H_2SO_4 (0.56 mL, 10 mmol) and [EtOHVIM]Cl (5.0 g, 10 mmol); a slow addition was maintained to prevent excessive heat generation and unwanted side reactions. The mixture was stirred vigorously in 30 mL of acetonitrile at room temperature for 24 h (Scheme 1.b). After that, acetonitrile was removed under reduced pressure, and the crude product was rinsed with diethyl ether (3 × 30 mL) to eliminate unreacted components and byproducts. The final ionic liquid was obtained by vacuum drying at reduced pressure for 3 hours to remove residual solvents.

2.3. Polymerization of [P-EtOHVIM][H_2PO_4]

According to scheme (2.a.b), [P-EtOHVIM]Cl and [P-EtOHVIM][HSO_4] were synthesized and characterized according to procedures reported previously (Chaker et al., 2018) .

For the preparation of [P-EtOHVIM][H_2PO_4] (Scheme 2.a.b) via an anion exchange reaction, a combination of [P-EtOHVIM]Cl (10 mmol, 1.82 g) and concentrated phosphoric acid (10 mmol, 0.53 mL), was vigorously agitated at room temperature for 48 hours. After completion of the reaction, contaminants were removed by washing the crude product with acetone.

To minimize water continuous agitation under vacuum conditions (≈10) at 70 °C for several hours.

For optimal preparation and complete drying, the product was further dried under a high vacuum (pressure $< 10^{-5}$ bar) and approximately 40 °C for two days. Finally, any residual moisture was removed using phosphorus pentoxide (P_2O_5) as a drying agent.

2.4. Characterizations

^1H and ^{13}C NMR spectra were acquired using a 400 MHz Avance spectrometer. The chemical shifts (δ) are stated in ppm and referred to the internal signal solvent D_2O.

Fourier Transform mid-infrared Total Reflectance Attenuated (FTIR /ATR) measurements were acquired on a Bruker Vertex II-70 RAM Spectrometer (Bruker Analytical, Madison, WI) operating with a Golden Gate diamond ATR accessory TM (Specac Ltd, Slough, United Kingdom). FTIR/ATR spectra [4000–600 cm^{-1}] were collected with a Resolution of $1cm^{-1}$ by co-adding 64 scans for each spectrum. The OPUS Software 6.0 for Windows was used for the management of the instrument.

For DSC characterization, a (NETZSCH DSC 204 F1) was used with a speed of heating and cooling of 10 °C /min, performing two heating and cooling cycles to remove traces of water and solvent in a temperature range of −60 °C to 200 °C under Argon.

To determine the degradation of [EtOHVIM][HSO_4] and [P-EtOHVIM][H_2PO_4], TGA and DTG experiments were made with NETZSCH STA 449 C (TGA-DSC) system coupled to a mass spectrometer for analysing the gas emitted, in a temperature range of 20 °C to 400 °C at a scan rate of 5 °C/min under a high purity argon flux (60 mL/ min).

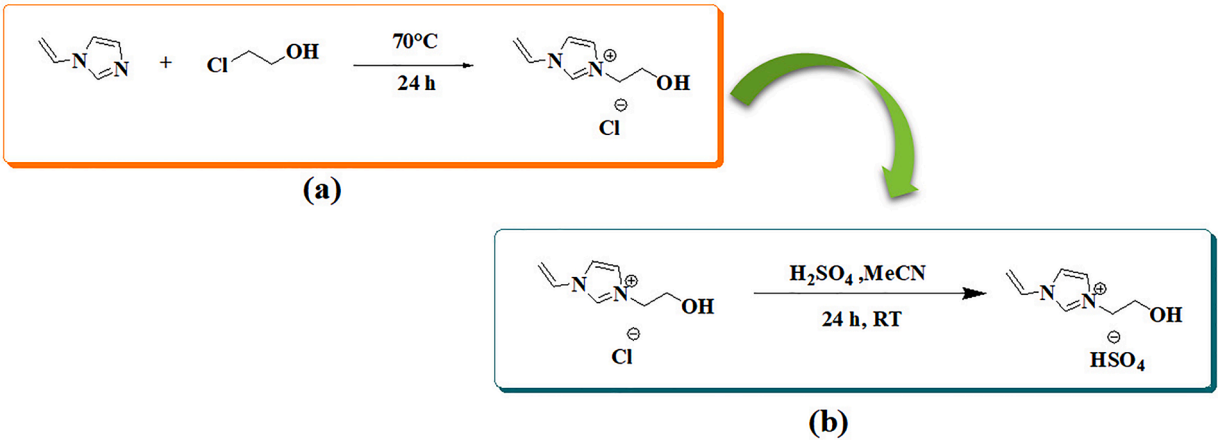

Scheme 1. (a) Amine quaternization and (b) Anion exchange reactions.

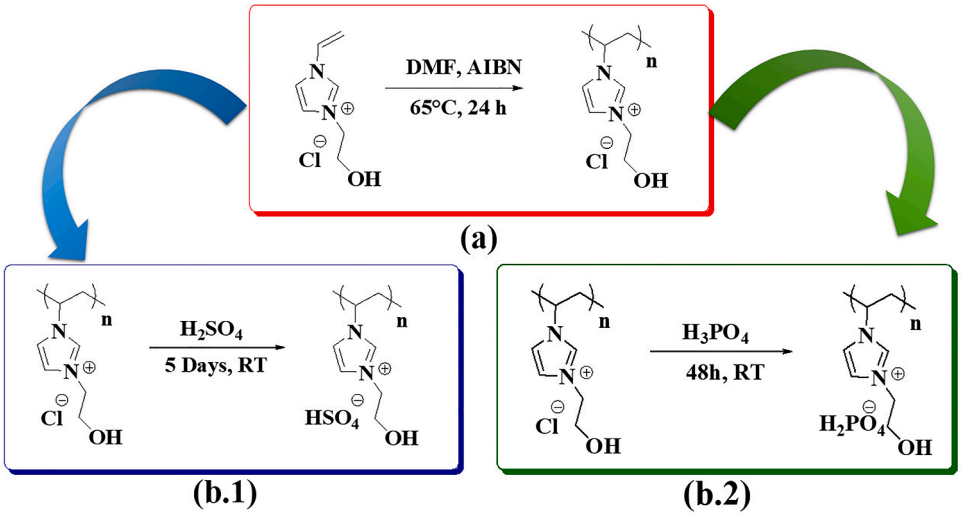

Scheme 2. (a) Polymerization and (b.1) (b.2) anion exchange reactions.

2.5. Conductivity measurements

Dielectric measurements were performed in the temperature range from 100 to 400 K and in the frequency range between 10 [and 2] and 10^6 Hz using a Novocontrol Alpha impedance analyzer. All the measurements are carried out isothermally, where the temperature was controlled by a Quatro Novocontrol cryo-system with stability of 0.1 K. The samples were prepared utilising brass spectrometer ground plates. Cylindrical glass fiber spacers with a diameter of 50 μm were employed to achieve a consistent electrode distance and planar geometry. Most samples utilized top brass electrodes with a 10 mm diameter (fig s1). However, due to the reactivity of the [EtOHVIM][HSO_4] sample, gold electrodes were used instead.

The sample cell was prepared in an open geometry configuration and subsequently annealed according to the specifications. All samples were subjected to a vacuum environment of approximately ~$1e^{-6}$ mbar for 24 h. Most samples underwent an annealing process for 12 h at elevated temperatures, and then the top electrodes were placed on the sample material while still under an inert atmosphere and then transported to the spectrometer. All measurements were conducted under an inert and dry nitrogen atmosphere to maintain consistent conditions during the experiments.

3. Results and discussions

3.1. NMR results

The structures of the acquired products were confirmed using ^{1}H and ^{13}C NMR spectroscopy, ensuring the absence of any significant impurities.

The ^{1}H NMR spectrum of [EtOHVIM][HSO_4] (Fig S.2) showed distinct signals corresponding to its structural features. The resonance at δ = 9.09 ppm (t, 1H) was assigned to the proton of the hydrogen sulfate group (HSO_4), while the singlet at δ = 8.95 ppm corresponded to the imidazolium proton H(d). The aromatic protons H (c) and H (c') appears as singlets at δ = 7.8 ppm and δ = 7.54 ppm, respectively. The multiplet observed at δ = 7.19 ppm was attributed to the proton H(b). The vinyl protons (-CH═CH_2) were represented by double doublets at δ = 5.81 ppm (J = 15.6, 2.6 Hz) and δ = 5.44 ppm (J = 8.7, 2.7 Hz), corresponding to H(a) and H (a'). the signal at δ = 4.79 ppm (m, 4H) was assigned to the methylene protons (2H(e) and 2H(f)), while the hydroxyl group proton (-OH) appeared as a multiplet at δ = 4.37 ppm.

The ^{13}C NMR spectrum revealed resonances consistent with the structural framework of the [EtOHVIM][HSO_4] ionic liquid. Both the carbons of the imidazolium nucleus and the vinyl carbons were observed in the unshielded part. Conversely, tow methylene carbons displayed chemical shifts between 50 and 60 ppm in the aliphatic section.

The ^{13}C NMR spectrum revealed resonances consistent with the

structural framework of the [EtOHVIM][HSO_4] ionic liquid. Both the carbons of the imidazolium nucleus and the vinyl carbons were observed in the unshielded part. Conversely, tow methylene carbons displayed chemical shifts between 50 and 60 ppm in the aliphatic section.

The only difference between [EtOHVIM][HSO_4] and [EtOHVIM][Cl] (Chaker et al., 2018) is the appearance of the peak at 9.09 ppm corresponding to the hydrogen sulfate group [HSO_4] anion.

Regarding poly ionic liquids (PILs), no significant difference appears between the ^{1}H NMR spectra of [P-EtOHVIM]Cl (Chaker et al., 2018) and [P-EtOHVIM][H_2PO_4] (Fig. S.2).

Similarly, the ^{13}C NMR spectrum shows the disappearance of two peaks in the more shielded region. These spectral changes provide strong evidence of polymerization, leading to the formation of [P-EtOHVIM]Cl (Chaker et al., 2018) and [P-EtOHVIM][H_2PO_4] (Fig. S.2). For [P-EtOHVIM][HSO_4], NMR characterization was not included in the study by Y. Chaker et al.; however, the structure of the polymer was confirmed through comprehensive vibrational analysis.

3.2. Comparative study on FTIR/ATR of investigated ILs

Fig. 1 illustrates the FTIR/ATR spectra [4000–600 cm^{-1}] of the five synthesized ionic liquids, while Table 1 summarizes the observed IR absorption bands and their corresponding vibrational assignments. These data confirm the successful synthesis and anion exchange processes, consistent with previous reports. (Chaker et al., 2018; Zaoui et al., 2021; Chaker et al., 2016)

In the low-frequency range (500 −700 cm^{-1}), we observed bending modes associated with δ(S–O) and δ(P–O) vibrations in [EtOHVIM][HSO_4], [P-EtOHVIM][HSO_4], and [P-EtOHVIM][H_2PO_4]. This demonstrated that the sulfate and phosphate anions remained following the anion exchange. The peaks around 647 cm^{-1} in all the samples are due to CH_3(N) wagging and CN stretching. The C—H and N—H deformations that are out of plane are responsible for the indistinct bands at approximately 684 −706 cm^{-1}.

There are several weak to medium bands in the range of 750 to 960 cm^{-1} that are caused by ρas(CH_2) and ω(C—H) vibrations. These bands are consistent with aliphatic chain architectures and vinyl groups. A distinctive sulfate stretching band about 966 cm^{-1} is observed in [HSO_4] based structures, and weak CH_3N stretching modes are also detected. Strong peaks that matched S-OH, C—O, and P-OH stretching vibrations were found between 1000 and 1150 cm^{-1}. The [P-EtOHVIM][H_2PO_4] sample had strong peaks at between 1016 and 1039 cm^{-1}, which showed that the phosphate had been successfully added.

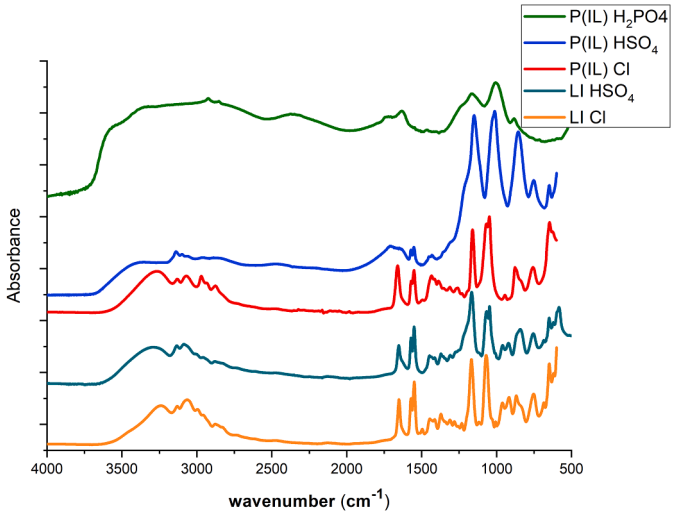

Fig 1. FTIR spectra of [EtOHVIM]Cl, [EtOHVIM][HSO_4], [P-EtOHVIM]Cl, [P-EtOHVIM][H_2PO_4] and [P-EtOHVIM][HSO_4].

In the 1150–1350 cm^{-1} range, absorptions associated to CH_2(N)/CH_3(N)CN stretching and ring in-plane asymmetric stretching were found. Peaks at 1161–1167 cm^{-1} were constant across IL and PIL samples, suggesting retention of the imidazolium framework. Weaker bands between 1232 and 1282 cm^{-1} further support the existence of substituted aromatic rings.

The 1350–1500 cm^{-1} range showed weak to medium intensity peaks due to δ(CH_2) and CH deformation modes, which support the aliphatic character of side chains in the produced compounds.

Strong absorptions at 1550–1577 cm^{-1} were attributed to asymmetric stretching of CH_2(N)/CH_3(N) and were consistently evident across all samples. A strong imidazole ring $C = N/C = C$ vibration was also visible between 1626–1659 cm^{-1}, with small shifts suggesting changes in anion environment and polymer backbone rigidity.

In the high-frequency region (2800–3300 cm^{-1}), multiple C—H stretching bands were identified. Asymmetric and symmetric stretching of CH_2 groups appeared at ~2875, 2921–2952 cm^{-1}, while =*C*—H stretching of aromatic imidazole rings appeared in the 3128–3135 cm^{-1} range. Broad O–H stretching modes observed at 3240–3380 cm^{-1} in [HSO_4] and [H_2PO_4] containing samples, consistent with the presence of acidic protons and hydrogen bonding interactions.

3.3. Thermal analysis

Fig. 2 presents a valuable graphical representation obtained by differential scanning calorimetry (DSC), which illustrates the thermal characteristics of the compounds [EtOHVIM][HSO_4] and [P-EtOHVIM][H_2PO_4].

For [EtOHVIM][HSO_4] (Fig. 2.a) showed a step change in heat flow corresponding to a glass transition temperature T_g = −8.5 °C, with no corresponding endothermic peak, indicating the absence of a defined melting point.

In the case of [P-EtOHVIM][H_2PO_4] (Fig. 2.b), T_g was detected at approximately 20 °C. Notably, the glass transition temperatures (T_g) for both compounds were determined from the second heating scan in the DSC measurements, which eliminated the effects of thermal history to ensure reliable data. Furthermore, [P-EtOHVIM][H_2PO_4] decomposition is characterized by a peak at 124 °C observed in the heating phase corresponding to the melting point (T_m). A similar peak at 146 °C marks a significant step in its decomposition process. However, an additional endothermic peak at 172 °C, observed in the DSC curve, indicates the complete decomposition of this poly ionic liquid. Finally, an exothermic peak was observed at 186 °C.

Fig 3. displays the TGA and DTG curves of [EtOHVIM][HSO_4] and [P-EtOHVIM][H_2PO_4].

Fig 3.a, [EtOHVIM][HSO_4]. This IL degrades in two phases between 20 °C and 400 °C, with decomposition starting at 50 °C remaining stable below this temperature. The first degradation stage, which proximately began at 50 °C and ended at 150 °C, resulted in a 3.53 % mass loss, corresponding to the removal of H_2O gas. The IL imidazolium cation decomposed in the second step, which began at 163 °C and finished at around 390 °C, resulting in a mass loss of 61.92 % due to dealkylation and degradation.

Fig 3.b, [P-EtOHVIM][H_2PO_4]. This PIL remains stable below 50 °C, and the degradation process started after this temperature and progressed in four phases until 600 °C. The first stage, begins at approximately 50 °C with a mass loss of 15.58 %, concluding at 150 °C, corresponding to the release of H_2O gas recognized from the TG mass spectrometry curve (fig. S4) due to dehydration processes or volatile solvents (Ping et al., 2001). The decomposition of organic functional groups (loss of 4.91 %) started at 180 °C and finished around 260 °C. The third stage, which occurred between 250 and 350 °C, with a loss of 11.63 % associated with the dealkylation degradation of the IL imidazolium cation. Final decomposition is the major decomposition of dihydrogen phosphate anion at 350 °C. In addition, temperatures greater than 600 °C are required for the poly ionic liquid (H_2PO_4) to completely

Table 1
Observed FTIR/ATR bands and their assignment of 1-(hydroxyethyl)-3-vinylimidazolium chloride, poly1-(hydroxyethyl)-3-vinylimidazolium chlorideand poly1-(hydroxyethyl)-3-vinylimidazolium sulfate (vw = very weak, *w* = weak, *m* = medium, *s* = strong, sh = shoulder, ν = Str = stretching, δ = deformation, bend = bending deformation, ω = wagging, ρ = rocking, *s* = symmetric, as = asymmetric).

[EtOHVIM]Cl (Chaker et al., 2018)	[EtOHVIM] [HSO_4]	[P-EtOHVIM]Cl (Chaker et al., 2018)	[P-EtOHVIM][HSO_4] (Chaker et al., 2018)	[P-EtOHVIM] [H_2PO_4]	Assignment	Refs
	584 (m)		611 (vw)	587 (vw)	δ(S–O), δ(P–O)	(Chaker et al., 2018; Zaoui et al., 2021; Chaker et al., 2016)
619 (w)		627 (sh)	622 (vw)		ω (N—H)/CH_3(N) CN Str	(Chaker et al., 2018; Zaoui et al., 2021)
647 (m)	647 (m)	647 (m)	647 (m)		ω (N—H)/CH_3(N) CN Str	(Chaker et al., 2018; Zaoui et al., 2021)
684 (vw)	684 (vw)		698 (m)	706 (vw)	ω (C—H) + ω (N—H)	(Chaker et al., 2018; Zaoui et al., 2021)
752 (m)	757 (m)	752(m)	753(m)		ω (C—H)	(Chaker et al., 2018; Zaoui et al., 2021)
833 (w)	848 (w)	835 (w)			$\rho_{as}(CH_2)$	(Chaker et al., 2018; Zaoui et al., 2021)
869 (w)		877 (sh)	854 (s)	879 (w)	$\rho_{as}(CH_2)$	(Chaker et al., 2018; Zaoui et al., 2021)
916 (w)	921 (w)				$\rho_{as}(CH_2)$	(Chaker et al., 2018; Zaoui et al., 2021)
960 (w)		944(vw)	945(sh)		ω (C—H)	(Chaker et al., 2018; Zaoui et al., 2021)
	966 (w)		968 (sh)		ν (S-O)	(Chaker et al., 2018; Zaoui et al., 2021)
	1039(s)		1004(s)		S-OH CH_3N Str/CH_2N Str	(Chaker et al., 2018; Zaoui et al., 2021)
				1016(s)	ν(C–O), ν(P–OH)	(Chaker et al., 2018; Zaoui et al., 2021)
1027 (w)		1048(s)	1044(sh)		CH_3N Str/CH_2N Str	(Chaker et al., 2018; Zaoui et al., 2021)
1069(s)	1067(s)	1069 (s)	1061		ν (C—O)	(Chaker et al., 2018; Zaoui et al., 2021)
1118 (vw)			1094(sh)		CC Str	(Chaker et al., 2018; Zaoui et al., 2021)
1167 (s)	1167 (s)	1161(s)	1157(s)	1161(s)	Rings CH_2(N) and CH_3(N)CN Str	(Chaker et al., 2018; Zaoui et al., 2021)
			1216(sh)		Ring ip as strstr	(Chaker et al., 2018; Zaoui et al., 2021)
1232 (vw)		1228(vw)		1243 (sh)	Ring ip as strstr	(Chaker et al., 2018; Zaoui et al., 2021)
1282 (vw)		1266 (vw)	1265		Ring ip as strstr	(Chaker et al., 2018; Zaoui et al., 2021)
1310 (vw)	1313 (vw)	1310(vw)	1312(vw)		ν (C—C)	(Chaker et al., 2018; Zaoui et al., 2021)
			1357 (w)		ν (C—C)	(Chaker et al., 2018; Zaoui et al., 2021)
1371 (w)	1367 (w)	1386 (w)	1380 (vw)		ρ(N—H)	(Chaker et al., 2018; Zaoui et al., 2021)
1431 (sh)	1413 (w)	1410 (m)			ρ(N—H)	(Chaker et al., 2018; Zaoui et al., 2021)
1447 (m)		1435 (sh)	1431 (m)		δ (CH_2)/CCH HCH as bend	(Chaker et al., 2018; Zaoui et al., 2021)
	1452 (w)		1452 (m)	14–2 (w)	δ (CH_2)/CCH HCH as bend	(Chaker et al., 2018; Zaoui et al., 2021)
1495 (w)		1495 (vw)	1492 (vw)		δ (CH_2)/CCH HCH as bend	(Chaker et al., 2018; Zaoui et al., 2021)
1549(s)	1550(s)	1550 (s)	1550 (s)		as Str CH_2(N)/ CH_3(N)CNStr	(Chaker et al., 2018; Zaoui et al., 2021)
1570 (sh)	1577 (s)	1570 (sh)	1570(s)		as Str CH_2(N)/ CH_3(N)CNStr	(Chaker et al., 2018; Zaoui et al., 2021)
1650 (m)	1659 (m)	1659 (s)	1646 (m)	1626 (w)	Ring *C* = *C* str, *N* = *C*—N str	(Chaker et al., 2018; Zaoui et al., 2021)
				1736 (w)	ν(*C* = *N*), ν(*C* = *C*)	(Chaker et al., 2018; Zaoui et al., 2021)
2737 (sh)	2729 (w)	2732 (sh)			Ring *C* = *C* str, *N* = *C*—N str	(Chaker et al., 2018; Zaoui et al., 2021)
2822 (sh)	2822 (w)	2822 (sh)	2852		Ring *C* = *C* str, *N* = *C*—N str	(Chaker et al., 2018; Zaoui et al., 2021)
2875 (m)	2885 (w)	2875 (m)		2854 (w)	ν_s (CH_2)	(Chaker et al., 2018; Zaoui et al., 2021)
2951 (m)	2952 (w)	2937 (sh)	2921 (m)	2927 (w)	ν_{as} (CH_2)	(Chaker et al., 2018; Zaoui et al., 2021)
		2973 (m)	2955 (vw)		ν_{as} (CH_2)	(Chaker et al., 2018; Zaoui et al., 2021)

(*continued on next page*)

Table 1 (*continued*)

[EtOHVIM]Cl (Chaker et al., 2018)	[EtOHVIM][HSO_4]	[P-EtOHVIM]Cl (Chaker et al., 2018)	[P-EtOHVIM][HSO_4] (Chaker et al., 2018)	[P-EtOHVIM][H_2PO_4]	Assignment	Refs
2992 (m)	3003 (w)	2969 (vw)			ν (C—H)	(Chaker et al., 2018; Zaoui et al., 2021)
			3027 (sh)		ν (C—H)	(Chaker et al., 2018; Zaoui et al., 2021)
3067 (m)	3088 (m)	3071 (m)	3092 (s)		ν (C—H)	(Chaker et al., 2018; Zaoui et al., 2021)
3128 (m)	3135 (m)	3132 (m)			=*C*—H Str	(Chaker et al., 2018; Zaoui et al., 2021)
3240 (s)	3292 (s)	3267 (s)	3269(sh)		ν (C—OH)	(Chaker et al., 2018; Zaoui et al., 2021)
			3381 (m)	3376 (m)	ν (C—OH)	(Chaker et al., 2018; Zaoui et al., 2021)

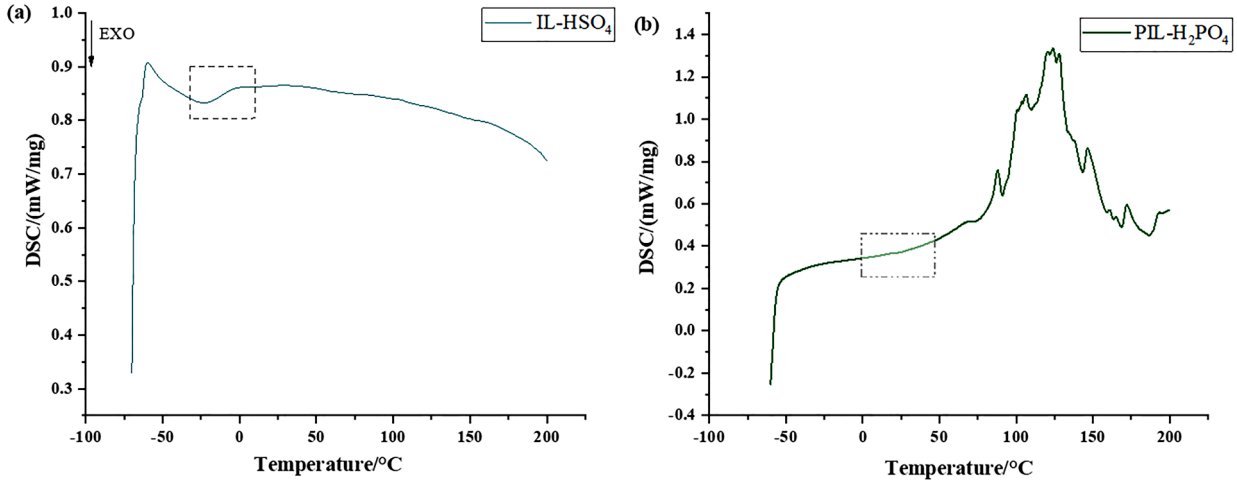

Fig. 2. (a) DSC thermogram of [EtOHVIM][HSO_4] and (b) [P-EtOHVIM][H_2PO_4] from −60 °C to 200 °C.

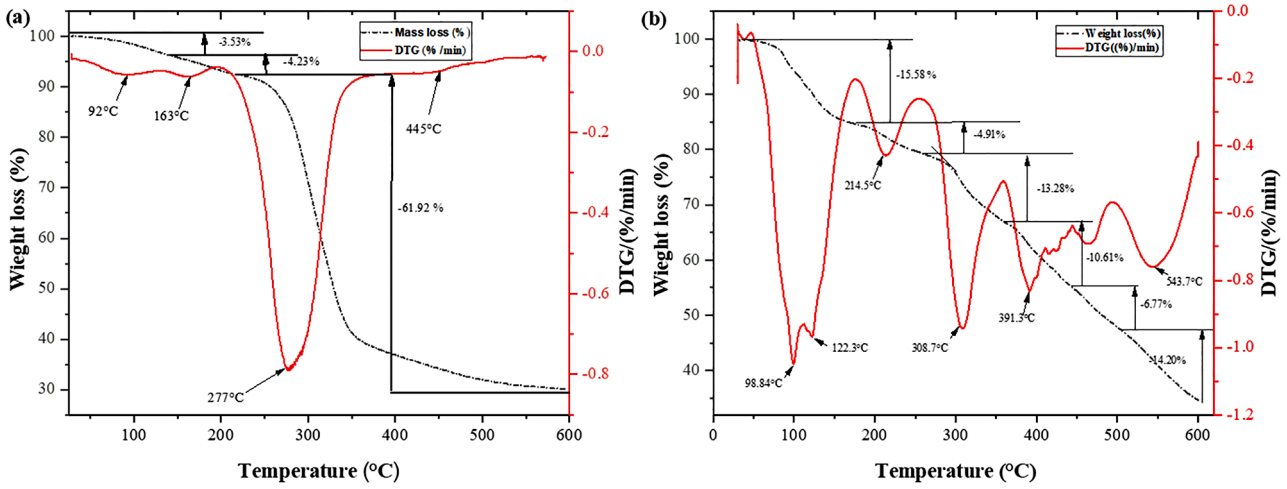

Fig. 3. (a) TGA and DTG curves of [EtOHVIM][HSO_4] and (b) [P-EtOHVIM][H_2PO_4] from 20 °C to 600 °C.

decompose thermally. Ultimately, the [P-EtOHVIM][H_2PO_4] demonstrated initial thermal stability up to approximately 50 °C, beyond which weight loss begins with a residual weight of ~ 35 % was observed, and multiple degradation steps that suggest complex thermal decomposition behavior, which is characteristic of polyionic liquids with interact molecular architecture.

The water loss can be attributed to the hydrophilic characteristic of this PIL (Fernandes et al., 2019). This hydrophilicity depends on its constituent ions' nature and ability to interact with water molecules (Mikkelsen, 1994; Bayliss and Schmidt, 2023). In more detail for this case, the dihydrogen phosphate anion [H_2PO_4] anion contains two -OH groups, allowing extensive hydrogen bonding with both water and polymer side chains (Rodrigues et al., 2021; Yousefi et al., 2017). This capability often indicates higher water retention, more hydrated structure and, certain level of hydrophilicity. Therefore, [P-EtOHVIM][H_2PO_4] can be considered as a hydrophilic ionic liquid.

At high temperatures, the [P-EtOHVIM][H_2PO_4] ability to decompose is limited by the development of a robust P–O···H–O–P network.

Additionally, [P-EtOHVIM][H_2PO_4] and [EtOHVIM][HSO_4] with hydrogen bonding networks have greater decomposition temperatures and superior mechanical stability as compared to those that mainly depend on van der Waals interactions (Yankova and Tankov, 2021).

A comparative assessment of the thermal stability across all MILs and PILs based on Y. Chaker et al. and T. Zaoui et al. (Chaker et al., 2018; Zaoui et al., 2021) studies indicates the following, while Table 2 summarizes their thermal decomposition proprieties.

(i) The decomposition process of [P-EtOHVIM][H_2PO_4] exhibited multiple endothermic peaks. In contrast, [P-EtOHVIM][HSO_4] showed a single endothermic peak at 144.9 °C, corresponding to its melting point and indicating a complete decomposition process. Additionally, [P-EtOHVIM]Cl displayed a slower decomposition behavior compared to the other polyionic liquids, with a melting point of 154 °C. The glass transition temperatures (Tg) were found to be 82 °C, −13 °C, and 20 °C for [P-EtOHVIM]Cl, [P-EtOHVIM][HSO_4], and [P-EtOHVIM][H_2PO_4], respectively. The DSC thermograms of molecular and polymer ionic liquid reveal a glass transition but no crystallization peak. This shows that they are amorphous at the observed temperatures (Casimiro and Nijmeijer, 2022).

(ii) The thermogravimetric curves of MILs and PILs show considerable thermal degradation above 300 °C, indicating degradation of the imidazolium ring. Among the samples, [P-EtOHVIM][H_2PO_4] exhibited the least thermal stability, with mass loss beginning as early as 100–150 °C and continuing gradually up to 500 °C, indicating a multi-step and extended decomposition process. On the other hand, [P-EtOHVIM][HSO_4] had a clearer and faster decomposition phase, with a significant mass loss starting at around 230 °C and the remaining mass dropping to about 10 % by 400 °C, which means it is more thermally stable. The decomposition profile of [P-EtOHVIM]Cl was similar to that of [EtOHVIM][HSO_4]. It started to break down between 230 and 250 °C and finished around 400 °C, which suggests that it has a similar level of thermal resistance. It was found that the monomeric forms, [EtOHVIM]Cl and [EtOHVIM][HSO_4], were not as stable when heated as the polymeric forms. [EtOHVIM]Cl broke down completely by 400 °C, which was earlier than [P-EtOHVIM]Cl. [EtOHVIM][HSO_4] lost mass quickly starting around 200 °C, which means it had moderate thermal stability. In general, the results indicate that polymerization renders ILs more thermally stable, particularly for ionic liquids based on [HSO_4] and Cl anions. On the other hand, the [H_2PO_4] anion based PIL is still less thermally stable.

DSC and Thermogravimetric analysis showed that [EtOHVIM][HSO_4] and [P-EtOHVIM][H_2PO_4] compared with MILs and PILS investigated in this study possess low glass transition temperature, a good thermal stability, and decomposition at higher temperatures. Furthermore, it must be noted that the chain polymerization and the type of anion significantly impacted thermal stability (Casimiro and Nijmeijer, 2022; Cao and Mu, 2014).

3.4. Dielectric analysis

Broadband dielectric spectroscopy (BDS) is ideally suited to compare and examine the dielectric properties of three polymeric ionic liquids [P-EtOHVIM][H_2PO_4], [P-EtOHVIM]Cl, [P-EtOHVIM][HSO_4] and two monomeric ionic liquids [EtOHVIM][HSO_4], [EtOHVIM]Cl with systematically varied anion composition. The research is centered on analysing of conductivity and dielectric relaxation processes in the frequency range of 10^{-2} to 10^{6} Hz.

The molecular dynamics and charge transport mechanism of the MILs and PILs under study are investigated using BDS spectroscopy. The BDS spectrum is characterised by a superposition of the real and imaginary components of the complex dielectric function ($\varepsilon^* = \varepsilon' - i\varepsilon''$) and the complex conductivity ($\sigma^* = \sigma' + \sigma''$), as shown in Fig. 4. This analysis identified and described a combination of phenomena, including (i) electrode polarization (EP), (ii) conductivity or charge transport, and (iii) molecular relaxation processes (Kremer and Schönhals, 2002; Anton et al., 2020; Frenzel et al., 2019; Chen et al., 2018; Frenzel et al., 2017; Frenzel et al., 2016).

Particularly remarkable at elevated temperatures and low frequencies, electrode polarization

(EP) is identified by a significant rise in ε' or σ'' versus frequency. This surge indicates the gathering of mobile charges, whether ionic or polaronic, at the interface connecting the sample and the electrode. Therefore, the surge mentioned above may reflect the contribution of both ionic and polaronic carriers to the overall charge accumulation at the electrode interface in the case of polyionic liquids (Kremer and Schönhals, 2002; Gao et al., 2021; Emin, 2013). In contrast, for monomeric ionic liquids (MILs), electrode polarization arises solely from the accumulation of ionic charge carriers. The distinct elevation in low-frequency behavior, especially in MILs, highlights the intricate nature of polymeric ionic liquids. The rationale behind this observation is rooted in the notion that the movement of charge carriers is considerably impeded or slowed down at the interface between the metal and the ionic conductor due to coulombic interactions (Serghei et al., 2009).This phenomenon is characteristic of polar dielectrics, as the temperature rise facilitates dipole orientation, leading to an augmentation in permittivity (Mohan et al., 2010). Although electrode polarization (EP) is generally more prominent in monomeric ionic liquids (MILs) than in polymeric ionic liquids (PILs), [EtOHVIM]Cl exhibits strong EP, particularly at elevated temperatures, due to the small and highly mobile Cl anion, which facilitates interfacial charge accumulation. In contrast, [P-EtOHVIM]Cl shows reduced EP, as polymerization restricts ion mobility and space charge formation. A similar trend is observed for [P-EtOHVIM][HSO_4] (Fig. 4c), while its monomeric counterpart [EtOHVIM][HSO_4] (Fig. 4d) displays pronounced and rapid EP. Interestingly, [P-EtOHVIM][H_2PO_4], despite being a PIL, exhibits strong EP comparable to the monomeric ILs, likely due to enhanced ion transport

Table 2
Thermal properties of [EtOHVIM]Cl, [EtOHVIM][HSO_4], [P-EtOHVIM]Cl, [P-EtOHVIM][HSO_4] and [P-EtOHVIM][H_2PO_4].

Temperature	T_g (°C)	T_m(°C)	DSC Peak Characteristics	Interpretation	T_d (°C)	T_{Td} (°C)	DTG - ATG Characteristics	Interpretation
[EtOHVIM]Cl	——	−44Chaker et al., 2018	Gradual, no peak	Likely glassy or decomposes before melting	294.1	445	Earlier, weaker peak	Lower stability, decomposes earlier
[EtOHVIM][HSO_4]	−8.5	116	Flat curve	Stable or no transition in this range	277	600	Similar to IL-Cl, slightly shifted	Lower thermal stability than PILs
[P-EtOHVIM]Cl	82	154Chaker et al., 2018	Clear melting (~250 °C)	Moderately stable	283	419	Deep, narrow peak around	High decomposition rate, single phase
[P-EtOHVIM][HSO_4]	−13	144.9Chaker et al., 2018	Strong melting peak (~280 °C)	High thermal stability	287	600	Deep, narrow peak around ~310–320 °C	Rapid, one-step decomposition
[P-EtOHVIM][H_2PO_4]	20	124	Broad, multiple transitions	least stable; overlapping melting and decomposition	308	< 600	Broader, slightly earlier peak	Multi-step or slower decomposition

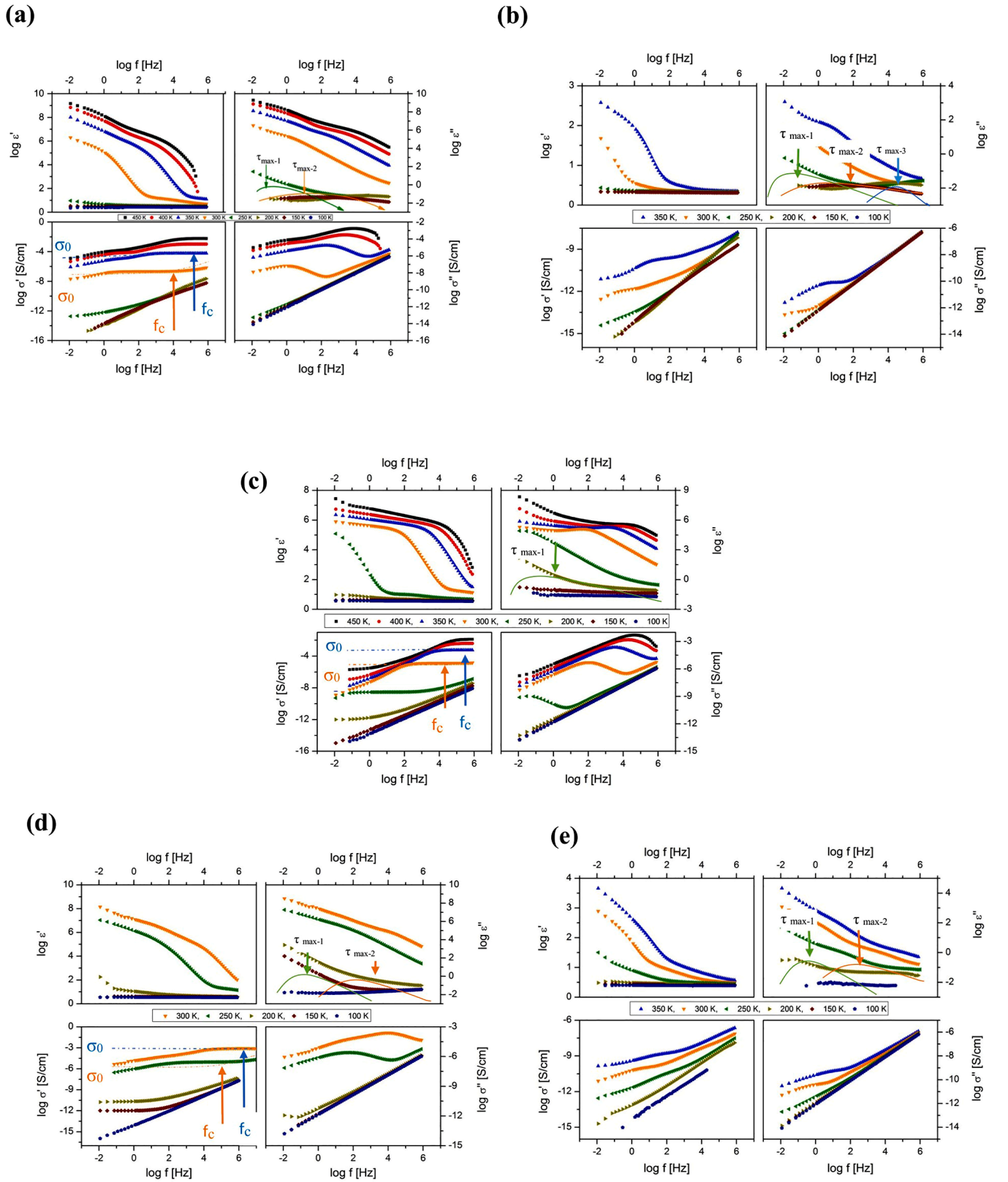

Fig. 4. Complex dielectric function (ε*=ε'(f)-iε''(f)) and complex conductivity function (σ*= σ'(f) + iσ''(f)) of (a) [EtOHVIM]Cl, (b) [P-EtOHVIM]Cl, (c) [P-EtOHVIM][H_2PO_4] (d) [EtOHVIM][HSO_4] and (e) [P-EtOHVIM][HSO_4], at different temperatures as indicated. Havriliak-Negami-function analysis using mean relaxation durations τ_{max-1} (green line), τ_{max-2} (orange line), and τ_{max-3} (blue line) reveals dielectrically active relaxation processes reflecting molecular dynamics in ε'' vs. f. Charge transfer is defined by DC-conductivity σ_0 and critical frequency $\omega_c = 2\pi fc$. The first is a plateau in σ_0 vs. f, whereas the second is the frequency necessary to overcome the highest DC-conductivity barrier, indicating a power law dependency $\sigma_0 \sim \omega_\chi$. The Dyre-function (dashed-dotted lines) analyzes σ_0 and ω_c in σ_0 vs. f.

associated with its hydrophilic character.

Concerning charge transport (ii), the dielectric spectra revealed one or more relaxation processes characterized by a distinct plateau in σ' versus frequency. This plateau represents the DC-conductivity σ_0 and the critical frequency ω_c, which marks the onest of a power-law relationship $\sigma' \sim \omega^x$. The frequency ω_c is interpreted as the crucial hopping rate of mobile charge carriers that contribute to σ_0 to overcome the highest potential barrier (Kremer and Schönhals, 2002; Dyre and Schrøder, 2000). (iii) Dielectric active relaxation processes provide information on the dynamics of molecules. The mean structural relaxation times $\omega_{max} = \tau_{max}^{-1}$ could be precisely found by examining ε''(f). Energy dissipation is shown by the graph's characteristic peaks, which must be analysed using the empirical Havriliak–Negami formula (Havriliak and Negami, 1967), which builds upon the Debye formula by incorporating two extra shape parameters, β, and γ (Debye, 1929).

Plotting the latter as a function of the inverse temperature 1000/T (Fig 5) allows us to find the temperature dependency of two somewhat separated, hence independent, processes. For all MILs and PILs, one observes a transition of σ_0 and τ_{max-1} in its thermal activation from VFT-like eq (1) to an Arrhenius-law by decreasing temperatures eq (2)

$$\tau = \tau_\infty \, exp\left(\frac{DT_0}{T - T_0}\right) \quad (1)$$

Where, τ_∞ represents the relaxation time at high temperatures, D is a shape constant commonly known as the fragility index, and T_0 is the Vogel temperature.

$$\tau = \tau_0 exp\left(\frac{E_a}{k_b T}\right) \quad (2)$$

Where, τ_0 pre- exponential factor, E_a activation energy, R gas constant, and T absolute temperature.

The calorimetric glass transition temperature T_g, calculated by conventional DSC, scales well with the average structural relaxation time τ_{max-1} associated with the dynamic glass transition, as measured by BDS (Table 3). The sample [P-EtOHVIM][H_2PO_4] exhibits a glass transition temperature ($T_{g\text{-}BDS}$) of 219 by almost 7 K less than the value of [P-EtOHVIM][HSO_4] and 81 K less than [P-EtOHVIM]]Cl].

These differences in $T_{g\text{-}DSC}$ so $T_{g\text{-}BDS}$ values can be attributed to several factors: (i) Reduced segmental mobility in the polymer, due to its maximal involvement in hydrogen bonding, increases the glass transition temperature (T_g) (Kuo, 2008). The Kamlet–Taft β parameter indicates the hydrogen-bonding capabilities of various anions and can be

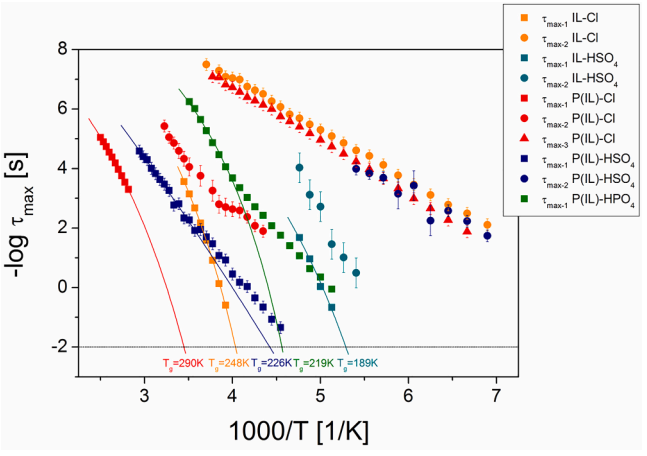

Fig. 5. Activation plot for all investigated samples. The presumably α-relaxations (τ_{max-1}) are depicted in squares, the secondary ones in circles and for [P-EtOHVIM]Cl one additional in triangles. The first ones are fitted with Vogel-Fulcher-Tammann functions; the extrapolated glass transition temperatures are indicated. The error-bars are comparable to the size of the symbols, if not explicitly indicated otherwise. The logarithm is to base 10.

Table 3
Comparison of the glass transition temperatures T_g as measured by DSC and extrapolated by BDS. VFT and Arrhenius-law equation regression values of temperature-dependent conductivity data of all MILs and PILs under study.

Temperature	$T_{g\text{-}DSC}$ (K)	$T_{g\text{-}BDS}$ (K)	σ_{RT} ($S{\cdot}cm^{-1}$)	E_a (eV)	T_0 (K)	D
[P-EtOHVIM]Cl	355Chaker et al., 2018	290	1.46E–12	0.371	——-	———
[P-EtOHVIM][HSO_4]	260Chaker et al., 2018	226	3.54E–11	0.331	———	———
[EtOHVIM]]Cl]	———	248	2.04E–07	0.076	188.51	10.81
[P-EtOHVIM][H_2PO_4]	293	219	1.99E–05	0.077	154.53	13.38
[EtOHVIM][HSO_4]	265	189	5.53E–04	0.038	163.61	6.18

used to understand their effects on the T_g of polymers. Chloride anion (Cl^-), as a small monatomic halide anion with high charge density, with a high β (0.84–0.95) value exhibits strong hydrogen-bonding accepting ability (Fukaya et al., 2006; Spange et al., 2014; Sappl et al., 2025), leading to strong interactions with cations, which restrict ion mobility and segmental motion, thereby raising T_g. On the other hand, hydrogen sulfate [HSO_4] and dihydrogen phosphate [H_2PO_4] function as asymmetric acidic anions with a moderate β value (~0.30–0.60) (Debeljuh et al., 2013; Shukla et al., 2012; Sulaimon et al., 2020). Their ability to interact with multiple but distant H-bond donor sites within the same cation results in a qualitative change in the H-bonding structures (Hunt et al., 2015). Such moderate hydrogen-bond basicity allows partial interaction with the cation, while their acidic hydrogen atoms can simultaneously act as hydrogen-bond donors (Joshi and Ghanty, 2013), facilitating interionic cross-linking (Song and Wang, 2020). This dual donor–acceptor character reduces polymer chain mobility, leading to low-to-intermediate T_g values compared to the Cl^- anion. (ii) differences in hydrophilicity degree - reflected in the residual water contents as determined by DSC and DTG analysis, (iii) and potentially different molecular weights which can influence segmental dynamics.

Moreover, the other mean relaxation rates are thermally Arrhenius-like activated, where the τ_{max-2} for [EtOHVIM]Cl and [P-EtOHVIM][HSO_4], as well as τ_{max-3} for [P-EtOHVIM]Cl, are similar, which indicates the same molecular origin, which is attributed to the liberation of the imidazolium ion with a mean activation energy $E_a = 0.064$ eV. The absence of secondary relaxation processes in [P-EtOHVIM][H_2PO_4], combined with a fragility index ($D = 13.38$), indicates that the polymer exhibits relatively strong glass-forming behavior. Besides the structural relaxation processes, the charge transport follows the Barton-Namikawa-Nakajima (BNN) relation, which relates the DC-conductivity σ_0 with the charge carrier hopping rate ω_0. This correlation holds accurate for all MILs and PILs over up to 9 orders of magnitudes (Fig. 6). Additionally, there is a correlation between the charge carrier hopping rate ω_c and the mean structural relaxation time τ_{max-1}, this indicates a 'dynamic glass transition assisted hopping' conduction (Frenzel et al., 2019; Frenzel et al., 2017; Frenzel et al., 2016; Barton and Morain, 1970; Turton et al., 2012; Frenzel et al., 2016; Sangoro et al., 2009).

On the one hand, the thermal activation of [P-EtOHVIM]Cl and [P-EtOHVIM][HSO_4] tends to be lower than their monomeric counterparts at absolute temperatures. This difference is evident in the higher values of T_g observed at a macroscopic level (Fig. 7). As was anticipated, [EtOHVIM][HSO_4] as a MIL with an asymmetric acidic anion shows an a VFT-type thermal activation above T_g with the highest direct current (DC) conductivity ($\sigma_{RT} = 5.53 \times 10^{-4}$ $S{\cdot}cm^{-1}$) among the investigated ionic liquids in this study (Table 3). For [P-EtOHVIM][H_2PO_4], the only investigated poly ionic that shows a noticeable shift in the thermal activation of σ_0 ($T_{\sigma 0}$). This shift can be observed in Fig. 7, where the dependence changes from a VFT-like behavior to an Arrhenius-law. $T_{\sigma 0}$

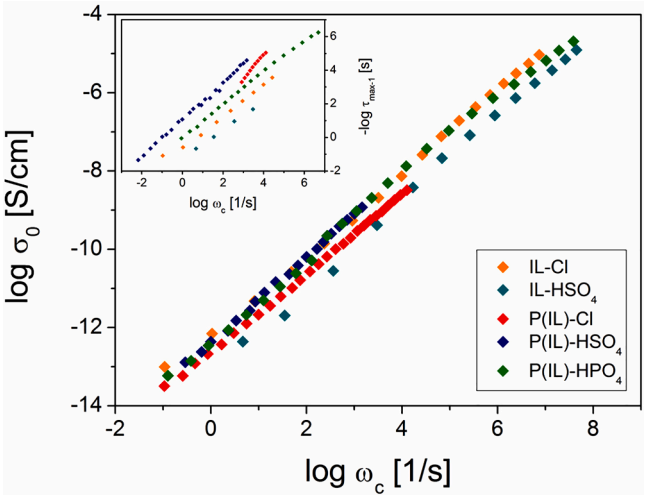

Fig. 6. Barton-Namikawa-Nakajima (BNN)-relation of the DC-conductivity σ0 and the charge carrier hopping rate ωc for all samples as indicated. Inset: correlation between the latter and the structural mean relaxation rate that is presumably assigned to the fluctuation of transient ion-pairs. The error-bars are comparable to the size of the symbols, if not explicitly indicated otherwise. The logarithm is to base 10.

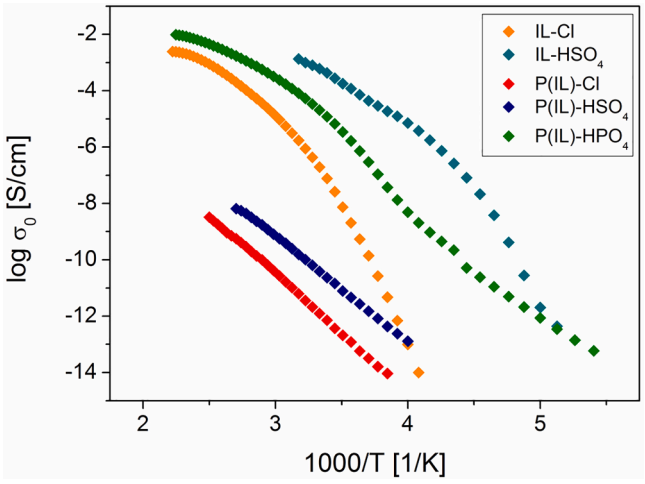

Fig. 7. Temperature-dependence of the DC-conductivity. For MILs and PILs one observes a transition at which its thermal activation changes from a VFT-law to an Arrhenius one. The error-bars are comparable to the size of the symbols, if not explicitly indicated otherwise. The logarithm is to base 10.

= 263 K was found to be close to the calorimetric glass transition T_g= 253 K.

Furthermore, [P-EtOHVIM][H_2PO_4] shows a comparably high DC-conductivity, which exhibits an ionic conductivity of $\sigma_{RT} = 1.99 \times 10^{-5}$ S·cm^{-1} (approaching the highest possible polymer ionic liquid conductivity of approximately ≈10^{-5} S·cm^{-1} at 25 °C, as reported by (Nosov et al., 2024)), this is remarkable for such an asymmetric acidic anion poly ionic liquid.

4. Conclusion

The anionic contribution of asymmetric hydrogen sulfate and dihydrogen phosphate for novel acidic ionic and polyionic liquids based on 1-(hydroxyethyl)-3-vinylimidazolium cation was comprehensively studied. The synthesis of [P-EtOHVIM][H_2PO_4], a polymeric ionic liquid and [EtOHVIM][HSO_4] as a monomeric ionic liquid were investigated using a range of techniques, including ^{1}H ^{13}C NMR, FTIR/ATR, DSC, and TGA, DTG.

These compounds exhibited interesting thermal and dielectric properties. (i) Thermal analysis revealed that both ionic liquids possess a good thermal stability and low glass transition temperature. [P-EtOHVIM][H_2PO_4] was identified as a hydrophilic polymeric ionic liquid with decomposition at higher temperatures. Furthermore, it must be noted that both chain polymerization, the type of acidic anion, leads to strong hydrogen bonds and a level of hydrophilicity; these effects significantly impact thermal stability. (ii) Dielectric analysis showed that [EtOHVIM][HSO_4], a MIL with an asymmetric acidic anion, exhibits a significant direct current (DC) conductivity and follows a VFT-type thermal activation behavior above Tg. The notable behaviors of the [P-EtOHVIM][H_2PO_4], such as hydrophilicity, a moderate thermal stability, the substantial impact of anion structure on glass transition temperature, and the hydrogen bonding networks, a transition from Vogel-Fulcher-Tammann to Arrhenius-type conductivity dependence at a characteristic temperature $T_{\sigma 0}$ all this proprieties alongside a significantly high ionic conductivity. In conclusion, [P-EtOHVIM][H_2PO_4] and [EtOHVIM][HSO_4] displayed, comparatively within the studied monomeric and polymeric ionic liquids, the highest ionic conductivity, making them good candidates for solid-acid electrolytes in electrochemical devices or as proton exchange membranes.

CRediT authorship contribution statement

Hadjer Guettaf: Writing – review & editing, Investigation, Formal analysis, Conceptualization. **Yassine Chaker:** Methodology, Formal analysis. **El Habib Belarbi:** Visualization, Validation, Supervision, Project administration, Methodology, Funding acquisition. **Mansour Debdab:** Validation, Supervision. **Taqiyeddine Moumene:** Formal analysis. **Abdelkader Benabdellah:** Formal analysis. **Serge Bresson:** Validation, Supervision.

Declaration of competing interest

The authors declare that they have no known competing financial interests or personal relationships that could have appeared to influence the work reported in this paper.

Acknowledgement

Authors affiliated to Synthesis and Catalysis Laboratory thank the ATRST-DGRSDT for financial support and Professor Freidrich KREMER and Mr. Falk Frenzel (University of Leipzig) for dielectric measurements.

Supplementary materials

Supplementary material associated with this article can be found, in the online version, at doi:10.1016/j.jil.2025.100175.

Data availability

Data sets generated during the current study are available from the corresponding author upon reasonable request.

References

Anton, A.M., Frenzel, F., Yuan, J., Tress, M., Kremer, F., 2020. Hydrogen bonding and charge transport in a protic polymerized ionic liquid. Soft Matter 16 (26), 6091. https://doi.org/10.1039/D0SM00337A.

Aschenbrenner, O., Supasitmongkol, S., Taylor, M., Styring, P., 2009. Measurement of vapour pressures of ionic liquids and other low vapour pressure solvents. Green Chem 11 (8), 1217. https://doi.org/10.1039/B904407H.

J. Barton, M. Morain, Hydrogen diffusion in silicate glasses, J. Non-Crystalline Solids, 3 (1) (1970) 115. https://doi.org/10.1016/0022-3093(70)90107-9.

Bayliss, N., Schmidt, B.V.K.J., 2023. Hydrophilic polymers: current trends and visions for the future. Prog. Polym. Sci. 147, 101753. https://doi.org/10.1016/j.progpolymsci.2023.101753.

Cai, R., Hu, G., Chenyang, Y., Huang, Z., Wang, X., Han, B., 2025. Amino-acid-functionalized methanesulfonate ionic liquids as effective and reusable catalysts for oleic acid esterification. Sustain. Mater. Technol. 43, e01190. https://doi.org/10.1016/j.susmat.2024.e01190.

Cao, Y., Mu, T., 2014. Comprehensive investigation on the thermal stability of 66 ionic liquids by thermogravimetric analysis. Ind Eng Chem Res 53 (20), 8651. https://doi.org/10.1021/ie5009597.

Casimiro, A., Nijmeijer, K., 2022. On the impact of the type of anion on the properties of solid-state electrolytes. Polymer (Guildf) 262, 125443. https://doi.org/10.1016/j.polymer.2022.125443.

Chaker, Y., Ilikti, H., Debdab, M., Moumene, T., Belarbi, E.H., Wadouachi, A., Abbas, O., Khelifa, B., Bresson, S., 2016. Synthesis and characterization of 1-(hydroxyethyl)-3-methylimidazolium sulfate and chloride ionic liquids. J. Mol. Struct. 1113, 182. https://doi.org/10.1016/j.molstruc.2016.02.017.

Chaker, Y., Debdab, M., Belarbi, E.H., Ilikti, H., Haddad, B., Moumene, T., Wadouachi, A., Van Nhien, A.N., Abassi, H.B., Abbas, O., Bresson, S., 2018. The influence of chloride and hydrogen sulfate anions in two polymerised ionic liquids based on the poly(1-(hydroxyethyl)-3-vinylimidazolium cation, synthesis, thermal and vibrational studies. Eur. Polym. J. 108, 138. https://doi.org/10.1016/j.eurpolymj.2018.08.032.

M. Chen, J.W. Dugger, X. Li, Y. Wang, R. Kumar, K.M. Meek, D.W. Uhrig, J.F. Browning, L.A. Madsen, T.E. Long, Polymerized ionic liquids: effects of counter-anions on ion conduction and polymerization kinetics, 56(13) (2018) 1346. https://doi.org/10.1002/pola.29015.

Chen, S., Frenzel, F., Cui, B., Gao, F., Campanella, A., Funtan, A., Kremer, F., Parkin, S.S.P., Binder, W.H., 2018b. Gating effects of conductive polymeric ionic liquids. J. Mater. Chem. C 6 (30), 8242. https://doi.org/10.1039/C8TC01936C.

Debeljuh, N.J., Sutti, A., Barrow, C.J., Byrne, N., 2013. Phase transition of poly(N-isopropylacrylamide) in aqueous protic ionic liquids: kosmotropic versus chaotropic anions and their interaction with water. J. Phys. Chem. B 117 (28), 8430. https://doi.org/10.1021/jp4043232.

P.J.L.H. Debye, Polare molekeln, (1929). https://doi.org/10.1038/125009a0.

L.E. Dickson, S. Brixi, C.L. Radford, J.G. Manion, T.L. Kelly, B.H.J.J.o.M.C.C. Lessard, Self-assembly of poly (ionic liquid) block copolymer based dielectrics on semiconductor formation and performance, Journal of Materials Chemistry C, 12 (44) (2024) 17902. https://doi.org/10.1039/D4TC03157A.

A.V. Dobrynin, M.J.P.i.p.s. Rubinstein, Theory of polyelectrolytes in solutions and at surfaces, 30(11) (2005) 1049. https://doi.org/10.1016/j.progpolymsci.2005.07.006.

J. Dupont, R.F. de Souza, P.A.J.C.r. Suarez, Ionic liquid (molten salt) phase organometallic catalysis, 102(10) (2002) 3667. https://doi.org/10.1021/cr010338r.

J.C. Dyre, T.B. Schrøder, Universality of ac conduction in disordered solids, Rev. Modern Phys., 72(3) (2000) 873. https://doi.org/10.1103/RevModPhys.72.873.

A. Eftekhari, T.J.E.P.J. Saito, Synthesis and properties of polymerized ionic liquids, 90 (2017) 245. https://doi.org/10.1016/j.eurpolymj.2017.03.033.

Emin, D., 2013. Polarons. Cambridge University Press.

L.C. Fernandes, D.M. Correia, C. García-Astrain, N. Pereira, M. Tariq, J.M. Esperanca, S.J. A.a.m. Lanceros-Mendez, interfaces, ionic-liquid-based printable materials for thermochromic and thermoresistive applications, 11(22) (2019) 20316. https://doi.org/10.1021/acsami.9b00645.

M. Forsyth, L. Porcarelli, X. Wang, N. Goujon, D. Mecerreyes, Innovative electrolytes based on ionic liquids and polymers for next-generation solid-state batteries, Acc. Chem. Res., 52(3) (2019) 686. https://doi.org/10.1021/acs.accounts.8b00566.

Frenzel, F., Folikumah, M.Y., Schulz, M., Anton, A.M., Binder, W.H., Kremer, F., 2016a. Molecular dynamics and charge transport in polymeric polyisobutylene-based ionic liquids. Macromolecules 49 (7), 2868. https://doi.org/10.1021/acs.macromol.6b00011.

Frenzel, F., Binder, W.H., Sangoro, J.R., Kremer, F., 2016b. Glassy dynamics and charge transport in polymeric ionic liquids. Dielectric Properties of Ionic Liquids, p. 115. https://doi.org/10.1007/978-3-319-32489-0_5.

F. Frenzel, M.Y. Folikumah, M. Schulz, A.M. Anton, W.H. Binder, F.J.M. Kremer, Molecular dynamics and charge transport in polymeric polyisobutylene-based ionic liquids, Macromolecules, 49(7) (2016) 2868. https://doi.org/10.1021/acs.macromol.6b00011.

Frenzel, F., Guterman, R., Anton, A.M., Yuan, J., Kremer, F., 2017. Molecular dynamics and charge transport in highly conductive polymeric ionic liquids. Macromolecules 50 (10), 4022. https://doi.org/10.1021/acs.macromol.7b00554.

Frenzel, F., Borchert, P., Anton, A.M., Strehmel, V., Kremer, F., 2019. Charge transport and glassy dynamics in polymeric ionic liquids as reflected by their inter- and intramolecular interactions. Soft Matter 15 (7), 1605. https://doi.org/10.1039/C8SM02135J.

Fukaya, Y., Sugimoto, A., Ohno, H., 2006. Superior solubility of polysaccharides in low viscosity, polar, and halogen-free 1,3-dialkylimidazolium formates. Biomacromolecules 7 (12), 3295. https://doi.org/10.1021/bm060327d.

T. Gao, J. Itliong, S.P. Kumar, Z. Hjorth, I. Nakamura, Polarization of ionic liquid and polymer and its implications for polymerized ionic liquids: an overview towards a new theory and simulation, J. Pharmac. Sci., 59(21) (2021) 2434. https://doi.org/10.1002/pol.20210330.

S. Havriliak, S.J.P. Negami, A complex plane representation of dielectric and mechanical relaxation processes in some polymers, 8 (1967) 161. https://doi.org/10.1016/0032-3861(67)90021-3.

P.A. Hunt, C.R. Ashworth, R.P. Matthews, Hydrogen bonding in ionic liquids, Chem. Soc. Rev., 44(5) (2015) 1257. https://doi.org/10.1039/C4CS00278D.

R. Joshi, T.K. Ghanty, Hydrogen bonding interaction between HO2 radical and selected organic acids, RCOOH (R= CH3, H, Cl and F), Chem. Phys. Lett., 584 (2013) 43. https://doi.org/10.1016/j.cplett.2013.08.025.

N. Kiriy, S. Özenler, P. Voigt, O. Kobsch, J. Meier-Haack, K. Arnhold, A. Janke, U.L. Muza, M. Geisler, A.. Lederer, Optimizing the ion conductivity and mechanical stability of polymer electrolyte membranes designed for use in lithium ion batteries: combining imidazolium-containing poly (ionic liquids) and poly (propylene carbonate), Int. J. Oral Maxillofac. Surg., 25(3) (2024) 1595. https://doi.org/10.3390/ijms25031595.

Kosmulski, M., Gustafsson, J., Rosenholm, J.B., 2004. Thermal stability of low temperature ionic liquids revisited. Thermochim. Acta 412 (1), 47. https://doi.org/10.1016/j.tca.2003.08.022.

Kremer, F., Schönhals, A., 2002. Broadband Dielectric Spectroscopy. Springer Science & Business Media. https://doi.org/10.1007/978-3-642-56120-7.

S.-W. Kuo, Hydrogen-bonding in polymer blends, J. Polym. Res., 15(6) (2008) 459. https://doi.org/10.1007/s10965-008-9192-4.

Lu, J., Yan, F., Texter, J., 2009. Advanced applications of ionic liquids in polymer science. Prog. Polym. Sci. 34 (5), 431. https://doi.org/10.1016/j.progpolymsci.2008.12.001.

Matuszek, K., Piper, S.L., Brzęczek-Szafran, A., Roy, B., Saher, S., Pringle, J.M., MacFarlane, D.R.J.A.M., 2024. Unexpected Energy Applications of Ionic Liquids, 2313023.

K.M. Meek, Y.A. Elabd, Polymerized ionic liquid block copolymers for electrochemical energy, 3(48) (2015) 24187. https://doi.org/10.1039/C5TA07170D.

R.L.J.F.r. Mikkelsen, Using hydrophilic polymers to control nutrient release, 38 (1994) 53. https://doi.org/10.1007/BF00750062.

Mirzaei-Saatlo, M., Asghari, E., Shekaari, H., Pollet, B.G., Vinodh, R., 2024. Performance of ethanolamine-based ionic liquids as novel green electrolytes for the electrochemical energy storage applications. Electrochim. Acta 474, 143499. https://doi.org/10.1016/j.electacta.2023.143499.

V. Mohan, W. Qiu, J. Shen, W. Chen, Electrical properties of poly (vinyl alcohol)(PVA) based on LiFePO 4 complex polymer electrolyte films, J. Polym. Res., 17 (2010) 143. https://doi.org/10.1007/s10965-009-9300-0.

P. Mohapatra, A.K. Barick, Ionic liquids based polymer electrolytes for supercapacitor applications, 626 (2025) 235749. https://doi.org/10.1016/j.jpowsour.2024.235749.

K. Morawska, C.J.C. Wardak, Application of ionic liquids in ion-selective electrodes and reference electrodes: a review, 25(7) (2024) e202300818. https://doi.org/10.1002/cphc.202300818.

Namazi, H.J.B.B., 2017. Polymers in Our Daily Life, 7, p. 73.

D.R. Nosov, E.I. Lozinskaya, D.Y. Antonov, D.O. Ponkratov, A.A. Tyutyunov, M. Alaa Eddine, C. Plesse, D.F. Schmidt, A.S.J.A.P.A. Shaplov, Design of highly conductive PILs by simple modification of poly (epichlorohydrin-co-ethylene oxide) with monosubstituted imidazoles, 4(6) (2024) 512. https://doi.org/10.1021/acspolymersau.4c00051.

W. Ogihara, S. Washiro, H. Nakajima, H.J.E.A. Ohno, Effect of cation structure on the electrochemical and thermal properties of ion conductive polymers obtained from polymerizable ionic liquids, 51(13) (2006) 2614. https://doi.org/10.1016/j.electacta.2005.07.043.

Pârvulescu, V.I., Hardacre, C.J.C.R., 2007. Catalysis in Ionic Liquids, 107, p. 2615. https://doi.org/10.1021/cr050948h.

Pan, J., Wang, Z., Zhang, Z., Chen, J., Cao, Y., 2025. Preparation and performance control of PVA proton exchange membrane incorporating ionic liquids with varying ΔpKa for direct methanol fuel cells. J. Power Sources 629, 236054. https://doi.org/10.1016/j.jpowsour.2024.236054.

Picálek, J., Kolafa, J., 2007. Molecular dynamics study of conductivity of ionic liquids: the Kohlrausch law. J. Mol. Liq. 134 (1), 29. https://doi.org/10.1016/j.molliq.2006.12.015.

Z. Ping, Q. Nguyen, S. Chen, J. Zhou, Y.J.P. Ding, States of water in different hydrophilic polymers—DSC and FTIR studies, 42(20) (2001) 8461. https://doi.org/10.1016/S0032-3861(01)00358-5.

Ray, A., Saruhan, B., 2021. Application of ionic liquids for batteries and supercapacitors. Materials (Basel).

Rodrigues, R.F., Freitas, A.A., Canongia Lopes, J.N., Shimizu, K., 2021. Ionic liquids and water: hydrophobicity vs. Hydrophilicity. Molecules 26 (23). https://doi.org/10.3390/molecules26237159.

R. Salas, R. Villa, F. Velasco, F.G. Cirujano, S. Nieto, N. Martin, E. Garcia-Verdugo, J. Dupont, P.J.G.C. Lozano, Ionic liquids in polymer technology, (2025).

J. Sangoro, C. Iacob, A. Serghei, C. Friedrich, F. Kremer, Universal scaling of charge transport in glass-forming ionic liquids, Soft Matter, 11(6) (2009) 913. https://doi.org/10.1039/B816106B.

Sappl, M., Gross, S., Hugger, P.T., D'Alessio, P., Palka, M., Fritz, S.Felix, Spange, S., Schröder, C., 2025. Decomposition, interpretation and prediction of various ionic liquid solvation parameters: kamlet-Taft, Catalán and Reichardt's ETN. J. Mol. Liq. 417, 126646. https://doi.org/10.1016/j.molliq.2024.126646.

Serghei, A., Tress, M., Sangoro, J.R., Kremer, F., 2009. Electrode polarization and charge transport at solid interfaces. Phys. Rev. B 80 (18). https://doi.org/10.1103/PhysRevB.80.184301.

Shaplov, A.S., Marcilla, R., Mecerreyes, D., 2015. Recent advances in innovative polymer electrolytes based on poly(ionic liquid)s. Electrochim. Acta 175, 18. https://doi.org/10.1016/j.electacta.2015.03.038.

Shin, J.-H., Henderson, W.A., Passerini, S., 2003. Ionic liquids to the rescue? Overcoming the ionic conductivity limitations of polymer electrolytes. Electrochem. Commun. 5 (12), 1016. https://doi.org/10.1016/j.elecom.2003.09.017.

S.K. Shukla, N.D. Khupse, A. Kumar, Do anions influence the polarity of protic ionic liquids?, Phys. Chem. Chem. Phys., 14(8) (2012) 2754. https://doi.org/10.1039/C2CP23256A.

Singh, S.K., Savoy, A.W., 2020a. Ionic liquids synthesis and applications: an overview. J. Mol. Liq. 297, 112038. https://doi.org/10.1016/j.molliq.2019.112038.

S.K. Singh, A.W.J.J.o.M.L. Savoy, Ionic liquids synthesis and applications: an overview, 297 (2020) 112038. https://doi.org/10.1016/j.molliq.2019.112038.
P. Song, H.J.A.M. Wang, High-performance polymeric materials through hydrogen-bond cross-linking, 32(18) (2020) 1901244. https://doi.org/10.1002/adma.201901244.
Spange, S., Lungwitz, R., Schade, A., 2014. Correlation of molecular structure and polarity of ionic liquids. J. Mol. Liq. 192, 137. https://doi.org/10.1016/j.molliq.2013.06.016.
Stark, A., Ott, D., Kralisch, D., Kreisel, G., Ondruschka, B., 2010. Ionic liquids and green chemistry: a lab experiment. J. Chem. Educ. 87 (2), 196. https://doi.org/10.1021/ed8000396.
Su, X., Liu, H., Tian, G., 2024. A green extraction process for the selective recovery of *Sc* (iii) based on hydrophobic betaine derivative ionic liquids. RSC Adv 14 (7), 4853. https://doi.org/10.1039/D3RA08238E.
A.A. Sulaimon, A.N. Masri, M.H.A. Shahpin, N.H.Z.O. Zailani, S.N.A. Baharuddin, M. Moniruzzaman, I.K. Salleh, I.M. Saaid, Synthesis of dihydrogen phosphate-based ionic liquids: experimental and COSMO-RS based investigation for methane hydrate inhibition, J. Molec. Liquids, 319 (2020) 114092. https://doi.org/10.1016/j.molliq.2020.114092.
D.A. Turton, T. Sonnleitner, A. Ortner, M. Walther, G. Hefter, K.R. Seddon, S. Stana, N.V. Plechkova, R. Buchner, K. Wynne, Structure and dynamics in protic ionic liquids: a combined optical Kerr-effect and dielectric relaxation spectroscopy study, Faraday Discuss., 154 (2012) 145. https://doi.org/10.1039/C1FD00054C.
R.L.J.J.o.M.L. Vekariya, A review of ionic liquids: applications towards catalytic organic transformations, 227 (2017) 44. https://doi.org/10.1016/j.molliq.2016.11.123.
S.P. Verevkin, D.H. Zaitsau, R.N. Nagrimanov, Y. Zhang, E.J. Maginn, A. Stark, Symmetry versus asymmetry game in vaporization enthalpies of imidazolium-based ionic liquids, J. Molec. Med., 395 (2024) 123850. https://doi.org/10.1016/j.molliq.2023.123850.
Welton, T.J.C.r., 1999. Room-temperature ionic liquids. Solvents for synthesis and catalysis 99 (8), 2071. https://doi.org/10.1021/cr980032t.
Welton, T., 2011. Ionic liquids in green chemistry. Green Chem 13 (2), 225. https://doi.org/10.1039/C0GC90047H.
Yankova, R., Tankov, I., 2021. Hydrogen bonding effect on the thermal behavior of acidic ionic liquids. J. Mol. Struct. 1238. https://doi.org/10.1016/j.molstruc.2021.130416.
Y. Ye, Y.A.J.P. Elabd, Anion exchanged polymerized ionic liquids: high free volume single ion conductors, 52(5) (2011) 1309. https://doi.org/10.1016/j.polymer.2011.01.031.
M. Yousefi, M. Abdouss, A.A. Miran Beigi, A.. Naseri, Synthesis and characterization of physicochemical properties of hydrophilic imidazolium-based ionic liquids, KSCE J. Civil Eng., 34 (2017) 2527. https://doi.org/10.1007/s11814-017-0150-x.
Zaoui, T., Debdab, M., Haddad, B., Belarbi, E.H., Chaker, Y., Rahmouni, M., Bresson, S., Baeten, V., 2021. Synthesis, vibrational and thermal properties of new functionalized 1- (2-hydroxyethyl) -3-methylimidazolium dihydrogenophosphate ionic liquid. J. Mol. Struct. 1236, 130264. https://doi.org/10.1016/j.molstruc.2021.130264.
Zhang, S.-Y., Zhuang, Q., Zhang, M., Wang, H., Gao, Z., Sun, J.-K., Yuan, J.J.C.S.R., 2020. Poly (ionic liquid) composites 49 (6), 1726. https://doi.org/10.3390/ma14112942.
Zhang, Y., Gu, X., Lin, Z., Suo, H., Xia, J., Zou, B., 2025a. In-situ aqueous phase encapsulation immobilized lipase assisted by acidic ionic liquids for the synthesis of isoamyl acetate. Food Biosci 63, 105607. https://doi.org/10.1016/j.fbio.2024.105607.
Zhang, S., Sun, Q., Martínez-Alanis, P.R., Chen, G., Li, J., Zeng, G., Biendicho, J.J., Ci, L., Cabot, A., 2025b. Towards flame retardant high-performance solid-state lithium metal batteries: poly(ionic liquid)-based lithiophilic ion-conductive interfaces and humidity tolerant binders. Nano Energy 133, 110424. https://doi.org/10.1016/j.nanoen.2024.110424.
Zhang, Z., Lu, L., Hong, B., Ye, Q., Guo, L., Yuan, C., Liu, B., Cui, B., 2025c. Starch/polyacrylamide hydrogels with flexibility, conductivity and sensitivity enhanced by two imidazolium-based ionic liquids for wearable electronics: effect of anion structure. Carbohydr. Polym. 347, 122783. https://doi.org/10.1016/j.carbpol.2024.122783.
M. Zhao, B. Wu, S.I. Lall-Ramnarine, J.D. Ramdihal, K.A. Papacostas, E.D. Fernandez, R. A. Sumner, C.J. Margulis, J.F. Wishart, E.W. Castner, Structural analysis of ionic liquids with symmetric and asymmetric fluorinated anions, J. Clin. Pathol., 151(7) (2019). https://doi.org/10.1063/1.5111643.
M. Zhu, Y.J.G.C. Yang, Poly (ionic liquid) s: an emerging platform for green chemistry, (2024). https://doi.org/10.1039/D4GC00202D.
Zhu, M., 2025. Ionic-liquid/metal–organic-framework composites: synthesis and emerging sustainable applications. Inorg. Chem. Front. 12 (1), 39. https://doi.org/10.1039/D4QI02383H.